Edge Illumination X-Ray Phase Contrast CT

Charlotte Klara Hagen

Department of Medical Physics and Bioengineering

University College London

A thesis submitted for the degree of

Doctor of Philosophy

May, 2014

I, Charlotte Klara Hagen confirm that the work presented in this thesis is my own. Where information has been derived from other sources, I confirm that this has been indicated in the thesis.

Signed: _____

Acknowledgements

My special thanks go to my primary supervisor Prof. Alessandro Olivo for his academic mentoring over the past three years. His enthusiasm, encouragement and support were essential for the completion of this thesis. I express my gratitude also to my second supervisor Prof. Robert Speller, for his open door, and for sharing his rich experience in x-ray imaging.

Special thanks go to the UCL X-Ray Phase Contrast group for the positive work environment, and to Dr. Konstantin Ignatyev and Dr. Magdalena Szafraniec for the joint experimental work in the early days of my PhD. I owe special thanks also to Dr. Peter Munro for fruitful discussions and his ongoing interest in my project.

I would like to thank the scientists of the SYRMEP beamline at Elettra, and of beamline ID17 at the ESRF for their support during the synchrotron experiments, and Dr. Massimo Marenzana and Giorgia Totonelli for making me understand the imaging demands in osteoarthritis and tissue engineering research, and for providing the imaged specimens.

Many thanks go to Dr. Marta Betcke for sharing her expertise in CT reconstruction, and to Patricio Farrell for creative discussions around the mathematical aspects of my work. I would like to express my gratitude to Prof. Olivo, Dr. Paul Diemoz and Tom Millard for proof-reading this thesis.

Finally and most personally, I owe thanks to my parents, my brother Arno and my partner Thomas for their continuous support, belief and reassurance.

Abstract

An unmet demand for high resolution 3D imaging modalities providing enhanced soft tissue contrast exists in a number of biomedical disciplines. X-ray phase contrast (PC) methods can provide a solution: contrast is driven by the refractive index decrement from unity (RID) rather than the absorption term, the former being much larger than the latter for low absorbing materials and energies typically used for biomedical imaging. However, most existing PC methods suffer from drawbacks affecting their implementation outside specialised facilities such as synchrotrons and therefore their applicability to biomedical research. The Edge Illumination (EI) PC method has the potential to overcome or at least mitigate most of these drawbacks. Its major strengths are its simple setup, compatibility with laboratory-based x-ray sources and potential for low-dose imaging. Until now, however, EI had *not* been implemented in computed tomography (CT) mode. The work presented in this thesis bridges this gap.

Practical and theoretical requirements for the CT extension were identified, and experimental EI-CT setups were implemented both at a synchrotron and in a standard laboratory. It was shown that EI-CT allows the reconstruction of maps of a number of physical quantities, including the RID and the absorption term. Quantitative imaging via the reconstruction of the RID was demonstrated to be feasible, and to be limited only by physical effects not accounted for in the phase retrieval model (namely coherence) and, to some extent, polychromaticity. An optimal sampling scheme was derived for laboratory-based EI-CT. This was demonstrated to be compatible with low-dose scans, which is important for *in vivo* imaging. The dose such a system

would deliver to a small animals (e.g. mice) was estimated, and found to be within acceptable limits.

Moreover, new scientific areas that can benefit from the method were identified (e.g. regenerative medicine), and the first ever PC-CT images of acellular organ scaffolds are presented.

Contents

List of Figures

List of Tables

Acronyms

ABI	Analyzer Based Imaging
ACM	Acellular Matrix
AOR	Axis of Rotation
CT	Computed Tomography
CTDI	Computed Tomography Dose Index
DET	Detergent Enzymatic Treatment
DP	Differential Phase
DPC	Differential Phase Contrast
EI	Edge Illumination
ESRF	European Synchrotron Radiation Facility
FBP	Filtered Back Projection
FDK	Feldkamp-David-Kress
FFT	Fast Fourier Transform
FSP	Free Space Propagation
FST	Fourier Slice Theorem
FOV	Field of View
FWHM	Full Width at Half Maximum
GI	Grating Interferometry
HS	Horizontal Sensitivity
IC	Illumination Curve
microCT	Micro Computed Tomography
MIP	Maximum Intensity Projection
MGD	Mean Glandular Dose
MRI	Magnetic Resonance Imaging
NHS	National Health Service

OA	Osteoarthritis
PC	Phase Contrast
PICASSO	Phase Imaging for Clinical Applications with Silicon Detector and Synchrotron Radiation
RID	Refractive Index Decrement
RC	Rocking Curve
SIC	Source-to-Isocentre distance
SYRMEP	Synchrotron Radiation for MEdical Physics
SEM	Scanning Electron Microscopy
TE	Tissue Engineering
TEM	Transmission Electron Microscopy
TLD	Thermoluminescent Dosimeter
TIE	Transport of Intensity Equation
VS	Vertical Sensitivity

Symbols

n	complex refractive index
δ	refractive index decrement
β	absorption term
μ	projected absorption term
Φ	phase function
I	intensity
E	energy
λ	wavelength
k	wave number
$\hbar$	Planck's constant
c	speed of light
κ	linear attenuation coefficient
ρ	electron density
r_e	electron radius
∇	gradient operator
∇^2	Laplacian operator
α	refraction angle
$\mathcal{O}$	object
(s, t)	coordinates in the source plane
(ξ, η)	coordinates in the object plane
(x, y)	coordinates in the detector plane
z	optical axis
z_{so}	source-to-object distance
z_{od}	object-to-detector distance
M	magnification

θ	CT rotation angle
f	object function
$\mathcal{F}$	1D Fourier Transform
$\mathcal{F}_2$	2D Fourier Transform
$\mathcal{R}$	Radon transform
$\mathbf{H}$	Hilbert filter
$C_1,\ C_2$	illumination curves for scanning EI method
C	illumination curve for coded aperture EI method
F	phase retrieval function
$\mathcal{S}$	source spectrum
w	spectral weight
N_{dither}	number of dithering steps
N_{angles}	number of CT angles
$(\Omega, \mathcal{E}, P)$	probability space
D_{medium}	absorbed dose in medium
D_{air}	absorbed dose in air
K_{air}	air kerma
f_c	conversion factor

Chapter 1

Introduction

1.1 The Limits of (Clinical) Radiography

For more than half a century after Wilhelm Roentgen discovered x-rays in 1895, radiography has suffered from two limitations: overlapping structures in a projection image, and poor contrast for low absorbing materials. While the first limitation could be overcome by the construction of the first computed tomography (CT) scanners in the mid-70s (Cormack and Hounsfield, Nobel Prize for Physiology and Medicine in 1979), the latter limitation to a good extent still applies until today.

Conventional radiography (both in 2D and 3D) is an invaluable tool in many instances and plays a well-established role in clinical practice, with an estimated number of 46 million x-ray examinations (including CT scans) carried out in the UK in 2008 (Hart et al. [2010]), trends growing. With x-ray instrumentation being relatively cheap, every hospital within the National Health Service (NHS) is nowadays equipped with radiographic equipment, making fast diagnostic decisions and extensive screening programmes possible.

However, not all diagnostic areas benefit as much as others: the poor contrast for low absorbing details affects areas where the visualisation and differentiation of soft tissues are vital. In mammography, for example, the distinction of tumour tissue from fibrous tissue, in particular in dense breasts, is often still a challenge (Keyrilaeinen et al. [2008], Drukteinis et al. [2013]).

Ways have been found to overcome the limit of poor soft tissue contrast, which are, however, often restricted to special applications. In angiography, for example, the injection of radio-opaque contrast agents into patients enhances the contrast between blood vessels and surrounding fluids and tissue types. In other instances, alternative imaging modalities can provide enhanced soft tissue contrast, but at the cost of acquisition speed or spatial resolution. Magnetic Resonance Imaging (MRI) has undergone rapid technical developments since the beginning of the 80s, facilitating good (and even functional) soft tissue visualisation without the use of ionizing radiation. However, the resolution is typically worse than what can be achieved with x-rays, at least within sensible examination times. Although intrinsically a low resolution device, ultrasound is a cheap and widespread method to examine certain soft tissue types, often in real time. Due to its low penetration depth, it is limited to organs that can easily be accessed by an ultrasound probe, such as the thyroid glands, the ovaries, and glandular tissue close to the surface of the female breast. The imaging of other organs such as brain and lungs is virtually impossible due to the fact that ultrasound waves cannot penetrate bone and, respectively, are strongly reflected by air.

The radiographic limit due to poor contrast for low absorbing details poses a problem also outside the clinics. An important tool for pre-clinical research is a small-animal scanner (usually based on x-ray micro computed tomography (microCT) technology as the organ size in a typical animal model requires high spatial resolution). In order to assess disease evolution or drug response, the correct visualisation of organs such as the lungs, brain, liver or the gastrointestinal tract are often vital. But in addition to poor absorption contrast for these organs, bones are typically present next to soft tissue, and, in a microCT image, the high signal due to the strong absorption properties of bone can have the unwanted effect of masking the low signal arising from the soft tissue almost entirely (Holdsworth and Thornton [2002]).

Although in the above only a few selected examples were listed, it has been emphasized that, although radiography has revolutionised the clinical and preclinical practice in many ways, there is a clear need for improved image contrast in many diagnostic areas, usually those associated with the visualisation of soft tissue types. In the following sub-chapter, an alternative to conventional radiog-

raphy (phase contrast imaging) is introduced. In particular, a physical effect (the phase shift) is described, which is complementary to the absorption properties of a material and which, if exploited in the right way, can lead to enhanced image contrast, specifically for low absorbing materials such as soft tissue.

1.2 Enhanced Contrast due to Phase Effects

When x-rays pass through an object, they do not only get attenuated but they also undergo a phase shift. Both physical phenomena can be linked to the complex refractive index of the object (Als-Nielson and McMorrow [2001]), a dispersive quantity given by:

$$n(E) = 1 - \delta(E) + i\beta(E), \tag{1.1}$$

where E stands for the energy of the x-ray beam used for imaging. The term β drives the absorption and is related to the linear attenuation coefficient of a material via $\kappa = (4\pi\beta)/\lambda$, where λ is the wavelength. The term δ, which is the decrement of unity of the real part of n (in the following shortened to refractive index decrement (RID)), is responsible for phase effects and is linked to the electron density ρ of a material via $\rho = (2\pi\delta)/(r_e\lambda^2)$, where $r_e = 2.82 \cdot 10^{-15}$ m is the electron radius. In the energy regime of x-rays, δ is positive, and, hence, the real part of the complex refractive index is smaller than 1. This is not at odds with relativity as it only implies that the phase velocity of the electromagnetic wave travels faster than light, however, the group velocity does not.

Contrast in conventional (clinical) radiographs is based solely on the attenuation of the x-ray beam. As stated previously, this can lead to insufficient image quality for diagnostic purposes when low absorbing features are imaged.

A fact is that for many materials, in particular low absorbing ones such as soft tissue, the RID can be up to three orders of magnitude larger than the absorption term in the energy range used for clinical x-ray imaging. As an example of this difference, both optical constants for the soft tissue equivalent material polymethyl methacrylate (PMMA) are shown in figure 1.1. The different orders of magnitude are highlighted. Consequently, if the RID can be exploited for

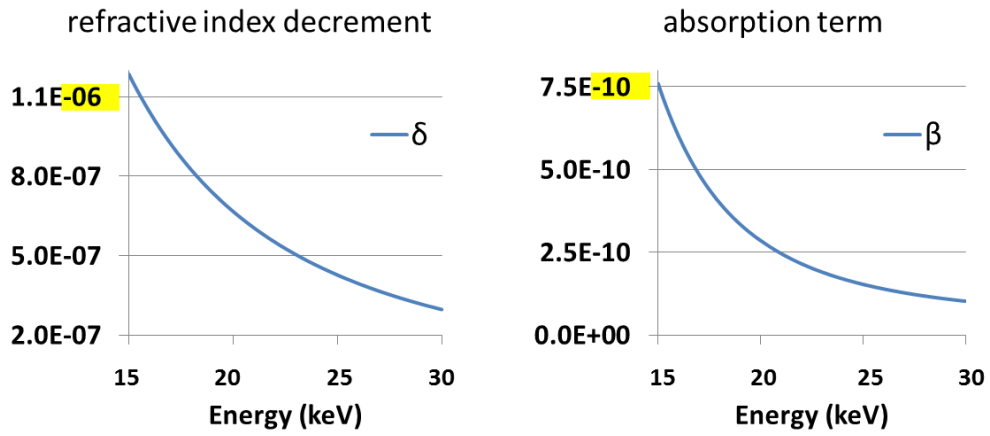

Figure 1.1: The refractive index decrement and the absorption term of the tissue-equivalent material polymethyl methacrylate (PMMA) plotted for x-ray energies from 15-30 keV. Note the different orders of magnitude (highlighted) of the two quantities.

contrast generation rather than or in addition to the absorption term, improved image quality can be expected. In addition, the RID drops slower with increasing energy than the absorption term ($\delta \propto 1/E^2$, $\beta \propto 1/E^4$, where photoelectric absorption is the dominant effect), which means that phase effects can potentially improve image contrast even at higher energies, leading to lower radiation doses deposited in the imaged object (Lewis [2004]).

The effect of the absorption and the phase shift experienced by an x-ray beam due to an object can be described mathematically using a ray optical approach (Gureyev et al. [1995], Gureyev and Wilkins [1998]) or a more complex but rigorous wave optical approach which is based on Fresnel-Kirchhoff diffraction integrals (Born and Wolf [1959], Langer et al. [2008]). Both models lead to approximately the same results if certain simplifying assumptions onto the x-ray beam and the imaged object are made (Peterzol et al. [2005]). To keep the formulas short in this early part of this thesis, only the key result of the ray optics approach, based on the well-known Transport of Intensity Equation (TIE), is presented.

Consider a monochromatic x-ray beam of intensity I_0 and of energy E being

emitted from a point source and being incident onto an object. The intensity of the beam in the plane of the detector located at distance z_{od} downstream of the object (the frame of reference is shown in figure 1.2), is given by:

$$I(x, y; E) = I_0 \cdot e^{-\mu(\xi,\eta;E)} \cdot \left[1 - \frac{z_{od}}{M} \cdot \nabla^2 \Phi(\xi, \eta; E)\right], \tag{1.2}$$

where $x = M\xi$ and $y = M\eta$ are the coordinates in the detector plane, magnified by $M = (z_{so} + z_{od})/z_{so}$, z_{so} is the source-to-object distance and $k = E/(\hbar c)$ is the wave number. The symbol ∇^2 denotes the Laplacian operator in two dimensions. The terms:

$$\mu(\xi, \eta; E) = 2k \cdot \int_{\mathcal{O}} \beta(\xi, \eta, z; E)\ dz \tag{1.3}$$

$$\Phi(\xi, \eta; E) = \int_{\mathcal{O}} \delta(\xi, \eta, z; E)\ dz, \tag{1.4}$$

describe the effect of an object $\mathcal{O}$ in the beam and are essentially the absorption term and the RID projected across the extent of the object along the optical axis. In fact, Φ is effectively the total (local) phase shift. In the course of this thesis, Φ will be referred to as phase function, or also as projected phase. We would like to remark that Φ is often defined with an additional factor of k, which, in this thesis, is consistently included in the associated formulas rather than the definition itself. The TIE can be derived from geometrical optics (Peterzol et al. [2005]), or, more generally in its differential form from the paraxial approximation to the wave equation (Zysk et al. [2010]).

From the TIE it is obvious that phase effects only occur at a distance from the object ($z_{od} > 0$), and are impossible to detect in the contact plane ($z_{od} = 0$), where the detector is placed in conventional radiography. It can also be seen that the strongest phase effects occur at the edges of the object and at boundaries of different features within it, as the phase function is modulated by the Laplacian operator. Therefore, phase effects manifest as fringes of increased and reduced intensity at sharp transitions between areas of different RIDs, and lead to an edge-enhancement effect in the image.

There are essentially two ways to approach the translation of phase effects

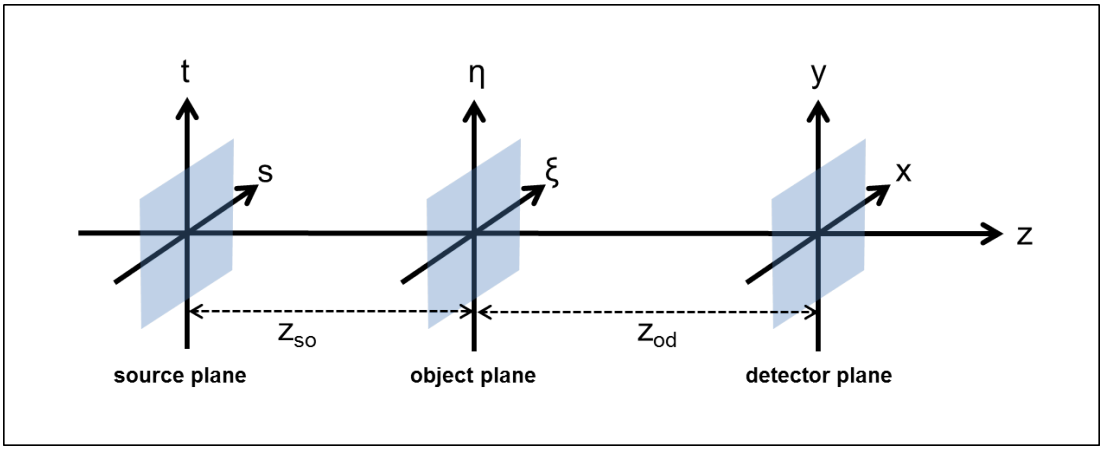

Figure 1.2: Frame of reference for the Transport of Intensity Equation. This reference frame is used for the entire remainder of this thesis.

into image contrast. The first one is to capture the fine interference pattern, generated by an object in the beam (see figure 1.3). A measurement of the intensity of this pattern would provide an edge-enhanced image of the object. The second approach is to note that a distortion of the incoming wave front is locally equivalent to a slight deviation of an individual photon from its original path, an effect known as refraction. The angle by which the photon is deviated (refraction angle) is related to the phase function via:

$$\alpha(\xi, \eta; E) = |\nabla \Phi(\xi, \eta; E)|. \tag{1.5}$$

The refraction angle, which is defined as the angle between the wave vectors of the wave before and after the object, is usually of the order of micro radians or below in the x-ray regime. As it goes with the gradient of the phase function, it is largest at the borders of the object and features within it. Imaging systems sensitive to the refraction angle would also provide edge-enhanced images.

The first phase contrast (PC) imaging method dates back to 1965 (Bonse and Hart [1965]). Since the mid-90s, several other methods to translate phase effects into image contrast have been developed. The first implementations have taken place at synchrotron facilities, leading to impressive publications that have

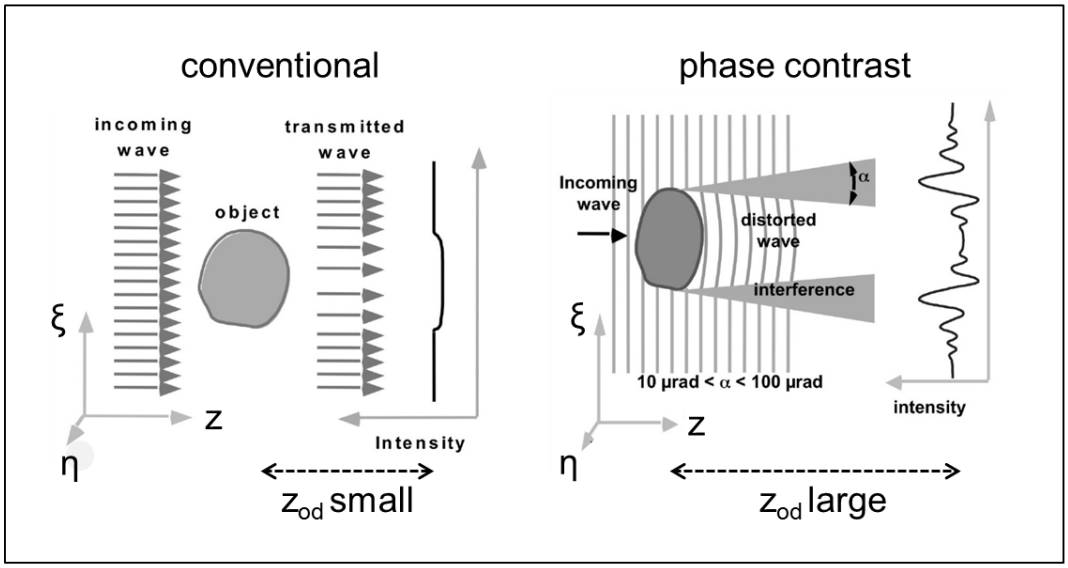

Figure 1.3: Contrast generation in conventional radiography and in x-ray phase contrast imaging.

triggered a huge scientific interest in the field (Snigirev et al. [1995], Ingal and Beliaevskaya [1995], Davis et al. [1995], Olivo et al. [2001], Momose et al. [2003]). Very soon after the first experiments, PC imaging was also demonstrated with micro-focal x-ray sources (Wilkins et al. [1996]). During the first decade of the 21st century, the translation of phase imaging methods from synchrotrons into laboratories was the focus of further extensive research - ultimately, the success of any imaging technique also depends on its practicability and widespread applicability -, and it was demonstrated that phase effects can be exploited also with standard non-micro focal x-ray sources (Pfeiffer et al. [2006],Olivo and Speller [2007a]). This has been considered a huge step forward, as the use of micro-focal x-ray sources for PC results in long acquisition times due to low flux (Wilkins et al. [1996]). A short review of the state-of-the art and remaining limitations of PC imaging methods is given in chapter 2.2, but can also be found in more detail in a recent review paper on the topic (Bravin et al. [2013]).

Alongside the development of the PC methods, an extensive investigation of various applications that can benefit from this alternative contrast mechanism has taken place. Breast (e.g. Pisano et al. [2000], Arfelli et al. [2000], Stam-

panoni et al. [2011], Olivo et al. [2013]) and cartilage (e.g. Mollenhauer et al. [2002], Marenzana et al. [2012]) imaging are two examples of applications that were identified to benefit from the exploitation of phase effects. A more detailed literature review of the application of PC to the imaging of cartilage is given in chapter 3.2.

1.3 The Need for Laboratory-Based Phase Contrast CT: Project Motivation

The demonstration that PC imaging can provide improved results in areas that are regarded difficult in absorption-based imaging has motivated the development of phase contrast CT (PC-CT) methods. In many applications (e.g small animal imaging) CT is required to fully appreciate the volumetric structures of organs and to assess disease development (e.g. via tumour margins) and treatment response. Another advantage of CT over planar imaging is that the reconstructed maps have the potential to be quantitative, i.e. the grey values in the voxels can be linked directly to specific materials (via the Hounsfield units in absorption-based CT, and the reconstructed RID in PC-CT).

Most planar PC methods have now been extended to CT (Momose et al. [1996], Cloetens et al. [1996], Dilmanian et al. [2000], Weitkamp et al. [2005], Momose et al. [2006]). A detailed review of the existing PC-CT methods is given in chapter 2.3.2. The possibility of PC-CT has rapidly broadened the spectrum of potential applications and has given further insight into applications that had been identified already in planar PC. PC-CT of the breast was performed by several groups (e.g. Bravin et al. [2007], Keyrilaeinen et al. [2008]). An important step towards PC-CT mammography, based on fast and low-dose acquisition schemes, was demonstrated by (Zhao et al. [2012]). PC-CT of articular cartilage was approached both *ex vivo* (Coan et al. [2008]) and *in vivo* (Coan et al. [2010b]). As mentioned before, the application of PC imaging to cartilage is discussed in more detail in chapter 3.2. The imaging of soft tissue organs was extended to liver (Noel et al. [2013]), pancreas (Tapfer et al. [2013]), lymph nodes (Jensen et al. [2013]) and brain (Pfeiffer et al. [2007b]). Furthermore, PC-CT was applied

to atherosclerotic plaques (Hetterich et al. [2013]).

As stated in the previous chapter, not all PC methods can be implemented with laboratory x-ray equipment (if sensible acquisition times are required). In fact, only two PC methods have so far been demonstrated to be compatible with non-synchrotron and non-micro focal x-ray sources (Pfeiffer et al. [2006], Olivo and Speller [2007a]). The factors that restrict some of the planar methods to synchrotrons also apply to their CT extensions. The possibility to perform PC-CT outside synchrotrons with conventional equipment is essential for a widespread application. The limited number of synchrotrons worldwide, together with strict application procedures for beam time mean that only a small group of researchers can have access. Synchrotron-based methods are therefore not suited to all applications. Small animal imaging, for example, requires scans to be performed repeatedly in order to follow disease development and to assess long term responses to new drugs. Such long term studies require PC-CT scanners directly installed in the laboratories where the research is taking place. Most importantly, the possibility to perform PC-CT with standard equipment is indispensable with regards to the highly desired translation into the clinical radiographic practice (Lewis [2004]).

The first PC method that can be implemented with laboratory-based x-ray sources is known as Talbot/Lau or Grating Interferometry (GI). CT extensions of the method (GI-CT) exist (Pfeiffer et al. [2007a], Bech et al. [2009], Herzen et al. [2009]). The laboratory implementations of GI and GI-CT are, however, associated with several shortcomings that have so far prevented their successful transition into clinical and pre-clinical practice, the most striking one being the delivery of unacceptable radiation doses (Tapfer et al. [2012]). Longer reviews of GI and GI-CT are given in chapters 2.2.3 and 2.3.2 respectively.

The other PC method that can be implemented with laboratory-based x-ray sources is the Edge Illumination (EI) method. EI originates from experiments at the Elettra synchrotron (Trieste, Italy) in the late 90s (Olivo et al. [2001]) and has, since then, been under continuous development at UCL (Olivo and Speller [2007b], Munro et al. [2010b], Munro et al. [2013b], Millard et al. [2013]). An introduction to the method, covering both its synchrotron and laboratory imple-

mentations, is provided in chapter 2.2.5. Besides an unprecedented phase sensitivity when implemented at synchrotrons (Diemoz et al. [2013]), and a sensitivity that is comparable to that of GI when implemented in laboratories (Diemoz et al., accepted for publication in Applied Physics Letters), EI overcomes some of the problems (e.g. excessive doses) of GI. This will also be discussed in chapter 2.2.5.

EI had, until now, been the only PC method *not* extended to CT. Motivated by EI's simple setup (explained in chapter 2.5.5), high sensitivity and compatibility with laboratory x-ray sources, the aim of this research project was to develop EI-CT. The development comprised the following steps:

- the identification of new scientific areas that can benefit from a laboratory-based EI-CT scanner;
- the provision of practical and theoretical requirements for the transition from planar to tomographic EI;
- the investigation of quantitative EI-CT imaging;
- the demonstration of the possibility of low-dose EI-CT scans.

The development of EI-CT is the content of this thesis and the efforts undertaken are outlined in the next sub-chapter.

1.4 Thesis Outline

The introduction is followed by a chapter providing additional background information on PC imaging. Therein, a brief presentation of the existing planar PC methods is given, together with the advantages and limitations associated with each of them. After a short introduction to the mathematics of CT, the existing PC-CT methods are reviewed with focus on their experimental setups, the used CT reconstruction procedures, quantitative imaging and dosimetry.

Before describing the development of EI-CT in chapters 4-6, chapter 3 is concerned with the identification of new applications that can benefit from PC-CT. Two experiments are described, in which existing PC-CT methods were applied

to new scientific areas that had not yet, or inadequately, been covered in the literature, showing proof-of-principle results that function as further motivation for the development of EI-CT.

In chapter 4, the practical and theoretical bases for a CT extension of EI are provided. These include the description of phase retrieval algorithms developed particularly for EI, which will prove to be the basis for quantitative phase tomography. Further, it is described how the mathematical framework of CT reconstruction can be adapted to EI and how an existing EI simulation software can be extended to a tomographic setting. Last, two experimental EI-CT setups (one at the Elettra synchrotron and one at the UCL radiation physics laboratories) are described that were used to acquire the data presented in chapters 5-6.

In chapter 5, it is demonstrated that EI-CT can enable material identification via the reconstruction of phase retrieved RID and absorption maps. A custom-built phantom of known materials was imaged with both monochromatic and polychromatic beams. In the latter case, the reconstructed maps were used to estimate the (phase and absorption) effective energies of the used EI-CT scanner. Furthermore, it is shown that an existing method to perform quantitative imaging without phase retrieval (Diemoz et al. [2011]) can be extended to EI-CT.

Chapter 6 is solely concerned with laboratory-based EI-CT. We provide a data acquisition scheme that is optimal in the sense that results cannot be further improved (in terms of quantitative reconstruction and image quality) by increasing the sampling rate of the scanner. This leads to the conclusion that in EI-CT a high sampling rate is simply a means to increase the spatial resolution in the reconstructed images, which enables a more flexible control of the delivered dose as no lower limit is set by sampling constraints. Following the derivation of this low-dose acquisition scheme, the dose delivered by the used EI-CT scanner is estimated for the particular case of small animal imaging. Images of selected biological objects acquired with the low-dose scheme are presented.

Finally, we summarize our work in chapter 7, draw conclusions and highlight our own contributions to the field of PC-CT. This thesis concludes with suggestions for the improvement of EI-CT. Reconstruction artefacts are discussed, some of which are well-known and occur also in absorption-based CT, and others which are specific to EI-CT. Furthermore, we discuss options to further reduce acquisi-

tion speed and dose, two crucial factors determining the usefulness for biomedical applications.

Chapter 2

Existing Phase Contrast Imaging Methods

2.1 Chapter Introduction and Outline

The first part of this chapter explains in brief the experimental setups of the existing PC methods and lists advantages and disadvantages associated with them. We mention how the phase function (equation 1.4) can be extracted from the PC projections, which, for all methods, show combined phase and absorption contrast, by means of method-specific procedures known as phase retrieval procedures.

As becomes clear in the second part of this chapter, the extraction of the phase function is important when performing PC-CT. The methods for which the phase function cannot be extracted directly, but rather its first derivative, can be classified as differential phase contrast (DPC) methods.

Following a short introduction to the mathematics behind tomographic image reconstruction, a detailed literature review on the existing PC-CT methods (all but the EI method) will be provided.

2.2 Planar Methods

2.2.1 Bonse/Hart Interferometry

The first ever developed PC method is Bonse/Hart interferometry, also known as crystal interferometry (Bonse and Hart [1965], Momose and Fukuda [1995]). The method is based on three perfect silicon crystals, which are positioned in front of a detector and aligned with an incoming x-ray beam (see figure 2.1). The first crystal (beam splitter) splits the beam into two identical beams. The second crystal (transmission mirror) redirects the two beams towards each other. Before the two beams meet in the plane of the third crystal (analyser), one of them passes through the object to be imaged, and experiences a distortion to both wave amplitude and phase. The other beam remains undistorted and serves as a reference. When the disturbed and undisturbed beams are recombined by the third crystal, an interference pattern is generated that can be measured by the detector.

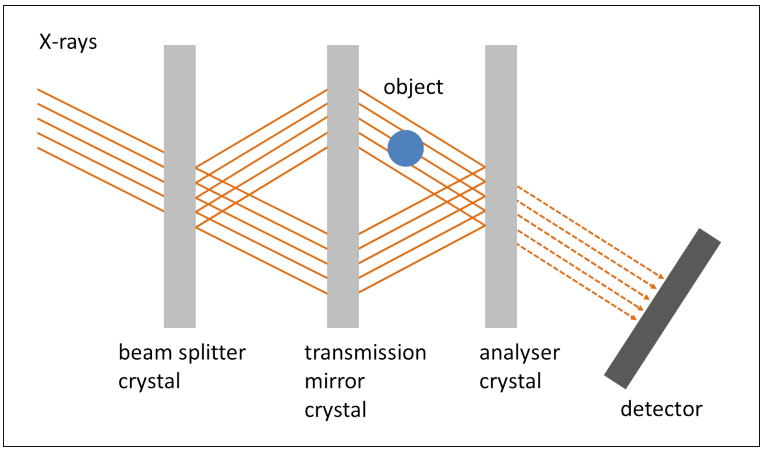

Figure 2.1: Schematic of a Bonse/Hart Interferometer.

The phase function can be extracted from the interference pattern (which encodes both phase and absorption information) via a fringe scanning procedure that requires several interferometric measurements (Momose and Fukuda [1995]). An alternative method to extract the phase function that requires only one interferogram was suggested in (Takeda et al. [1982]).

Bonse/Hart interferometers are highly sensitive to phase effects (Momose [2005]). The method's disadvantage is that a very high stability and precise alignment of the three crystals is required. Due to the high demand on stability, the interferometer is typically cut from a single silicon block, which can only be achieved for small fields of view (FOV) (Momose et al. [1996]). Furthermore, the crystals act as a monochromator, which leads to a considerable reduction of flux, hence to long acquisition times unless powerful synchrotron sources are used. For this reason, the method is not suited for an implementation outside synchrotrons, at least for imaging within sensible acquisition times.

2.2.2 Free Space Propagation

The most straightforward PC method in terms of its experimental setup is Free Space Propagation (FSP), sometimes also referred to as In-Line Holography (Cloetens et al. [1999]). FSP was developed in the early days of PC imaging, using both synchrotron radiation (Snigirev et al. [1995], Cloetens et al. [1996]) and micro-focal x-ray sources (Wilkins et al. [1996]). A FSP setup resembles the one used in conventional radiography, as it only comprises an x-ray beam and a detector and involves no further optical elements. The key difference is, however, that the detector is not placed in contact with the object, but at some distance from it (see figure 2.2). The aim in FSP is to measure the interference pattern that emerges as a consequence of the distortion of the incoming wave front.

The phase function can be extracted if a series of interference patterns are measured at multiple propagation distances (Cloetens et al. [1999]). Another method that requires only a single measurement of the interference pattern is described in (Paganin et al. [2002]). This approach relies on the assumption that the object consists of a single material. The method by Paganin et al. is explained in chapter 3.3. Several other approaches to extract the phase functions are described and compared in Langer et al. [2008] and Burvall et al. [2011].

The advantage of FSP is its simple experimental setup. However, while the demand on temporal coherence is relatively low (Pogany et al. [1997], Olivo and Speller [2006]), the method requires a high degree of spatial coherence (Wu and Liu [2007]). The latter can be achieved at synchrotrons, and outside synchrotrons

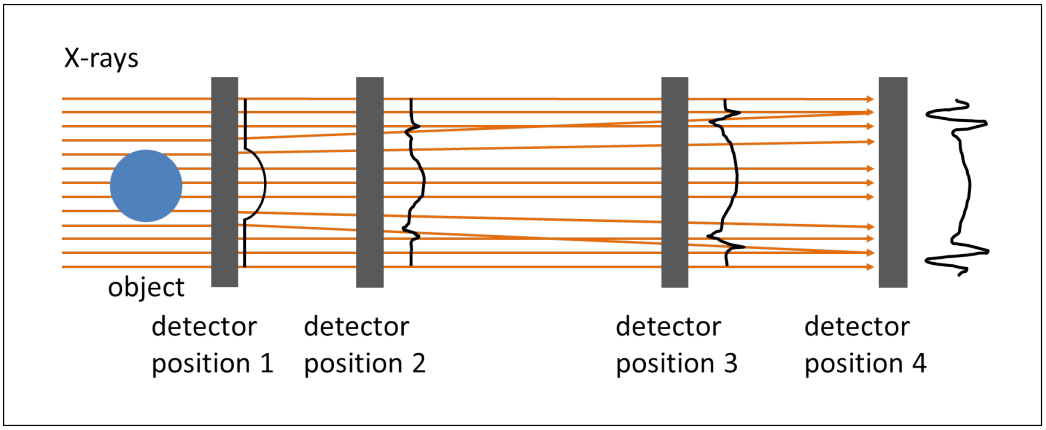

Figure 2.2: Schematic of a Free Space Propagation setup. In contrast with conventional radiography, the detector is placed at some distance from the object.

using micro-focal x-ray sources. However, the low flux of micro-focal x-ray sources can lead to long exposure times for most practical applications (Wilkins et al. [1996]). Moreover, FSP requires high resolution detectors to resolve the fine interference pattern, unless high magnification geometries are used (Pogany et al. [1997]). The latter, however, impose restrictions on the FOV size.

2.2.3 Analyser-Based Imaging

Analyser-Based Imaging (ABI) requires a perfect crystal in addition to a (monochromatic) x-ray beam and a detector. The crystal is positioned between the object and detector as depicted in figure 2.3.

ABI is sensitive to x-ray refraction. For the translation of the refraction angle into image contrast, the method makes use of Bragg diffraction: the crystal's reflectivity is a function of the angle of the incoming beam (known as rocking curve (RC)), which implies that the crystal can be used as an "angular analyser". The RC is monotonically increasing until it reaches its maximum (100 % reflectivity) at the Bragg angle, then monotonically decreasing. Without the object, the intensity measured on the detector is defined by the crystal's reflectivity for the incoming beam angle. If this angle corresponds to one of the slopes of the RC (e.g. to 50% reflectivity), an object in the beam can cause a higher (lower) in-

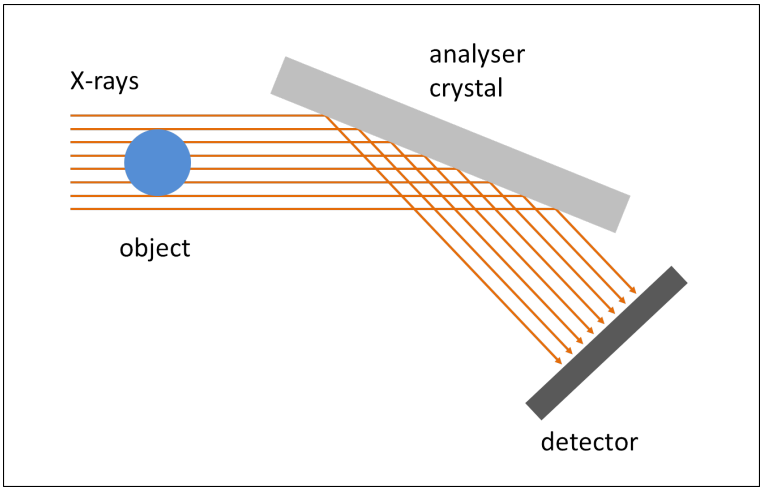

Figure 2.3: Schematic of an Analyser-Based Imaging setup.

tensity measured at the detector due to refraction by a positive (negative) angle. The refraction contrast in ABI can be inverted by rocking the crystal from one slope of the RC to the other.

The first derivative of the phase function can be extracted if two images are acquired with the crystal rocked to both slopes of the RC (Chapman et al. [1997]). Alternative methods, for which the required number of images varies from two to several, are described and compared in Diemoz et al. [2010a]. All methods simultaneously yield the projected absorption term (equation 1.3).

One of the disadvantages of ABI is the high precision alignment of the crystal, requiring a very stable experimental setup. Moreover, as the RC is usually very narrow, the incoming beam needs to be quasi-parallel. This can be achieved by collimation, which, however, leads to a reduction of flux unless powerful synchrotron sources are used. Additionally, the crystal acts as a monochromator, which again implies a flux reduction. Therefore, ABI is not suited for imaging outside synchrotrons, at least within sensible acquisition times.

2.2.4 Grating Interferometry

Another method allowing PC imaging is grating interferometry (GI) (David et al. [2002], Momose et al. [2003]), also known as Talbot or Talbot/Lau interferometry.

The method is based on the Talbot self-imaging effect. Besides an x-ray source and a detector, a typical GI setup contains two gratings (see figure 2.4): a phase grating generates an interference pattern that is a replica of the pattern itself at a given set of (Talbot) distances; typically an absorption (analyser) grating is placed at one of these distances, with a detector immediately behind it. An object introduced upstream of the phase grating distorts the interference pattern, and these distortions manifest as local changes of the intensity in the detected images.

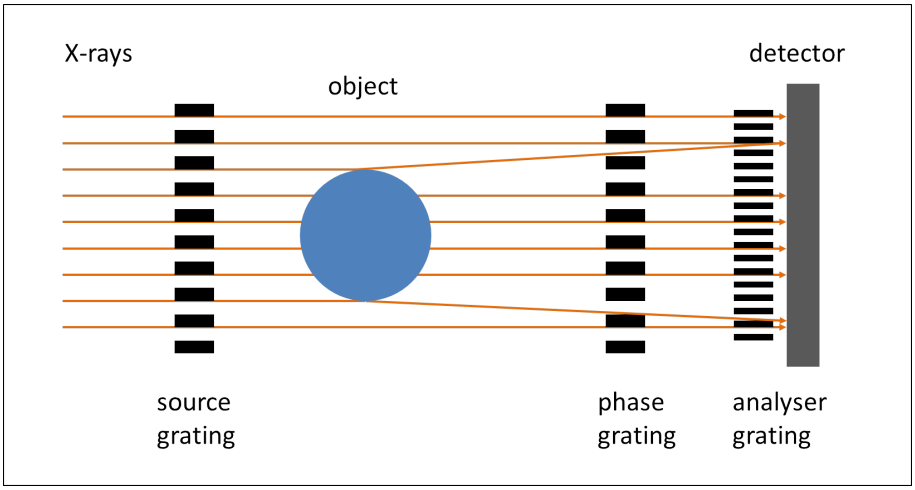

Figure 2.4: Schematic of a grating interferometer in Talbot/Lau configuration. The phase and absorption (analyser) gratings are present in every interferometer; the first grating (source grating) is necessary when the method is used with an incoherent x-ray source.

GI relies on the use of a coherent source (synchrotron or micro-focal), as the formation of a Talbot self-image is an intrinsically coherent effect. However, the method works with extended sources if a third grating is placed in front of the source, generating mutually incoherent but individually coherent source-lets (Pfeiffer et al. [2006]). Adding this source grating corresponds to switching from a Talbot to a Talbot/Lau configuration.

The first derivative of the phase function can be extracted via a phase stepping procedure (Weitkamp et al. [2005]), i.e. by scanning one of the gratings in the transverse (orthogonal both to the grating trenches and x-ray propagation)

direction, and by comparing the distorted intensity with the non-distorted one that has been measured in absence of the object. Phase stepping typically requires images to be taken at several positions of the grating's scan. The procedure simultaneously yields the projected absorption term (equation 1.3).

The laboratory implementation of GI still presents some important shortcomings, which have so far prevented its deployment in "real-world" applications. First, the periods of the gratings are on the order of a few microns, which makes their alignment sensitive to environmental vibrations, and the gratings are difficult to fabricate up to large FOVs (David et al. [2007a]). Especially for high energies, gratings with very high aspect ratios are required, which makes them difficult to produce. Second and most importantly, the radiation dose in GI is not used efficiently. As the phase and absorption (analyser) gratings are placed downstream of the object, a significant fraction of radiation that delivers dose to the object does not contribute to the image formation process. In theory, the phase grating is designed only to introduce a phase shift and not to absorb any radiation; however, in reality, a material with this property does not exist. Also, the phase shifting material must be plated onto a substrate. The absorption grating, on the other hand, is typically made from a high Z material and therefore absorbs a significant amount of radiation. The inefficient use of radiation dose could be one factor leading to delivered doses that are unacceptable in pre-clinical let alone clinical practice when the method is operated in CT mode (Tapfer et al. [2012]). Last, the source grating required when a conventional x-ray source is employed leads to a reduction in flux, and hence to longer exposure times.

2.2.5 Edge Illumination

The last PC method to be presented is the Edge Illumination (EI) method, which was first developed at the Elettra synchrotron using a relatively simple experimental setup (Olivo et al. [2001]): a thin laminar beam is aligned with the edge of a row of pixels, in such a way that a part the beam cross-section falls within the pixel row and the other part falls outside it (figure 2.5 (a,b)).

An object placed in the laminar beam causes attenuation, as well as a slight deviation of its direction (refraction). The effect of having the beam aligned with

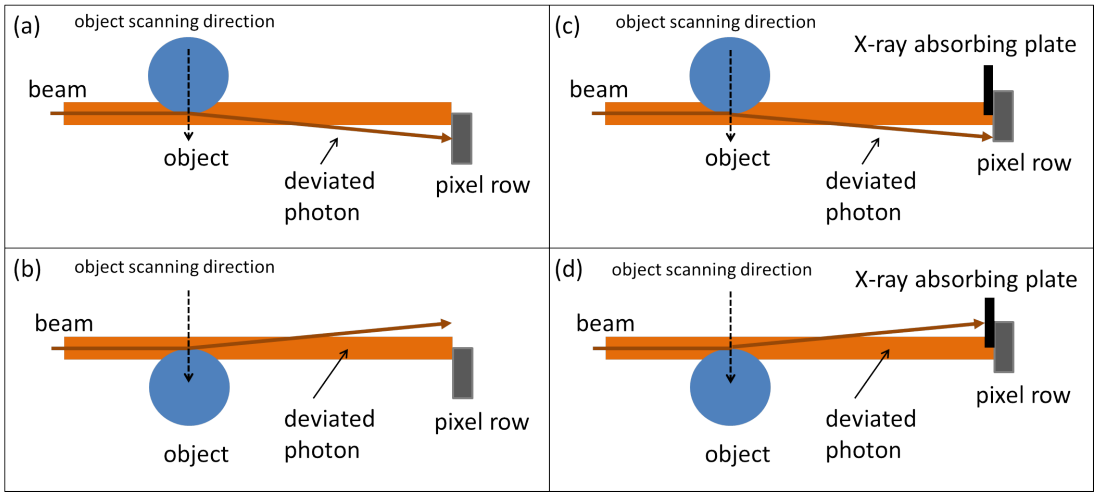

Figure 2.5: Schematic of two possible Edge Illumination setups: a laminar beam illuminates the edge of a pixel row (a,b), and the edge of an x-ray absorbing plate (c,d) positioned in front of the pixels. For each setup, two possible sample positions and the corresponding refraction effects are shown. The object needs to be scanned through the setups in order to build up an image. The drawing extends uniformly into the plane of the paper.

the edge of the pixel row is similar to positioning the beam corresponding to one of the slopes of the RC in ABI: if the beam is refracted by a positive (negative) angle, it gets deviated further out of (further into) the pixel row, which leads to a decrease (increase) of the detected intensity. Changing the beam positioning from one edge of the pixel row to the other leads to the inversion of the refraction contrast, just as it happens when the beam positioning is changed from one slope of the RC to the other in ABI. The same effect as by illuminating the edge of a pixel row can be achieved by placing an x-ray absorbing edge (plate) in front of the pixels and by illuminating the edge of the plate (figure 2.5 (c,d)). In the same way as changing from one edge of the pixel row to the other, the refraction contrast is inverted if the location of the edge is changed from covering one half of the pixels to covering the other. The use of an edge is often more convenient in practice, as it enables the application of the method also with detectors that do not feature sharp pixel transitions. With such setups, a full image of the object can be built up if this is scanned in the vertical direction through the

beam/detector configuration. Therefore, such setups are in the following referred to as scanning EI method. As mentioned in the introduction, the scanning EI method has recently been demonstrated to be extremely sensitive to phase effects when implemented at synchrotrons: notably, refraction angles on the nanoradian scale can be resolved (Diemoz et al. [2013]).

The need to scan the object in order to build up an image is often considered impractical, and the acquisition of a "single-shot" image is favoured. By means of opportunely designed x-ray masks, the EI principle can be extended to large FOVs and the need to scan the object can be eliminated by replicating the EI configuration for multiple rows of pixels. An extended (including divergent) x-ray beam, a 2D area detector and two sets of masks (sometimes termed coded apertures) are required for this extension (Olivo and Speller [2007a], Olivo and Speller [2007b]). One set of coded apertures is placed immediately in front of the detector, and creates insensitive regions between the pixels (detector mask). The other set (sample mask) is positioned immediately upstream of the object, where it splits the incoming beam into individual beamlets. The period of the coded apertures is designed to match the detector pixel size; however the period of the sample apertures needs to be downscaled in order to account for the magnification in case of a divergent beam. If the two sets of apertures are positioned with respect to each other in such a way that each of the beamlets hits the edge of one of the apertures in the detector mask, the EI principle is simultaneously achieved for each row of pixels in a 2D area detector (see figure 2.6) and no object scanning is necessary. Such a setup is in the following referred to as coded aperture EI method.

The sampling rate in coded aperture EI imaging is intrinsically determined by the period of the sample mask. The contrast in the images arises from the beamlets that illuminate the object; conversely, the parts of the object which are not illuminated do not contribute to the image, and the system is in fact "blind" to these areas. However, the sampling rate can be artificially increased by taking multiple projections, each one after the object was moved by a sub-pixel amount, such that eventually the entirety of the object was illuminated by the beamlets. These "frames" can then be combined to a single, resolution-enhanced image. This procedure is known as "dithering". Dithering is different from the

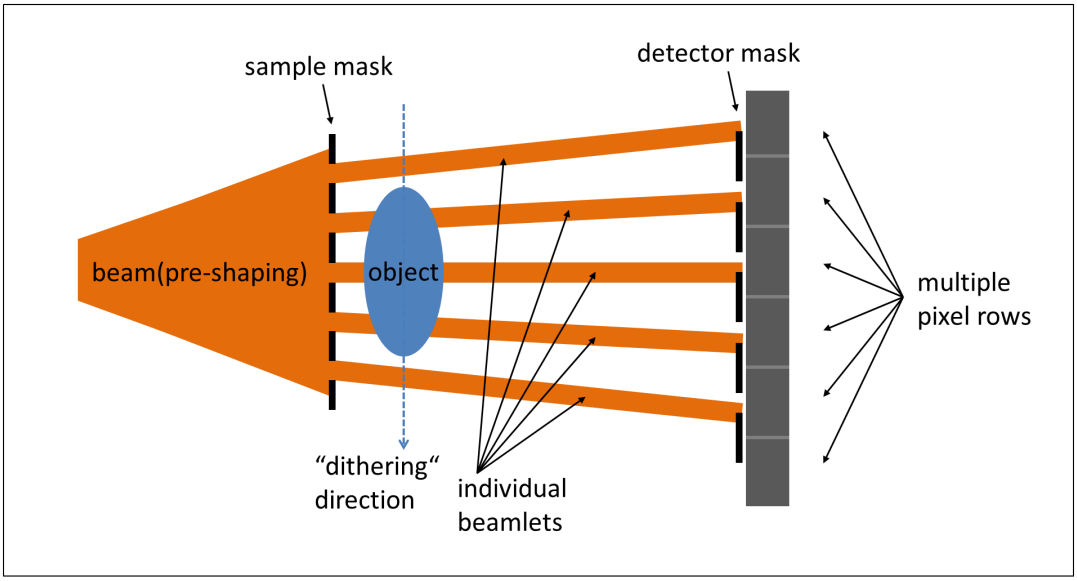

Figure 2.6: Schematic of the Edge Illumination setup implemented with coded apertures. The direction for "dithering" is indicated. The drawing extends uniformly into the plane of the paper.

object scanning required with the scanning EI method, as it is *not* a mandatory requirement to build up a 2D image; instead, dithering is a means to obtain an image with a higher rate of spatial information. The number of required object displacement steps ("dithering steps") depends on the imaged object: if an object is known to consist of bulky structures, a low number, or, in fact, no dithering at all may be sufficient to achieve a high enough sampling rate. If, on the other hand, the object has small features which are of interest, a high number of dithering steps may be necessary to fully capture these in the image. The effect of dithering on quantitative imaging with the coded aperture EI method will be discussed in detail in chapter 6.2

It should be noted that, unlike Bonse/Hart interferometry, FSP and GI, the EI method is totally non-interferometric. The beamlets in the coded aperture EI implementation are separated by a distance sufficiently large for them not to interfere with each other and typically they do not even overlap (Olivo et al. [2011]). In addition, the method was demonstrated not to suffer significantly from the

use of conventional, incoherent x-ray sources. It could further be shown that the setup is achromatic, i.e. all energies present in the source spectrum contribute to the image formation process, including the high energies (Ignatyev et al. [2011]), and that no significant loss in image contrast takes place for sources with focal spot sizes of up to 100 μm (Olivo and Speller [2007b]). The cone-shaped beam emitted by a conventional x-ray source can be used directly and without any further collimation or aperturing. As mentioned in the introduction, more recently, the sensitivity to refraction angles in a coded aperture EI setup implemented with a standard mammography source has been analysed, and estimated to be on the order of about 250 nano radians (Diemoz et al., accepted for publication in Applied Physics Letters).

Because of its compatibility with conventional x-ray sources, the coded aperture EI method is typically used in a laboratory environment, while, for synchrotron experiments, the scanning EI method is often sufficient, as synchrotron beams are laminar and as fast imaging despite object scanning is possible due to the high available x-ray flux.

The derivative of the phase function can be extracted from the EI images showing combined phase and absorption contrast if two projections are acquired: one with the beam aligned with one edge of the pixel row and one with the other for the scanning EI method (one with the beamlets hitting the edges of the detector mask on one side and one on the other for the coded aperture EI method) (e.g. Munro et al. [2012], Munro et al. [2013a], Munro et al. [2013b]). Simultaneously, the projected absorption term (equation 1.3) can be extracted. The extraction of both is discussed in detail in chapter 4.3.

The major strength of the EI method is its versatility. It can be considered a highly sensitive imaging tool at synchrotrons, and, at the same time, has the potential for a widespread application due to its compatibility with conventional x-ray sources. The radiation dose delivered to the object is comparable to that delivered in clinical practice (Olivo et al. [2013]). This is mainly due to the fact that the sample mask is located upstream of the object and, therefore, shields it from parts of the incoming beam that do not contribute to the image formation. Another strength of the method is that the pitch of the masks is much larger than in GI: the lower aspect ratio makes the masks easier and cheaper to fabricate. As

a result of the low aspect ratio, the stability constraints are less strict than in GI, where the period of the used gratings is typically 2-4 micrometers. An automatic alignment procedure for the masks has been developed recently (Millard et al. [2013]), which can be used for a machine-controlled feedback mechanism that keeps the system within stringent alignment bounds throughout an acquisition.

2.3 Extension to CT

2.3.1 The Mathematical Framework of Computed Tomography

Computed Tomography (CT) is a 3D imaging method providing a solution to the problem of overlapping structures in planar radiography. The first CT scanners entered clinical practice in the mid-70s, but the underlying theoretical principle dates back to a paper by the Austrian Mathematician Johann Radon published in 1917.

Radon could show that volumetric objects can be reconstructed from a set of projections acquired from several view angles. In a practical setup, this means that a radiographic imaging system rotates around the object and a series of radiographic images are acquired. Clinical CT scanners make use of a gantry carrying the x-ray source and detector that rotate around the patient bed. An equivalent approach, often used in prototype scanners, is to keep the source/detector combination stationary while the object, placed on a dynamic stage, is rotated. The total rotation of the gantry or the dynamic object stage is required to cover at least 180 degrees.

In its simplest form, CT reconstruction is performed on a slice-by-slice basis ("tomography" is the Greek word for "slice imaging"), and a volumetric representation of the imaged object is created by stacking up the reconstructed slices. Algorithms for CT reconstruction can be categorised into one of two classes: filtered back-projection type algorithms that are based on an analytic approach, and iterative algorithms that are based on algebraic or statistical approaches. In this section, the most commonly used representative of the first category, the filtered back-projection (FBP) formula, is briefly presented together with an im-

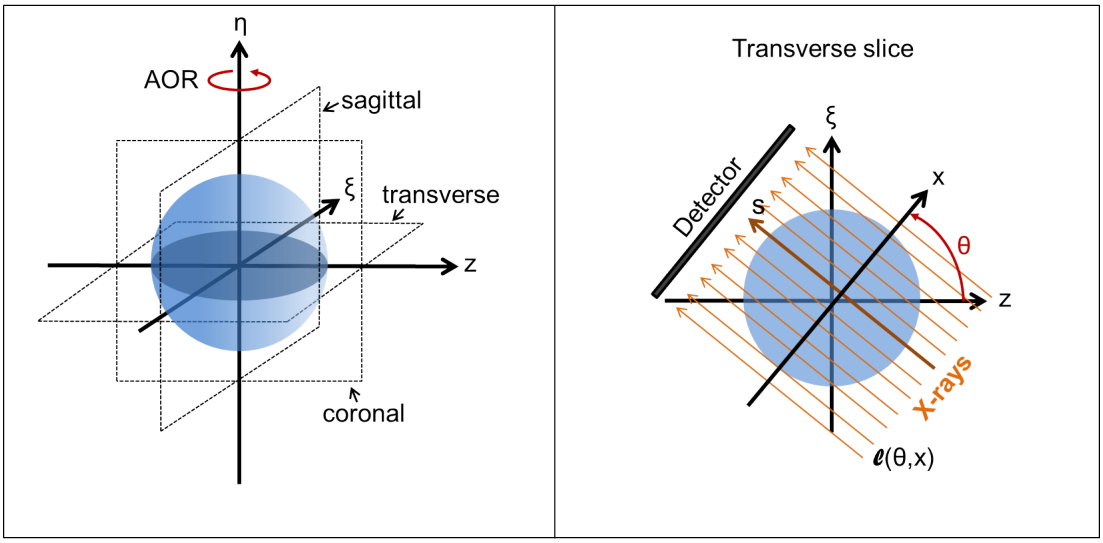

Figure 2.7: Frame of reference for a rotating imaging system and a stationary object.

portant underlying theoretical result, the Fourier Slice Theorem (FST). The use of iterative reconstruction algorithms goes beyond the scope of this thesis, however, possible advantages over the FBP will be discussed in the context of future work in chapter 7. For a more detailed introduction to the mathematics of CT, we refer to standard textbooks such as (Natterer [1986], Kak and Slaney [1987], Feeman [2010]).

2.3.1.1 Radon Transform, Fourier Slice Theorem and Filtered Back Projection

In the following, the reference frame shown in figure 2.7 will be considered. Let $f = f(\xi, z)$ denote a function describing a physical quantity within a transverse slice of an object that is supposed to be reconstructed, in the following referred to as object function. An x-ray traversing the object in that transverse slice can be described by:

$$\ell(\theta, x; s) = (x\cos\theta - s\sin\theta, x\sin\theta + s\cos\theta), \tag{2.1}$$

where x denotes the position of the ray on the detector, θ is the rotation angle

and s is a parameter describing the ray path. The Radon transform of f is defined as its integral along the line ℓ (line integral), i.e.

$$\mathcal{R}f(\theta, x) \coloneqq \int_{\ell(\theta,x;s)} f ds = \int_{-\infty}^{\infty} f(x\cos\theta - s\sin\theta, x\sin\theta + s\cos\theta) ds. \tag{2.2}$$

The Radon transform can be recorded during a CT scan as it is formed by the set of angular projections. The Radon transform, also called a sinogram, is related to f not only via the forward projection given by equation 2.2, but also via a Fourier transform relationship known as Fourier Slice Theorem:

$$\mathcal{F}_2(f)(S\cos\theta, S\sin\theta) = \mathcal{F}(\mathcal{R}f)(S, \theta). \tag{2.3}$$

It states that the one-dimensional Fourier transform (denoted by $\mathcal{F}$) of a projection of the object function is equal to the two-dimensional Fourier transform (denoted by $\mathcal{F}_2$) of the object function itself, evaluated along a straight line through the origin, rotated by the angle θ (see figure 2.8). The FST implies that the object function can be reconstructed via Fourier inversion if an infinite number of projections is acquired. However, as this number is in practice finite, this inversion method requires the interpolation of the missing data points in Fourier space, which is associated with reconstruction artefacts Feeman [2010]. Therefore, in practice, equation 2.2 is inverted in a different fashion, namely via the widely used FBP formula:

$$f(\xi, z) = \frac{1}{2\pi} \int_0^{\pi} \left\{ \mathcal{F}^{-1} \left[|S| \mathcal{F}(\mathcal{R}f)(S, \theta) \right] \right\} d\theta. \tag{2.4}$$

The effect of the FBP is basically a "smearing" (back-projection) of the projections along the trajectories given by ℓ. Prior to the back-projection, it is essential to filter the projections, which is explained by the FST: the data points in Fourier space lie on a radial grid and their density decreases with the radius. The data points further away from the origin are the high frequencies in the image, which have to be amplified in order to prevent the reconstruction of f from being blurred. The analytically correct filter is the absolute value function (represented in equation 2.4 by the term $|S|$). In practice, this function is often

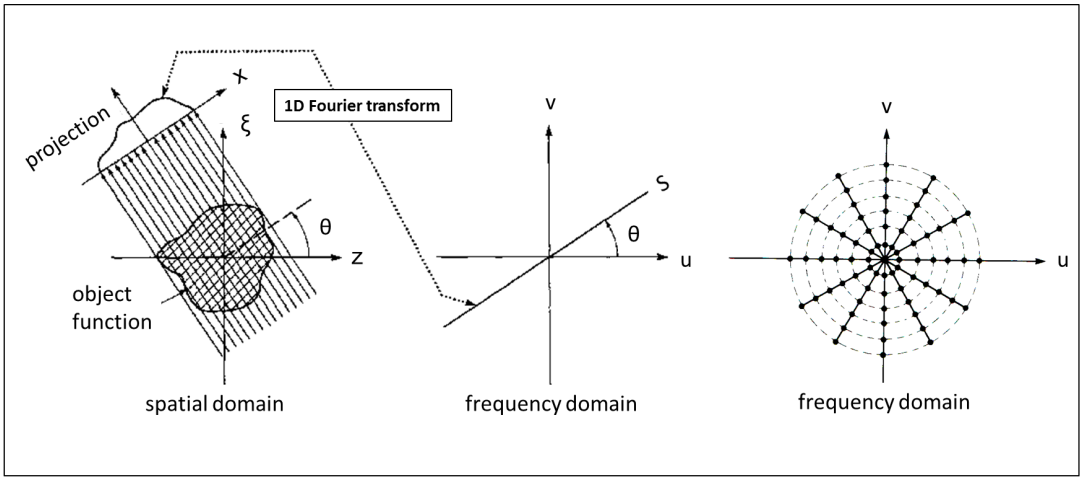

Figure 2.8: Graphical visualisation of the Fourier Slice Theorem. Figure adopted from (Kak and Slaney 1988).

set to zero above a certain frequency, in order to crop off high frequency noise. This Ram-Lak (or ramp) filter is the most common, but also other filter functions such as the Shepp-Logan filter, the cosine filter and the Hamming window can be encountered. Often, the filter function is tailored to the noise properties of the imaging system.

In the above, it was assumed that a laminar and parallel beam is used for the CT data acquisition. This condition can be achieved via collimation of the beam, which can lead to reduced flux for non-synchrotron sources. In practice, an uncollimated cone-beam is often used. If the cone angle is sufficiently small (for example for small FOVs), the FBP can still be applied for the reconstruction. Otherwise, an extension of the FBP to a cone-beam geometry has to be applied, the most common being the Feldkamp-David-Kress (FDK) algorithm (Feldkamp et al. [1984]).

2.3.1.2 The Importance of the Phase Function for Phase Contrast CT

In conventional radiography, a line integral relationship between projections and object function is given by the Beer-Lambert law:

$$P(x,y) = -\ln \frac{I(x,y)}{I_0} = \mu = 2k \cdot \int_{\mathbb{O}} \beta(\xi,z,\eta)\ dz, \tag{2.5}$$

where x and y are the coordinates on the detector. The object function is the absorption term, i.e. $f = \beta$. In a CT geometry, i.e. when the imaging system rotates around the object, P becomes proportional to the Radon transform of β:

$$P(\theta,x) = -\ln \frac{I(\theta,x)}{I_0} = \mu = 2k \cdot \int_{\ell(\theta,x;s)} \beta(\xi,z)\ ds = 2k \cdot \mathcal{R}\beta(\theta,x). \tag{2.6}$$

The dependence on the vertical coordinates y and η has been dropped as only a single transverse slice is considered. A map of β can be reconstructed from the sinogram P by applying the FBP.

In PC imaging, a line integral relationship between projections and object function is given by the phase function. The object function is the RID, i.e. $f = \delta$. In PC-CT, i.e. when the phase function is extracted at every rotation angle, it becomes the Radon transform of δ:

$$P(\theta,x) = \Phi(\theta,x) = \int_{\ell(\theta,x;s)} \delta(\xi,z)\ ds = \mathcal{R}\delta(\theta,x). \tag{2.7}$$

If Φ is known, a map of δ can be reconstructed with the FBP. However, as explained above, for the DPC methods the phase function cannot be extracted directly, but only its first derivative. Hence, the sinograms are of the form:

$$P(\theta,x) = \frac{\partial}{\partial x}\Phi(\theta,x) = \frac{\partial}{\partial x}\mathcal{R}\delta(\theta,x). \tag{2.8}$$

The derivative needs to be accounted for in the reconstruction, which will be explained in the next sub-chapter.

Besides the (first derivative of) the phase function, the phase retrieval procedures for the DPC methods simultaneously yield the projected absorption term

(equation 2.6). Therefore, the maps of β can always be reconstructed as a by-product. The reconstruction of the absorption term actually makes PC-CT intrinsically "multi modal".

2.3.1.3 Reconstruction From First Derivative Data

For the DPC methods, the extracted derivative of the phase function corresponds, depending on the experimental setup, to the horizontal or the vertical direction. The corresponding sinograms are given by:

$$P_{hor}(\theta, x, y) = \frac{\partial}{\partial x}\mathcal{R}f(\theta, x, y) \tag{2.9}$$

$$P_{ver}(\theta, x, y) = \frac{\partial}{\partial y}\mathcal{R}f(\theta, x, y), \tag{2.10}$$

where $f = \delta$. In either case, f can be reconstructed via the FBP if the sinogams are integrated prior to back-projection:

$$f(\xi, z, \eta) = \frac{1}{2\pi}\int_0^\pi \left\{\mathcal{F}^{-1}\left[|S|\mathcal{F}(\int_{x_0}^{x} P_{hor}dx)(S, \theta)\right]\right\} d\theta \tag{2.11}$$

$$f(\xi, z, \eta) = \frac{1}{2\pi}\int_0^\pi \left\{\mathcal{F}^{-1}\left[|S|\mathcal{F}(\int_{y_0}^{y} P_{ver}dy)(S, \theta)\right]\right\} d\theta \tag{2.12}$$

The constant of integration can be fixed by noting that the object is surrounded by an empty region where $f = 0$.

By exploiting the fact that the Fourier transform of a derivative of a function equals the Fourier transform of the function itself multiplied by a frequency term, an equivalent inversion formula can be derived when the derivative corresponds to the *horizontal* direction:

$$\mathcal{F}(\frac{\partial}{\partial x}\mathcal{R}f)(S) = iS \cdot \mathcal{F}(\mathcal{R}f), \tag{2.13}$$

which implies that f can be recovered from P_{hor} if the filter function $|S|$ is scaled

by the frequency term $1/iS$:

$$f(\xi, z) = \frac{1}{2\pi} \int_0^{\pi} \left\{ \mathcal{F}^{-1} \left[\frac{|S|}{iS} \mathcal{F}(P_{hor})(S, \theta) \right] \right\} d\theta. \tag{2.14}$$

Note that the filtering term in equation 2.14 can be written as:

$$\mathbf{H}(S) = \frac{|S|}{iS} = -i \cdot \text{sign}(S). \tag{2.15}$$

Since $\mathbf{H}$ describes the Hilbert transform in Fourier space, this filter function is known as the Hilbert filter. The Hilbert filter plays an important role in PC-CT reconstruction and has, therefore, been "derived" in a number of publications in the field (Huang et al. [2006], Qi and Chen [2008]). However, the role of the Hilbert transform had already been appreciated by Johann Radon himself and is part of his original reconstruction formula published in 1917 (Feeman [2010]).

In equations 2.9 and 2.10, it is allowed in practice to move the derivative operator inside the Radon transform, which would imply the reconstruction of the differential of f. This can be beneficial in situations where it is important to visualise boundaries and sharp transitions within the object. In the case of a vertical derivative, the FBP can be applied directly to $P_{ver} \approx \mathcal{R}(\partial f/\partial y)$:

$$\frac{\partial f}{\partial y}(\xi, z) = \frac{1}{2\pi} \int_0^{\pi} \left\{ \mathcal{F}^{-1} \left[|S| \mathcal{F}(P_{ver})(S, \theta) \right] \right\} d\theta \tag{2.16}$$

In the case of a horizontal derivative, the FBP *cannot* be applied directly to $P_{hor} \approx \mathcal{R}(\partial f/\partial x)$. One of the key requirements for CT reconstruction to work is that the function inside the Radon transform operator does not change with the rotation angle (Kak and Slaney [1987]). This is not fulfilled as the direction of the derivative changes with the rotation (the coordinate x lies on the detector which rotates around the object). It is, however, possible to reconstruct the differential of f from P_{hor} by linking the rotating derivative operator $\partial/\partial x$ to the derivative operators with respect to the stationary object coordinates ξ and z via

$\partial/\partial\xi = \partial/\partial x \cdot \cos\theta$ and $\partial/\partial z = \partial/\partial x \cdot \sin\theta$ (Zhu et al. [2005]):

$$\frac{\partial f}{\partial \xi}(\xi, z) = \frac{1}{2\pi} \int_0^{\pi} \left\{ \mathcal{F}^{-1} \left[|S| \mathcal{F}(P_{hor} \cdot \cos\theta)(S, \theta) \right] \right\} d\theta \tag{2.17}$$

$$\frac{\partial f}{\partial z}(\xi, z) = \frac{1}{2\pi} \int_0^{\pi} \left\{ \mathcal{F}^{-1} \left[|S| \mathcal{F}(P_{hor} \cdot \sin\theta)(S, \theta) \right] \right\} d\theta. \tag{2.18}$$

Sometimes it can be advantageous to reconstruct directly from the mixed PC-CT projections showing combined phase and absorption contrast, instead of from the extracted first derivative of the phase function. However, the reconstruction from mixed phase and absorption sinograms has to be treated carefully as, although mixed PC-CT projections are not directly proportional to the first derivative of the phase function, the phase contrast is still differential in nature (edge-enhancement). When the differential phase contrast corresponds to the vertical direction (i.e. it coincides with the axis of rotation (AOR) of the PC-CT system), it does *not* change with rotation. Then, mixed sinograms can be directly input to the FBP, and maps showing combined absorption and phase contrast can be reconstructed. Conversely, when the differential phase contrast corresponds to the horizontal direction it *does* change with rotation. In this situation, strong reconstruction artefacts occur when the FBP is applied to the mixed sinograms.

2.3.2 State-of-the-Art of Experimental Setups and Reconstruction Methods, and Key Previous Developments in Phase Contrast CT

In the following, we provide a review of the existing PC-CT methods. Since the literature is extremely vast, we will focus on the basics required for the transition from planar to CT, such as the integration of an object rotation stage, defining an AOR, into the systems. Furthermore, the used reconstruction procedures will be reviewed. For each PC-CT method, we will also highlight important experimental work that has been undertaken. The focus here will be on quantitative imaging, on dosimetry, and on selected research highlights such as the development of a prototype small animal PC-CT scanner and the first time-resolved imaging. The review will not cover the applications of PC-CT, as this has been dealt with in

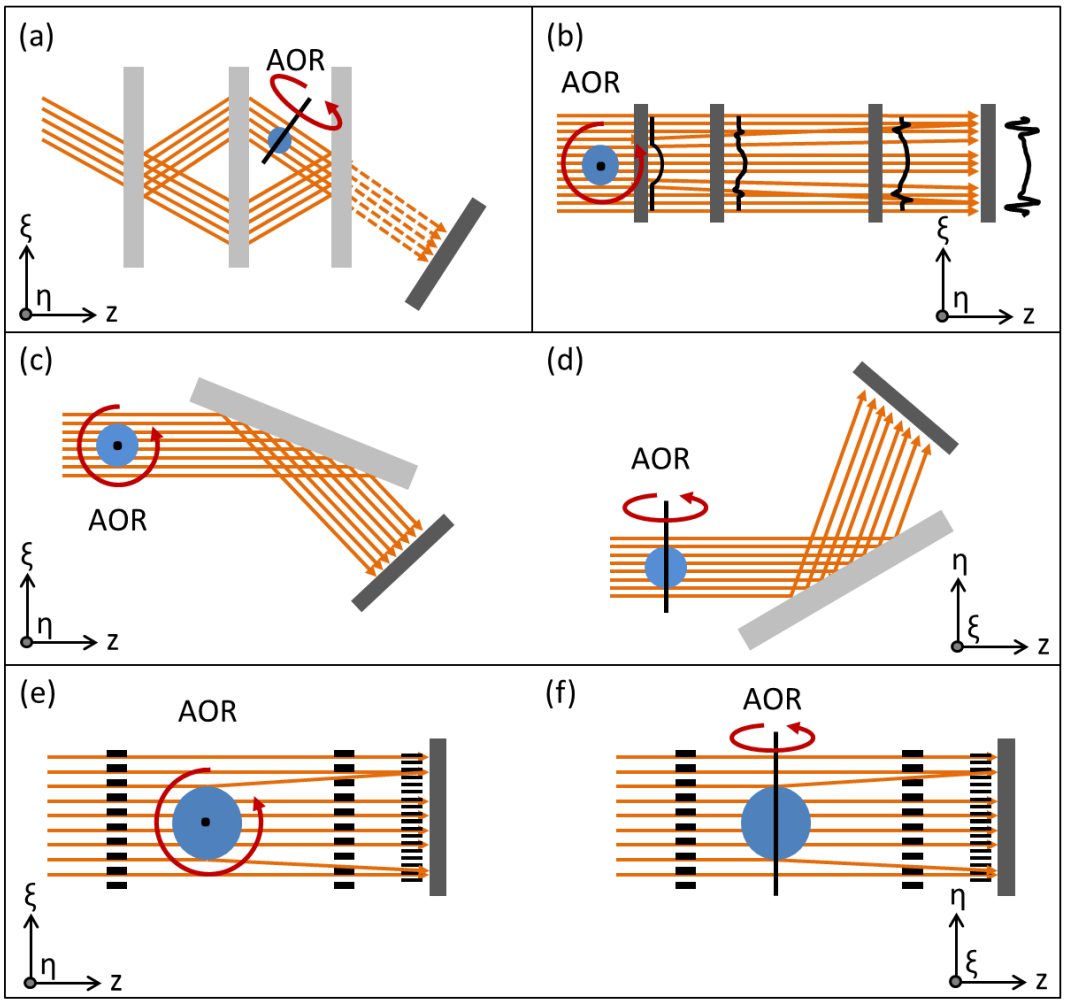

Figure 2.9: Schematic showing the position of the axis of rotation for the existing PC-CT methods based on Bonse/Hart interferometry (a), Free Space Propagation (b), Analyser-Based Imaging (c,d) and grating interferometry (e,f). For the DPC methods (Analyser-Based Imaging and grating interferometry), two possibilities to position the axis of rotation with respect to the direction of phase sensitivity exist. Please note the different frames of reference, describing the coordinate system of the object, for the different setups. The labels of the setup components have been omitted in this schematic.

the introduction and will partially be discussed again in chapter 3.

Bonse/Hart Interferometry CT

The position of the AOR is shown in figure 2.9 (a). As the phase retrieval methods yield the phase function directly, Bonse/Hart Interferometry does not belong to the class of DPC methods, which implies that the CT reconstruction is straightforward. A direct application of the FBP with the ramp filter to the phase function sinograms yields maps of the RID.

The first PC-CT images acquired with a Bonse/Hart interferometer were published in (Momose et al. [1996]). The authors show RID maps, however, those were not compared to nominal values in order to confirm their quantitative accuracy. To the best of our knowledge, this has not yet been done for Bonse/Hart-CT images.

Also, again to the best of our knowledge, the doses delivered during a Bonse/Hart-CT scan are not reported in the literature.

Free Space Propagation CT

The position of the AOR is shown in figure 2.9 (b). As the phase retrieval methods yield the phase function directly, FSP does not belong to the class of DPC methods either, which implies that the corresponding sinograms can therefore be directly input to the FBP yielding maps of the RID (Gureyev et al. [2009]). Some suggestions were made as to how the phase retrieval procedure can be incorporated directly into the reconstruction method in the form of a frequency filtering step (Bronnikov [2002], Gureyev et al. [2006], Groso et al. [2006]).

Langer et al. [2008] demonstrated that the quantitative accuracy of the reconstructed RID maps strongly depends on the phase retrieval method. In their study, RID maps of known materials (ranging from weakly to highly absorbing) were reconstructed and compared to nominal values for several different phase retrieval methods. The best match was achieved with the method by (Guigay et al. [2007]).

Those experiments were performed with a monochromatic synchrotron beam. Approaches to quantitative FSP-CT imaging using micro-focal x-ray sources with polychromatic spectra are published in Arharti et al. [2008] and Luu et al. [2011];

however, only for homogeneous objects. RIDs retrieved from polychromatic measurements correspond to effective energies. Recently, a paper was published (Munro and Olivo [2013]) discussing the concept of effective energy in PC imaging. The article points out that the effective energies for phase and absorption effects are in general different, due to the different dependency of the RID and the absorption term on energy, and that effective energies can be affected by beam hardening. The effective energy for phase effects, which in Luu et al. [2011] was determined from the retrieved polychromatic RIDs, was found to be higher than the spectrum mean, a result that is in agreement with the findings by Munro and Olivo. In Arharti et al. [2008], the same observations were made.

Although it is mentioned in the literature that the dose delivered in FSP-CT is potentially lower than in conventional CT (e.g. Groso et al. [2006]), actual dose measurements are rarely reported. Some dose figures are reported for planar FSP, for example in publications on the only existing PC mammography program currently running at the SYRMEP (SYnchrotron Radiation for MEdical Physics) beamline of the Elettra synchrotron in Trieste, Italy (Arfelli et al. [2000]). The reported Mean Glandular Doses (MGD) are comparable to those in standard mammography. From these dose figures, it is difficult to draw conclusions about the doses in FSP-CT scans, as the acquisition parameters (such as pixel size and exposure time) could be entirely different. We feel that the literature lacks publications on dosimetry in FSP-CT imaging. One explanation could be that FSP-CT is mainly restricted to synchrotron and micro-focal x-ray sources due to the high coherence requirements. Therefore, the method qualifies mainly for applications outside clinics, where dose is often not an issue.

Analyser-Based Imaging CT

From ABI measurements, the first derivative of the phase function can be extracted, therefore the method belongs to the class of DPC methods. The direction of sensitivity is determined by whether the analyser crystal is oriented vertically or horizontally. This implies two possibilities for setting up an ABI-CT system, schematically shown in figure 2.9: the crystal can be orientated perpendicular to the AOR (c), or in the same plane as the AOR (d). Setups as those shown in (c) are sensitive to phase effects in the horizontal plane, and as shown in (d) are

sensitive to vertical phase effects. The two possible ABI-CT setups are described in (Zhu et al. [2005]) and (Sun et al. [2007]).

Sinograms acquired with setups such as shown in figure 2.9 (c) (in the following referred to as horizontal sensitivity (HS) setups) are of the form of equation 2.9. This implies that RID maps can be reconstructed via the FBP with the Hilbert filter. Corresponding experimental results are reported in Huang et al. [2006] and Gasilov et al. [2013].

In addition to RID maps, the RID gradient can be reconstructed within the horizontal plane from ABI-CT measurements in HS mode; however, prior to back-projection the correction method by Zhu et al. [2005] has to be applied (equations 2.17 and 2.18). Apart from some experimental results shown in Zhu et al. [2005],Wang et al. [2006] and Sun et al. [2007], such reconstructions are hardly reported in the literature.

Sun et al. [2007] have also suggested to reconstruct the RID by first reconstructing its horizontal gradient components, and then, as a second step, to recover it via one-dimensional integration of one of them. Although mathematically this is a valid approach, in practice it leads to stripe artefacts in the RID maps, as errors which are present in the gradient (such as noise) get propagated in one fixed direction during the integration step. To the best of our knowledge, this approach to reconstruct RID maps was not adopted by any other group. One way of overcoming the stripe artefacts due to the one-dimensional integration could be to apply a regularisation method (Thuering et al. [2011]). Another possibility could be to use a method suggested by Kottler et al. [2007], which was derived for GI. Their method is based on a Fourier inversion of the gradient operator, in which both RID gradient components are used instead of one.

Much more frequently than in the HS mode, an ABI-CT system was used in the vertical sensitivity (VS) mode shown in figure 2.9 (d). In this case, sinograms are of the form of equation 2.10, and the vertical derivative of the RID can be reconstructed via the FBP with the ramp filter. This was performed experimentally by Dilmanian et al. [2000], Zhu et al. [2005], Sun et al. [2007], Rigon et al. [2008a] and Diemoz et al. [2010b].

Considering that from HS and VS measurements the horizontal and vertical RID gradient components can be reconstructed respectively, the reconstruction of

the entire RID gradient is a logical step (Wang et al. [2006]). The reconstructed gradient can either be rendered as a vectorial map (e.g. via colour coding of its components), or as a scalar map through its absolute value. The reconstruction of the entire gradient is an interesting topic, and its advantage becomes clear considering that an object generally consists of structures extending in three dimensions. A differential RID reconstruction obtained from HS or VS measurements yields edge-enhanced images of the object, but the edge-enhancement is present only in *either* the horizontal, *or* the vertical plane. Therefore, some structural information may be missed. Conversely, reconstructions of the entire gradient guarantee the visualisation of all structures present. The downside is the required performance of two ABI-CT scans, in addition to taking two projections at each angle in order to perform phase retrieval. Not only does this lead to increased scan time and dose, but it is also difficult to realise in practice: the object must stay in exactly the same position for the two scans, while the experimental setup is changed from the one shown in figure 2.9 (c) to that shown in figure 2.9 (d). This issue could explain why no further results on full gradient reconstruction are published in the literature on ABI-CT.

In addition to the reconstruction from phase retrieved differential sinograms, the literature is rich in experimental results where images showing combined phase and absorption contrast were reconstructed from non-phase retrieved sinograms (e.g. Coan et al. [2008], Sztrokay et al. [2012]). As required for the reconstruction, the data was obtained with ABI-CT scanners in VS mode. The frequent use of this approach may be explained by the fact that, because no phase retrieval is performed, only a single projection is needed at each angle, enabling faster scans with less delivered dose.

Reconstructed RID maps tested for their quantitative accuracy were first published by Dilmanian et al. [2000]. For their experiments, an ABI-CT scanner in VS mode was used. Phase retrieval (according to Chapman et al. [1997]) was applied and the vertical derivative of the RID was reconstructed via the FBP. The phantom contained several oil-filled cylindrical channels which were tilted with respect to the vertical axis. Because of the known geometry, the reconstructed vertical RID gradient component could be related to one of the horizontal RID components. The RID for the oil in the phantom could be recovered via integra-

tion of this horizontal component, although it was slightly under-estimated with respect to the nominal value.

The same experimental setup and geometrical approach were used to recover the RID of a known sample by Diemoz et al. [2010b]. Several phase retrieval methods for ABI-CT were compared with respect to how they affect the quantitative accuracy of the retrieved RID. Indeed, the results show that the chosen phase retrieval method greatly influences the retrieved values, with all tested methods leading to an under-estimation. The phase retrieval method by Nesterets et al. [2006] provided RIDs that were closest to the nominal values. The results of Dilmanian et al. and Diemoz et al. were both obtained with monochromatic synchrotron sources.

The reconstruction of quantitatively accurate RID maps for a breast was approached by Gasilov et al. [2013]. For the experiments, ABI-CT scans in HS mode were performed using a monochromatic synchrotron source. The phase retrieved sinograms were used to reconstruct the RID within slices of the breast using the FBP with the Hilbert filter. For selected areas of the breast, the retrieved RIDs were related to the breast density and found to be in good agreement with tabulated values.

The possibility of low-dose ABI-CT was demonstrated in a number of publications (e.g. Mollenhauer et al. [2002], Bravin et al. [2007], Kao et al. [2009]). In particular, in a study by (Keyrilaeinen et al. [2008]), ABI-CT images of breast specimens are shown, which provide diagnostically superior information compared to absorption-based CT images, at a lower radiation dose. The MGD for these images was 1.9 mGy (which is comparable to the MGD delivered in conventional planar mammography), compared to 6.9 mGy calculated for the conventional CT images. An even more promising result was published in (Zhao et al. [2012]). In this study, ABI-CT images of breast specimens are presented that were acquired at an even lower MGD ($\approx$ 0.8 mGy). These images were assessed by radiologists and evaluated as diagnostically superior with respect to images taken with a conventional CT scanner. This remarkable result was obtained thanks to a modification of the reconstruction method: instead of the FBP, an iterative algorithm known as Equally Sloped Tomography (EST) (Miao et al. [2005]) was used. Iterative algorithms such as EST have the advantage that potentially less

projections are required in order to achieve satisfactory CT reconstructions.

Grating Interferometry CT

As the derivative of the phase function can be extracted, GI also belongs to the class of DPC methods (Weitkamp et al. [2005], Pfeiffer et al. [2006]). As for ABI, there are two possibilities of setting up a GI-CT system. The direction of phase sensitivity is determined by the orientation of the gratings with respect to the AOR, and setups in HS mode (figure 2.9 (e)) and VS mode (figure 2.9(f)) need to be distinguished.

Since the mathematical problem is equivalent for all DPC methods, the reconstruction methods applied to ABI-CT can be used for GI-CT, e.g. to obtain maps of the RID and/or its gradient. This was performed experimentally by a number of groups (Momose et al. [2006], David et al. [2007b], Donath et al. [2008], Qi and Chen [2008], Bech et al. [2009], Herzen et al. [2009]).

An interesting reconstruction approach for GI-CT, in addition to the methods suggested for ABI-CT, is provided by Rutishauser et al. [2011]. The aim is again the reconstruction of the entire (vectorial) RID gradient, but some of the practical issues associated with the method suggested by Wang et al. [2006] for ABI-CT are overcome. Instead of two complete datasets (acquired in HS and VS modes), a single dataset was shown to be sufficient if a modified GI-CT setup is used. The proposed setup consists of tilted gratings, resulting in simultaneous horizontal and vertical phase sensitivity. As described by Rutishauser et al., all three RID gradient components can be extracted via a mathematical procedure from measurements taken over an angular range of 360 degrees. The method overcomes the problem of having to change the sensitivity mode of the setup between the two scans needed, as suggested by Wang et al. On the other hand, the need to acquire projections over 360 instead of 180 degrees does not reduce the radiation dose compared to the method by Wang et al. Rather conversely, phase stepping has to be performed at every angle, implying an even higher dose. If, however, the approach suggested by Rutishauser et al. was applied to other DPC methods that require only two projections at each angle for phase retrieval (i.e. ABI or EI), the problem of excessive doses would be mitigated.

Several publications deal with quantitative GI-CT imaging. In an experiment

described by Zanette et al. [2011], a GI-CT setup in HS mode was used together with a monochromatic synchrotron source, and, after phase retrieval, RID maps were reconstructed using the FBP with the Hilbert filter. A phantom consisting of a number of known materials, amongst which was water, was imaged. Instead of stating the absolute values of the recovered RIDs, Zanette et al. present the values relative to that retrieved for water. The experimentally retrieved relative values were compared to theoretical ones and were found to be in good agreement. This demonstrates the possibility of retrieving the correct trend for the RIDs of different materials; however, it does not prove the accuracy of the retrieved RIDs. On the other hand, the correct RIDs could be recovered using a calibration function in the case of an offset.

In another experiment with a synchrotron source, this time monochromatised to the significantly higher energy of 82 keV, the recovery of the absolute RID was demonstrated with high accuracy in comparison to nominal values (Willner et al. [2013]). Also in this case, the GI-CT setup was operated in HS mode, and CT reconstruction was performed with the FBP with the Hilbert filter after performing phase retrieval at every angle.

Prior to these synchrotron experiments, the quantitative accuracy of reconstructed RID maps was investigated for polychromatic x-ray tubes (Herzen et al. [2009]). A phantom consisting of known materials was imaged with a horizontally sensitive GI-CT setup operated in Talbot/Lau configuration (a third "source grating" was added to the interferometer to account for the spatially incoherent beam). RID maps were reconstructed using the FBP with the Hilbert filter after performing phase stepping at every angle. In addition to the RID, maps of the absorption term were reconstructed. As in Zanette et al. [2011], Herzen et al. state the retrieved RID and absorption term values relative to those retrieved for water. In order to assess their accuracy, effective energies (for phase and absorption) were defined in the following manner: one material in the phantom was selected, for which tables of optical constants versus energy were interpolated at the retrieved RID and absorption term. These effective energy values were then used to assess the accuracy of the RID and absorption term for the remaining materials. A close match with the nominal values was found, however, slight discrepancies were present. These may be explained by the fact that effective

energies for phase and absorption are not only different, but are also influenced by the material itself (Munro and Olivo [2013]), which was not taken into account by the authors.

An interesting approach to quantitative imaging not based on the reconstruction of phase-retrieved RID maps was published by Diemoz et al. [2011]. The authors demonstrate that quantitatively meaningful mixed images showing combined phase and absorption contrast can be reconstructed. As explained previously, the reconstruction of mixed images is mathematically valid for GI-CT systems in VS mode. When scanning the phase or analyser grating with respect to the other, a sinosoidal intensity pattern can be measured on the detector. Diemoz et al. showed that, if projections are acquired in a situation where the gratings' positions correspond to the approximately linear part of that pattern, the reconstructed mixed images are linear combinations of the vertical RID gradient component and the absorption term. Due to the fact that only a single projection is required at each angle instead of the performance of phase stepping, the method can reduce scan time and delivered dose significantly. Moreover, it is directly applicable to the other DPC techniques. The applicability of the method to EI-CT will be demonstrated in chapter 5.4.

As in planar, the laboratory implementation of GI-CT has some important shortcomings. Considering in particular two recent publications (Tapfer et al. [2011], Tapfer et al. [2012]), the issues become apparent. In the articles, the development of a laboratory-based pre-clinical PC-CT scanner, intended for small animal scanning, was reported. Although in principle a research highlight in the field for the fact that, for the first time, a rotating gantry was used instead of a rotating object stage, some problems may affect the usefulness of the scanner in practice. First, due to the small periods of the gratings, the gantry setup is sub-optimal as the required high precision alignment cannot be preserved during its rotation Tapfer et al. [2012]. A post-processing correction method has been suggested (Tapfer et al. [2012]). Second, it is stated explicitly in the article by Tapfer et al. [2012] that the scanner delivers doses of "several Grays", making it unsuitable for the imaging of live animals as this dose is considered lethal (Holdsworth and Thornton [2002]). At the same time, the authors emphasize that the scanner has not yet been optimised for dose. Acquisition schemes for

GI-PC that have the potential to lower the radiation dose exist (Zhu et al. [2010], Zanette et al. [2012]) but have not been implemented in the scanner.

Delivered doses ten times higher than what is considered clinically acceptable were reported for planar GI images of the breast (Stampanoni et al. [2011]). Also in this case, the authors emphasize that the used setup was not optimised for dose.

Finally, a research highlight was published by Momose et al. in 2011, who showed the first ever dynamic PC-CT images. A GI-CT setup in HS configuration was used, and RID maps were reconstructed following phase retrieval with a method that does not rely on phase stepping (Takeda et al. [1982]). In addition, a white synchrotron beam was used to achieve a high flux. The result was a short exposure time, and the achieved time resolution was 0.5 s, which was sufficient to visualise the insides of a living worm (Momose et al. [2011]). On the downside, the delivered radiation dose was sufficiently high as to kill the animal.

2.4 Chapter Summary and Conclusion

The existing PC methods were presented. Three of them, amongst which EI, belong to the class of DPC methods. While all methods can be implemented at synchrotrons, only two of them (GI and EI) are fully compatible with conventional x-ray equipment, at least if sensible acquisition times are required. It was explained that the laboratory implementation of GI has a number of shortcomings related to stability and dose, which can be overcome or mitigated by EI.

In the second half of the chapter, the mathematics of CT were discussed and the most commonly used reconstruction formula, the FBP, was presented. It was explained how maps of the RID within an object can be reconstructed using the FBP with the Hilbert filter if the derivative of the phase function is known. It was also mentioned that it is possible under certain conditions to reconstruct mixed images showing a combination of phase and absorption contrast.

Finally, the literature on the existing PC-CT methods was reviewed. The focus was on the orientation of the AOR, the reconstruction procedures, quantitative imaging and dosimetry. It was noted that the same reconstruction procedures are applicable to all DPC methods. With respect to quantitative imaging,

it is important whether monochromatic or polychromatic sources are used, as the latter requires the determination of effective energies. Dose figures reported in the literature vary significantly between the methods. While for ABI-CT the reported doses were in accordance with pre-clinical and clinical standards, the doses for GI-CT, in particular those reported for a recently developed small animal scanner, were at unacceptable levels.

Chapter 3

Synchrotron Implementation of Existing Phase Contrast CT Methods to Investigate New Scientific Problems

3.1 Chapter Introduction and Outline

PC-CT methods have already been applied to and shown to be beneficial for a variety of biomedical applications. But as research progresses, new applications emerge. In particular, innovative areas which require non-destructive imaging of soft tissues, on a small scale and in 3D, can benefit from PC-CT. In this chapter, we discuss two applications of PC-CT, which would benefit especially if scans could be performed directly in the research laboratories, e.g. with EI-CT.

The first application is the imaging of articular cartilage for the study of osteoarthritis in murine models. The need for improved cartilage imaging is not new, and PC methods have already been applied to tackle the demand. However, to the best of our knowledge, PC-CT of murine cartilage were obtained only with micro-focal x-ray sources, at the cost of excessive exposure times.

The second application is related to regenerative medicine and specifically tissue-engineered replacement organs. Current research is focused on the genera-

tion of acellular natural matrices which serve as scaffolds for the stem cells of the organ recipient. Non-destructive imaging of acellular natural matrices is highly needed, but standard modalities such as electron microscopy, microCT and MRI all have significant limitations. We argue that PC-CT can overcome these issues and we show what are, to the best of our knowledge, the first ever PC-CT images of acellular scaffolds.

For the investigation of these two potential applications, we have chosen to use well-established PC-CT methods together with synchrotron sources, with the aim of achieving proof-of-concept results that would inform and drive the development of the (laboratory-based) EI-CT method.

3.2 3D Phase Imaging of Murine Cartilage Using Analyser-Based Imaging for a Better Understanding of the Development of Osteoathritis

Osteoarthritis (OA) is the most common form of arthritis, a degenerative joint disease, with over 30% of the elderly population affected. The number of patients is expected to increase in the next decade because of the aging population, and the resulting costs for national health care systems, already large, will grow as a consequence (Krasnokutsky et al. [2007]).

Although the development of OA is not fully understood yet, its early stage is associated with a shrinking or damage of the layer of articular cartilage that forms a protective coating to the joint (Braun and Gold [2011]). The knee is one of the most common sites for OA to occur (Goldring and Goldring [2007]). Figure 3.1 shows schematically the structure of healthy and osteoarthritic knee joints. While in the healthy joint the cartilage layer is intact and has a relatively constant thickness, a reduction in thickness and areas completely lacking cartilage can be identified in the diseased joint.

Chronic pain usually marks the advanced stages of OA, and it is often only at that point that patients report to their GP. Currently, the diagnosis of OA

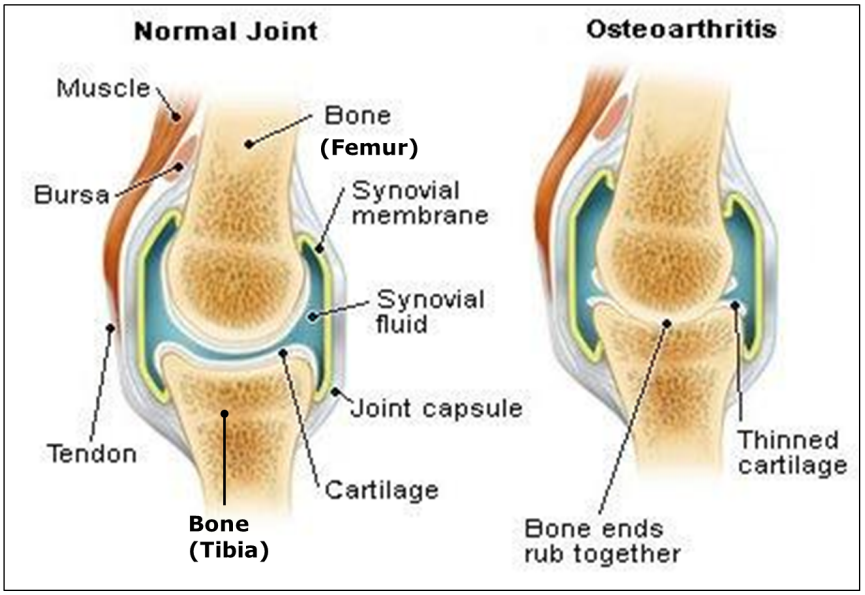

Figure 3.1: Schematic of a healthy ("Normal Joint") and diseased ("Osteoarthritis") knee joint. Characteristic for osteoarthritis is a shrinking of the cartilage layers covering the femur and tibia. Image has been adopted from phc-online.com.

involves a combination of anamnesis and medical imaging. Conventional radiography can provide indirect insight by revealing the distance between the two bone ends, as a reduced joint gap indicates a shrinking of the cartilage layers (Braun and Gold [2011]). The direct visualisation of the cartilage is hardly possible due to its low absorption properties. Therefore, an early stage diagnosis is challenging and rare. While the progression of promptly detected OA may be mitigated by life style changes, there is currently no cure for the advanced disease (Krasnokutsky et al. [2007], Goldring and Goldring [2007]).

Animal models can help to gain a better understanding of the origin and progression of OA, which, in turn, can provide the basis for the development of drugs and alternative therapies. Murine models of OA are currently believed to be the best choice for the purpose, as genetic modifications are easily induced (Marenzana et al. [2013]). Murine models enable the much needed investigation of artificially induced OA in its early stages (Braun and Gold [2011]), which however requires the visualisation of thin cartilage layers and the detection of

faint changes within them. Cartilage is notoriously x-ray transparent, and its small size particularly in the mouse (on the order of tens of microns) makes its visualisation challenging, even more so considering that ideally a 3D approach is required.

Histology can provide detailed images of the bone joints and the overlaying cartilage when specific staining methods are used. Not only does histological analysis facilitate estimating the cartilage layer thickness, it can also show whether it is damaged or not. Being a destructive technique, histology cannot be used *in vivo*. Moreover, it is time consuming and costly, and therefore not suited for the routine visualisation needed to monitor the beginning and development of OA (Marenzana et al. [2012]). MRI struggles to achieve the necessary spatial resolution needed to show murine cartilage, at least within sensible acquisition times (Wagner et al. [2013]). Therefore, and due to limited access to scanners, MRI is not ideal as a modality for routine imaging of mouse models of OA. MicroCT scanners have been used to image thin cartilage layers. While the necessary resolution can be achieved, the image contrast is extremely poor (Braun and Gold [2011]). The x-ray absorption properties of cartilage are extremely similar to those of the surrounding fluids, and, due to the small scale in mice, absorption itself is very low. The problem is worsened by the fact that articular cartilage is attached to the bone: the absorption properties of bone are much higher, and the resulting strong signal can mask the very faint signal arising from the cartilage layer. MicroCT imaging in combination with specific contrast agents has been demonstrated to yield promising results (Xie et al. [2009], Bansal et al. [2010]). However, these techniques are difficult to realise *in vivo* due to variability in the uptake of the contrast agents and associated unreliability (Marenzana et al. [2013]).

PC imaging has the potential to overcome or at least mitigate the above issues. The natural suitability of PC methods to the imaging of soft tissues triggered a number of experiments on articular cartilage. Most of them have been carried out at synchrotrons using the ABI method, and were focused on imaging cartilage layers that are thicker than in mice (Mollenhauer et al. [2002], Muehlemann et al. [2004], Coan et al. [2010a], Diemoz et al. [2010b]). However, *in vivo* imaging of small animal cartilage (guinea pig) has also been reported (Coan et al. [2010b]).

Generally, a laboratory-based implementation of PC is considered advantageous compared to a synchrotron one for reasons given previously. Several non-synchrotron-based experiments on cartilage have been described in the literature. ABI of cartilage in combination with a micro focal x-ray source was demonstrated by Muehlemann et al. [2009]; however, due to the narrow energy band selected by the analyser crystal and the resulting flux reduction, excessive exposure times were needed. Some other studies demonstrated the feasibility of visualising articular cartilage also with non-micro focal laboratory sources, in particular using the GI method (Kido et al. [2010], Stutman et al. [2011]). In these experiments, a chicken wing (cartilage layer $\approx$ 1 mm) and the small joints of the human hand (cartilage layer $\approx$ 0.6 mm) were imaged, respectively. The only experiments where murine cartilage was imaged are reported in (Lee et al. [2010], Ruan et al. [2013]). The imaging method was FSP-CT implemented with a micro-focal source, which also led to lengthy exposure times (Wilkins et al. [1996]).

An alternative for laboratory-based cartilage imaging is provided by the EI method. It has been demonstrated recently that planar EI can correctly visualise the cartilage layer of dissected rat tibia (thickness $\approx$ 100-300 μm) also with a non-microfocal laboratory x-ray source, both in air and in a saline solution (Marenzana et al. [2012]), the latter mimicking the *in vivo* situation. The obtained image contrast was high enough to enable the estimation of the cartilage thickness via an automated detection procedure. Additionally, manually induced damages (dents) to the cartilage surface could be correctly detected. These results demonstrated the high sensitivity of EI (Diemoz et al. [2013], Diemoz et al., accepted for publication in Applied Physics Letters) on a practical example.

The article by Marenzana et al. demonstrated that laboratory-based phase contrast imaging of cartilage layers in rodent models is possible. In order to proceed from the reported proof-of-concept experiment towards a valuable research tool for the study of OA using mouse models, two upgrades of the EI method are required: increased resolution (to resolve the cartilage in the mouse knee, of thickness $<$100 μm) and extension to CT (to show the 3D structure of the cartilage and potential damages). The feasibility of the first upgrade was demonstrated recently (Endrizzi et al., manuscript in preparation). The second upgrade is the content of this thesis. In this sense, the experiment by Marenzana et al.

has greatly motivated the development of EI-CT.

As a preliminary investigation on the challenges associated with moving from a rat to a mouse model and from planar to CT, murine tibiofemoral joints were imaged at a synchrotron, using a fully developed PC-CT method. The aim of the experiment was to obtain "gold standard" images of what the (laboratory-based) EI-CT method could possibly achieve.

Materials and Methods

The chosen method was ABI-CT, first, because the nature of the detected signal is very similar to that detected with EI (Munro et al. [2013b]), and second, ABI had earlier been used for cartilage imaging achieving good results (although on larger specimens). An ABI-CT setup in VS mode was used, and the bone cartilage samples were placed such that cartilage layer was oriented perpendicular to the direction of phase sensitivity, such that the phase effects occurring at the contour of the cartilage layer would be picked up. Further, the VS mode implies that mixed images showing combined phase and absorption contrast can be reconstructed without the need of extracting the phase function (see chapter 2.3.2).

The experiment was carried out at the SYRMEP beamline of the Elettra synchrotron in Trieste, Italy. A photograph of the facility and a schematic of the experimental setup at the beamline are shown in figure 3.2. The Elettra storage ring is operated at 2.4 GeV and SYRMEP uses a bending magnet source (B = 1.45 T). The experimental hutch is located approximately 22 m from the source, resulting in an estimated source size of 135 (H) x 80 (V) μm^2, expressed as full width at half maximum (FWHM). The beam was monochromatised by a double Si (1,1,1) crystal in Bragg configuration to an energy of 16 keV (Δ E/E $\approx$ 0.2%). The beam dimensions after the monochromator were 120 (H) x 4 (V) mm^2. The object, located at a distance of approximately 23 m from the source, was fixed on a PI rotation stage (PI GmbH, Karlsruhe, Germany). A Si (1,1,1) crystal placed 40 cm downstream of the object stage was used as analyser. The images were recorded by a CCD camera system (Photonic Science Ltd., Robertsbridge, United Kingdom) with fibre optics taper coupled to gadolinium oxysulphide scintillating optics. The effective pixel size was 4.5 x 4.5 μm^2.

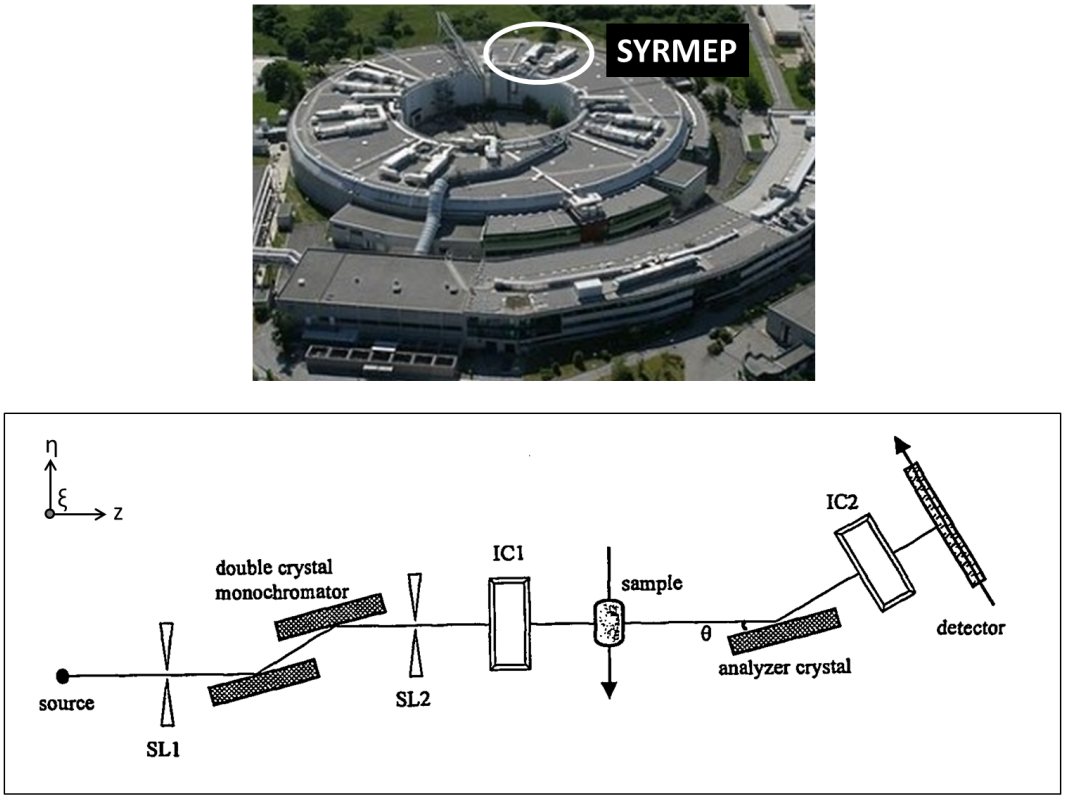

Figure 3.2: Photograph showing the storage ring at Elettra (above), and a schematic of the ABI-CT setup used at SYRMEP (below). Please note the reference frame (describing the object) indicating the VS mode. SL1 and SL2 are collimating slits, and IC1 and IC2 denote ion chambers. The figures have been adapted from www.elettra.trieste.it.

The imaged samples were prepared in the following manner. Mice were kept in accordance with UK home office regulations. First, tibiofemoral joints were dissected from 12 weeks old healthy animals and fixed in 10% buffered formalin for 24 hours before they were placed in a 70% ethanol solution. Four weeks before they were sacrificed, one mouse was induced with OA on the right knee via a procedure that destabilises the medial meniscus (Marenzana et al. [2013]), while its left knee was left normal and served as control. For the healthy samples, the joints were dissected from adjacent soft tissues, leaving the cartilage surface exposed to air. The OA-induced specimen and the corresponding control were

kept intact. Before imaging, the specimens were rehydrated in a saline solution for at least 2 hours.

For imaging, the analyser crystal was first tuned to a position corresponding to the top of the rocking curve, and then to a position corresponding to 50% reflectivity on its left slope. On the top, the phase contrast in the images arises because the refraction of the beam (either by a positive or a negative angle) leads to a lower intensity incident on the detector. As described in chapter 2.2.3, when the crystal is rocked to the left slope of the RC, phase contrast is due to an increase (decrease) of the intensity as a result of the refraction by a positive (negative) angle. In addition to phase contrast, absorption contrast is present in both cases. During the CT scans, 720 projections were recorded with angular offsets of 0.25 degrees, covering a total range of 180 degrees. Gain and offset corrections were applied to the raw images before the sinograms were generated. No phase retrieval was performed. CT reconstruction of combined phase and absorption images was performed via the FBP with the ramp filter. The software used for the CT reconstruction was PITRE (Phase-sensitive x-ray Image processing and Tomography REconstruction) (Chen et al. [2012]).

3D datasets were reconstructed from which coronal slices were selected and rendered, as in this orientation the surface and the thickness of the cartilage layer are best appreciable. Volumetric renderings were created using the open source software 3DSlicer (www.slicer.org).

Results and Discussion

Figure 3.3 (a) shows a coronal slice extracted from the reconstructed ABI-CT dataset for one of the dissected specimens (healthy). As the FOV was narrow (4 mm in the vertical direction), only the top part of the tibia is visible. The cartilage layers covering both shoulders (lateral and medial) of the tibia can be recognised easily, moreover, it can be clearly seen that its surface is intact. A zoom of the medial cartilage layer is shown in figure 3.3 A. The analyser crystal had been tuned to a position corresponding to the top of the RC for this experiment, and the visible contrast is due to both phase and absorption effects. We would like to point out, however, that the cartilage is only outlined by the strong signal at the cartilage-air interface, which is due to a difference in RID between the two.

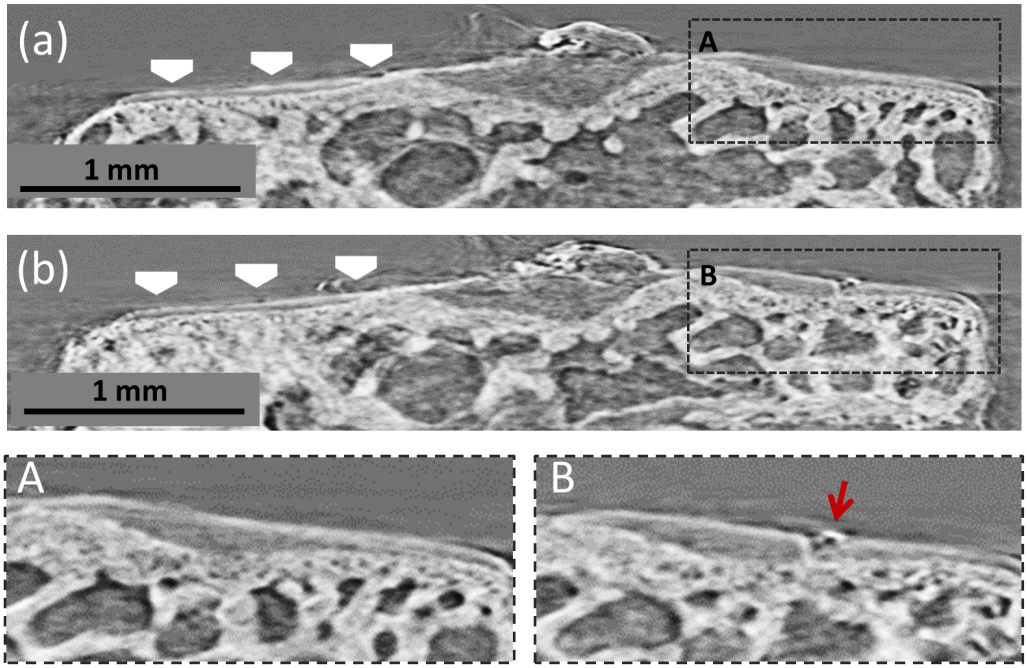

Figure 3.3: Coronal slices extracted from reconstructed ABI-CT datasets, showing murine tibia and the coating by articular cartilage. Images (a) and (b) show the same dissected specimen, however in (b) a small lesion has been manually induced to the medial cartilage surface. A and B show a zoom of the regions specified in (a) and (b).

Absorption contrast that manifests as a brighter grey value is almost not present inside the cartilage layer, and without the bright fringe marking its boundary the cartilage would be invisible.

After the first CT scan, damage to the medial side cartilage in the form of two dents has been induced manually using a scalpel, after which the specimen has been imaged again. A coronal slice extracted from the resulting 3D dataset is shown in figure 3.3 (b). The slice has been selected with the aim of visualising the same part of the specimen as in (a). While the lateral side cartilage is identical to the one in (a), i.e. fully intact, one of the dents on the medial side cartilage can be clearly seen and is highlighted by an arrow in the zoom in figure 3.3 B.

In order to prove that the feature indicated in figure 3.3 B is actually one of the dents and not an artefact, histological analysis of the specimen was subsequently

performed. For the histological results, which have in fact confirmed the presence of the lesion, we refer the reader to the article by Marenzana et al. from 2013.

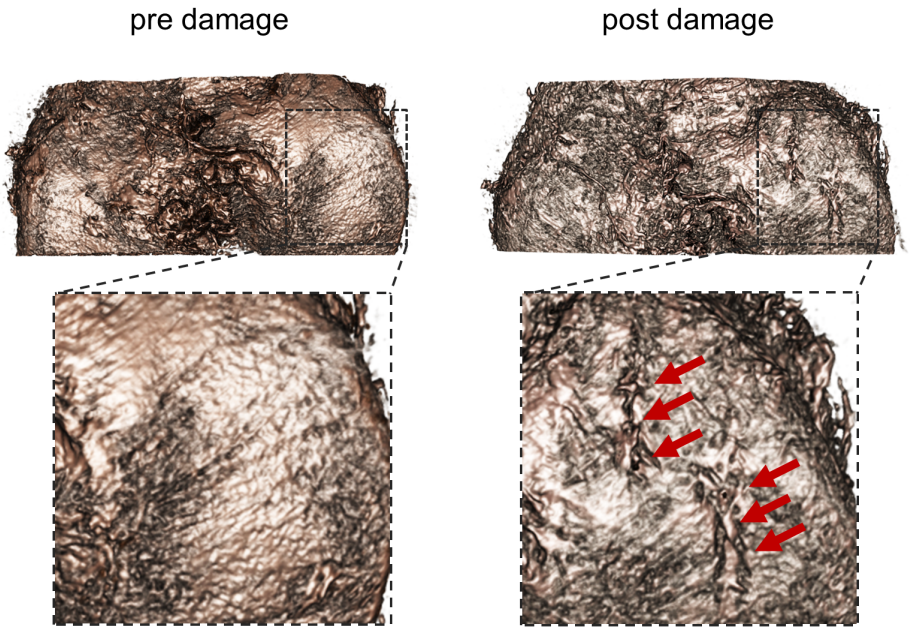

Figure 3.4: Volumetric rendering of the cartilage surface (seen from top) of the murine tibia shown in figure 3. The dents in "post damage" are clearly visible and are indicated by arrows.

The presence of the dents is made even more evident by the volumetric renderings of the reconstructed images ("pre" and "post damage") shown in figure 3.4, in which the cartilage covered tibia is seen from the top. The surface on the medial shoulder of the tibia "pre damage" is smooth, whereas, in the rendering of the "post damage" dataset, the two dents are clearly visible and are indicated by arrows.

The correct visualisation of both the intact cartilage layer and the manually induced dents is a very important result for OA research. The enhanced contrast at the cartilage-air interface makes it possible to measure the thickness of the layer, which can give information on the early stages of the disease. The

visualisation of the induced dents can be helpful in understanding secondary OA, which is typically caused by unwanted impacts on the knee joint (as caused by an accident for example). Secondary OA is different from primary OA, for which the origin and cause of the disease is poorly understood. Images such as those shown in figures 3.3 (b) and 3.4 ("post damage") would enable assessing the effect of cartilage damage with respect to disease progression.

While the optimised acquisition conditions leading to the image quality visible in figures 3.3 and 3.4 can only be achieved *ex vivo* (cartilage exposed to air), the intact specimens (OA-induced and healthy control) mimicked a situation much closer to *in vivo* imaging. Tibia and femur are connected via soft tissues, and the cartilage layers surrounded by fluids naturally present in the knee (synovial fluid). It is far more challenging to visualise articular cartilage immersed in a liquid instead of in air. Not only are the absorption properties of cartilage and the surrounding fluid extremely similar, but also the RIDs are close to each other, resulting in weak phase effects.

The images in figure 3.5 show coronal slices extracted from the reconstructed ABI-CT datasets for the intact specimens. The images of the healthy control can be seen in (a), and that of the OA-induced knee joint in (b). Due to limitations in the FOV, both images show only parts of the anatomy of the knee joint: the top of the tibia is clearly visible in both images, and (b) also shows the lower end of the femur and a part of the meniscus. Once again, in this case all anatomical parts are surrounded by synovial fluid. Despite the close match in RID, the cartilage/fluid interface on the tibia can still be seen. The cartilage edge is, however, not as clearly defined as in the previous case where cartilage was imaged in air. For this experiment, the analyser crystal was tuned to a position corresponding to 50% illumination on the left slope of the RC meaning that the image contrast is due to both phase and absorption effects. At this position the RC is steepest, and a very small angular deviation of the photon is translated into contrast due to a significant change in the crystal's reflectivity, which makes this position ideal for visualising very faint details such as the cartilage/fluid interface.

The thickness and integrity of the cartilage appear to be similar for the OA-induced specimen (figure 3.5 (b)) and the healthy control (figure 3.5 (a)), and

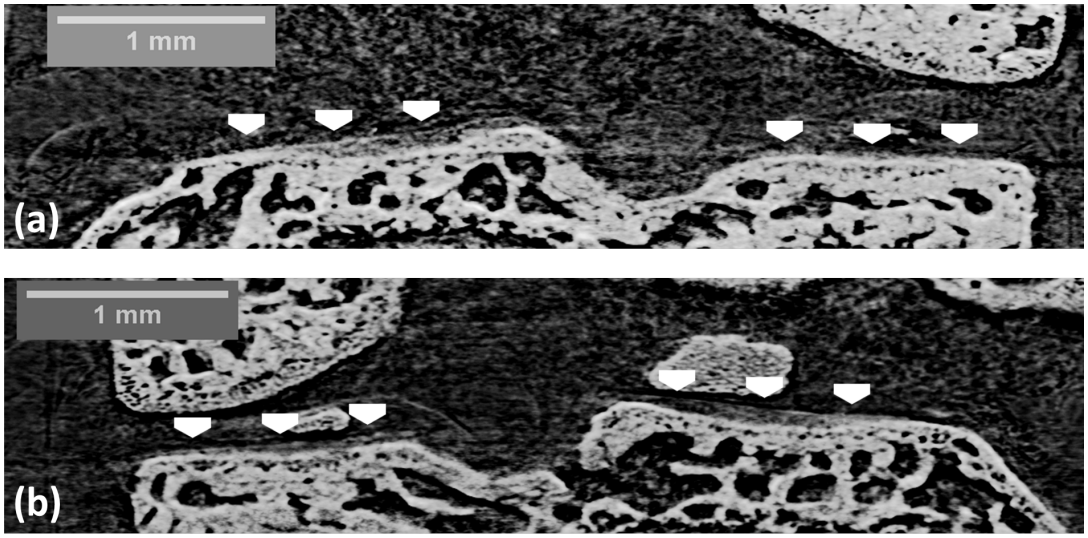

Figure 3.5: Coronal slices extracted from reconstructed ABI-CT datasets showing intact murine tibiafemoral joints. The bone structure and cartilage layers are surrounded by fluids naturally present in the joints. (a) shows the OA-induced knee, while (b) shows the healthy control.

clear OA lesions were not found in the cartilage layer of the former. This could be due to the unreliable nature of the OA-induction process, or because the four weeks gap between the induction and the imaging may not have been long enough for the disease to develop.

Conclusion

Being able to image cartilage *in vivo* is highly important for the long term study of OA. Disease-induced mice could be imaged on a regular basis such that the progression of the condition can be monitored. Moreover, it would enable testing the response of animals to newly developed drugs or alternative therapies.

In the present study, we demonstrated that murine articular cartilage can be visualised both in air and in synovial fluid using PC-CT. Moreover, we showed that manually induced lesions were correctly visualised.

Following these results, it can be concluded that PC-CT has a significant potential for the study of OA in animal models, with sizes down to the scale of mice. The described experiment was carried out at a synchrotron; however,

the EI-CT method has the potential to achieve comparable results also in a laboratory. The images shown in this chapter will serve as "gold standard" for a laboratory-based EI-CT scanner.

3.3 High Resolution 3D Propagation-Based Phase Imaging of an Acellular Rabbit Oesophagus Scaffold for Regenerative Medicine Applications

Tissue engineering (TE) is an emerging sub-discipline of regenerative medicine that has the potential to overcome some major issues connected with organ replacement in humans: the shortage of suitable donor organs, and the problem of organ rejection with consequent need for immunosuppression (Totonelli et al. [2013]). Several approaches towards tissue engineered replacement organs exist, all of which are based on using acellular scaffolds with the objective of populating them with stem cells of the organ recipient, either post-operatively through natural growth, or through pre-operative seeding (Badylak et al. [2012]). Acellular scaffolds can be generated from biocompatible materials ("smart polymers") (Dhandayuthapani et al. [2011]), collagen constructs (Saxena et al. [2010]), or the matrices of the replacement organs themselves (Badylak et al. [2012]). It was suggested that these natural acellular matrices (ACMs) are the optimal choice for tissue engineered organs due to the fact that native biomechanical properties are naturally present. This is nicely exemplified by a recent TE success story: a paediatric patient, who has undergone an emergency TE aided replacement of the trachea, has been reported to be able to lead a "normal" life after a two-year follow up (Elliot et al. [2012]).

Natural ACMs are typically obtained via a decellularisation procedure (Badylak et al. [2012]). The exact method is highly organ specific, and the main challenge is the preservation of the organ structure while eliminating the entire cell population and DNA of the donor. The decellularisation of the trachea is considered relatively simple (Totonelli et al. [2012]), and the focus of current research is

on the decellularisation of more complex organs such as the pancreas, the heart, and the organs belonging to the gastrointestinal tract.

The visualisation of the ACMs is crucial for the assessment of whether or not a newly developed decellularisation method is effective in preserving the structure of a specific organ; however, the TE community currently suffers from a lack of an appropriate imaging modality. The challenges are the 3D nature of the scaffold, the small scale of the structural features, poor soft tissue contrast, and the necessity to image ACMs routinely, ideally with a high throughput.

Histological examination can reveal the structural properties of ACM. However, being a destructive technique, it cannot be used as a method to test a scaffold prior to transplantation. Scanning Electron Microscopy (SEM) and Transmission Electron Microscopy (TEM) have been demonstrated to provide high resolution images that reveal sufficient structural information (Totonelli et al. [2012]). On the downside, both modalities are intrinsically 2D, which means that they can only be used to provide information about the scaffold surface but fail to visualise the entire 3D construct. MRI has been shown to be a suitable imaging modality for certain ACMs (Cheng et al. [2010]). The high cost and the resulting limited distribution of MRI scanners in combination with a low resolution and/or long scan times, however, make MRI unsuited as a cheap and fast imaging routine. MicroCT has, to the best of our knowledge, not been applied to visualise acellular scaffolds as extremely low x-ray absorption leads to insufficient soft tissue contrast.

All listed imaging modalities thus have significant shortcomings, and the need for a fast, cheap, widely available 3D imaging modality providing high soft tissue contrast with sufficient spatial resolution is still unmet. We propose as a solution the use of PC-CT, which has the potential to fulfill these demands, and report on a proof-of-principle experiment showing suitability of the method for the 3D structural visualisation of the soft tissue constructs. In particular, we show PC-CT images of a rabbit oesophagus ACM obtained through a newly developed decellularisation method called detergent-enzymatic treatment (DET). The DET method has already been used sucessfully to obtain rat small intestine ACMs (Totonelli et al. [2012]) and pig oesophagus ACMs (Totonelli et al. [2013]), and is a good candidate for the decellularisation of more complex organs. The pre-

sented PC-CT images were assessed by clinicians and rated with respect to the structural information provided.

Materials and Methods

The PC-CT method we used in this case was FSP-CT. The intensity pattern in a FSP projection can be related to the thickness of the specimen $T(\xi, \eta)$ via the relation:

$$T(\xi, \eta) = -\frac{1}{2k\beta} \ln \left(I(x, y) * P \right). \tag{3.1}$$

The variable $I(x, y)$ denotes the intensity measured at the detector plane, k is the wave number and P is the Paganin filter given by:

$$P = \mathcal{F}^{-1} \left(\frac{2k\beta I_0}{z_{od}\delta(u^2 + v^2) + 2k\beta} \right). \tag{3.2}$$

The variables u and v describe the coordinates in Fourier space, and z_{od} is the object-detector distance. The Paganin filter can be derived from the differential representation of the transport-of-intensity equation by assuming an object consisting of a single material only (Paganin et al. [2002]), but has been shown to yield good results also when the assumption is relaxed (Burvall et al. [2011]). By noting that the object thickness is equal to its integral along the direction of x-ray propagation, it possible to apply the concepts of CT and to reconstruct a volumetric image once the intensity is recorded from a number of rotational views (see chapter 2.3).

The PC-CT experiment described in this section was carried out at the Biomedical Beamline (ID17) of the European Synchrotron Radiation Facility (ESRF) in Grenoble, France. A photograph and a schematic of the beamline are shown in figure 3.6. The ESRF storage ring is operated at 6 GeV and the x-rays for ID17 are generated by a 21-pole variable-field wiggler (B = 1.6 T). The sample was placed approximately 150 m from the source, which has a size of 123 (H) x 24 (V) μm^2, expressed as FWHM. The beam was monochromatised by a double Laue/Laue silicon (1,1,1) crystal to 26 keV (ΔE/E $\approx$ 0.02%) and filtered using 0.8 mm of copper and 3 mm of aluminium. The object-to-detector distance was 3.45 m. The sample was placed on a rotation stage (PI miCos GmbH, Eschbach,

Germany). The images were recorded by a FReLoN CCD camera (Coan et al. [2006]) coupled to a of 47 μm thick gadolinium gallium scintillator. The effective pixel size was 3.5 x 3.5 μm^2.

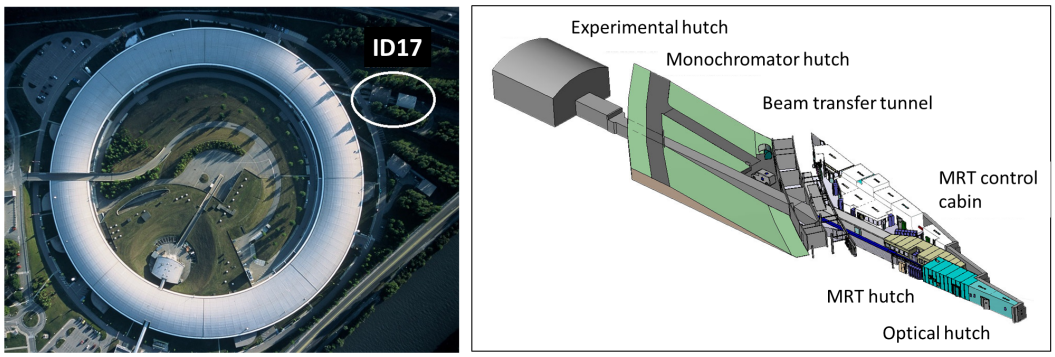

Figure 3.6: Photograph showing the storage ring at the ESRF (left), and a schematic of the beamline ID17 (right). The figures have been adapted from www.esrf.eu.

The imaged specimen was prepared as follows. The oesophagus was harvested from a rabbit in accordance with UK Home Office guidelines, under the Animals (Scientific Procedures) Act 1986 and the local ethics committee. After euthanisation of the animal, the oesophagus was harvested from the cervical portion to the gastroesophageal junction and washed with phosphate buffererd saline (PSP) containing 5% antibiotic antimycotic solution. Next, the oesophagus was completely decellularised through DET. A detailed description of DET is provided elsewhere (Totonelli et al. [2013]). In preparation for imaging, the specimen was fixed in 2% glutaraldehyde, followed by a procedure known as "ultra-drying", which is also described in detail in (Totonelli et al. [2013]). Tissue segments of approximately 1 cm length were mounted on a support to present the full sample thickness to the beam.

During the PC-CT scan, 2000 projections were acquired, with a 0.18 degree angular step and over a total angular range of 360 degrees. For each projection, the sample was exposed for 2 seconds. The projections were corrected for detector gain and offset before the phase retrieval method described by equation 3.1 was applied. CT slices were reconstructed via the FBP in combination

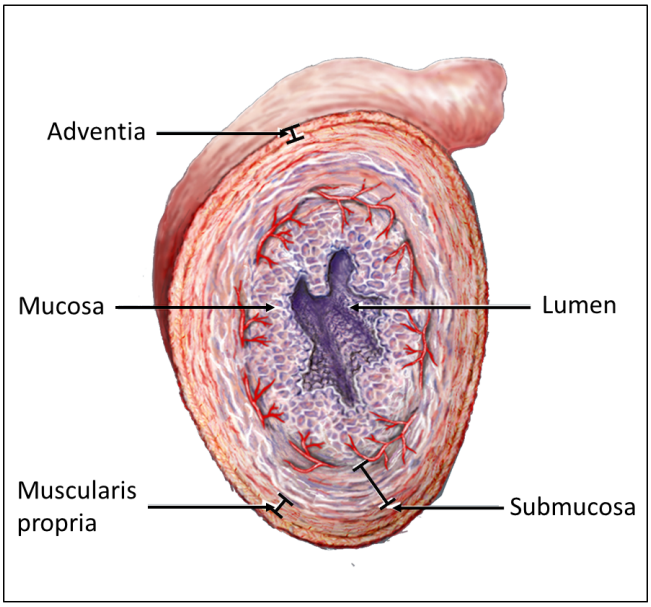

Figure 3.7: Schematic showing the structure of an oesophagus. The main components are labelled. The figure has been adopted from alebady.com.

with the ramp filter, using the free pyHST (High Speed Tomography in PYthon) software (https://forge.epn-campus.eu/html/pyhst2/). No further image processing was applied post reconstruction. Subsets of the reconstructed datasets were extracted showing transverse, coronal and sagittal slices of the specimen. Additionally, datasets were volume rendered using the open source software ImageJ (http://rsbweb.nih.gov/ij/).

The reconstructed images were assessed by clinicians, with focus on the structure of the ACM. All clinicians were requested to assess whether the achieved image quality (image contrast and resolution) was sufficient to draw a conclusion about the success of the used decellularisation method.

Results and Discussion

A healthy oesophagus consists of five main structural components, which appear in the form of circular layers (see schematic in figure 3.7). The innermost component is the lumen, i.e. the cavity for the incoming nutrition. The mucosal layer's

functionality can be described as absorption and secretion. The sub-mucosal layer contains the mucous secreting glands and connective tissue structures. The two outermost components (muscularis propria and adventia) are muscular layers that induce the oesphagal movements needed for swallowing. In order to guarantee the full digestive functionality of the tissue-engineered oesophagus, it is important that all five components are preserved and intact in the ACM, because the scaffold structure serves as a "guide" when the ACM is repopulated with stem cells of the organ recipient, either post-operatively or via pre-operative seeding.

Figure 3.8 shows the reconstructed PC-CT images of the decellularised oesophagus. Four rendering modes were selected: transverse, coronal and sagittal cross-sections (a-c) and a 3D visualisation of the entire specimen (d). In all four modes, the structural layers can clearly be identified (labelled 1-5).

A zoom of selected areas in the transverse cross-section (marked by boxes and letters A-C in figure 3.8 (a)) are shown in figure 3.9. We would like to highlight in particular the enhanced image contrast between similar tissue types, which can be attributed entirely to phase effects. For example, the mucosa and sub-mucosa vary significantly in grey value and can therefore be differentiated (figure 3.9 A). Also, we would like to point out that the achieved spatial resolution is sufficiently high to see not only the scaffold structure, but also ultra-structural details within the different organ components. In particular, we would like to emphasize the level of detail within the muscular layers (figure 3.9 B-C).

The images were assessed by clinicians, and the image quality was rated sufficiently high to extract the necessary clinical information; more precisely, the detailed visualisation facilitated the conclusion that all components are present and intact in the ACM, which has then been backed by a histological analysis of the specimen (not shown in this thesis). As a result of these findings, the PC-CT images have been judged to provide sufficient information to draw the conclusion that the DET is a suitable method for the decellularisation of the oesophagus, preserving the ultra-structural characteristics of native tissue.

More generally, the clinicians' feedback indicated that the PC-CT method could be used as a tool to assess any newly developed decellularisation method and whether or not it is suited for the generation of ACMs of more complex organs.

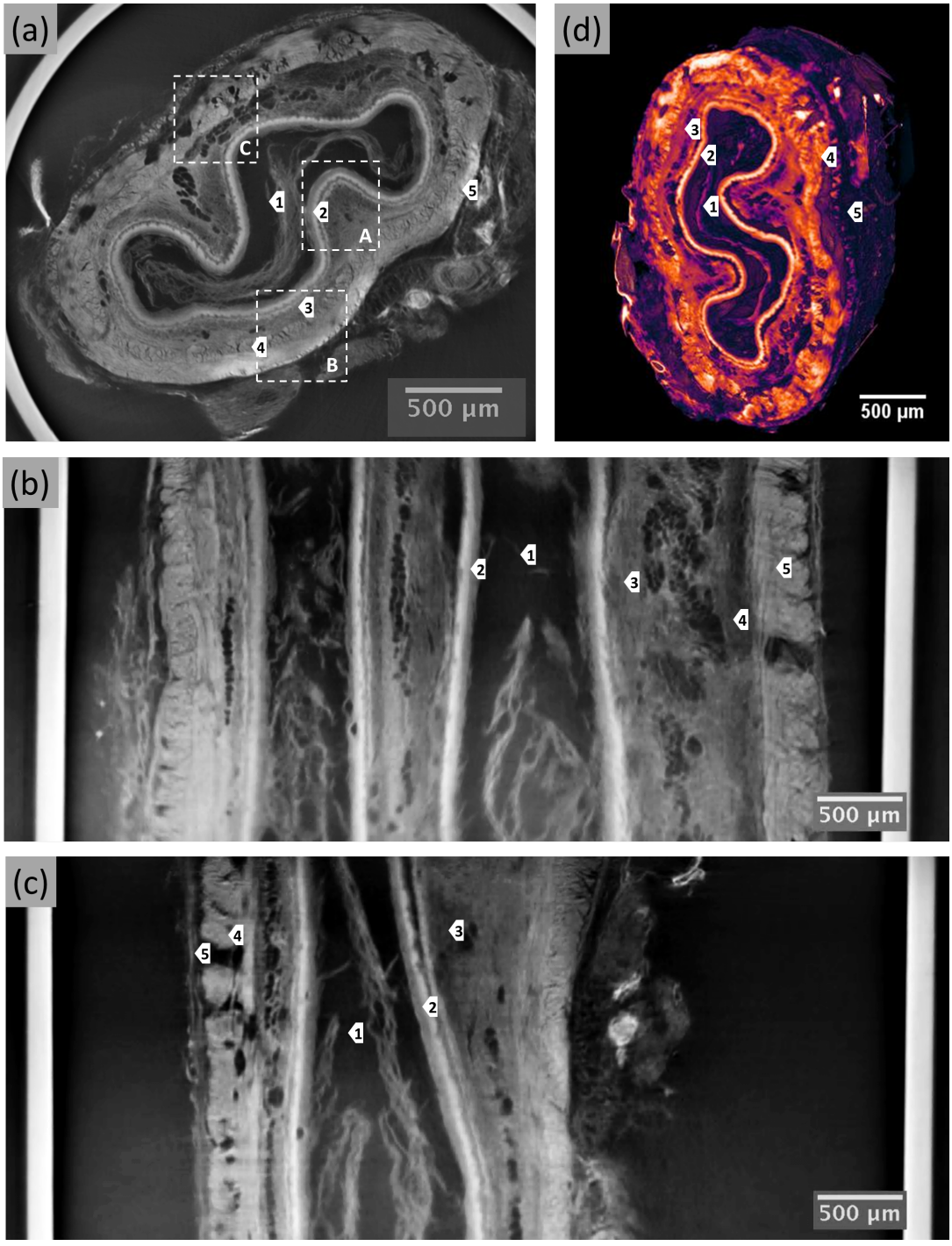

Figure 3.8: PC-CT images of the oesophagus acellular matrix: (a) transverse cross-section, (b) coronal cross-section, (c) sagittal cross-section and (d) volumetric rendering. The main structural components of the oesophagus are clearly visible and labelled 1. Lumen, 2. Mucosa, 3. Submucosa, 4. Muscularis Propria and 5. Adventia.

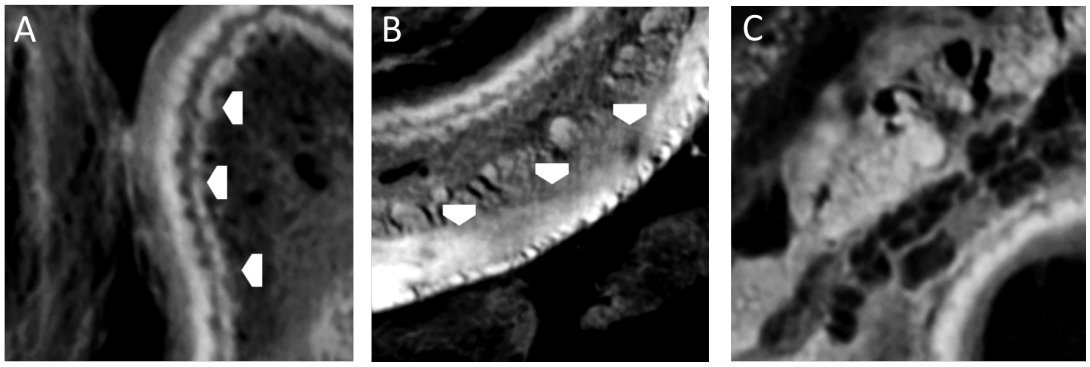

Figure 3.9: Zoom of the areas specified in figure 3 (a) showing the mucosa / sub-mucosa interface (A), the muscularis propria / adventia interface (B) and another sub-region of the muscularis propria (C).

Conclusion

PC-CT imaging was applied to the ACM of an oesophagus obtained from a rabbit animal model with the purpose of addressing the need for a fast, cheap, easily accessible, high resolution and high contrast 3D imaging modality. An FSP-CT setup at the ESRF was used to image the specimen, and a volumetric dataset was reconstructed using basic CT reconstruction concepts together with a method-specific phase retrieval procedure. The resulting images were assessed by clinicians who have established the structural preservation within the ACM. Therefore, it could be concluded that the application of the DET decellularisation method to the oesophagus was successful.

We would like to repeat at this point that similar conclusions (assessment of DET for the decellularisation of a pig oesophagus) had been drawn earlier (Totonelli et al. [2013]). However, in that publication, destructive and non-intrinsically 3D methods such as histologic analysis, SEN and TEM were the main tools to assess the structural preservation in the ACM. As highlighted before, neither of these imaging modalities qualifies as a tool for a routine structural assessment of acellular scaffolds. In this sub-chapter, we demonstrated that PC-CT can provide structural information that is comparable to that obtained with histology and electron microscopy in terms of its clinical value. Due to the compatibility of some PC methods with conventional equipment, PC-CT has the

potential for a wide-spread application, with the realistic perspective of installing scanners directly in the TE research laboratories. Most importantly, unlike other methods, it could be used *in vivo* (e.g. initially on animal models) for post-implantation assessment. As a next step, and to demonstrate this potential, we anticipate the imaging of ACMs with a laboratory-based PC-CT scanner (e.g. using EI-CT).

3.4 Chapter Summary and Conclusion

Two important scientific fields were targeted where 3D high definition imaging is crucially required, but for which suitable modalities do not exist. The imaging of thin layers of articular cartilage is important for the improved understanding of OA, and the visualisation of acellular organ scaffolds is essential for a rapid development of regenerative medicine. Both applications were demonstrated to benefit from PC-CT. Proof-of-concept experiments using existing PC-CT methods (ABI-CT and FSP-CT) were carried out at synchrotrons to show that images with a sufficient quality, as needed by the respective clinical purposes, can be achieved.

It would be highly desirable to obtain results similar to the ones presented in this chapter with a laboratory-based setup instead of a synchrotron, which can possibly be achieved with EI-CT. Therefore, the obtained results serve as an additional significant motivation for the development of EI-CT.

Chapter 4

Practical and Theoretical Bases for Edge Illumination Phase Contrast CT

4.1 Chapter Introduction and Outline

In the following, practical and theoretical considerations that form the basis for EI-CT will be discussed.

As a starting point, phase retrieval procedures for the separation of the combined phase and absorption contrast present in EI projections will be described in detail. Phase retrieval establishes line integral relationships between EI projections and the optical constants, which is a necessary requirement for performing CT.

Like in ABI and GI, the phase sensitivity in EI is unidirectional. A two-directional approach has been developed (Olivo et al. [2009]), but so far it has only been implemented with synchrotron radiation, and is not considered for a CT extension at this stage. As a consequence of the unidirectional phase sensitivity, two possibilities exist to set up an EI-CT scanner. These two sensitivity modes will be discussed in detail for both the scanning and coded aperture EI method.

A central part of this chapter deals with the adaptation of the CT reconstruction procedures to the EI method. It will be discussed which quantities can be

reconstructed from EI-CT measurements, with and without the performance of phase retrieval.

The chapter continues with the description of the adaptation of an existing simulation software for planar EI to enable the simulation of EI-CT scans.

Finally, two experimental EI-CT setups are described: one based on the scanning EI method set up at the Elettra synchrotron, the other one based on the coded aperture EI method using a conventional x-ray source, that is installed at UCL.

4.2 Phase Retrieval

As explained in chapter 2, CT reconstruction requires a line integral relationship between the object function and the projections. While in absorption-based CT this relationship is established via the Beer-Lambert law, in PC-CT it is given by the phase function. For EI, the first derivative of the phase function can be extracted by applying a phase retrieval procedure to the projections. In the following, phase retrieval formulas for EI will be provided, differing slightly for the scanning and the coded aperture EI methods; hence, both cases will be treated separately. The formulas for the coded aperture EI method are the ones published in (Munro et al. [2013b]). For the derivation of those for the scanning EI method, the approach described by Munro et al. [2013b] was adapted to the specific setup discussed in this thesis, ultimately yielding results that are equivalent to those published in Diemoz et al. [2013]. Before the derivation of the formulas, a characteristic quantity of EI, the illumination curve (IC), will be introduced.

Not only is phase retrieval required to establish line integral relationships, it is also important for quantitative imaging, as it enables the reconstruction of separate RID and absorption term maps.

The Illumination Curve

A quantity that plays a major role in EI phase retrieval is the IC, a system specific calibration measure that is obtained *without* the object in place. It describes how the intensity hitting the detector varies depending on the position of the absorbing edge or the pre-sample apertures respectively (see figures 2.5 and 2.6

in chapter 2.2.5).

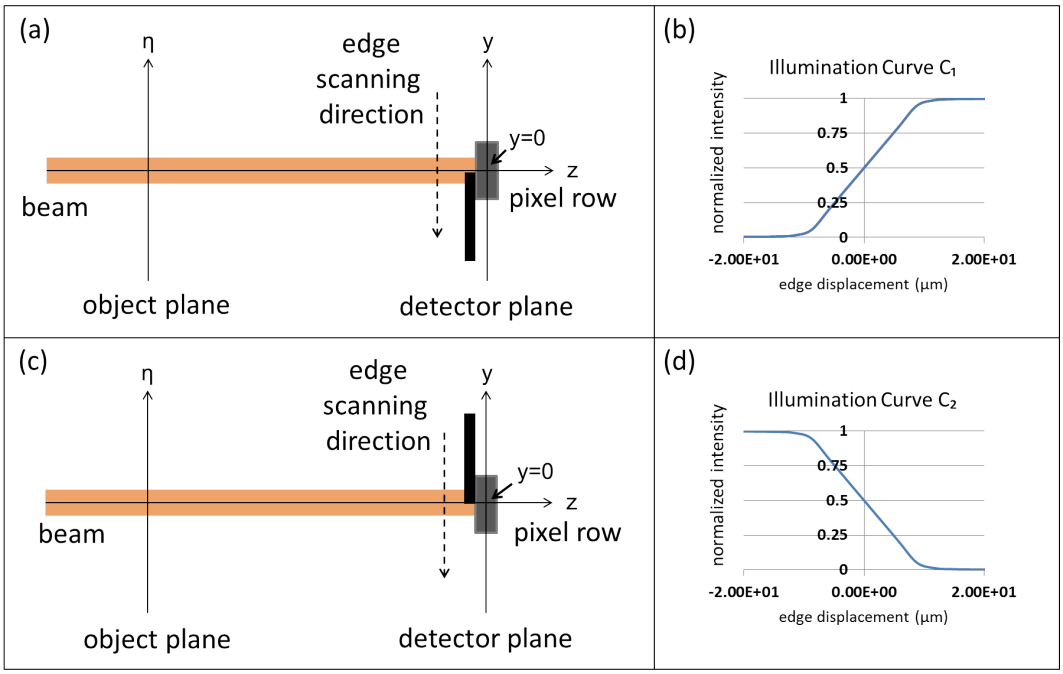

Figure 4.1: The two configurations in which the scanning EI method can be used: the x-ray absorbing edge can be positioned such that it covers to bottom (a) or the top half (c) of the row of pixels. The respective illumination curve can be measured by scanning the edge along the indicated direction and by recording the corresponding intensity. The illumination curve measurements take place without an object in the beam. Scanning around the two indicated positions of the edge lead to inverted illumination curves (b,d). The drawings in (a,c) extend uniformly into the plane of the paper.

For the scanning EI method, the IC can be measured by moving the absorbing edge through the beam/detector configuration as indicated in figure 4.1 and by recording the corresponding intensities. The IC is monotonically increasing or decreasing, depending on whether the edge is moved away from (a) or towards (c) the laminar beam. In both cases, the IC assumes its maximum and minimum when the entire beam falls onto the active pixel surface and onto the absorbing edge respectively. In the following, we will distinguish the increasing and decreasing ICs by referring to them with the symbols C_1 and C_2. The distinction is necessary because the absorbing edge could be too large to move it through

the beam entirely in a single scan. Simulated ICs (obtained from the software developed by Vittoria et al. [2013]) assuming a Gaussian-shaped beam are shown in figure 4.1 (b,d).

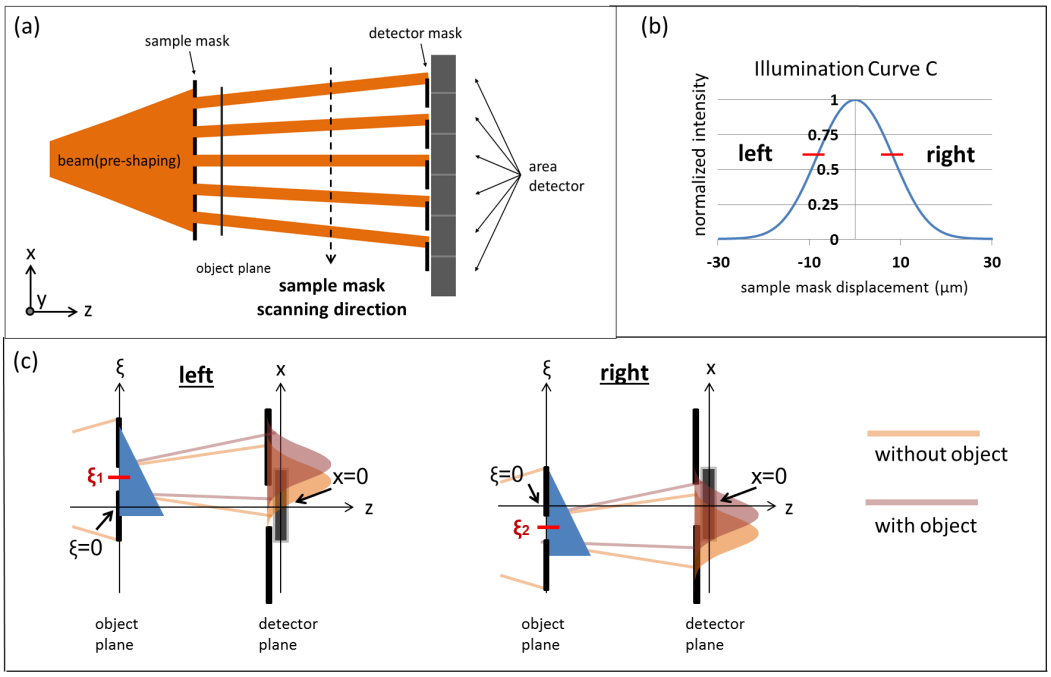

Figure 4.2: Schematic of a coded aperture EI setup (a) and the illumination curve (b) obtained by scanning the sample mask along the indicated direction. (c) shows "zoomed" sketches of a single aperture pair positioned corresponding to the left slope and the right slope of the IC, which are typically used for imaging. An object introduces attenuation and refraction-induced displacement of each beamlet. The drawing extends uniformly into the plane of the paper.

For the coded aperture EI method, the IC can be obtained by keeping the detector mask in a fixed position, and scanning the sample mask in the direction transverse to the apertures (as indicated in figure 4.2 (a)) while recording the corresponding intensities. For this setup, the IC is a periodic function that assumes its maximum when the transmitting parts of both sets of apertures overlap, and its minimum when the absorbing parts of the sample apertures cover the transmitting parts of the detector apertures. The IC for the coded aperture EI method will be referred to as C. A single period of a simulated IC (assuming a Gaussian-

shaped beam) is shown (figure 4.2 (b)), as are zoomed schematics showing the relative positions of a single sample/detector aperture pair corresponding to the left and right slopes of the IC. The effect of an object (e.g. a wedge) in the beam (refraction) is indicated in (c) as well.

The role of the IC in EI is similar to that of the rocking curve in ABI. If the laminar beam in the scanning EI method (or, respectively, the sample mask in the coded aperture EI method) is positioned corresponding to the slope of the IC, an edge illumination condition is achieved and refraction effects can be detected with a high sensitivity. Changing from the monotonically increasing C_1 to the monotonically decreasing C_2 in the scanning EI method (or, respectively, changing the position from one slope of C to the other in a coded aperture EI method) has the effect of inverting the detected phase contrast.

Phase Retrieval for the Scanning EI Method

Phase retrieval methods for EI are based on the following mathematical model. Considering the scanning EI setup sketched in figure 4.1, the intensities for the relative positions of the beam and the absorbing edge shown in (a) and (c) *without* an object in place are given by:

$$I_1 = I_0 \cdot C_1(0) \tag{4.1}$$

$$I_2 = I_0 \cdot C_2(0), \tag{4.2}$$

respectively. The symbol I_0 denotes the intensity measured on top of the respective illumination curve C_1 or C_2. An object introduced to the setup causes attenuation and a displacement (due to refraction) of the beam. These effects can be described mathematically as:

$$A = e^{-\mu} \tag{4.3}$$

$$D = \frac{\partial \Phi}{\partial \eta} \cdot \frac{z_{od}}{M}, \tag{4.4}$$

where μ and Φ are the projected absorption term and the phase function, z_{od} is

the object-to-detector distance, and M is the magnification. The intensities for the relative positions of beam and edge shown in figures 4.1 (a) and (b) *with* an object in place are given by:

$$I_1 = I_0 \cdot A \cdot C_1(D) \tag{4.5}$$

$$I_2 = I_0 \cdot A \cdot C_2(D), \tag{4.6}$$

respectively. Here, the role of the ICs become apparent: they describe the intensity variation caused by a displacement (refraction) of the beam. We would like to underline that the general relation:

$$C_1(\eta) + C_2(\eta) = 1 \qquad \forall \eta \tag{4.7}$$

holds for the ICs obtained for the configurations shown in figures 4.1 (a) and (c) due to the existing symmetry. Therefore, the sum of the intensities I_1 and I_2 (with the object in place) normalised by the beam intensity yields the attenuation:

$$\frac{I_1 + I_2}{I_0} = A \cdot (C_1(D) + C_2(D)) = A, \tag{4.8}$$

and therefore, as a direct consequence, the projected absorption term:

$$\mu = -\ln\left(\frac{I_1 + I_2}{I_0}\right). \tag{4.9}$$

Please note that the latter formula is consistent with the Beer-Lambert law.

On the other hand, computing the difference between I_1 and I_2 yields:

$$I_1 - I_2 = I_0 \cdot A \cdot (C_1(D) - C_2(D)). \tag{4.10}$$

By inserting the relation given in 4.8 it follows that:

$$\frac{I_1 - I_2}{I_1 + I_2} = C_1(D) - C_2(D). \tag{4.11}$$

At this point, a function:

$$F(D) \coloneqq C_1(D) - C_2(D) \tag{4.12}$$

can be defined that maps the displacement caused by the object onto the difference between the two corresponding IC values. The function F for the simulated ICs C_1 and C_2 is shown in figure 4.3 (blue curve). Please note that F is a strictly monotonic function and, hence, can be inverted. The value of D can therefore be recovered by applying the inverse of F, yielding:

$$D = F^{-1}\left(\frac{I_1 - I_2}{I_1 + I_2}\right). \tag{4.13}$$

According to equation 4.4, this expression is equivalent to:

$$\frac{\partial \Phi}{\partial \eta} = F^{-1}\left(\frac{I_1 - I_2}{I_1 + I_2}\right) \cdot \frac{M}{z_{od}}, \tag{4.14}$$

which is in fact the first derivative of the phase function.

Phase Retrieval for the Coded Aperture EI Method

For the coded aperture EI method, a similar mathematical model can be used. Again, two positions of the sample mask lead to an edge illumination condition: when the individual beamlets hit either side of the absorbing septa on the detector mask. The two positions correspond to the left and the right slope of the IC, and are depicted schematically as a zoom in figure 4.2 (c) ("left" and "right"). The intensities at the detector plane for the left and right position *without* an object in place are given by:

$$I_1 = I_0 \cdot C(\xi_1) \tag{4.15}$$

$$I_2 = I_0 \cdot C(\xi_2). \tag{4.16}$$

The quantities ξ_1 and ξ_2 denote the respective shifts of the sample mask that lead to the left and right edge illumination conditions, and are in the following referred to as "working" points. The variable I_0 refers to the maximum intensity

that is measured when the apertures in the two masks overlap. If the beamlets are smaller than the detector mask apertures, I_0 is equal to the intensity of the incoming beam after pre-shaping by the sample mask, otherwise the intensity I_0 is a fraction of that, as determined by the detector apertures.

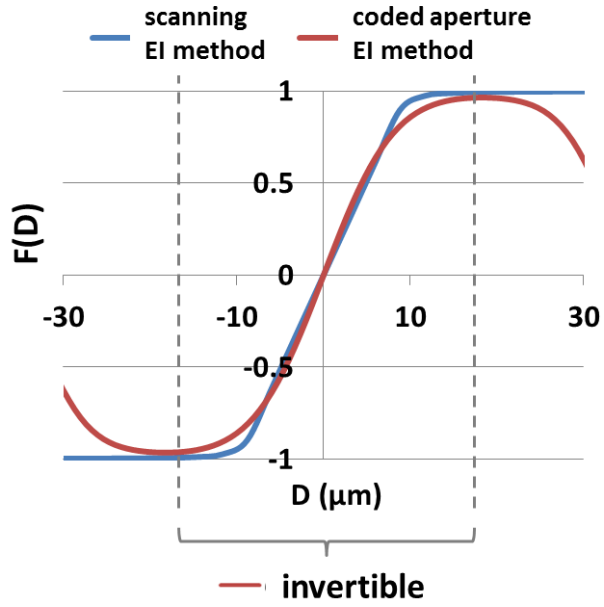

Figure 4.3: The function F is essential for EI phase retrieval. The quantity can be obtained directly from the measured illumination curve(s). This graph shows the function f for the scanning EI method (blue curve) and the coded aperture EI method (red curve). Please note that F is not invertible everywhere in the latter case.

An object positioned downstream of the sample mask causes attenuation and deviation of the beamlets, both effects again being described by equations 4.3 and 4.4. Therefore, *with* an object in place, the measured intensities are:

$$I_1 = I_0 \cdot A \cdot C(\xi_1 + D) \tag{4.17}$$

$$I_2 = I_0 \cdot A \cdot C(\xi_2 + D). \tag{4.18}$$

Computing the sum of I_1 and I_2 yields:

$$I_1 + I_2 = I_0 \cdot A(C(\xi_1 + D) + C(\xi_2 + D)). \tag{4.19}$$

Solving for A yields:

$$A = \frac{(I_1 + I_2)/I_0}{C(\xi_1 + D) + C(\xi_2 + D)}. \tag{4.20}$$

Making the assumption that the working points ξ_1 and ξ_2 are chosen symmetrically about the origin and correspond to the parts of the IC which are approximately linear, the relation:

$$C(\xi_1 + D) + C(\xi_2 + D) \approx C(\xi_1) + C(\xi_2) \tag{4.21}$$

holds. Therefore, the formula for the projected absorption term is obtained as:

$$\mu = -\ln\left(\frac{(I_1 + I_2)/I_0}{C(\xi_1) + C(\xi_2)}\right). \tag{4.22}$$

Considering the difference of I_1 and I_2:

$$I_1 - I_2 = I_0 \cdot A \cdot (C(\xi_1 + D) - C(\xi_2 + D)) \tag{4.23}$$

and substituting equation 4.20 into this expression yields:

$$\frac{I_1 - I_2}{I_1 + I_2} = \frac{C(\xi_1 + D) - C(\xi_2 + D)}{C(\xi_1 + D) + C(\xi_2 + D)}. \tag{4.24}$$

In the same manner as before, we can now define a function F:

$$F(D) \coloneqq \frac{C(\xi_1 + D) - C(\xi_2 + D)}{C(\xi_1 + D) + C(\xi_2 + D)} \tag{4.25}$$

that maps the displacement of the beamlets onto a combination of corresponding IC values. An example of the function F for the simulated IC and symmetrically positioned working points $\xi_1 = -\xi_2$ is shown in figure 4.3 (red curve). Unlike for the scanning EI method, in the case of coded apertures F is not necessarily injective everywhere. Therefore, before inversion, F has to be restricted to its strictly monotonic parts. As F is effectively a function of the refraction angle

(see equations 1.5 and 1.5), the restriction implies that angles beyond a certain limit cannot be recovered. This issue of phase retrieval for the coded aperture EI method is discussed in chapter 5.3. For small refraction angles (i.e. the majority of the cases encountered, especially in biological applications), the displacement of the beamlets can be recovered via:

$$D = F^{-1}\left(\frac{I_1 - I_2}{I_1 + I_2}\right), \tag{4.26}$$

which yields the expression:

$$\frac{\partial \Phi}{\partial \xi} = f^{-1}\left(\frac{I_1 - I_2}{I_1 + I_2}\right) \cdot \frac{M}{z_{od}} \tag{4.27}$$

for the derivative of the phase function.

In conclusion, phase retrieval can be performed for EI, with slightly different formulas for the scanning and coded aperture implementations. In both cases, the formulas yield the derivative of the phase function and the projected absorption term, and require two images as input, acquired whilst opposing edges are illuminated. The two formulas can be explained intuitively. It was mentioned previously that changing the illumination from one edge to the other has the effect of reversing the phase contrast in the images, while the absorption contrast remains unaffected. Therefore, it is evident that, by summing the two images, only the absorption information survives, while their subtraction causes the absorption to cancel out, such that only the phase contrast remains.

4.3 Horizontal and Vertical Phase Sensitivity

Phase effects occur at transitions between materials with different RIDs, which are typically present in all directions. However, due to its unidirectional phase sensitivity, only one component of these effects can be picked up by an EI system (implemented either with the scanning or the coded aperture EI method). In fact, the direction of phase sensitivity determines which features of an object are seen in the projections and which ones are not: features parallel to the direction of phase

sensitivity generate contrast, while features oriented in the other direction do not. When acquiring planar EI images and some features of the object geometry are known in advance, the unidirectional sensitivity can be optimally exploited by orienting the object according to the main direction of the desired object features. Generally speaking, planar EI systems with different sensitivity (either in the horizontal or vertical direction) are equivalent, because a change in the object orientation transforms one into the other.

This is different when CT is performed. As a result of the unidirectional phase sensitivity, two different EI-CT systems need to be distinguished, shown schematically for the scanning and coded aperture EI methods in figures 4.4 and 4.5. EI-CT systems sensitive to phase effects within the plane perpendicular to the AOR will be referred to as horizontal sensitivity (HS) mode and those sensitive in the plane containing the AOR as vertical sensitivity (VS) mode.

Figure 4.4 (a) shows a scanning EI-CT setup in VS mode. A sinogram for the illuminated cross-section can be obtained by rotating the object and taking images while this is kept in a fixed vertical position. In order to acquire sinograms for other transverse cross-sections, the object has to be scanned vertically, and the same rotation applied at each position of the scan. Figure 4.4 (b) shows a scanning EI-CT setup in HS mode. In this setup, the laminar beam illuminates a coronal cross-section of the object. However, since CT allows for the reconstruction of transverse slices only, horizontal object scanning is required at each rotation angle in order to obtain the sinograms. This requirement leads to a lengthy acquisition procedure. Therefore, scanning EI-CT setups are typically operated in VS mode.

Figures 4.5 (a) and (b) show coded aperture EI-CT setups in VS and HS mode. Thanks to the coded apertures, no object scanning is needed for either mode, hence CT acquisitions only require the rotation of the object. Therefore, both sensitivity modes are equivalently practical.

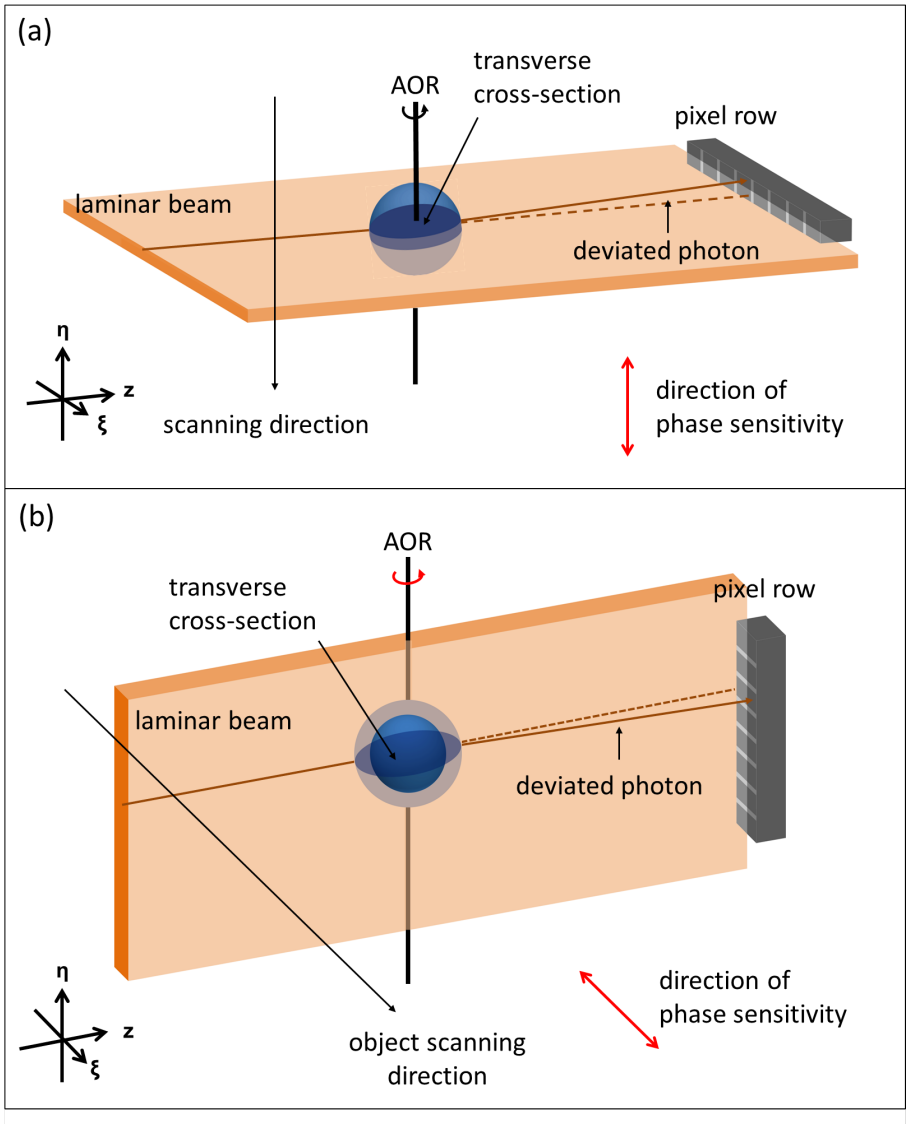

Figure 4.4: The two sensitivity modes of scanning EI-CT: setups sensitive to refraction angles in the vertical direction (a) and the horizontal direction (b) are shown. The indicated frame of reference provides the coordinates of the object. Please note that object scanning along the indicated direction is required to build up an image.

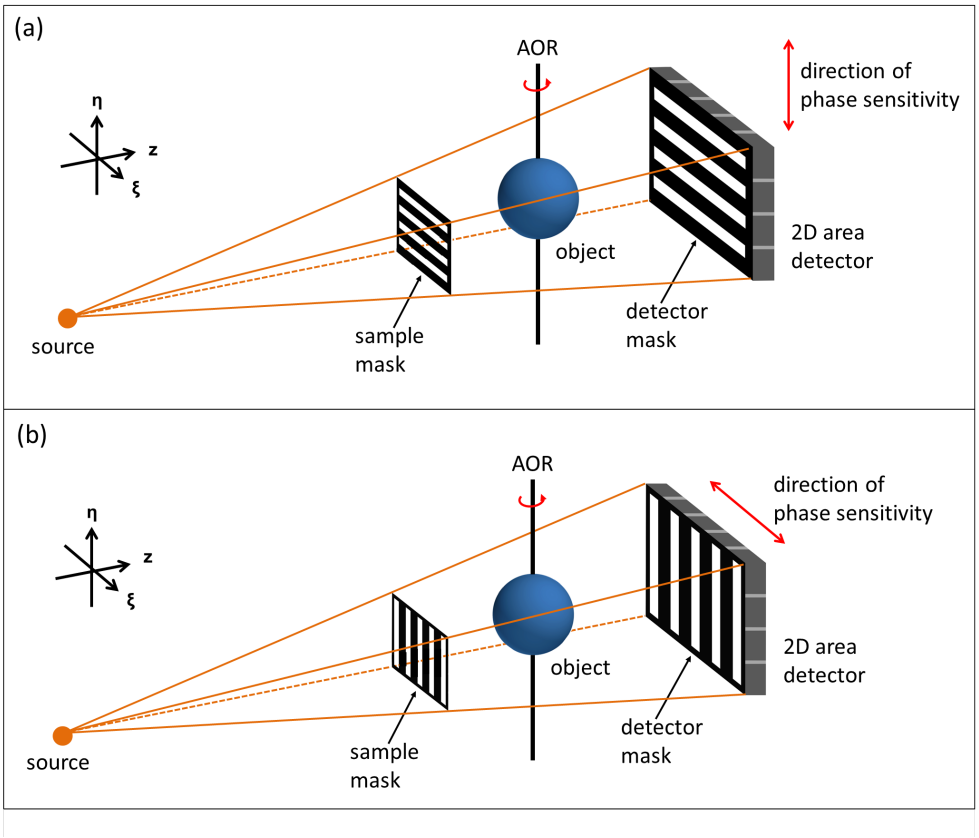

Figure 4.5: The two sensitivity modes in coded aperture EI-CT: setups sensitive to refraction angles in the vertical direction (a) and the horizontal direction (b) are shown. The indicated frame of reference provides the coordinates of the object. Due to the plurality of beamlets made available by the coded apertures, no sample scanning is required to build up an image.

4.4 Adaptation of CT Reconstruction Procedures to the Method

The sensitivity mode determines whether or not the performance of phase retrieval is mandatory, and which physical quantities the reconstructed EI-CT maps will contain (the RID or its gradient components, the absorption term, or a combination of both). The different options, phase retrieval requirements, and corresponding reconstruction formulas are listed in table 4.1. The notation P_{EI} was adopted to refer to EI-CT sinograms, with the respective sensitivity mode

being indicated by superscripts VS or HS. "Post phase retrieval sinograms", i.e. sinograms showing differential phase function or projected absorption terms, are referred to by additional subscripts *phase* or *abs*. For the two sensitivity modes, these are given by (see chapter 4.2):

$$P^{VS}_{EI,phase}(x,y,\theta) = \frac{\partial}{\partial y}\Phi(x,y,\theta) \tag{4.28}$$

$$P^{HS}_{EI,phase}(x,y,\theta) = \frac{\partial}{\partial x}\Phi(x,y,\theta) \tag{4.29}$$

$$P^{VS}_{EI,abs}(x,y,\theta) = P^{HS}_{EI,abs}(x,y,\theta) = \mu(x,y,\theta). \tag{4.30}$$

Please note that the reconstruction of all but combined phase and absorption maps require the performance of phase retrieval. Also, RID and absorption term maps can be reconstructed from VS *and* HS mode measurements. In the following, the advantages and disadvantages connected to the reconstruction of the different maps will be discussed.

The reconstruction of RID maps, i.e. of $\delta(\xi, z, \eta)$, is essential for quantitative imaging, i.e. the identification of the imaged materials. In this sense, the role of the RID in PC-CT is equivalent to that of the Hounsfield units in conventional CT, with the difference that the former can lead to improved soft tissue contrast. RID maps do not show edge-enhancement, which can be advantageous when an assessment by clinicians (who may not be used to seeing edge-enhanced images) is required. The images of the oesophagus shown in chapter 3.3 are a good example of the strength of RID maps. The disadvantage is the necessity to perform phase retrieval, which requires doubling the scan time. Moreover, the integration step in the reconstruction can lead to artefacts. The reconstruction from VS EI-CT data can cause unidirectional stripes, as local errors in the sinograms are smeared along the one-dimensional integration paths. Maps reconstructed from HS EI-CT data can also be affected by artefacts; however, these would not appear in the form of stripes as the integration implicitly performed by the Hilbert filter is two-dimensional. Instead, the low spatial frequencies can be affected, generating artefacts in the RID maps that take the form of gradually changing shades.

Map	Phase Retrieval	Reconstruction Formula(s)
$\delta(\xi, z, \eta)$	yes	$\text{FBP}_{ramp}[\int_{y_0}^{y} P^{VS}_{EI,phase}(x, y, \theta)\ dy](\xi, z, \eta)$
		$\int_{\eta_0}^{\eta} \text{FBP}_{ramp}[P^{VS}_{EI,phase}(x, y, \theta)](\xi, z, \eta)\ d\eta$
		$\text{FBP}_{Hilbert}[P^{HS}_{EI,phase}(x, y, \theta)](\xi, z, \eta)$
$\frac{\partial}{\partial \eta}\delta(\xi, z, \eta)$	yes	$\text{FBP}_{ramp}[P^{VS}_{EI,phase}(x, y, \theta)](\xi, z, \eta)$
$\frac{\partial}{\partial \xi}\delta(\xi, z, \eta)$	yes	$\text{FBP}_{ramp}[P^{HS}_{EI,phase}(x, y, \theta) \cdot \cos\theta)](\xi, z, \eta)$
$\frac{\partial}{\partial z}\delta(\xi, z, \eta)$	yes	$\text{FBP}_{ramp}[P^{HS}_{EI,phase}(x, y, \theta) \cdot \sin\theta)](\xi, z, \eta)$
$\beta(\xi, z, \eta)$	yes	$\frac{1}{2k} \cdot \text{FBP}_{ramp}[P^{VS}_{EI,abs}(x, y, \theta)](\xi, z, \eta)$
	yes	$\frac{1}{2k} \cdot \text{FBP}_{ramp}[P^{HS}_{EI,abs}(x, y, \theta)](\xi, z, \eta)$
combined phase and absorption	no	$\text{FBP}_{ramp}[P^{VS}_{EI}(x, y, \theta)](\xi, z, \eta)$

Table 4.1: List of physical quantities that can be reconstructed from EI-CT measurements. The required sensitivity mode (VS or HS) is indicated, as well as whether or not the performance of phase retrieval is required. The corresponding CT reconstruction formulas are provided.

"Gradient" artefacts only appear as a result of significant errors in the sinograms, examples of which will be given when discussing future work in chapter 7.

The reconstruction of differential phase maps, i.e. of either $\frac{\partial}{\partial \eta}\delta(\xi, z, \eta)$ or $\frac{\partial}{\partial \xi}\delta(\xi, z, \eta)$ and $\frac{\partial}{\partial z}\delta(\xi, z, \eta)$, can be valuable whenever edges and contours need to be visualised. Due to the unidirectional phase sensitivity of EI, however, not *all* edges within an object are enhanced simultaneously. This would require the reconstruction of the full RID gradient, i.e. $\nabla\delta = (\partial\delta/\partial\xi, \partial\delta/\partial z, \partial\delta/\partial\eta)$. However, as for ABI-CT and GI-CT, this is not practical, as it requires two complete EI-CT scans, in between which the setup has to be changed from VS

to HS mode while the object is kept in exactly the same position.

The possibility to reconstruct absorption term maps, i.e. $\beta(\xi, z, \eta)$, in addition to RID maps, makes EI-CT intrinsically "multi-modal". Absorption term maps can provide supporting quantitative information for material identification.

The reconstruction of mixed maps showing combined phase and absorption contrast can be advantageous whenever keeping scan time and delivered dose to a minimum is a key requirement. Mixed maps effectively provide an edge-enhancement effect in addition to conventional absorption information, which helps in identifying faint details.

4.5 Extension of an Existing Simulation Software to a CT Geometry

The EI method in its planar setup has undergone significant development over recent years, enabled in part by the possibility to simulate the imaging modality using software implementations of mathematical models. Two approaches have been followed in the simulations: one based on geometrical optics (Olivo and Speller [2007b]), and one based on a wave optics formulation (Munro et al. [2010b], Vittoria et al. [2013]). The latter is more rigorous, as it takes coherence effects into account and, hence, is better suited for the simulation of synchrotron experiments. The geometrical optics approach is an approximation, however, under conditions of limited coherence, both approaches give equivalent results (Munro et al. [2010a]). Provided appropriate degrees of coherence were assumed, both approaches were demonstrated to be in accordance with experimental results.

Thin, low absorbing wires (such as plastic threads and fibres) are often used as phantoms in PC studies for several reasons. First, they are almost invisible when imaged with a conventional radiographic system, and thus ideal to demonstrate the difference between conventional and phase sensitive methods. Secondly, the phase shifts introduced by wires varies smoothly from weak to strong thanks to their circular geometry, yielding a signal with bright and dark fringes on either side of the wire. From an application point of view, wires can mimic various

biological structures, such as tissue fibres and cartilage structures. In a practical setting, wire phantoms can be easily built as manufacturers offer thin threads and fibres of varying diameters for a wide range of materials. At the same time, it is straightforward to generate numerical phantoms that match the experimental ones for use in computer simulations. The existing EI models were used primarily to simulate projections of single wires, either in air or in a background material.

Besides a preliminary extension of the geometrical optics model by Olivo and Speller to a pseudo 3D tomosynthesis (limited angle tomography providing partial depth information) geometry (Szafraniec et al. [2014]), the existing software has, until now, been limited to the simulation of a planar system. The extension to a full 3D simulation, providing sinograms as acquired during EI-CT scans, will be described in the following. The CT extension is a modification of the implementation of the wave optical model by Vittoria et al. [2013], which was chosen over that by Munro et al. [2010b] because of its superiority in terms of computational speed. Speed is an important factor when simulating CT experiments, as data for a large number of angles has to be generated.

In short, the wave optical model describes the propagation of x-rays via the Fesnel propagator (i.e. via Fresnel-Kirchhoff diffraction integrals). The sample mask which is part of a coded aperture EI system is included via a periodic transmission function (square wave type). The object is modelled by another transmission function:

$$T(\xi) = \exp(-i \cdot (k\Phi(\xi) + i\mu(\xi))), \tag{4.31}$$

where Φ and μ are the phase function and projected absorption term. The dependence upon the vertical coordinate has been dropped. The intensity of the propagated x-rays that hit the detector plane after having passed through the sample mask and the object is integrated within the active pixel areas left uncovered by the detector mask, yielding the final detected signal. An extended x-ray source can be included by convolving the intensity obtained for a point source with the actual source distribution. Similarly, the intensity arising from a polychromatic source can be calculated as the weighted sum of the monochromatic

intensities for all spectral energies. Vittoria et al. [2013] suggest a way to express the Fresnel propagator as a convolution integral, which is equivalent to a multiplication in Fourier space and can therefore be efficiently computed using the Fast Fourier Transform (FFT). Like the original model by Vittoria et al., also the CT extension has been implemented using the MATLAB platform (MathWorks, USA).

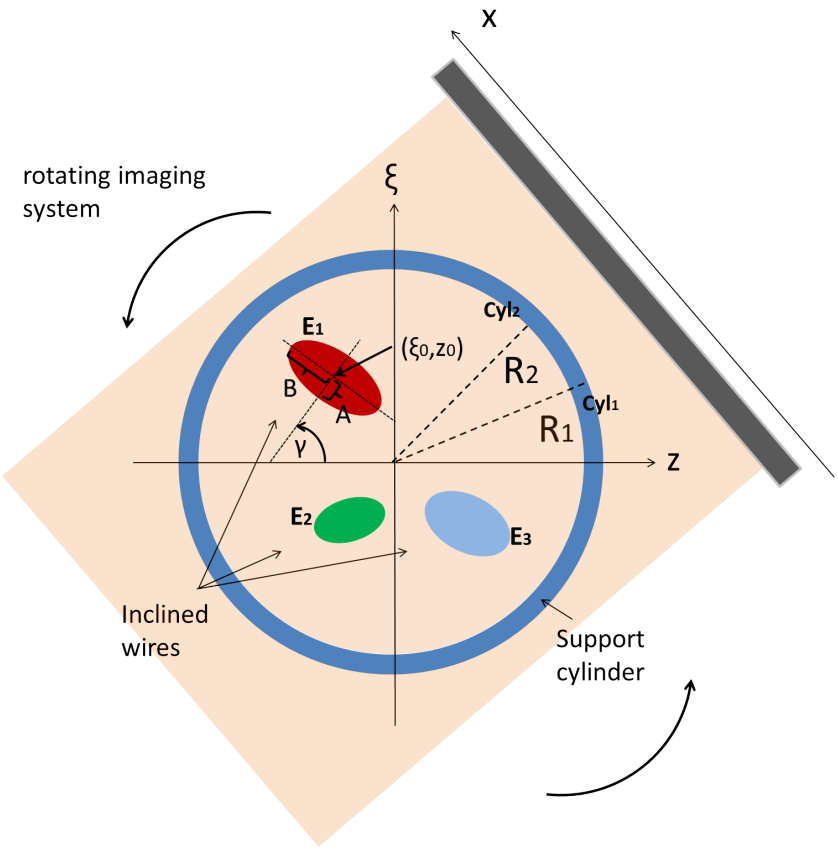

Figure 4.6: Schematic of the numerical phantom designed for the simulation of EI-CT. A transverse cross-section of the phantom is shown.

For the EI-CT simulation, it is assumed that the imaging system is rotated and the object is kept stationary. The acquisition of multiple projections is easily simulated by running the existing code a number of times (equal to the number of angles) in a loop. At the same time, the object transmission function (equation 4.31) has to be updated at every angle, which requires a 3D numerical phantom.

Similarly to other phantoms used in planar EI, the numerical phantom for EI-CT consists of three wires of different materials and diameters, which are inclined with respect to the vertical direction and arranged in 3D space. In order to ensure that the numerical phantom can easily be replaced by a corresponding real one in experimental validations, a cylinder was included in the model which surrounds and supports the wires. A cross-section of the numerical phantom is shown in figure 4.6. Due to their inclination, the wires' cross-sections are elliptical. Wires and surrounding cylinder, described by Cyl_1 and Cyl_2, are assumed to be homogeneous, and associated with a specific value for δ and β describing the optical properties of the respective materials. Each ellipse is described by its central point (ξ_0, z_0), its rotation with respect to the z-axis given by the angle γ, and its half axes A and B. The surrounding cylinder is described by outer and inner radii R_1 and R_2.

In order to simulate the rotation of the imaging system, an angular dependence has to be assigned to Φ and μ in the object transmission function. As discussed previously, Φ and μ describe Radon transforms of δ and β when angular projections are acquired. The object transmission function for the CT simulation is therefore given by:

$$T(\xi) = \exp(-i \cdot (k\mathcal{R}[\delta(\xi, z)(x, \theta)] + 2ik\mathcal{R}[\beta(\xi, z)(x, \theta)])). \tag{4.32}$$

The Radon transforms for the described phantom can be easily computed by considering the linearity of the operation:

$$\begin{aligned}\mathcal{R}_O[\delta(\xi, z)](x, \theta) =& \mathcal{R}_{Cyl_1}[\delta_{Cyl_1}](x, \theta) - \mathcal{R}_{Cyl_2}[\delta_{Cyl_2}](x, \theta) \\ &+ \mathcal{R}_{E_1}[\delta_{E_1}](x, \theta) + \mathcal{R}_{E_2}[\delta_{E_2}](x, \theta) + \mathcal{R}_{E_3}[\delta_{E_3}](x, \theta)\end{aligned} \tag{4.33}$$

$$\begin{aligned}\mathcal{R}_O[\beta(\xi, z)](x, \theta) =& \mathcal{R}_{C_1}[\beta_{C_1}](x, \theta) - \mathcal{R}_{C_2}[\beta_{C_2}](x, \theta) \\ &+ \mathcal{R}_{E_1}[\beta_{E_1}](x, \theta) + \mathcal{R}_{E_2}[\beta_{E_2}](x, \theta) + \mathcal{R}_{E_3}[\beta_{E_3}](x, \theta).\end{aligned} \tag{4.34}$$

This concept is schematically shown in figure 4.7. This enables us to write the Radon transform for one of the phantom's components (e.g. for the ellipse E_1 in figure 4.6), which can then be used to compute the Radon transforms for all

remaining components (including the cylinder, the circular cross-section of which can be considered as a special case of an ellipse).

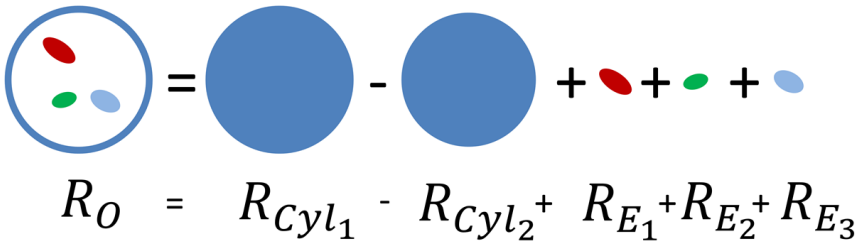

Figure 4.7: The concept of linearity applied to the simulation of our CT phantom. The Radon transform for the entire object is equal to the linear combination of the Radon transforms of the object's components.

The Radon transform of the RID and absorption term of the ellipse E_1 are given by:

$$\mathcal{R}_{E_1}[\delta_{E_1}](x,\theta) = \delta_{E_1} \cdot P_{E_1}(x,\theta) \tag{4.35}$$

$$\mathcal{R}_{E_1}[\beta_{E_1}](x,\theta) = \beta_{E_1} \cdot P_{E_1}(x,\theta), \tag{4.36}$$

where $P(x,\theta)$ denotes the parallel projection of the ellipse along the propagation direction of the x-rays for angle θ, given by:

$$P(x,\theta) = \begin{cases} 2AB\sqrt{a-(x-s\cos(\nu-\theta))^2}/a, & \text{if } x < \sqrt{a}. \\ 0, & \text{otherwise,} \end{cases} \tag{4.37}$$

with:

$$a = A^2\cos^2(\theta-\gamma) + B^2\sin^2(\theta-\gamma) \tag{4.38}$$

$$s = \sqrt{\xi_0^2 + z_0^2} \tag{4.39}$$

$$\nu = \tan^{-1}(\xi_0/z_0) \tag{4.40}$$

(Kak and Slaney [1987]). Please note that equations 4.35 and 4.36 refer to a single transverse cross-section.

The substitution of equations 4.35 and 4.36 into the object transmission function (equation 4.32) completes the extension of the planar model to a tomographic geometry. In the practical implementation of the simulation, the rotation angle and the parameters describing the object (optical constants, dimensions and locations of the ellipses, and radii of the hollow cylinder) are added to the set of input parameters, facilitating easy and flexible operations.

An example of a simulated EI-CT image of the described numerical phantom is given in chapter 6.3.

4.6 Description of two Experimental Edge Illumination CT Setups

In the following, the two experimental EI-CT setups that were used for the acquisition of the data presented in chapters 5 and 6 will be described. The first one is an implementation of scanning EI-CT at a synchrotron, and the second one is an implementation of coded aperture EI-CT in combination with a conventional laboratory source.

Scanning EI-CT

The experimental scanning EI-CT setup described below was operated in VS mode and is schematically shown in figure 4.8 (a). It was installed at the SYRMEP beamline of the Elettra synchrotron in Trieste, Italy. The beamline characteristics (source type and dimensions, monochromator, etc.) were provided in chapter 3.2. The laminar beam was obtained by collimating the primary beam (which has full dimensions of 120 (H) x 4 (V) mm^2) using a Huber slit (Huber GmbH, Rimsting, Germany), placed at approximately 22 m from the source. The horizontal dimension of the Huber slit was 2 cm and its flexible opening was set to 20 μm in the vertical direction. The size of the laminar beam was therefore of 20 (H) x 0.020 (V) mm^2.

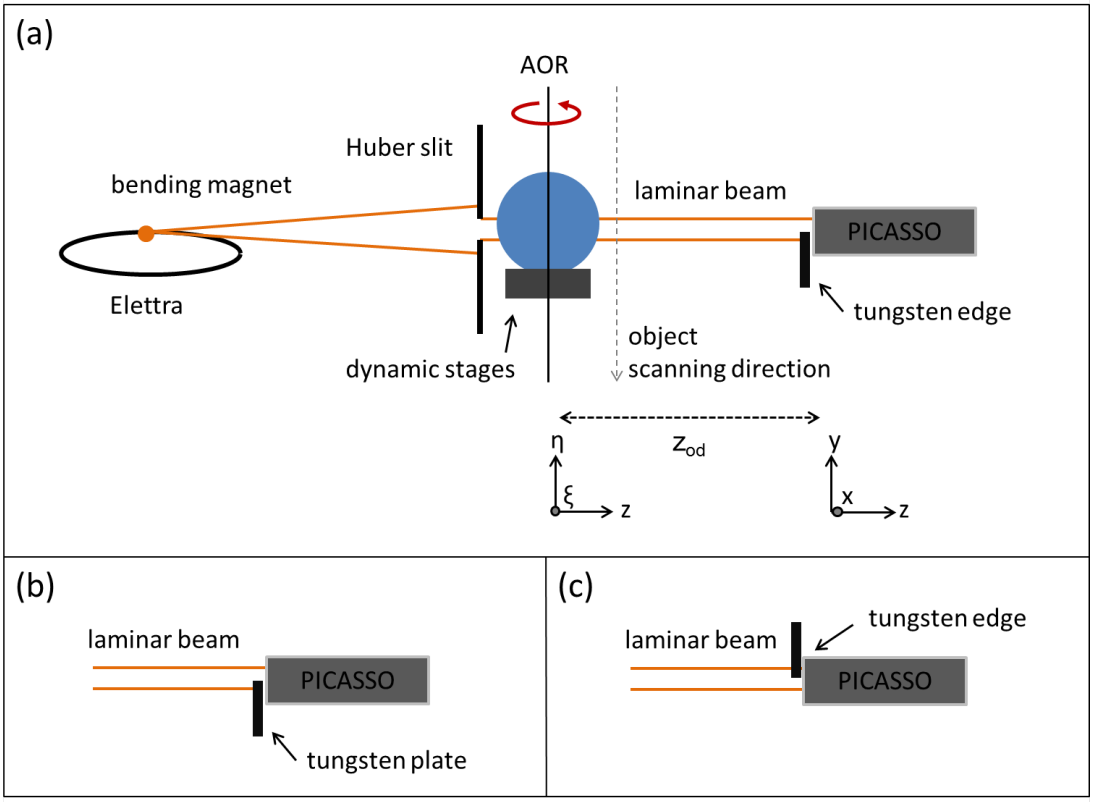

Figure 4.8: Schematic of the scanning EI-CT setup installed at the SYRMEP beamline of the Elettra synchrotron (a). Two possible positions for the tungsten edge are shown in (b) and (c).

A detector based on silicon microstrip technology and fast single photon-counting read-out electronics, developed within the PICASSO (Phase Imaging for Clinical Application with Silicon detector and Synchrotron radiation) project (Rigon et al. [2008b]), was positioned approximately 90 cm downstream of the Huber slit. The detector active surface is 210 mm wide, and the pixel size is 50 (H) x 300 (V) μm^2. The practically linear detector active surface was positioned as to match the orientation of the laminar beam. The used row of pixels was located at the centre of the detector. In order to obtain a sharp sensitivity edge on the pixel row, a tungsten edge was placed in front of the detector and aligned with its centre, leaving 150 um of the pixel row's active surface uncovered. The

tungsten edge was thick enough to absorb all x-rays at the energies used in the experiments. Again, the desired edge illumination condition is achieved when the laminar beam is positioned such that half its intensity hits the tungsten edge, and the other half hits the active area of the pixels. The inversion of the phase contrast signal can be achieved by changing the vertical position of the tungsten edge from one that covers the lower half of the pixels' active area to one that covers the upper half (see figure 4.8 (b,c)).

For the given detector/tungsten edge combination, the illumination curves C_1 and C_2, which are required for performing phase retrieval, are acquired by scanning the edge vertically across the detector active surface, with no object placed in the beam.

The object movimentation stage was located 0.7 m upstream of the detector/tungsten edge combination. This stage consisted of several motors. A rotation stage (PI GmbH, Karlsruhe, Germany) enabled rotation around the vertical axis. Two goniometers (Kohzu Precision Co., Ltd., Kawasaki Kanagawa, Japan) placed below the rotation stage enabled the vertical alignment of the AOR, which has to be obtained before every experiment. A translation stage (Newport Corporation, Irvine, California, USA) placed at the bottom of the stack enabled the vertical object displacement, which is required to build up a 2D image.

Coded Aperture EI-CT

In the following, we describe a prototype EI-CT scanner based on coded apertures, which is in operation in the UCL radiation physics laboratories. The scanner operates in HS mode, which implies that the coded apertures are oriented parallel to the AOR. A graphical rendering of the scanner can be seen in Figure 4.9.

The scanner comprises the following components. A Rigaku M007 x-ray source (Rigaku Corporation, Tokyo, Japan) with a rotating molybdenum target is used. The source focal spot has been measured to be $\sim$ 70 um in the horizontal direction (the direction of phase sensitivity). The source is typically operated at 35 kV and 25 mA, resulting in a polychromatic source spectrum centred on a mean energy of 18 keV. Depending on the experiment, a 30 μm thick molybdenum filter can be placed in front of the source to attenuate the low energy components of the spectrum.

The detector used is the Anrad "SMAM" amorphous selenium direct conversion flat panel (Analogic Canada Corporation, Saint-Laurent, Quebec, Canada) with a pixel size of 85 x 85 μm^2. The detector is located at a distance of 2 m from the source, making the system relatively compact.

The coded aperture masks have been manufactured by Creatv Microtech Inc. (Potomac, MD), by electroplating a gold layer on a graphite substrate. The thickness of the gold was designed to be 30 μm, but during the manufacturing process the masks have been slightly underplated, resulting in an estimated gold thickness of approximately 25 μm. This thickness is insufficient to guarantee a total absorption of the incoming x-ray spectrum, and the partial transmission results in a slight decrease of the phase contrast signal at the energies used for imaging. The masks in the current prototype cover a field of view of 5 x 5 cm^2. The detector mask is placed about 3.5 cm upstream of the detector. The sample mask is located at an approximate distance of 1.6 m from the source, immediately followed by the sample stage, resulting in an object-to-detector distance of approximately $\sim$ 40 cm. Both masks and the sample stage are mounted on a stack of translation and rotation stages (Newport Corporation, Irvine, CA) and goniometers (Kohzu Precision Co., Ltd., Kawasaki Kanagawa, Japan), allowing for fine alignment of six degrees of freedom. Before every experiment, the two coded aperture masks are aligned with the detector and with respect to each other using the procedure described in (Millard et al. [2013]). Moreover, the AOR is aligned with the vertical axis of the system, i.e. with the detector pixel columns. The pitch of the detector mask is 83.5 μm with a 24% open fraction (20 μm), and the sample mask pitch is 66.8 μm with an 18% open fraction (12 μm). The dimensions of the sample mask have been scaled down to account for the system magnification which is present due to the beam divergence.

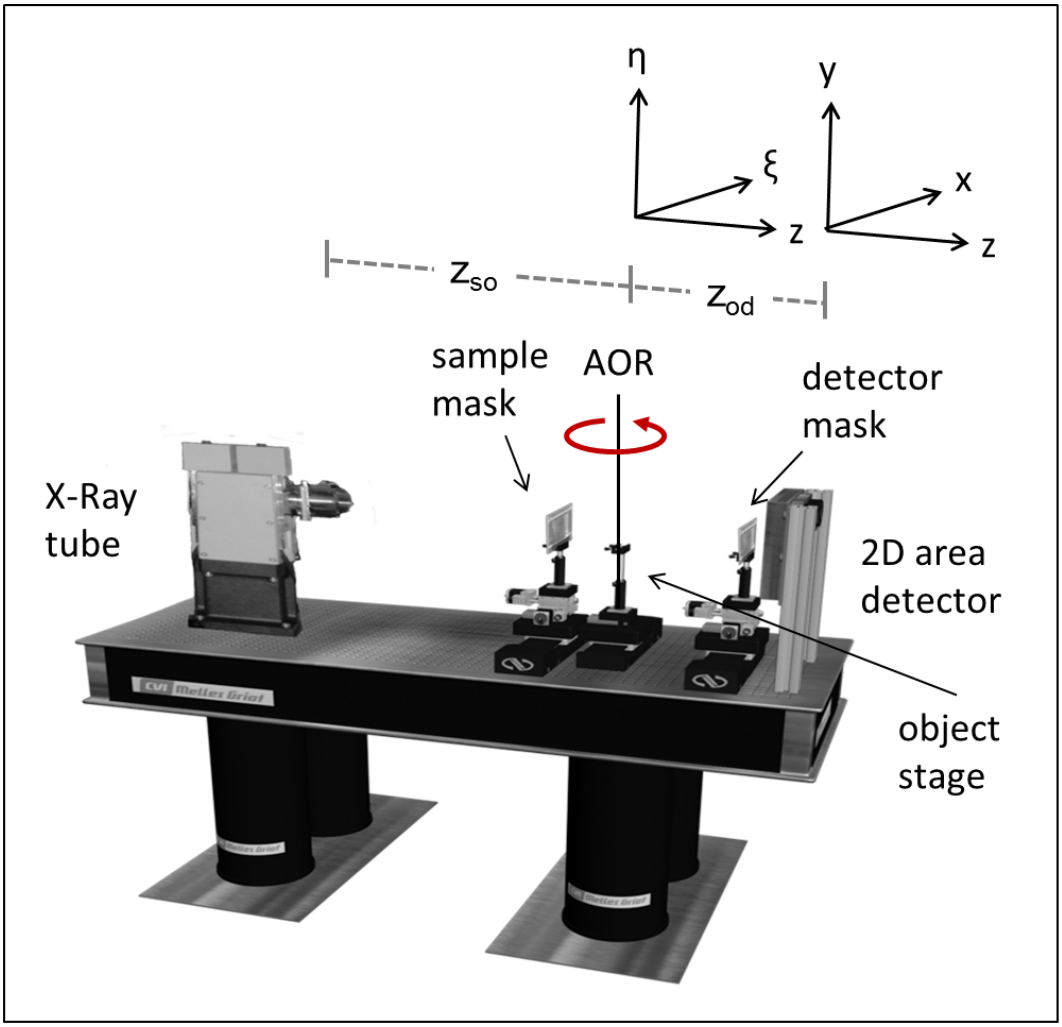

Figure 4.9: Pictorial representation of the phase contrast CT scanner prototype based on the coded aperture EI method that is installed at UCL.

The IC is acquired by scanning, without the object in place, the sample mask with respect to the stationary detector/detector mask combination in the horizontal direction. For the described scanner, the FWHM of the IC corresponds to approximately a 16 μm shift of the sample mask.

4.7 Chapter Summary and Conclusion

The theory required for a CT extension of the EI method was discussed. Some important aspects were related to the derivation of phase retrieval procedures, which establish line integral relationships between the projections and optical constants, were highlighted, and the mechanism on the basis of which the unidirectional phase sensitivity of the method leads to two different EI-CT setups was described. Moreover, the variety of physical quantities that can be reconstructed from EI-CT measurements were listed, together with the corresponding reconstruction procedures. Advantages and disadvantages associated with the reconstruction of the different maps were discussed. Furthermore, it was explained how EI-CT measurements can be simulated for a custom wire phantom. Finally, two experimental EI-CT scanners were described, one installed at a synchrotron and one at the UCL laboratories. These scanners were used to obtain the results presented in the following chapters (e.g. for the investigation of quantitative EI-CT discussed in the next chapter).

Chapter 5

Investigation of the Method's Potential for Quantitative Imaging

5.1 Chapter Introduction and Outline

After presenting the practical and theoretical bases of EI-CT, this chapter is concerned with the possibility to use the method for quantitative imaging. In planar, quantitative imaging is possible only to a limited extent, because object geometry and quantitative information (such as optical constants) are "entangled" in the projections. Therefore, quantitative information can only be extracted if the object geometry is relatively simple and fully known, which is normally not the case. In CT, on the other hand, geometric and quantitative information are separated during the reconstruction process, therefore enabling the extraction of quantitative information for general objects.

The following questions will be tackled:

- Can we reconstruct RID and absorption term maps which are quantitatively accurate, i.e. which can be used for material identification?
- Can some degree of quantitative information also be extracted from non-phase retrieved, mixed maps, showing combined phase and absorption in-

formation?

A combination of simulation, theory and experiment will be employed. Results for a simple custom-built phantom containing "geometric" details of known RID and absorption term, and for a biological object (a domestic wasp) will be shown.

5.2 Reconstruction of Refractive Index Decrement and Absorption Term Maps

The possibility to reconstruct CT images in which the grey values are related to the imaged materials is highly valuable. The best example can be found in clinical (absorption-based) CT, where reconstructed images are effectively maps of the Hounsfield units of the patient's body. The Hounsfield units are related to tissue types which, provided the contrast in the image is sufficient, enables clinicians to differentiate them and to detect abnormalities. As mentioned before, the corresponding quantity in PC-CT is the RID (Donath et al. [2010]). As chapters 4.2 and 4.4 have demonstrated, the theory for the reconstruction of maps of the RID *and* the absorption term from EI-CT datasets exists, implying the potential for "multi-modal" quantitative imaging.

The review of the existing PC-CT methods in chapter 2 has shown that quantitatively accurate RID and absorption term maps could be reconstructed from ABI-CT and GI-CT data. This chapter will investigate whether this is possible also from EI-CT data.

As discussed previously, the pre-requirement for the reconstruction of RID and absorption term maps is the performance of phase retrieval. The phase retrieval algorithms presented in chapter 4.2 are based on simplifying assumptions made on the underpinning physical mechanisms. In particular, when modelling the phase signal to be proportional to the beam displacement due to refraction, it is assumed that the refraction is constant over the height of the laminar beam and over the apertures respectively. Furthermore, the definitions of the phase function and the projected absorption term are based on the assumption that photons pass through the object along straight lines, and that no refraction occurs inside it. This is only valid for thin objects with slowly varying phase. Also, coherence effects are not

taken into account. As a consequence of the simplifying model, the phase retrieval algorithms currently available, and the consequential possibility to reconstruct RID and absorption term maps, do not necessarily imply quantitative accuracy. In fact, whether quantitative imaging is possible with EI-CT depends on how closely the used setup (in particular with respect to the beam characteristics) and the object meet the assumptions that underpin the developed models.

In order to evaluate whether an EI-CT setup and the imaged object meet the assumptions, two steps are necessary. First, simulations of the used setup need to be performed for numerical phantoms, and the resulting simulated data can be used to recover the RIDs and the absorption terms. These can then be compared to those that had been given as input to the simulation. If they match, setup and object parameters are in accordance with the assumptions underpinning the phase retrieval algorithms. Otherwise, system and object parameters violate some of the model's assumptions, which implies that the phase retrieval algorithm cannot provide quantitatively accurate results. In this case, it is important to evaluate to what extent the retrieved optical constants are affected by this violation to establish whether they could still be useful in practice.

The EI-CT simulation described in chapter 4.5 can be used for this purpose. However, since the geometry of a numerical phantom is fully known, it is actually sufficient to rely on a planar simulation, which is advantageous in terms of computation time. As stated in the introduction of this chapter, the phase function and the projected absorption term retrieved at a single angle contain the entire quantitative information of the object, albeit "entangled" with the object geometry. Knowledge of the latter enables separation of the two via division by the object thickness, thus yielding the RID and the absorption term.

The second step towards the demonstration of quantitative imaging is to perform an experimental EI-CT scan of phantoms consisting of known materials, and to compare the retrieved RIDs and absorption terms to nominal ones. In addition to a possible violation of the assumptions underlying the phase retrieval method, however, experimental data are prone to additional error sources such as noise and reconstruction artefacts. These problems may affect the accuracy of the reconstructed maps, but they can also be overcome or at least mitigated by optimisation of the acquisition parameters (longer exposure time, improvement of

acquisition schemes, etc). For this experimental part, the two setups described in chapter 4.6 were used, which are implementations of scanning and coded aperture EI-CT.

The monochromatic or polychromatic nature of the x-ray beam used is key to the concept of quantitative imaging. The use of a single energy beam implies that the recovered optical constants can be directly compared to nominal values at that energy. Conversely, if a polychromatic source is used, an adaptation of the concept of effective energy to phase imaging is required.

5.2.1 Monochromatic Synchrotron Source

For the above reason, the investigation was started from the simpler case of a monochromatic x-ray beam. The potential for quantitative imaging was investigated for the scanning EI-CT method, using the experimental setup described in chapter 4.6.

Materials and Methods

The EI-CT system was set up at the Elettra synchrotron (Trieste, Italy). The beam was monochromatised by a double Si (1,1,1) crystal in Bragg configuration. In order to be as general as possible, we investigated quantitative imaging at two energies: 20 and 25 keV.

Prior to the experimental session, we simulated planar acquisitions performed with the setup using the software developed by Vittoria et al. [2013]. The input parameters were selected to match exactly the experimental ones, and data was simulated at 20 and 25 keV. The vertical scanning step was 0.5 μm. This very fine step size was chosen to exclude any possible errors due to under-sampling.

As numerical phantoms, six vertically oriented wires were used. The wires were of different materials and diameters, as listed in table 5.1. The nominal RIDs and absorption terms, provided on the left hand side of table 5.2, were calculated according to Henke et al. [1993] using the chemical formulas and densities listed in table 5.1. In order to study the quantitativeness of the phase retrieval method in a wide range of conditions, the materials were chosen to vary from low absorbing (nylon) to high absorbing (titanium). The EI datasets for each

Material	Nominal Diameter	Formula	Density
PBT	180 μm	$C_{12}H_{12}O_4$	1.31 g/cm3
nylon 6.6	150 μm	$C_6H_{11}ON$	1.14 g/cm3
PEEK	450 μm	$C_{19}H_{14}O_3$	1.32 g/cm3
sapphire	250 μm	Al_2O_3	3.99 g/cm3
aluminium	250 μm	Al	2.70 g/cm3
titanium	250 μm	Ti	4.50 g/cm3

Table 5.1: Specification of the wires used as numerical phantoms for the planar simulations and in the custom-built 3D phantom used for the CT experiment.

wire were simulated separately, and each dataset contained two images obtained in complementary illumination conditions (corresponding to the absorbing edge covering either side of the pixel row) to enable application of the phase retrieval algorithm. The illumination curves for the two opposite edge illumination conditions were also simulated. Phase retrieval was then performed on each simulated wire. The RIDs were recovered by first integrating the derivative of the phase function, then by dividing its maximum by the wire diameter. Accordingly, the absorption term was recovered by dividing the maximum of its projection by the wire diameter d:

$$\delta = \max(\Delta\eta \cdot \sum_{i_0}^{i} \frac{\partial}{\partial\eta}\phi)/d \tag{5.1}$$

$$\beta_{rec} = \max(\mu_{rec})/d. \tag{5.2}$$

The index i denotes the discrete pixel coordinate, and $\Delta\eta$ the vertical scanning step. The recovered values were compared to the ones that had been given as input to the simulation (the nominal values).

Following the simulations, an EI-CT scan was performed experimentally. A

3D phantom was built by gluing six wires of the materials listed in table 5.1 to a support. All wires were tilted with respect to the vertical direction to ensure that a degree of phase signal was created in the direction of phase sensitivity. A schematic of the phantom, a transverse cross-section and a photograph are shown in figure 5.1. All materials were sourced from Goodfellow Ltd. (Huntingdon, UK). The chemical formulas and densities reported in table 5.1 match the specifications given by the supplier.

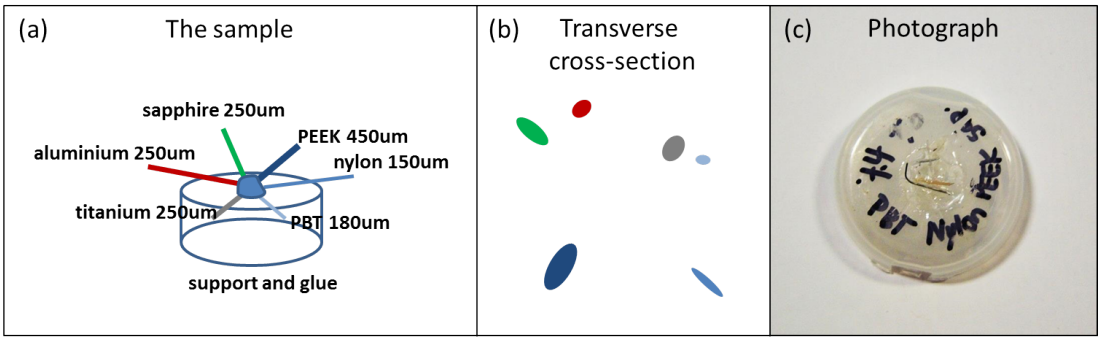

Figure 5.1: The 3D wire phantom used for the experiment: a schematic (a), a transverse cross-section (b) and a photograph (view from top) (c).

Before the experiment at each energy, the two illumination curves C_1 and C_2 were acquired. Subsequently, the absorbing (tungsten) edge was positioned such that the upper half of the laminar beam (i.e. 10 of the total 20 μm) fell onto the active area of the detector (corresponding to the slope of C_1). After one CT scan was performed, the illumination condition was reversed by placing the tungsten edge such that the lower beam half fell onto the active area (corresponding to the slope of C_2), and a second CT scan was performed.

The acquisition protocol for each CT scan was the following. The phantom was rotated with an angular step of 0.5 degrees over a total range of 180 degrees, resulting in 360 projections corresponding to transverse cross-sections of 20 μm thickness (equal to the width of the laminar beam). Since the final goal was to integrate the retrieved differential phase function along the vertical direction in order to recover the RID, it was necessary to acquire data corresponding to a number of transverse-cross sections. The used system was an implementation of the scanning EI-CT method; therefore, vertical sample scanning was needed. For

the acquisition of data corresponding to subsequent transverse cross-sections, the sample stage was displaced vertically by 5 μm after each 180 degree rotation. We deliberately used a step size resulting in a slight oversampling, in order to make sure not to miss any data required for the following phase integration procedure. For technical reasons related to the way in which sample rotation is implemented at the SYRMEP beamline, the phantom was rotated by an additional 11.06 degrees during the vertical displacement. Afterwards, the 180 degree scan was repeated, however, with a start angle offset by 191.06 (180+11.06) degrees with respect to the previous one. This acquisition protocol, which is schematically shown in figure 5.2, was repeated 200 times until 1 mm of the phantom had been scanned vertically. The exposure time for each projection was 0.1 s.

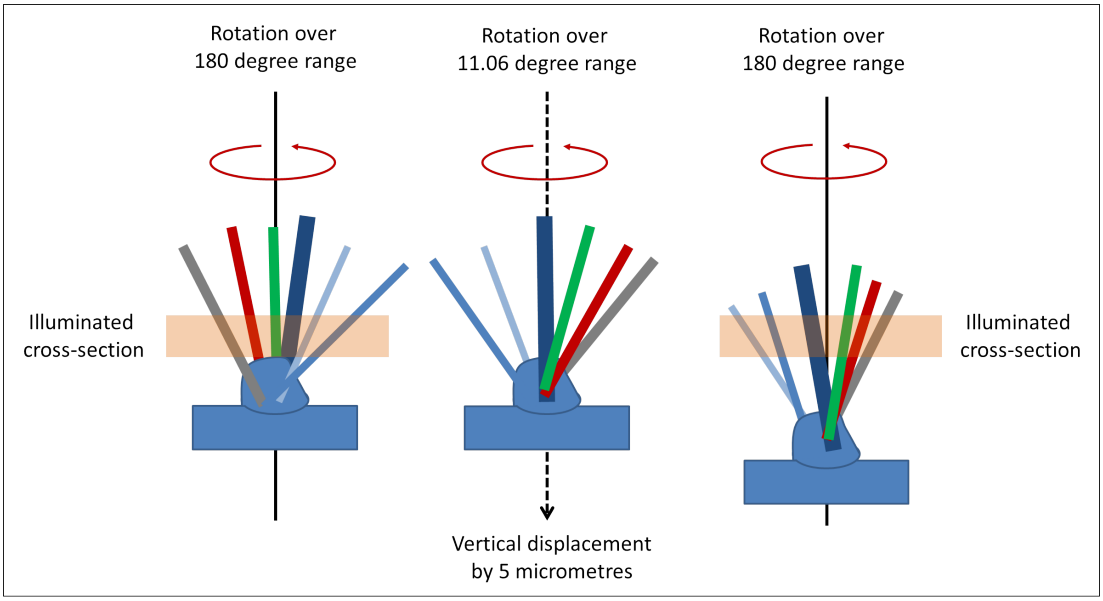

Figure 5.2: Scan protocol used for the EI-CT experiment described in this section. Each 180 degree rotation of the object was followed by a vertical displacement during which the object was rotated by an additional 11.06 degrees.

Each projection was corrected for gain and offset variations of the detector. As a consequence of the rotation during the vertical scan, the sinograms had to be aligned with each other such that they all had the same start angle. Unfortunately, because the angular offset between the slices (191.06 degrees) was not

exactly a multiple of the angular step (0.5 degrees), perfect alignment was not possible, a fact that may be responsible for artefacts in the reconstructed images mentioned in the Results and Discussion section. Next, phase retrieval was performed for each transverse slice, combining the two sinograms acquired at the different positions of the absorbing edge in front of the detector. The incorrect alignment of the transverse slices may also have posed a problem during the phase retrieval, as each pair of symmetrically illuminated sinograms did not have the exact same start angle, hence did not match exactly. As a result of the phase retrieval, sinograms showing the vertical derivative of the phase function and the projected absorption term were obtained. The reconstruction of RID map was then performed in two steps. First, the vertical derivative of the RID was reconstructed for each slice using the FBP with the ramp filter. The resulting images were stacked to form a 3D dataset, which was then integrated along the vertical direction:

$$\delta(i,j,k) = \Delta\eta \cdot \sum_{k'=k_0}^{k} \frac{\partial}{\partial\eta}\delta(i,j,k') \tag{5.3}$$

The indices (i,k,j) discretise the coordinates (ξ,z,η), and $\Delta\eta$ again denotes the step size of the vertical scan. The absorption term map was reconstructed by applying the FBP with the ramp filter to the sinograms showing its projections. Due to the high noise level in these sinograms, the ramp filter had been set to zero at a relatively low frequency, which resulted in a slight blurring of the reconstructed images.

The artefacts in the RID map that arose during the integration step that are due to the inaccurate alignment of the transverse cross-sections made some post-processing necessary: the wires were segmented and the background was subtracted. The same processing was applied to the absorption term map for consistency.

For the quantitative analysis, a region-of-interest (ROI) was selected within each wire and the corresponding RID and absorption term values were averaged inside it. This was repeated for 100 slices of the reconstructed datasets, corre-

sponding to 0.5 mm of the vertical dimension of the phantom, and the extracted optical constants were averaged over these slices. The recovered RIDs and absorption terms were then compared to the nominal values for each wire.

Finally, the process was repeated on a biological object (a domestic wasp), which was imaged under the same experimental conditions (E = 20 keV only), but with a larger (13 μm) step size for the vertical scanning, in order to be able to cover the entirety of the insect ($\approx$ 4 mm) within an acceptable acquisition time. Maps of the RID and the absorption term within the wasp were reconstructed in the same manner as for the wire phantom. Coronal slices were extracted from the resulting 3D datasets, and RID and absorption term profiles for a selected region within the wasp (the torso) were plotted. The contrast-to-noise ratio (CNR), defined as:

$$CNR = \frac{I_{feature} - I_{background}}{\sigma_{background}} \tag{5.4}$$

was calculated for both profiles. The symbol I stands for the grey value within the area indicated by the subscript, and σ denotes its standard deviation.

Results and Discussion

The results from the planar simulation at 20 keV and 25 keV are listed in table 5.2. The recovered absorption term values vary insignificantly from the nominal ones, and, in fact, we believe the discrepancies to be solely due to numerical errors. The recovered RID values show an acceptable agreement with the nominal ones; however, in particular for the low absorbing PBT, nylon and PEEK wires, they tend to be slightly larger than expected. On the contrary, the RID of sapphire is somewhat underestimated at both energies. The values for aluminium and titanium at 20 keV are close to the nominal ones; however, the values at 25 keV are slightly overestimated. This behaviour could indicate that the parameters of the EI system may slightly violate the assumptions made in the phase retrieval model. In order to gain a better understanding of the origin of these discrepancies, we plotted the extracted first derivative of the phase function for

the wires in figure 5.3 (a). The profiles show the typical shape for a differential phase profile of a cylindrical object: positive and negative fringes at the edges, and a smooth slope between them that passes through zero at the centre. However, a zoom around the edges (shown only for the positive peak, see figure 5.3 (b)) reveals a slightly "rippled" structure. These ripples may be attributed to coherence effects: when the edge is illuminated by the laminar beam, diffraction occurs, which is observable thanks to the high degree of spatial coherence (small synchrotron source at a large distance from the sample) (Munro et al. [2010b]). Depending on their oscillation direction, the ripples contribute in a negative or positive way during the integration step in the data processing (see equation 5.1), which may explain the slight (positive or negative) mismatch between the retrieved and nominal RID values. Moreover, at the edges, the phase of the wires is discontinuous, therefore, is not "slowly varying", as was assumed in the model underlying the phase retrieval.

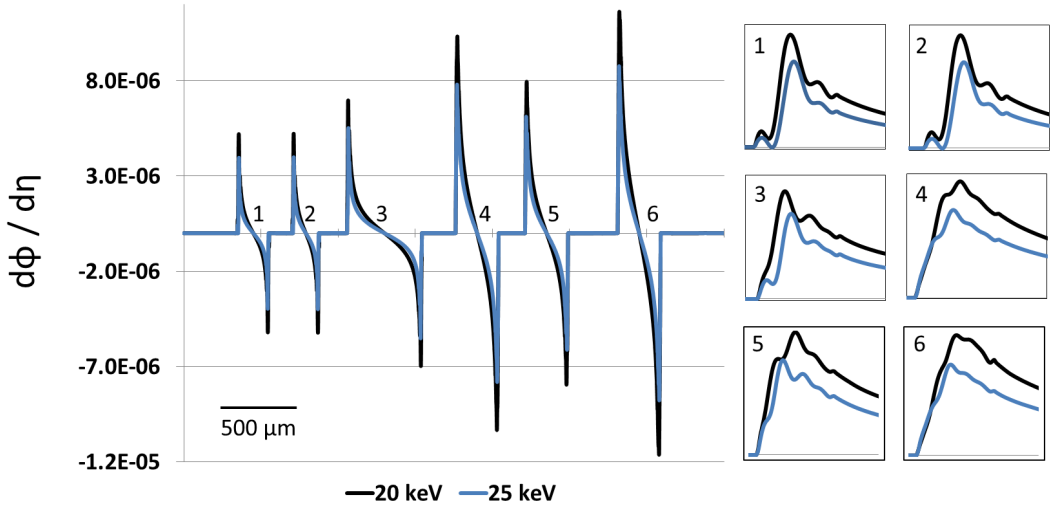

Figure 5.3: Extracted first derivative of the phase function from simulated EI data for the following wires: 1. PBT (180 μm), 2. nylon 6.6 (150 μm), 3. PEEK (450 μm), 4. sapphire (250 μm), 5. aluminium (250 μm), 6. titanium (250 μm). The zooms on the right clearly reveal a "rippled" structure of the positive peaks.

The results from the CT experiment are shown in figure 5.4 and plots 5.5 and 5.6. Figure 5.4 shows the reconstructed RID (a) and absorption map (b) for a

Material	$\boldsymbol{\delta_{nom}}$ **(20 keV / 25 keV)**	$\boldsymbol{\delta_{rec}}$ **(20 keV / 25 keV)**
PBT	6.50×10^{-7} / 4.15×10^{-7}	6.75×10^{-7} / 4.51×10^{-7}
nylon 6.6	7.20×10^{-7} / 4.59×10^{-7}	7.46×10^{-7} / 4.79×10^{-7}
PEEK	7.1×10^{-7} / 4.6×10^{-7}	7.24×10^{-7} / 4.94×10^{-7}
sapphire	2.00×10^{-6} / 1.30×10^{-6}	1.80×10^{-6} / 1.27×10^{-6}
aluminium	1.36×10^{-6} / 8.60×10^{-7}	1.32×10^{-6} / 8.86×10^{-7}
titanium	2.17×10^{-6} / 1.39×10^{-6}	2.18×10^{-6} / 1.51×10^{-6}

Material	$\boldsymbol{\beta_{nom}}$ **(20 keV / 25 keV)**	$\boldsymbol{\beta_{rec}}$ **(20 keV / 25 keV)**
PBT	2.50×10^{-10} / 1.37×10^{-10}	2.49×10^{-10} / 1.37×10^{-10}
nylon 6.6	3.10×10^{-10} / 1.64×10^{-10}	3.09×10^{-10} / 1.63×10^{-10}
PEEK	2.8×10^{-10} / 1.58×10^{-10}	2.8×10^{-10} / 1.59×10^{-10}
sapphire	4.00×10^{-9} / 1.80×10^{-9}	3.99×10^{-10} / 1.8×10^{-10}
aluminium	4.20×10^{-9} / 1.75×10^{-9}	4.19×10^{-10} / 1.75×10^{-10}
titanium	3.40×10^{-8} / 1.43×10^{-8}	3.39×10^{-10} / 1.43×10^{-10}

Table 5.2: Nominal optical constants and those recovered from the planar EI simulation at 20 and 25 keV.

transverse slice of the 3D wire phantom, acquired at 20 keV. The maps acquired at 25 keV are not shown, as visually they are identical. Due to the fact that the phantom contained high refracting and absorbing materials (in particular, titanium), the wires with lower refraction and absorption (PBT, nylon and PEEK) are not very well visible in both maps due to the windowing. In order to visualise them within their specific grey value range, they are shown in separate zoomed ROIs on the right hand side. In the ROIs, the wires appear slightly blurred, which is primarily due to the following reasons. First, the horizontal pixel size of the PICASSO detector (50 μm) was only a third of the smallest wire (150 μm).

Second, the noise level present in the absorption projections forced us to select a low cut-off frequency for the ramp filter during the backprojection. Moreover, the reconstruction of the RID images involved integration, an operation that also has a smoothing effect. In the absorption map, some of the wires, in particular PBT and PEEK, are (partially) contoured by a bright line. This is due to phase effects occurring in the horizontal direction. The used EI system is only sensitive to vertical effects; however, due to the spatial coherence of the beam, the phase shift in the beam gives rise to intensity fringes in the horizontal direction as a consequence of free space propagation. Finally, some artefacts are visible in the RID map: the grey level inside the wires is not uniform (particularly for the titanium, aluminium and PEEK wires), where some areas on their edges appear to be brighter than at their centre. This is due to the integration artefacts that have been mentioned in the Materials and Methods section. Besides the common problem that the smallest local errors in the experimental data get smeared along the integration path, we faced the additional problem that the transverse slices in the integration volume could not be perfectly aligned. Therefore, the vertical integration of the volume (described by equation 5.3) did not yield a region of zero RID outside the wires, but instead caused strong stripy offsets. As the wires were segmented, these are not visible in the background of the RID map. However, because of the wires' inclination, some stripe artefacts that originated from a position in the 3D integration volume lower than that of the considered transverse slice, intersected the wires in that slice.

Not only did the resulting grey value non-uniformity affect the visual appearance of the maps, but also the extracted quantitative results for the RIDs and the absorption terms of the wires. Plots 5.5 and 5.6 show the values of δ and β retrieved at 20 and 25 keV. The error bars show one standard deviation of the set of values that were averaged to obtain the results. In comparison with the nominal ones, the retrieved absorption term values are reasonably accurate for all materials and both energies. A slight under-estimation can be observed for the titanium wire, whereas the values for the low absorbing wires are slightly over-estimated. This could be due to the fact that the sinograms that were combined during phase retrieval were not correctly aligned with each other. As a result, some information that was supposed to be present in the extracted absorption

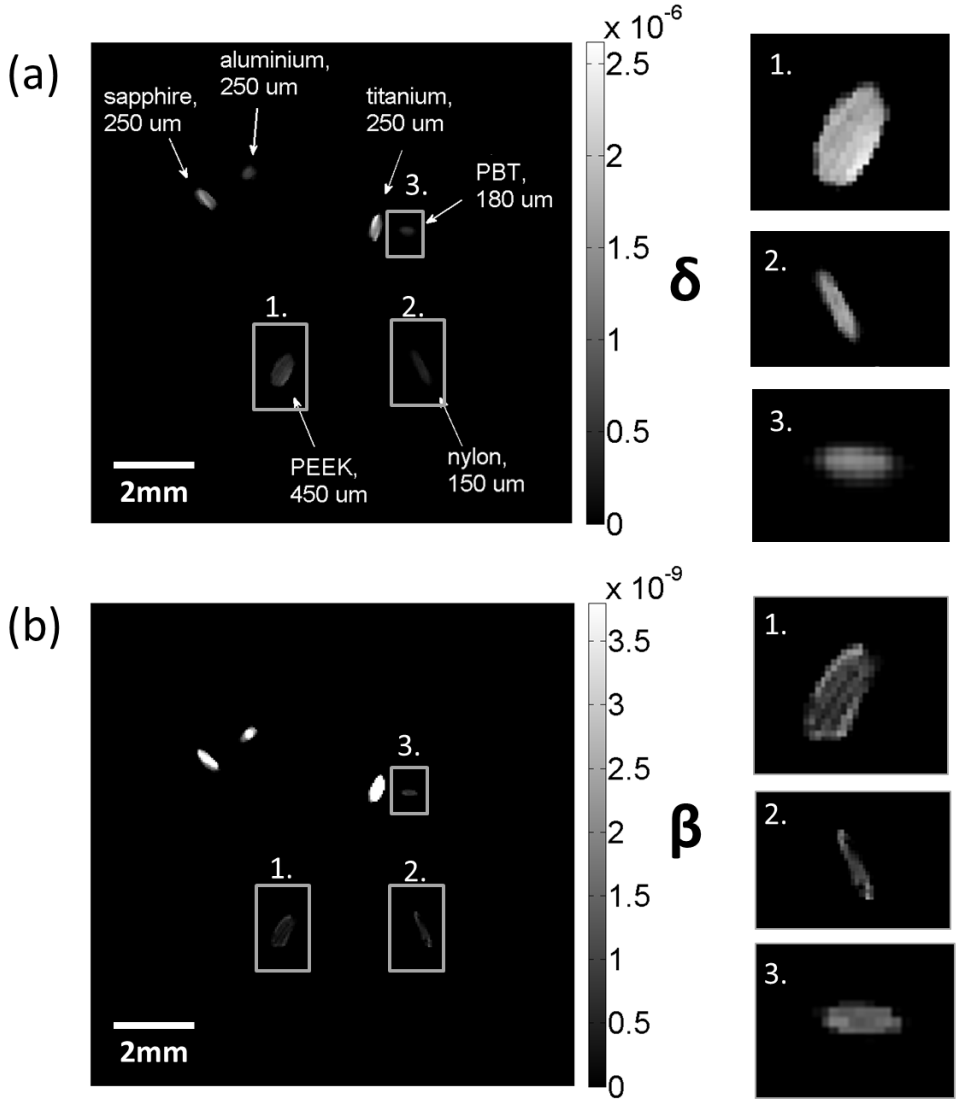

Figure 5.4: Reconstructed maps of the optical constants δ (a) and β (b) at 20 keV. The low refracting/absorbing wires (1-3) are masked by the highly refracting/absorbing wires, therefore they are shown separately in the zoomed ROIs on the left.

image may have ended up in the extracted phase image and vice versa. The different size of the error bars reflect the different diameters of the imaged wires: due to the low cut-off frequency of the ramp filter, the degree of blurring of the smaller wires is stronger, making them more uniform in grey value than larger wires.

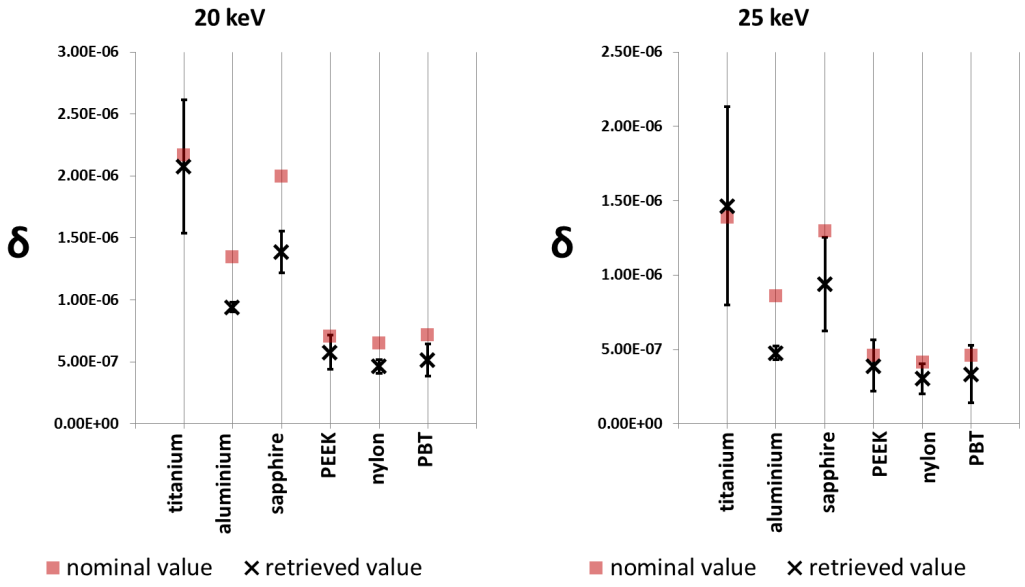

Figure 5.5: Plots showing the nominal values and the retrieved values of the refractive index decrement δ for the materials present in the phantom at 20 and 25 keV. The error bars correspond to one standard deviation.

The retrieved RID values show the correct trend for all wires and both energies. Still, a clear under-estimation of the nominal values can be seen. We believe that this is due to three facts: first, as hinted on above by the simulated results, the beam coherence is not accounted for in the phase retrieval model, which hinders the accurate recovery of the RID. Second, and possibly more importantly, the imperfect alignment between corresponding symmetrically illuminated sinograms may have resulted in an inaccurate separation of phase and absorption information during the phase retrieval. Finally, the imperfect alignment between the transverse slices led to integration artefacts in the vertical direction, that resulted in stripy offsets in the RID map which affected the grey values of the wires.

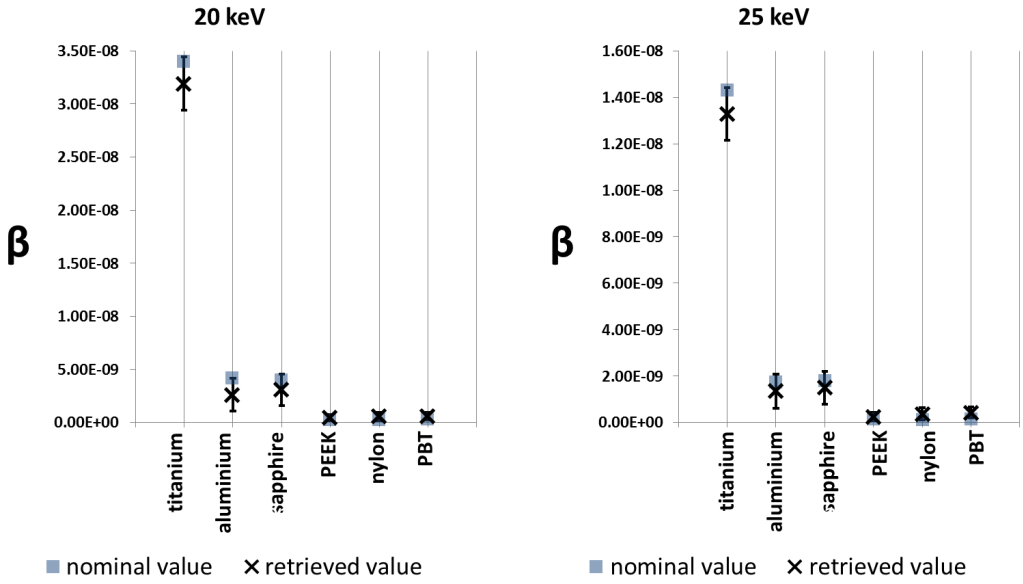

Figure 5.6: Plots showing the nominal values and the retrieved values of the absorption term β for the materials present in the phantom at 20 an 25 keV. The error bars correspond to one standard deviation.

Not only did the artefacts affect the recovered values, but they also affected the homogeneity within the set of values that were averaged to obtain the results. This had an additional effect on the larger differences in the error bars in plot 5.5, on top of the wire thickness. It is reasonable to expect that, if the experiment were repeated with a conventional acquisition scheme (180 degree rotation of the sample, then vertical displacement, then another rotation starting from the same angle, and so on), less artefacts would be present in the images and the retrieved values would be closer to the nominal ones. On the other hand, the values recovered from the present experiment can still be useful. As they follow the correct trend, relative instead of absolute values could be considered, similarly to what was reported by Zanette et al. [2011] (see chapter 2.3.2).

Figure 5.7 shows the results for the domestic wasp. The images on the left in (a) and (b) show coronal slices of RID and absorption term maps within the animal. The selected coronal slice is located roughly in the middle of the wasp, such that it shows a cross section of the head and the thorax, but not the wings

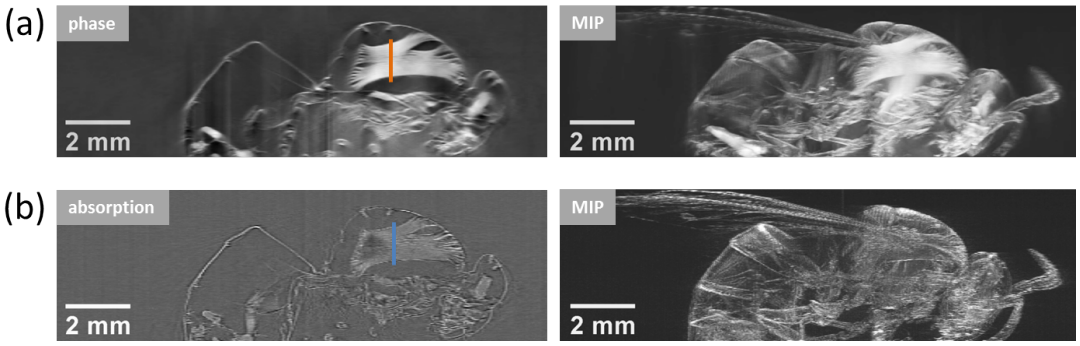

Figure 5.7: The left side of the figure shows coronal slices extracted from the reconstructed RID (a) and absorption term (b) maps for a domestic wasp. On the right, the corresponding maximum intensity projections of the volumes are shown.

and the antennas. The RID map contains some artefacts in the form of vertical stripes, due to the above mentioned problems with the phase integration. The RID map generally appears smoother than the absorption map, which is due to the integration step in the reconstruction. In the absorption map, some parts of the wasp, in particular the legs and the shell of the rump, consist of a bright line contoured by a faint dark line. We believe that these features are visible solely due to free space propagation effects, as they are very thin and their x-ray absorption is virtually negligible. Apart from the slight blurring, most features are much more visible in the RID map than in the absorption map. Particularly, the horizontal structure of the thorax can be appreciated. In order to further demonstrate and quantify the improved contrast, we plotted a profile across the thorax (indicated by the orange bar) for both maps. The profiles are shown in figure 5.8. The contrast in the phase profile (extracted from the RID map) is clearly higher than in the absorption profiles, but we would like to point out that the units in this plot are arbitrary as the images from which they were extracted were scaled to unsigned 16-bit integer format. For a quantitative evaluation, we therefore calculated the CNR for the thorax with respect to the background, as this measure is independent from scaling. When we calculated the CNR for the absorption profile, we neglected the high oscillations (fringes) at the edges of the thorax, since, as said, these were attributed to free space propagation

effects. The CNR values, reported in the plots, confirm what can be perceived visually. Actually, the CNR for the absorption profile is slightly lower than the Rose criterion (CNR = 5).

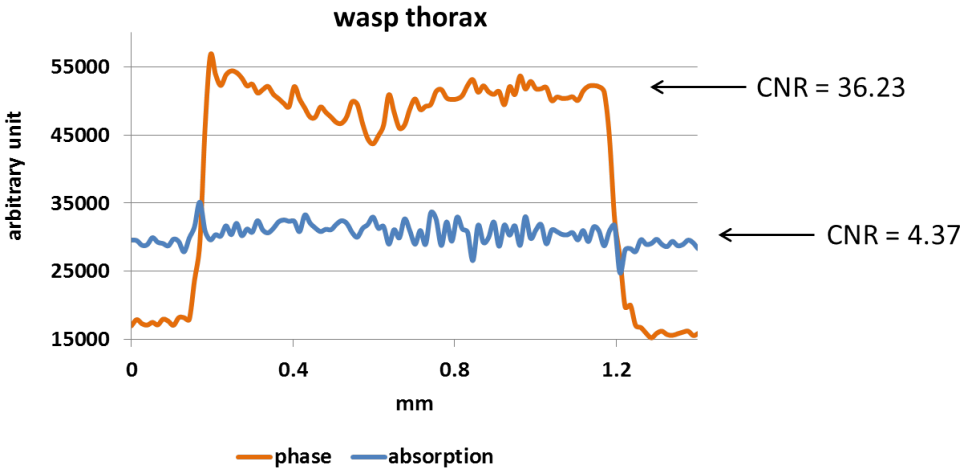

Figure 5.8: Plot showing the profiles across the indicated lines in 5.7 (thorax). The CNR for the phase profile (orange curve) is significantly higher than for the absorption profile (blue curve).

In order to appreciate the full structure of the wasp, maximum intensity projections (MIPs) of the 3D RID and absorption term maps are provided on the right hand side of figure 5.7. Besides also showing the insect's wings and antennas, the increased contrast in the RID map can be better appreciated.

In summary, in this sub-chapter, we have tested the feasibility of reconstructing quantitatively accurate RID and absorption term maps from EI-CT datasets acquired with the setup described in chapter 4.6. As a first step, we demonstrated that, even in theory, a perfect recovery of the RID is not possible for the fact that the mathematical model that underlies the phase retrieval algorithm does not take into account possible coherence effects. This notwithstanding, acceptable values can be retrieved. Furthermore, we have demonstrated that accurate maps of the absorption term can be retrieved experimentally. The experimentally retrieved RID maps followed the correct trend, while however underestimating

the expected values. We argue that, besides the general difficulties associated with the reconstruction of the RID due to the integration step involved, the additional complication of a misalignment between the sinograms used for phase retrieval and the adjacent transverse slices crucially affected our results. This notwithstanding, we demonstrated that, for low absorbing materials, RID maps are clearly superior in terms of contrast and CNR compared to absorption maps.

5.2.2 Laboratory-Based X-Ray Tube with a Polychromatic Spectrum

We further investigated the possibility of quantitative imaging with the other experimental setup described in chapter 4.6, i.e. the laboratory implementation of the EI-CT method through the use of coded apertures. The setup operates with a conventional x-ray tube with a polychromatic molybdenum spectrum; therefore, the data treatment required the concept of effective energies. As mentioned previously, a recent publication by Munro and Olivo [2013] has demonstrated that, for PC imaging, this concept has the following characteristics. First, effective energies are in general different for phase and absorption images, with the one for phase typically higher than that for absorption. Second, effective energies are object (material and size) specific, primarily because of beam hardening. And finally, as for all polychromatic imaging techniques, effective energies are strongly dependent on the x-ray tube spectrum and the energy response of the detector.

The spectrum of the molybdenum target tube at operation conditions of 25 mA and 35 keV was calculated according to Boone et al. [1997], and is shown in figure 5.9. The absorption by the graphite substrate in the coded aperture masks and by air have been taken into account. In these conditions, and if no further filtering is applied, the spectrum's mean energy is equal to 18 keV. The ANRAD detector is energy integrating, which implies that a specific weight is added for each energy. However, its actual energy response is not disclosed by the manufacturer. For this reason, and because different effective energies are expected for different materials, the comparison of the reconstructed RID and absorption term values with the respective nominal ones was not attempted. Instead, the retrieved values were used to determine the effective (phase and absorption) en-

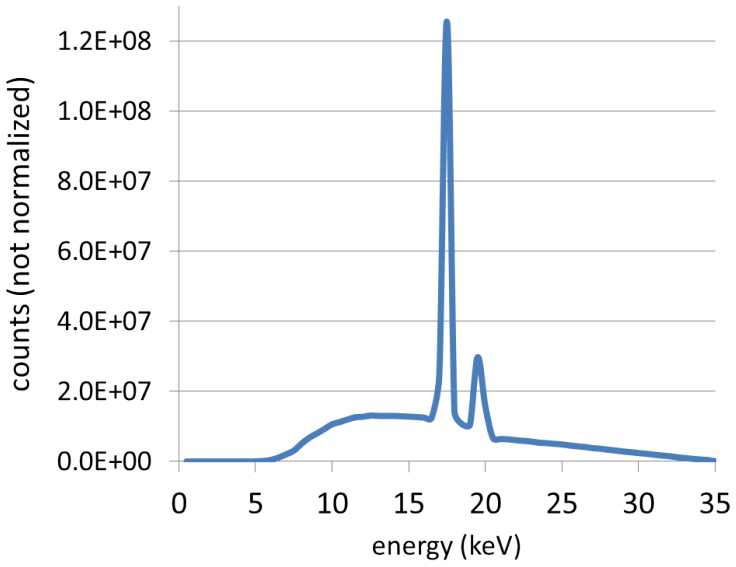

Figure 5.9: Calculated source spectrum, including the effect of the graphite substrate in the coded aperture masks and of the absorption by air, for the employed molybdenum target x-ray tube.

ergies for the respective material and thickness of the wire, and to show that they are in agreement with the characteristics derived in the paper by Munro et al. An additional aim was to assess the theoretical possibility to perform quantitative imaging with the used coded aperture EI-CT scanner.

Materials and Methods

The assessment process was the same as in the previous sub-chapter. First, we tested the general feasibility of accurate optical constant recovery using simulated data, and, as a second step, we performed experimental EI-CT scans.

Although the experimental data was acquired with a polychromatic x-ray tube, for the simulations we considered a monochromatic beam. In fact, a polychromatic EI signal can be written as a weighted integral of monochromatic signals (Olivo and Speller [2006]):

$$I_{poly} = w(E) \int_{\mathcal{S}} I_{mono}(E) dE. \tag{5.5}$$

The symbol $\mathcal{S}$ denotes the tube spectrum, and $w(E)$ is the energy specific weight. Thanks to equation 5.5, the question as to whether the parameters of setup and imaged object satisfy the assumptions at the basis of the phase retrieval algorithm in the polychromatic case can be answered separately for each spectral component. Moreover, the unavailability of the energy response function for the ANRAD would have made an accurate simulation practically impossible.

The simulation software was again based on the implementation of the planar model by Vittoria et al. [2013]. The simulation parameters matched those of the used coded aperture EI-CT scanner. The chosen energy was the mean spectral energy of 18 keV. The same six wires (specified in table 5.1) as in the previous sub-chapter were considered as numerical phantoms. Their nominal RIDs and absorption terms at 18 keV, calculated according to Henke et al. [1993], are listed in table 5.3. As before, data for each wire were simulated on both slopes of the IC. The specific working points (shifts of the sample mask with respect to the detector mask, see chapter 4.2) were chosen to be symmetric: $|\xi_1| = |\xi_2| = 8$ μm. When scaled by the system magnification (M = 1.25), this value corresponds to half the width of the slits in the detector mask (20 μm). This means that 50% of each beamlet falls onto the active pixel area, while 50% is absorbed by the detector mask: this is actually the ideal condition for phase retrieval Munro et al. [2013b]. A number of 60 horizontal "dithering" steps (corresponding to a step of ≈ 1 μm) has been used. This high number was chosen to exclude from the analysis any potential errors due to under-sampling.

Also in this case, the derivative of the phase function Φ and the projected absorption term μ were extracted from the two profiles via phase retrieval for each wire. Subsequently, the former was integrated using the sum rule given previously (equation 5.3). The RID and the absorption term were extracted by finding the maximum values of Φ and μ and by dividing them by the wire diameter. Finally, a comparison between retrieved and nominal values was performed.

For the actual CT experiment, the same wire phantom as described previously (see figure 5.1) was used. The phantom was placed on the rotation stage indicated in figure 4.9. The source was operated at the typical parameters of 25 mA and 35 kV without additional filtration. A 180 degree rotation of the sample with an angular step of 1 degree was performed. Furthermore, horizontal sample dithering with 32 dithering steps (corresponding to a sampling step of approximately 2 μm) was applied. Data acquisition was performed on both slopes of the IC, corresponding to the working points ξ_1 and ξ_2. Also in the experiment, these working points were chosen to be $|\xi_1| = |-\xi_2| = 8\mu$m. The exposure time for each frame was 3 seconds.

The conditions of the EI-CT scanner are slightly unstable when operated over a long period of time, due to a drift of the source focal spot. The high number of projection images required implies a relatively long acquisition time, and, therefore, an optimised acquisition protocol was developed to take the system drift into account and minimises its impact on the resulting reconstructed CT images. The following procedure was performed at every angle. First, the sample mask was shifted to working point ξ_1 and a flat field (image without the sample in place) was taken. Subsequently, the sample was moved into place and the dithering steps on the first IC slope were acquired. Afterwards, the sample was again moved out of the FOV, the sample mask was shifted to the second working point ξ_2 and another flat field was acquired. Then the sample was moved back in and frames at each dithering step on the second slope of the IC were acquired. Subsequently, the sample was rotated to the next angle, and the above procedure was repeated. This "dither-rotate" acquisition scheme ensured that drifts of the system manifested as errors between data acquired at different rotation angles, and not between dithering steps. This is advantegeous because the CT reconstruction scheme is more robust against angular errors than against errors in recombination of the "dithered" projections.

As already discussed, the use of a coded apertures meant that no vertical scanning of the sample was necessary to build up a 2D image, as opposed to the scanning EI-CT method used at the synchrotron.

The processing of the acquired data involved the following steps. First, each projection was corrected for gain and offset variations of the detector. Second,

the dithering steps at each angle were combined into single, resolution-enhanced projections. From these projections, sinograms corresponding to the transverse slices of the phantom were generated in correspondence with each individual detector line. For each transverse slice, the two sinograms corresponding to the two slopes of the IC were given as input to the phase retrieval algorithm, which yielded the separate differential phase and absorption sinograms. The reconstruction of the RID map was performed by applying the FBP with the Hilbert filter to the differential phase sinograms. The absorption term map was reconstructed from the absorption sinograms via the FBP with the ramp filter. As the noise level in the absorption sinograms was high, a relatively low cut-off frequency for the ramp filter was chosen. The reconstruction of the absorption term map as given in table 4.1 involves the division by the wave number k. However, because no effective value for k could be assigned at this point of the processing due to the polychromaticity, this division was omitted. This means that a map of the quantity $\beta \cdot k$ was reconstructed rather than a map of β, where β and k correspond to the same effective energy. On the other hand, the formula for the reconstruction of the RID map does not require the division by the wave number. As a consequence, the reconstructed RID map represented, as in the monochromatic case but corresponding to an effective energy, the distribution of the quantity δ.

We would like to remark that the parallel beam formulation of the FBP was used for the reconstructions, although the used coded aperture EI-CT scanner featured a cone beam. The parallel beam approximation was still valid in this case, for the reason that the phantom covered only a small proportion of the FOV (≈ 1 cm^2). Considering that the source-to-sample distance (1.6 m) is large compared to these dimensions, the used part of the conical beam had an opening angle of less than 0.2 degrees in every direction.

For the quantitative analysis of the reconstructed data, a single transverse slice was selected from the maps. Wire specific ROIs were selected, over which the polychromatic RID and absorption term ($\beta \cdot k$) values were averaged. The averaging over several transverse slices was not necessary, for the reason that no strong reconstruction artefacts were present in the images, which also meant that no wire segmentation and background subtraction was needed.

In order to show that the experimental results are in agreement with the find-

ings of Munro and Olivo [2013], the retrieved polychromatic RID and absorption term ($\beta \cdot k$) values were used to determine effective energies for each wire, by interpolating look-up tables providing the nominal optical constants (δ for the RID and $\beta \cdot k$ for the absorption term) as a function of energy.

Finally, in analogy with the previous sub-chapter, a domestic wasp was imaged under the same experimental conditions as the wire phantom. The RID and absorption maps were reconstructed in the same manner. Again, coronal slices were extracted from the reconstructed volumes, and profiles across the wasp's torso were plotted. The CNR was calculated for both profiles.

Results and Discussion

The optical constants retrieved from the simulated data at the tube spectrum's mean energy of 18 keV are listed in table 5.3. It appears that the recovered values of the absorption term β are marginally higher than the nominal values for the low absorbing materials. We believe this to be solely due to computational errors (on the order of 10^{-10}), which is supported by the fact that the retrieved values for the high absorbing materials (on the order of 10^{-9} or higher) are in good agreement with the nominal ones.

Material	$\boldsymbol{\delta}_{nom}$ / $\boldsymbol{\delta}_{rec}$	$\boldsymbol{\beta}_{nom}$ / $\boldsymbol{\beta}_{rec}$
PBT	8.76×10^{-7} / 8.52×10^{-7}	4.22×10^{-10} / 4.32×10^{-10}
nylon 6.6	7.93×10^{-7} / 7.77×10^{-7}	3.32×10^{-10} / 3.49×10^{-10}
PEEK	8.70×10^{-7} / 8.45×10^{-7}	3.80×10^{-10} / 3.82×10^{-10}
sapphire	2.50×10^{-6} / 2.20×10^{-6}	5.90×10^{-9} / 5.91×10^{-9}
aluminium	1.66×10^{-6} / 1.56×10^{-6}	6.30×10^{-9} / 6.30×10^{-9}
titanium	2.66×10^{-6} / 2.30×10^{-6}	5.10×10^{-8} / 5.08×10^{-8}

Table 5.3: Nominal optical constants and those recovered from the planar monochromatic simulation at 18 keV.

The retrieved RID values are slightly below the nominal ones, with the dis-

crepancy being larger for the wires with high refraction than for those with low refraction. This is not surprising considering that the coded aperture EI method was simulated instead of the scanning EI method. In the scanning EI method, the maximal displacement of the laminar beam caused by refraction that can be measured is given by the pixel size of the used detector. The pixel size is typically large compared to the refraction angles encountered, which implies that deviated photons cannot get lost by being refracted beyond the pixel dimension (see figure 5.10 (a), green arrow). This is different for the coded aperture EI method. The maximum measurable displacement of the beamlets is determined by the slit width of the detector mask, which is a fraction of the pixel size. For large refraction angles such as those encountered at the edges of the wires, the displacement of the beamlets may be large enough to send them onto the adjacent absorbing septa instead of onto the aperture (see figure 5.10 (b), red arrow). In this case, deviated photons, which in a scanning EI system would contribute to the measured signal, are missed. These missing photons explain the slight under-estimation of the nominal RID values. The higher the refraction of the material, the higher the amount of "lost" photons, and, consequently, the higher the discrepancy between retrieved and nominal figures. This explanation is further supported by considering the shapes of the derivative of the phase function for the wires, plotted in figure 5.11. A zoom of the positive peaks reveals a "dip" at the top, where, in theory, the profile should take on its highest value due to maximum refraction. This flattening, most pronounced for high refracting wires, is a typical sign of photon loss: the peak cannot continue to grow as photons are sent beyond the corresponding detector aperture. In other words, the inclination of the profile corresponds to the beamlets getting refracted more and more towards the active pixel surface, implying an increased photon count. However, at the point where the refraction is the strongest (at the edge of the wire), the displacement becomes too large, and the beamlets hit the detector mask on the other side of the active areas, which results in a decreased photon count.

In fact, the design of a coded aperture EI scanner determines the largest displacement (and hence, refraction angle) that can be resolved. If the beamlets were perfectly square, the maximum displacement would be given by the aperture width in the detector mask minus half the width of the beamlets when

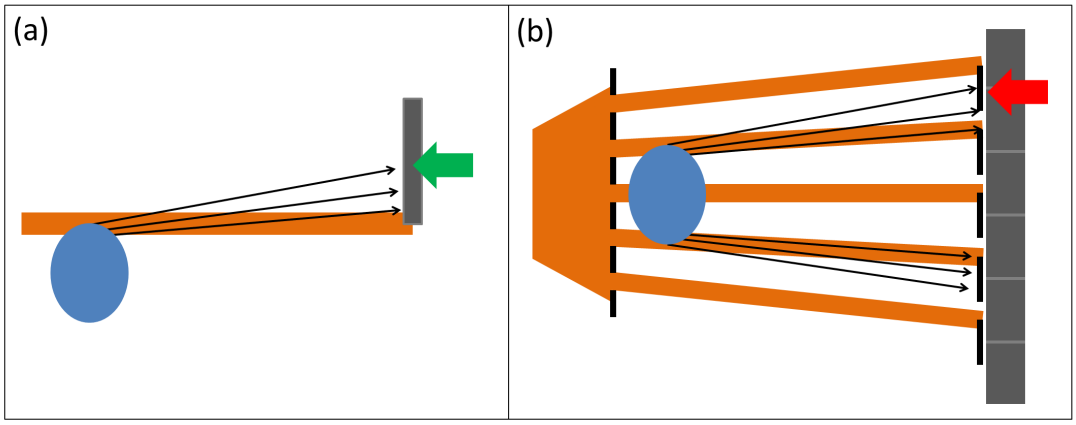

Figure 5.10: Schematics of the scanning EI (a) and the coded aperture EI methods showing the system's response to strong refraction of the laminar beam / beamlets respectively: while the active pixel area in the scanning EI method is typically large enough to detect all refracted photons (indicated by the green arrow), the smaller active area in the coded aperture EI method can result in the loss of highly refracted photons, as they impinge on the adjacent absorbing part of the detector mask (indicated by the red arrow).

they hit the detector plane. For the described system, this would be $D_{max} = 20\ \mu m\ -(12/2)\cdot 1.25\ \mu m\ =\ 12.5\ \mu m$. The maximum displacement is related to the maximum refraction angle via equations 4.4 and 1.5, which, for the described system, would result in $\alpha_{max} = 18.75\ \mu$rad. In practice, however, the beamlets are not square. In fact, the beamlets have been modelled to be approximately of Gaussian shape in the simulation, which is a much closer approximation of the real situation. For this reason, the actual maximum resolvable displacement is larger than the one computed above. It is worth noting that the maximum resolvable displacement corresponds to the injective (invertible) region of the phase retrieval function F (see figure 4.3) that was defined in equation 4.25.

The experimental results for the 3D wire phantom are given in figures 5.12 to 5.14. Figure 5.12 shows transverse slices of the reconstructed maps of the quantities δ and $\beta \cdot k$. The selected slices do not exactly match those presented for the scanning EI method in the previous sub-chapter, however, the relative

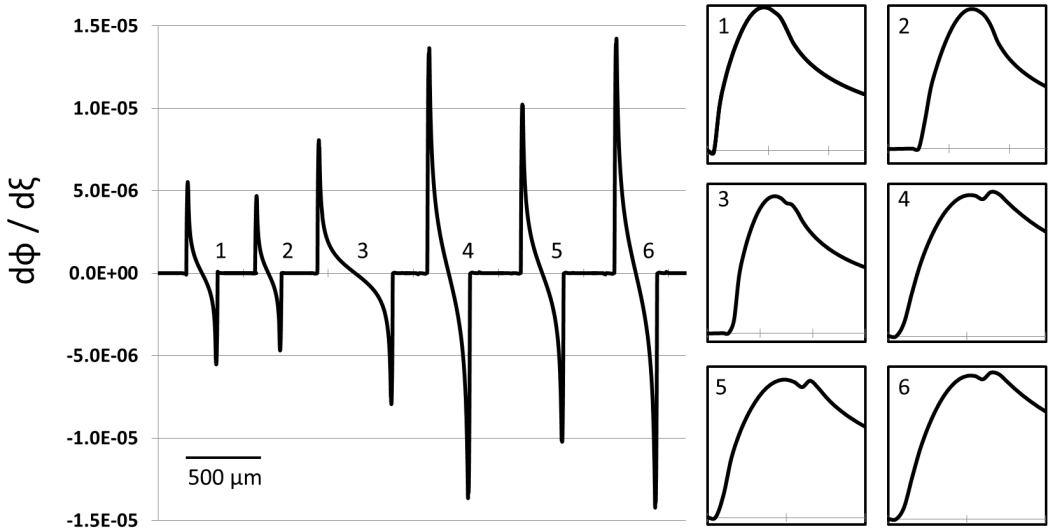

Figure 5.11: Plots showing the first derivatives of the phase function which were extracted from the simulated data for the six wires: 1. PBT, 2. nylon 6.6, 3. PEEK, 4. sapphire, 5. aluminium, 6. titanium. The zoom of the positive peaks of the profiles reveals a decrease on the top, particularly pronounced for the highly refracting materials.

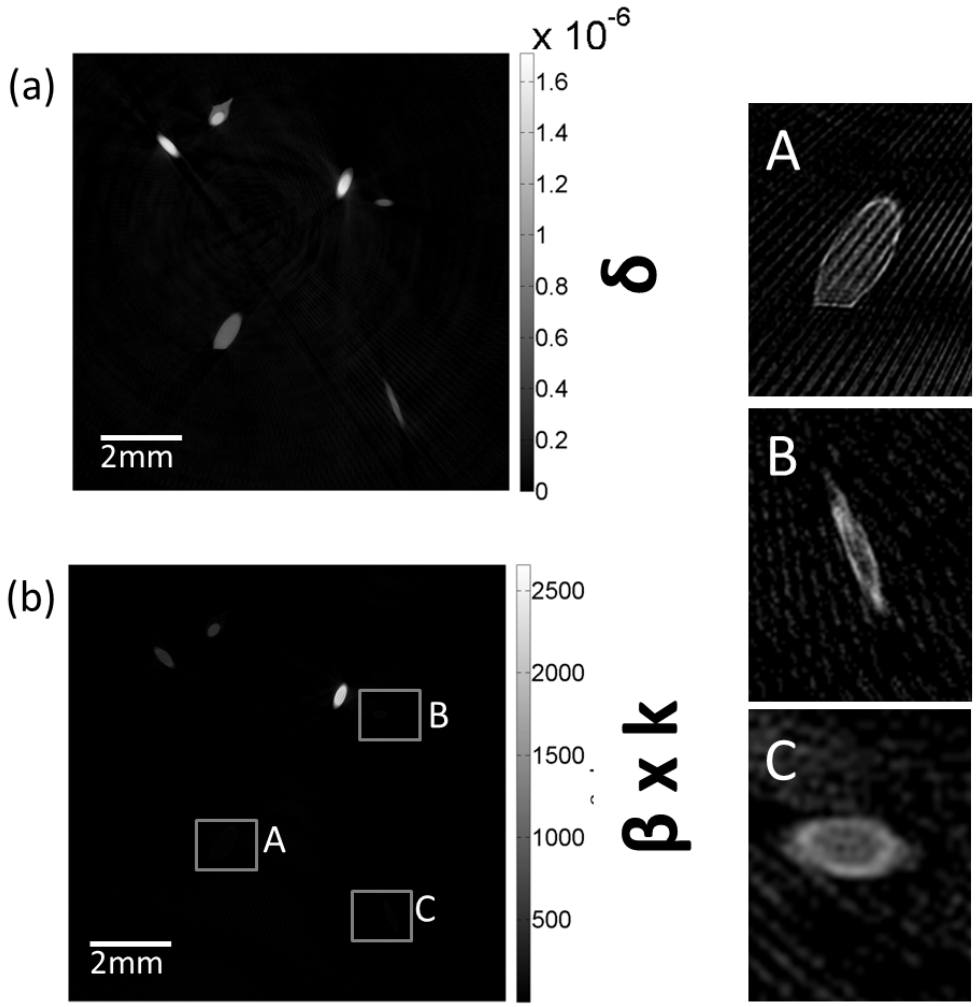

Figure 5.12: Reconstructed, experimentally acquired maps showing the quantities δ (a) and $\beta \cdot k$ (b) within a transverse slice of the wire phantom. Zooms of the regions indicated with the letters A-C are shown on the right hand side.

positions of the wires are the same. The light grey halo attached to the top-right side of the aluminium wire is a drop of glue that was used to fix the wires to the phantom support.

The values in the δ-map are on the order of 10^{-7}-10^{-6}, while the values in the $\beta \cdot k$-map are on the order of 10^{1}-10^{3}. Both orders of magnitude are sensible

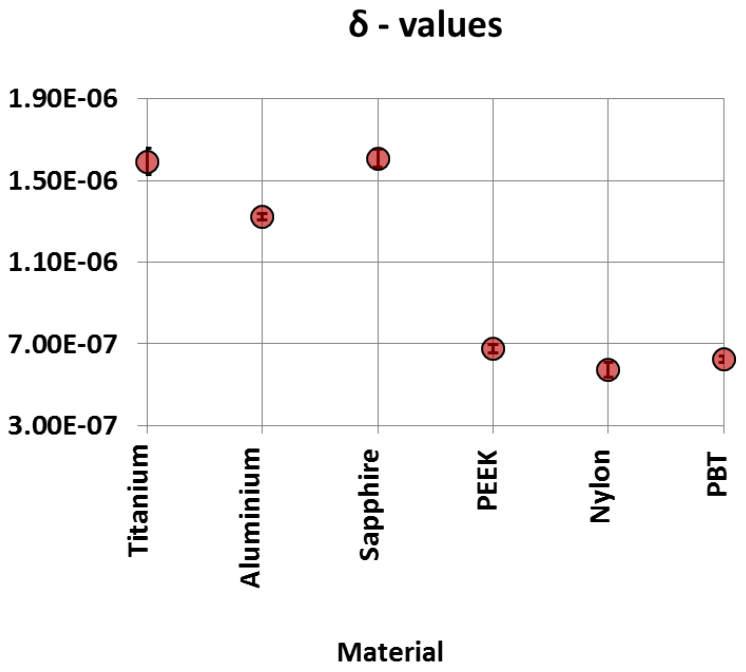

Figure 5.13: Plot showing the recovered polychromatic values of the RID for the six wires. The error bars correspond to one standard deviation.

($\delta_{nom} \sim 10^{-7}$-$10^{-6}$, $\beta_{nom} \sim 10^{-10}$-$10^{-8}$, and $k \sim 10^{10}$-10^{11} at the spectrum mean of 18 keV and for all expected effective energies). The low absorbing wires in the $\beta \cdot k$ map are invisible when windowed alongside the high absorbing wires, hence, they are shown in separate ROIs on the right hand side of the figure. The zooms reveal "star pattern" artefacts, most prominent for the PEEK wire shown in A, which are typical for CT measurements with an insufficient number of angular projections. The optimal number of angles required for an artefact-free CT reconstruction is discussed in chapter 6.

The plots in figures 5.13 and 5.14 show the retrieved δ- and $\beta \cdot k$-values for the six wires. A zoom on the left hand side of figure 5.14 reports the $\beta \cdot k$-values for the low absorbing wires on a different scale, as their values are too small to be readable. The error bars in the figures correspond to one standard deviation of the set that was averaged to obtain the results. The retrieved values for both quantities follow the correct trend compared to the nominal values at 18 keV.

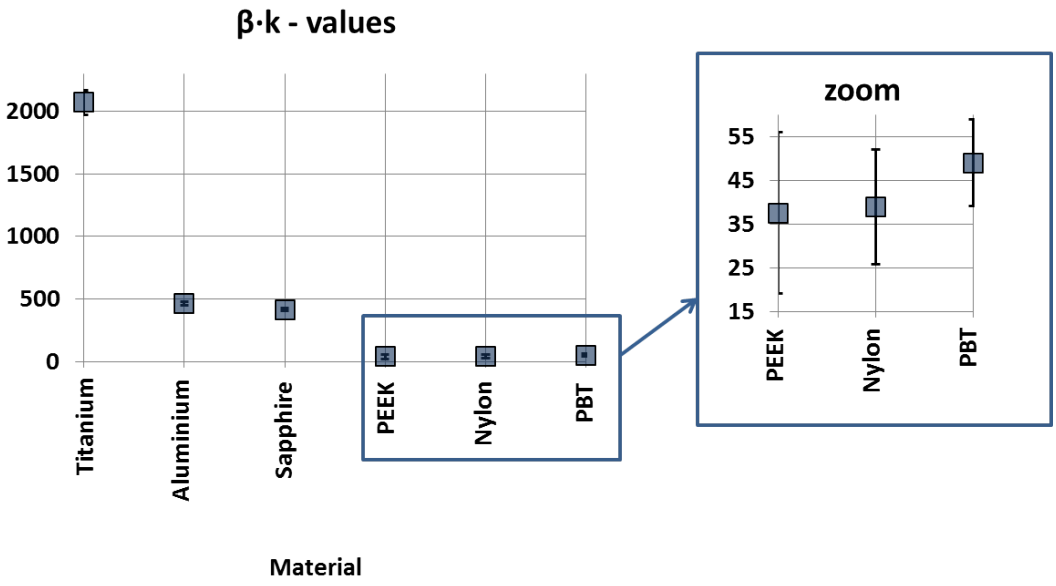

Figure 5.14: Plot showing the recovered values of $\beta \cdot k$ for the six wires. A zoom of the indicated region is shown on the right. The error bars correspond to one standard deviation.

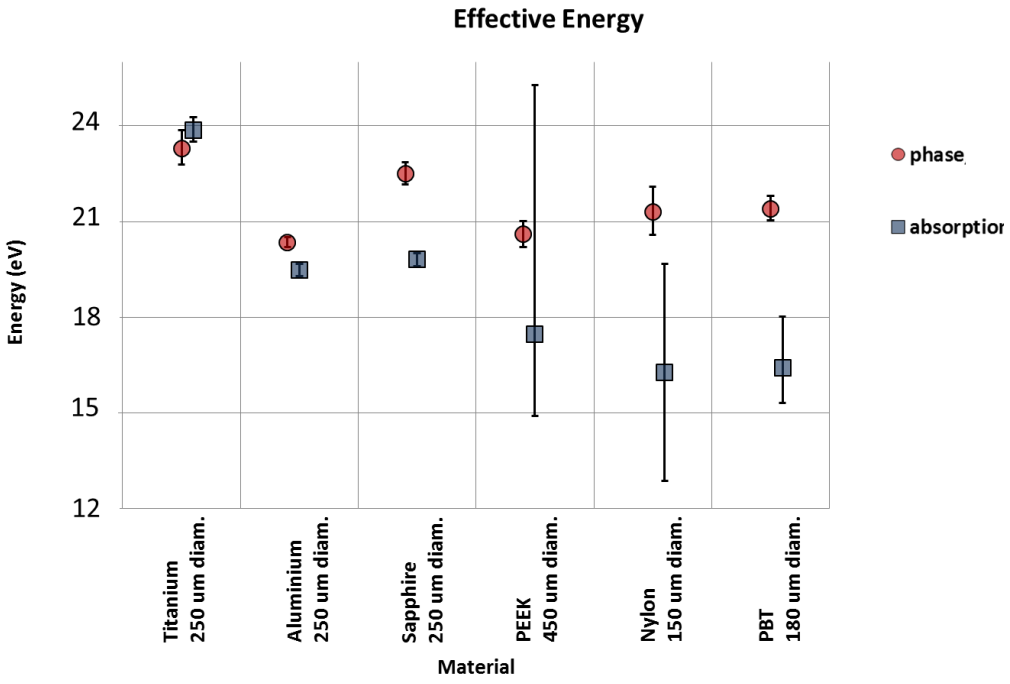

Figure 5.15: The effective energies that correspond to the quantities plotted in figures 5.13 and 5.14

.

However, since a polychromatic source was used, a direct comparison to nominal values was not attempted due to unknown spectral response of the used detector, and due to the influence of sample material and size onto the effective energy. The error bars are of roughly the same size for all wires, which is due to the fact that no strong reconstruction artefacts were present in the images. The artefacts due to angular undersampling, which were revealed in figure 5.12 (zoom on the right), only affect the retrieved $\beta \cdot k$-values for the low absorbing wires: the error bars are relatively large in comparison to their means.

The effective energies that correspond to the values reported in figures 5.13 and 5.14, and which were determined by interpolating energy dependent look-up tables of nominal values for the different materials, are shown in figure 5.15. The results are almost entirely in agreement with the findings reported in Munro and

Olivo [2013]. First, for all wires, the effective energies are different for phase and absorption; in particular, the ones for phase (red dots) are higher in all cases but for the titanium wire where beam hardening is very strong. This confirms the different dependence on energy of the two optical constants: the RID does not decrease with energy as fast as the absorption term, and, consequently, the higher end of the polychromatic spectrum has a higher influence on the recovered RID values. Second, the effective energies are different for each material, which reflects the predicted dependence of the effective energy on the sample material. The absorption effective energies (blue dots) for the high absorbing wires seem to be slightly higher than those for the low absorbing wires, which can be explained by beam hardening. Again, in particular for the highly absorbing titanium wire, the beam hardening leads to a significant increase of the absorption effective energy. Conversely, the effective energies for phase do not seem to be influenced by beam hardening, which is unexpected and requires further investigation. The error bars on the absorption effective energies for the low absorbing wires are larger than for the other wires, which is due to the fast decrease of the absorption term with energy.

These results, as well as the findings reported in the paper by Munro and Olivo, imply that accurate quantitative imaging of objects of unknown composition with a polychromatic source is intrinsically impossible. In order to identify materials from the reconstructed images, effective energies have to be defined to compare the retrieved optical constants to the nominal ones. However, even if all spectral characteristics of the imaging system are known, these effective energies still depend on the imaged object itself.

Provided all features within an object are of similar thickness, a possible solution could be to estimate effective energies for phase and absorption effects which are a good approximation for a range of materials. These effective energies can then be used to perform a comparison between retrieved and nominal optical constants, and eventually for material identification. In this case, the retrieved quantitative results can only be approximate. From the results in figure 5.15, the phase and absorption effective energies for the tested coded aperture EI scanner can be estimated as 22-23 keV and 18 keV respectively. Yet, it is worth noticing that the simulated results presented above indicated a slight under-estimation

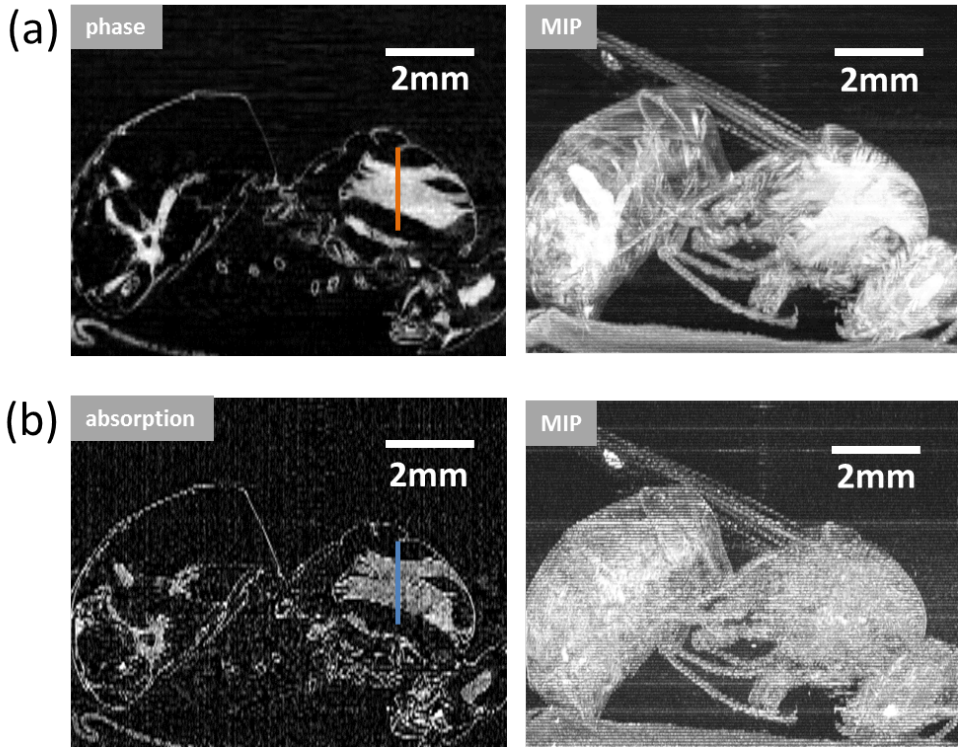

Figure 5.16: Images of the domestic wasp acquired with the laboratory-based coded aperture EI-CT scanner. Coronal slices extracted from the reconstructed RID (a) and absorption term (b) maps are shown on the left hand side of the figure. On the right, the corresponding maximum intensity projections of the volumes are shown.

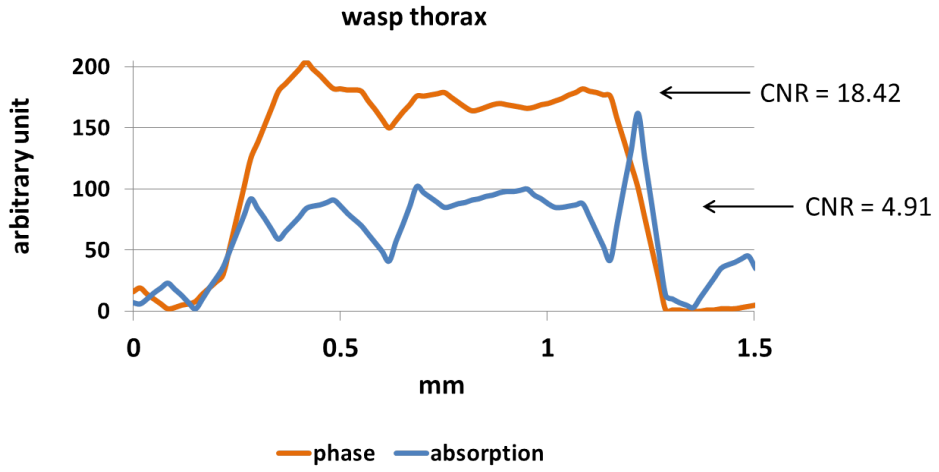

Figure 5.17: Plot showing the profiles across the indicated lines in 5.16 (thorax). The CNR for the phase profile (orange curve) is again higher than for the absorption profile (blue curve).

of the RID due to photon loss, in particular for the highly refracting wires. An under-estimation of the RIDs is effectively equivalent to an over-estimation of the corresponding effective energies. Therefore, the effective energy for phase could be slightly lower. Further experiments involving the imaging of wires of additional materials and diameters will be necessary to confirm and establish these values for future quantitative imaging.

Finally, the images of a domestic wasp are shown in figure 5.16: coronal slices showing the central part of the animal have been extracted from the reconstructed RID (a, left) and absorption term (b, left) maps. The corresponding maximum intensity projections revealing also the wings, legs and parts of the antennas are shown on the right hand side of the figures. The coronal slices do not show any obvious reconstruction artefacts. Visually, these laboratory acquired images are in fact similar in quality to the wasp images acquired at the synchrotron (figure 5.7), which is remarkable and highlights the translatability of EI-CT to conventional x-ray sources. Profiles across the wasp's thorax, extracted along the indicated trajectories in figure 5.16, are plotted in figure 5.17. The plot

features arbitrary units as the images were scaled to 8-bit unsigned integer images before the rendering. It is easily appreciated that the contrast in the phase profile (orange line) is significantly higher than in the absorption profile (blue line). This perception is confirmed by the calculated CNR values for the torso, reported in the graph. The absorption CNR is similar to that calculated for the synchrotron image given in figure 5.8. The phase CNR is only half of that calculated for the corresponding synchrotron image, however, it is still significantly higher than than the absorption CNR.

To sum up, we demonstrated that the design of the tested coded aperture EI-CT scanner is suited for quantitative imaging. An obstacle is given by the polychromaticity of the used x-ray source. We showed experimentally that the spectral behaviour of the scanner is in accordance with the concepts derived in the 2013 paper by Munro and Olivo. We also provided, for the range of samples which were investigated, estimates of the scanner's effective phase and absorption energies, which, after further confirmation, can be used for future quantitative polychromatic EI-CT.

5.3 Demonstration of the Possibility to Reconstruct Quantitative Mixed Differential Phase and Absorption Contrast Maps

All quantitative imaging discussed in the previous two sub-chapters involved the application of a phase retrieval procedure to separately reconstruct RID and absorption term maps. An alternative approach is to reconstruct mixed maps, combining phase and absorption contrast in a single dataset. As mentioned in chapter 4.4, the reconstruction of mixed maps is straightforward if the EI-CT scanner is operated in VS mode. Again, the reconstruction of mixed maps can be beneficial for certain applications, e.g. when the edge-enhancement due to phase contrast can improve detail visibility or help distinguishing different (low absorbing) materials. Moreover, as no phase retrieval needs to be performed, the acquisition of only a single projection is required at each angle, which offers

opportunities for a dose reduction. This is particularly important for biomedical applications.

Diemoz et al. [2011] developed this mixed approach for GI-CT, and showed that the reconstructed mixed maps can be written as a linear combination of phase and absorption contrast. This can be useful both for quantitative image analysis and material identification.

The required settings of the GI-CT system that enable applying the theory of Diemoz et al. were mentioned in chapter 2.3.2. Diemoz et al. model the intensity in a single GI projection as arising from a combination of transmitted and refracted photons. The intensity contribution due to refracted photons is observed in the shape of a sinusoidal pattern that arises when one of the gratings is scanned while the other system components are kept stationary. By linearising this pattern via its Taylor expansion, Diemoz et al. derive a formula for the total intensity that combines transmission and refraction intensities in a linear manner: this linear combination can then be reconstructed in the CT maps.

In this chapter, we demonstrate that the same mixed approach can also be applied to EI-CT. We adopt the strategy used by Diemoz et al. to derive our own theory resulting in a formula that links the mixed maps to the object's RID and absorption term. Finally, we verify our theory with experimental results.

Materials and Methods

Consider again the model for the intensity measured with an EI phase contrast system (irrespective of scanning or coded aperture EI) in the absence of a sample, given by equation 4.15:

$$I = I_0 \cdot C(\eta_0). \tag{5.6}$$

The coordinate η_0 denotes the working point, which is equal to the position of the absorbing edge in the scanning EI method, and to the shift of the sample mask in the coded aperture EI method. In the case of the scanning EI method, depending on which side of the pixel row is left uncovered, C actually refers to either of the illumination curves C_1 and C_2. The introduction of an object in the

beam changes equation 5.6 to:

$$I = I_0 \cdot A \cdot C(\eta_0 + D), \tag{5.7}$$

where A and D again denote the induced attenuation and refraction-related displacement. Insertion of the definitions of A and D (equations 4.3 and 4.4) into the latter formula, and calculating the logarithm of both terms yields:

$$\log\left(\frac{I}{I_0 \cdot C(\eta_0)}\right) = \log\left(\frac{e^{-\mu} \cdot C(\eta_0 + \frac{\partial\Phi}{\partial\eta}\frac{z_{od}}{M})}{C(\eta_0)}\right), \tag{5.8}$$

which, by applying the basic properties of logarithms, can be further modified to:

$$\log\left(\frac{I}{I_0 \cdot C(\eta_0)}\right) = -\mu + \log\left(C(\eta_0 + \frac{\partial\Phi}{\partial\eta}\frac{z_{od}}{M})\right) - \log\left(C(\eta_0)\right). \tag{5.9}$$

Effectively, the left hand side of equation 5.9 describes a (normalised) EI projection, and the right hand side links it to the optical constants of the object. To be used in CT reconstruction, this relation must take the form of a line integral. The projected absorption term μ is a line integral by definition, and the term $\log\left(C(\eta_0)\right)$ is a constant. In order to write also the second summand on the right of equation 5.9 as a line integral, we linearise it by its Taylor series around the working point η_0:

$$\log\left(C(\eta_0 + \frac{\partial\Phi}{\partial\eta}\frac{z_{od}}{M})\right) \approx \log\left(C(\eta_0)\right) + \frac{C'(\eta_0)}{C(\eta_0)} \cdot \frac{\partial\Phi}{\partial\eta}\frac{z_{od}}{M}, \tag{5.10}$$

where C' denotes the first derivative of the IC. The Taylor expansion is valid if the working point η_0 corresponds to the approximately linear part of the IC, as here the second derivative vanishes ($C''(\eta_0) = 0$). Its validity is further restricted to small refraction angles, which is satisfied for most refraction angles encountered in biomedical applications. Substituting equation 5.10 into equation 5.9 yields:

$$-\log\left(\frac{I}{I_0 \cdot C(\eta_0)}\right) = \mu - \frac{C'(\eta_0)}{C(\eta_0)} \cdot \frac{\partial \Phi}{\partial \eta} \frac{z_{od}}{M}. \tag{5.11}$$

Note that the constant terms have cancelled out. The phase function Φ is a line integral by definition, and the factor $C'(\eta_0)/C(\eta_0)$ is a constant. Therefore equation 5.11 can finally be written as:

$$-\log\left(\frac{I}{I_0 \cdot C(\eta_0)}\right) = \int_{\mathcal{O}} \left(2k \cdot \beta - \frac{C'(\eta_0)}{C(\eta_0)} \frac{z_{od}}{M} \cdot \frac{\partial \delta}{\partial \eta}\right) dz. \tag{5.12}$$

The variable z denotes the propagation direction of the x-rays. If the projection data is acquired for a 180 degree rotation of the object, the following 3D object function can be reconstructed by applying the FBP with the ramp filter to the right hand side of equation 5.12:

$$\frac{f(\xi, z, \eta)}{2} = k \cdot \beta(\xi, z, \eta) - \frac{A(C, \eta_0, z_{od}, M)}{2} \cdot \frac{\partial \delta}{\partial \eta} \tag{5.13}$$

with the constant factor A defined as:

$$A(C, \eta_0, z_{od}, M) \coloneqq \frac{C'(\eta_0)}{C(\eta_0)} \frac{z_{od}}{M}. \tag{5.14}$$

Equation 5.13 states that the reconstructed mixed maps are a linear combination of the absorption term and the differential of the RID, with the relative weight of the two terms depending only upon system-specific parameters.

For the experimental verification of this theoretical result we considered again the EI-CT datasets that were used for the investigation of quantitative imaging in chapter 5.2.1, which were acquired with the scanning EI-CT setup implemented at the Elettra synchrotron. The datasets comprised projections of a wire phantom (acquired at 20 and 25 keV) and a domestic wasp (acquired at 20 keV). In the context of the present chapter, mixed instead of separate RID and absorption

term maps were reconstructed from these datasets, which required only the data for the first position of the absorbing (tungsten) edge. The projections were corrected for detector gain and offset, and sinograms for each transverse slice were generated. These sinograms were directly given as input to the FBP with the ramp filter.

In order to verify that equation 5.13 holds, the phase retrieved data generated in the context of chapter 5.2.1 was additionally considered. The extracted differential phase sinograms were given as input to the FBP with the ramp filter, which resulted in a reconstruction of the vertical RID gradient component, i.e. $\partial\delta/\partial\eta$. From the extracted absorption sinograms, maps of $\beta \cdot k$ were reconstructed also using the FBP with the ramp filter. For the verification of equation 5.13, the factor A was calculated for the system parameters and the respective energy, and the linear combination was calculated. The four reconstructed maps (mixed phase and absorption, the absorption term and differential phase maps, and their linear combination) were rendered and compared visually. Moreover, profiles were extracted from the four maps and compared visually. The analysis was carried out for two of the wires (a low absorbing and a high absorbing one) in the wire phantom and for two features (thorax and head) of the domestic wasp.

Results and Discussion

Figure 5.18 shows transverse slices of the four different maps for the wire phantom, acquired at 20 keV: the scaling factor for the differential phase map was $A/2 = -2.70 \cdot 10^4$. Visually, the mixed map and the linear combination look the same. It can also be observed that the colour bars on the right of the images have the same limits, which is further supports the validity of equation 5.13. The respective maps reconstructed from the data acquired at 25 keV are not shown, as visually they look identical to those acquired at 20 keV. The scaling factor for the differential phase map at 25 keV was calculated to be $A/2 = -1.42 \cdot 10^4$.

Profile plots extracted from all four maps, for both 20 and 25 keV, along the indicated lines in figure 5.18 (a) (across the titanium and the nylon wires), are shown in figures 5.19 and 5.20. Two plots for each wire/energy combination are provided to prove the following points: 1. The values in the mixed map are equal (within the experimental uncertainty) to the values in the map obtained

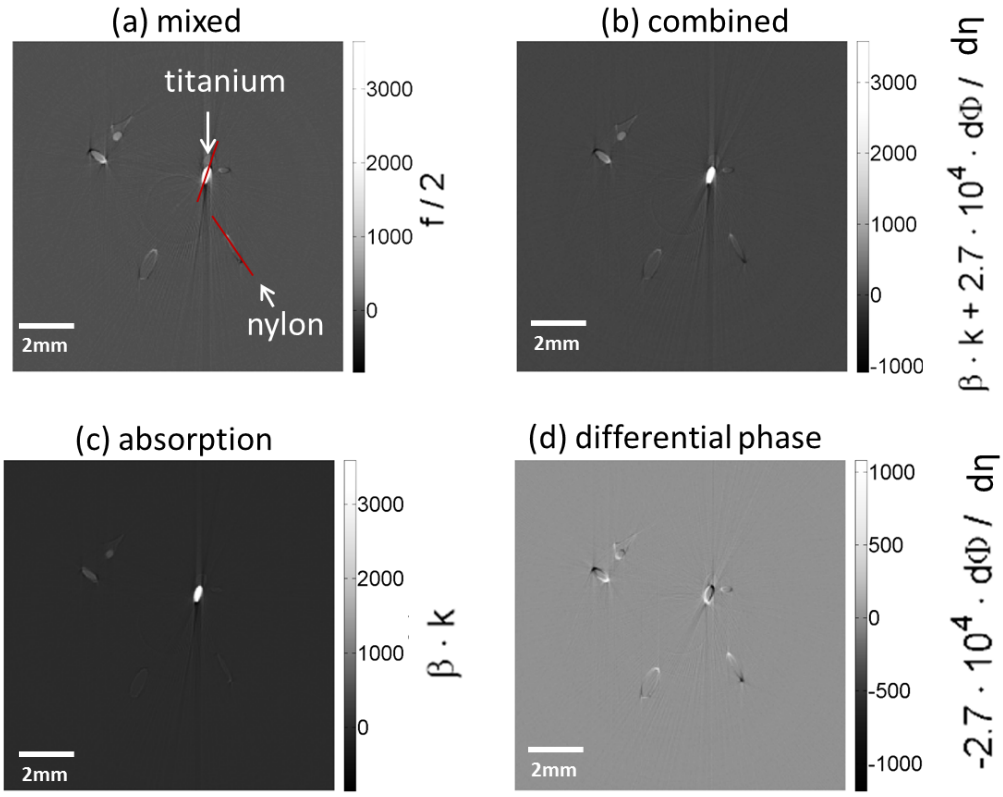

Figure 5.18: Transverse slices showing four different maps of the 3D wire phantom: a mixed phase and absorption map (a), separate maps of the scaled absorption term (c) and differential RID (d), and a map of the linear combination of the latter two (b), which has been computed according to equation 5.13. The red lines in (a) indicate the positions where profiles were extracted across the nylon and the titanium wire. These profiles are shown in the subsequent figures.

via linear combination (as stated by equation 5.13). 2. The scaling by k and $A/2$ ensures that the differential phase and absorption values have the same order of magnitude as in the mixed map. In figure 5.19, (a) and (b) show the profiles extracted from the mixed (black line) and linearly combined (red line) maps for the nylon wire at 20 and 25 keV respectively. For both energies, the two profiles match. A slight discrepancy can be observed only at the edges of the wire, which is not surprising, as these are critical points for the phase retrieval method (the assumption of slowly varying phase is not valid), which implies that the differential phase maps may be inaccurate at these points. A good match between mixed and combined maps can also be observed in the corresponding plots for the titanium wire, shown in figure 5.20 (a,b). Here, the profiles seem to agree also at the edges, which may be explained by the fact that absorption is the dominant contrast mechanism.

The plots of the individual, scaled absorption and differential phase profiles, together with their linear combination, are shown in figure 5.19 (c,d) for the nylon wire and in figure 5.20 (c,d) for the titanium one. For the nylon wire, the main contribution to the contrast in the combined plot comes from the differential phase, which is not surprising, as the absorption is very low. This observation holds at both 20 and 25 keV. However, at 25 keV, the absorption profile is somewhat more visible due to high oscillations at the edges of the wire (indicated by arrows). These are due to free space propagation effects in the horizontal direction. The relative weight of these effects is more prominent in the 25 keV image than in the 20 keV because at this energy the absorption of the nylon wire is even lower. We would like to remark that the profiles of the nylon wire clearly demonstrate the superiority of PC over conventional imaging in the case of samples with very low absorption.

For the titanium wire, the absorption clearly contributes most to the combined profile, which is not surprising since titanium is a very strong absorber. This is apparent at both energies. The high difference between absorption and phase properties makes it even more remarkable that the quantitative analysis reported in chapter 5.2.1 provided absorption and RID values which were reasonably close to the nominal values, although the latter was slightly under-estimated. No free space propagation effects are visible in any of these plots, which can be explained

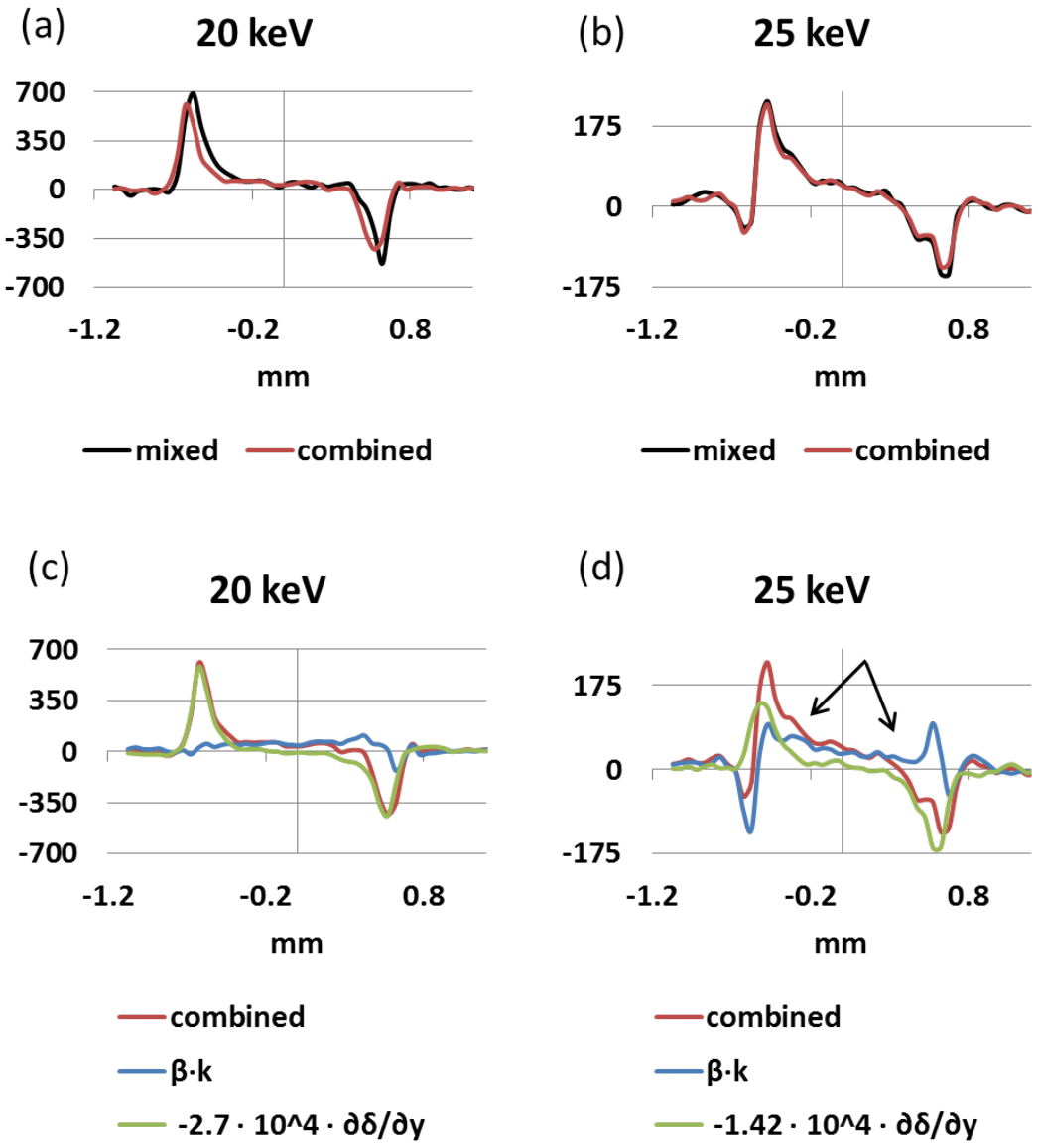

Figure 5.19: Profiles across the nylon wire extracted from the four maps acquired at 20 keV (a,c) and at 25 keV (b,d). The upper plots show the profiles extracted from the mixed and the combined maps, the lower plots show the scaled absorption term and differential RID profiles as well as their linear combination. The arrows indicate the additional fringes due to free space propagation effects.

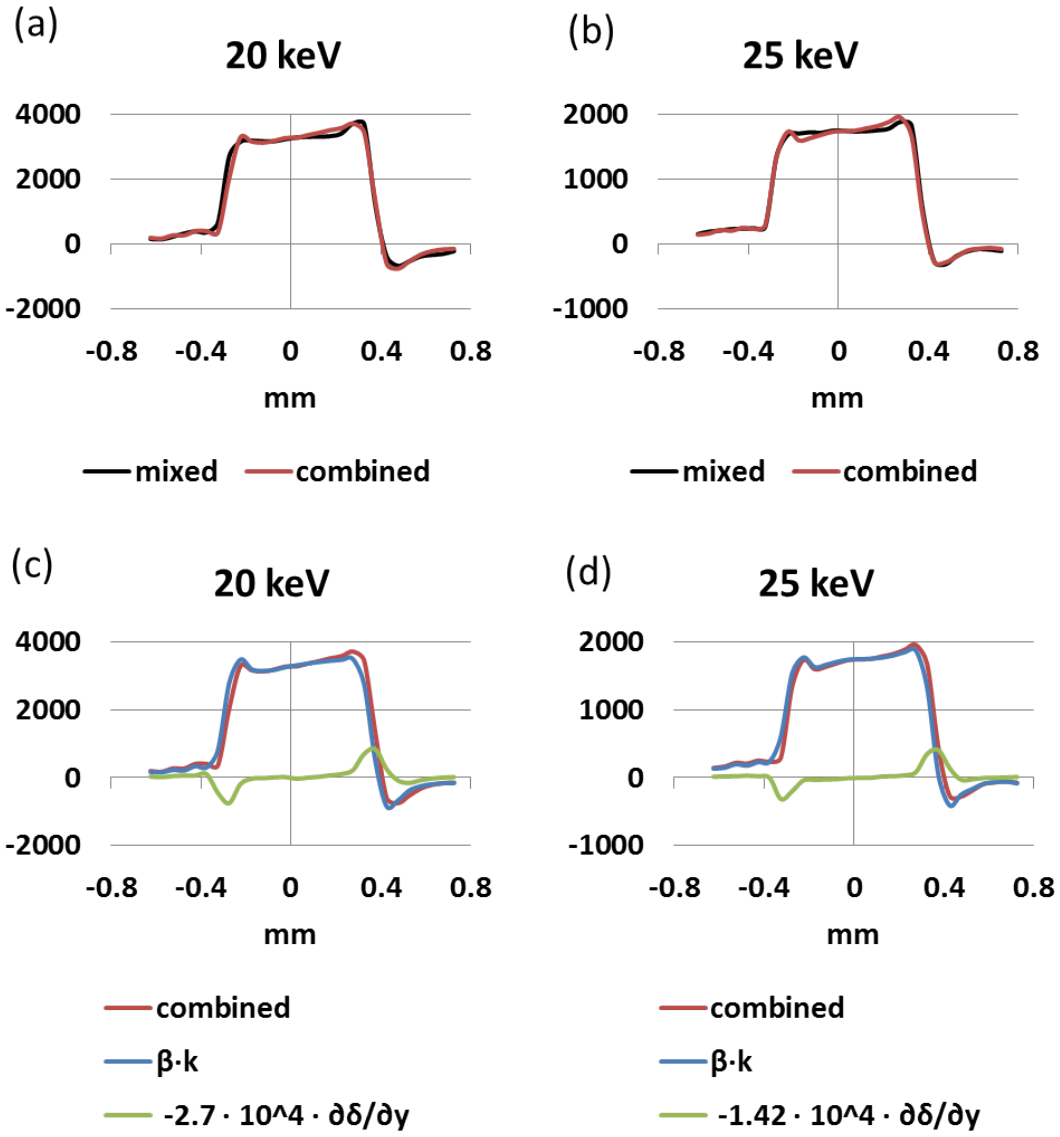

Figure 5.20: Profiles across the titanium wire extracted from the four maps acquired at 20 keV (a,c) and at 25 keV(b,d). The upper plots show the profiles extracted from the mixed and the combined maps, the lower plots show the scaled absorption term and differential RID profiles as well as their linear combination.

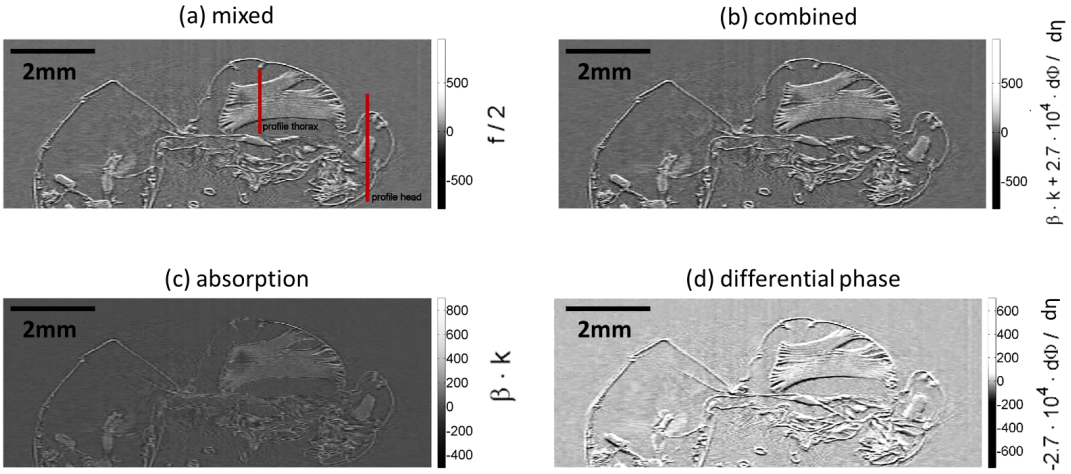

Figure 5.21: Coronal slices extracted from the following reconstructed maps of the domestic wasp: (a) mixed phase and absorption, (c) scaled absorption, (d) scaled differential phase, (b) linear combination of the latter two. The lines across the insect's thorax and head indicate the origin of the profile plots in figure 5.22

by the fact that they are masked by the strong absorption.

The results for the domestic wasp are shown in figures 5.21 and 5.22. The images, again showing (coronal) slices of the four different maps, present the same characteristics that were discussed for the wire phantom: visually, the mixed (a) and combined (b) maps are identical, and the grey values in the colour bars on the left of the images also match. By considering the combined map together with the scaled absorption (c) and differential phase (d) maps, it becomes apparent that the main contribution to image contrast comes from the latter. Certain features of the wasp, in particular the internal structure underneath the thorax, are difficult to spot in the absorption map, but are clearly visible in both the differential phase and the combined maps due to the edge enhancement effect. The profile plots shown in figure 5.22, extracted across the thorax and the head of the animal, confirm what was already observed on the basis of the visual appearance of the images. The comparison of the mixed and the combined profiles (a,b) shows an accurate match, apart from at the points where the signal is highest. As for the wires, these correspond to sharp transitions between areas of different

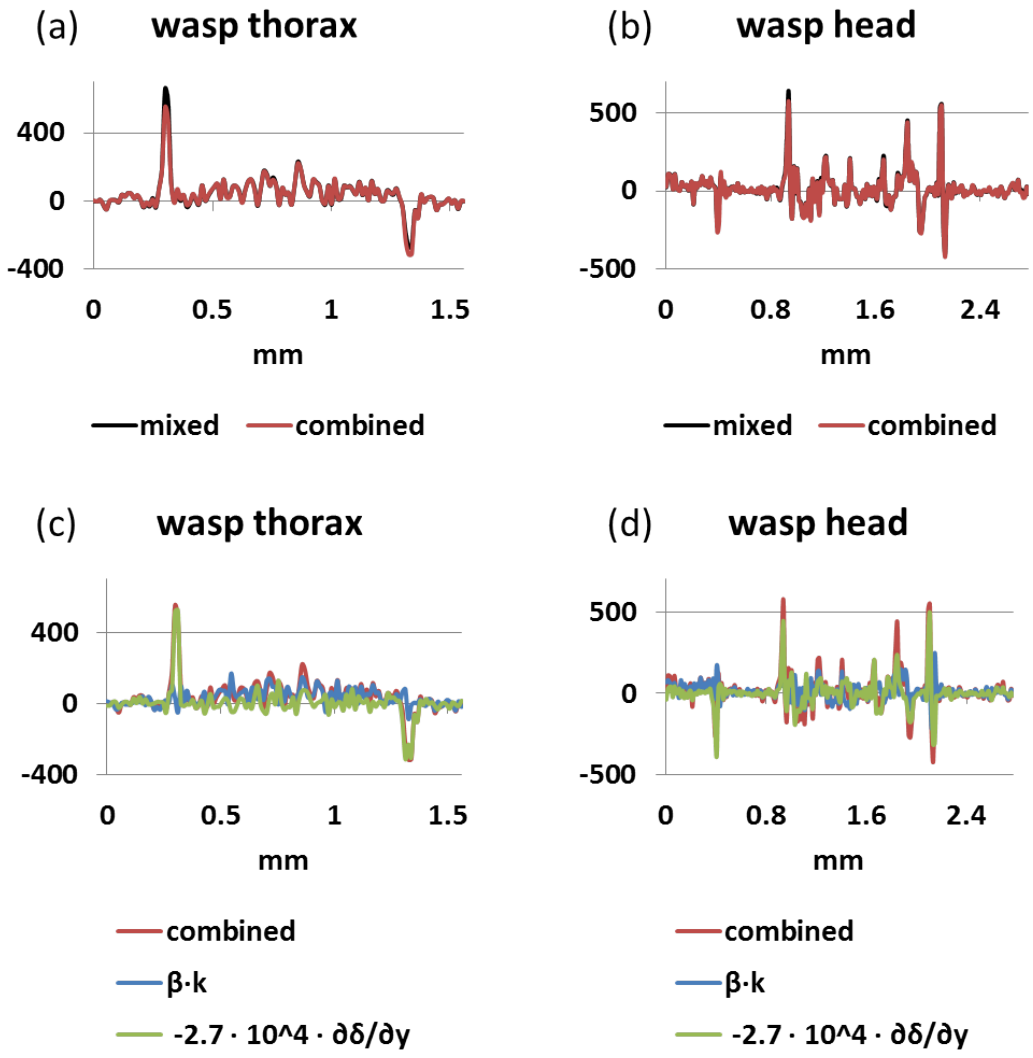

Figure 5.22: Plots of profiles across the wasp's thorax and head: (a,b) show the mixed profile and the linear combination, (c,d) show the linear combination and its absorption and differential phase contribution.

refractive index, which thus violate the assumptions of the model underlying the phase retrieval method. We would like to highlight that the profiles are in very good agreement even for the complex structure within the insect's head. Plots (c) and (d) confirm the dominance of differential phase over absorption contrast in the combined image.

In summary, we derived a theory specific to EI-CT that enables quantifying the (linear) contributions of absorption and differential phase. We validated this theory through experimental data and obtained a very good agreement. The method holds equally well for high and low absorbing materials, which demonstrates its robustness. The images of the wasp demonstrated that the method can also be reliably applied to more complicated structures.

The system used for the experimental verification was a scanning EI-CT implementation set up at a synchrotron. However, we would like to emphasize that, for the derivation of the theory, no assumptions on the implementation of the method (scanning or coded aperture EI-CT) or on the x-ray source were made. Therefore, the theory can also be applied to coded aperture EI-CT scanners implemented with laboratory-based sources. In order to do this, however, it is required that the used EI-CT scanner is operated in VS mode.

5.4 Chapter Summary and Conclusion

This chapter positively answered the question as to whether it is possible to perform quantitative imaging with EI-CT. First, the possibility to reconstruct quantitatively accurate RID and the absorption term maps was investigated. For this purpose, two experimental implementations of the method were considered. Simulations demonstrated that the optical constants can be recovered within a sufficient level of accuracy for both the scanning and the coded aperture EI method. However, the extreme importance of the monochromatic or polychromatic nature of the x-ray source was highlighted. While a comparison of retrieved and nominal optical constants is straightforward in the monochromatic case, the polychromatic case requires the determination of (phase and absorption) effective energies. A further important aspect affecting the accuracy of the retrieved

optical constants are reconstruction artefacts.

Besides material identification, the superiority of RID map over absorption maps in terms of CNR was demonstrated.

The second part of the chapter dealt with the derivation of a theory specific to EI-CT enabling the reconstruction of combined phase and absorption maps that also have a quantitative meaning. The theory was tested experimentally for a wire phantom and a domestic wasp, in order to demonstrate that it holds for both simple and complex structures with different absorption properties. A good agreement between theory and experiments was observed. The derived theory has a strong impact as no phase retrieval is required, which can reduce scan time and dose by a factor of two.

Chapter 6

An Optimal Sampling Scheme for Laboratory-Based Edge Illumination CT and the Potential for Low-Dose Imaging

6.1 Chapter Introduction and Outline

In the previous chapter, we demonstrated that EI-CT can be used for quantitative imaging. The used data was acquired with a very high sampling rate in order to exclude any possible under-sampling effects from the analysis. However, an increased sampling rate comes at the cost of higher radiation dose and long acquisition times. In this chapter, we assess the effect of the sampling rate on image quality and on the extracted quantitative results. We will focus here only on the laboratory-based implementation of the coded aperture EI-CT method (described in chapter 4.6). The investigation of the sampling rate is particularly important for the laboratory implementation, because it determines its potential usefulness for *in vivo* applications, for example as a pre-clinical small animal scanner. We provide a sampling scheme that is optimal in the sense that further increasing the sampling rate does not lead to further improvements in the results (in terms of quantitative reconstruction and image quality).

The second part of the chapter deals with dosimetry. The dose delivered during EI-CT scans of small animals (e.g. mice) will be estimated. Moreover, EI-CT images acquired under low-dose conditions of selected biological objects will be shown.

6.2 The Effect of Object Dithering on Image Quality and Quantitative Results

Quantitative imaging as presented in chapter 5.2 requires the extraction of the derivative of the phase function to retrieve the RID within an object. For simple objects with known geometry, the RID can be retrieved by dividing the phase function by the object thickness. Generally, however, the acquisition of differential phase sinograms and tomographic reconstructions of the RID are required. In both cases, the retrieval of the RID requires the integration of the derivative of the phase function. In the planar case, a unidirectional integration of the derivative of the phase function is required. In CT, the integration is performed implicitly during the FBP by the Hilbert filter. As well known to the PC community, the integration of differential phase data is a delicate task (Kottler et al. [2007], Thuering et al. [2011]), since the propagation of local errors causes artefacts (e.g. stripe or "gradient" artefacts). Not only do these errors corrupt the resulting images qualitatively, but they may also affect their quantitative meaning, making material identification ambiguous and, therefore, possibly challenging.

Local errors are common in differential phase images and can be of various origins. Integration artefacts can, for example, be caused by noise with a non-zero mean, or other (systematic) errors introduced by the setup or the processing (i.e. during phase retrieval). Another important issue that can cause erroneous differential phase data is the sampling rate of the projections. Differential data typically contain high frequency components which, according to Nyquist-Shannon's theorem, need to be sampled at a high rate to be fully captured. If sampled at too low a rate, the differential dataset is incomplete, making artefact-free integration impossible.

As explained previously, the sampling rate in coded aperture EI can be in-

creased by dithering. This requires the object to be displaced horizontally by sub-pixel amounts and images to be taken at each displacement and to be combined. In dithered images, the sampling rate is equal to the period of the sample mask divided by the number of dithering steps. Although, from a technical point of view, the highest achievable sampling rate is dictated by the precision of the motor movement, a lower rate may be sufficient to satisfy Nyquist-Shannon, for the reason that blurring induced by the projected source size imposes a physical limit on the highest frequency present in the data. While leading to enhanced spatial resolution, object dithering comes at the cost of increased scan times and dose delivery. Moreover, in a CT scan, the number of dithering steps and required projection angles are interlinked. A rule of thumb states that, if the number of pixels covering the object in a projection is N_{pixels}, the number of angular projections required over a 180 degree range is:

$$N_{angles} = \frac{\pi}{2} \cdot N_{pixels} \tag{6.1}$$

(Kak and Slaney [1987]). If this relationship is satisfied, the resolution in the reconstructed CT image is optimised. Dithering increases the number of pixels in a projection image by a factor equal to the number of dithering steps N_{dither}, and, consequently, increases the overall number of required projections (dithering steps and angles combined) by a factor $(N_{dither})^2$. Therefore, while dithering may be considered acceptable in planar imaging, it may be impractical when performing CT, especially for applications in which dose is a concern.

Figure 6.1 shows examples of the effect of under-sampling in planar coded aperture EI for a wire phantom. The plot in (a) shows differential phase profiles extracted from correctly sampled (black line) and under-sampled data (coloured lines). The data were generated using the simulation code developed by Vittoria et al. [2013]. The sampling rate for all under-sampled cases was the same, however, the specific locations of the sampling points were varied. The plot in 6.1 (b) shows the profiles in (a) after integration. While in the differential profiles errors due to under-sampling appear mainly locally at the edges of the wire, the integrated profiles are globally affected. In particular, the offset from the

correctly sampled data corrupts their quantitative meaning. The fact that all under-sampled profiles show a different offset clearly indicates that, in case of under-sampling, the quantitative results depend on the location of the sampling points. This is further demonstrated in figure 6.2, which shows experimental planar data acquired with the coded aperture EI scanner. Images (a,b) show the retrieved first derivative of the phase function of a wire, and (c,d) show the integrals. The images on the left (a,c) result from data acquired with a sufficiently dense sampling rate (32 dithering steps), while the images on the right (b,d) are under-sampled (no dithering). As can be clearly seen, the phase function shown in (d) has stripe artefacts along the integration trajectories, indicated by the red arrow. Moreover, the colour bar in (d) shows different grey values than the one for the correctly sampled case (c). In particular, also negative values appear, which has no physical meaning. The wide variation of values in the colour bar in itself demonstrates that extracted quantitative values cannot be considered to be accurate.

Figures 6.1 and 6.2 indicate that, in planar coded aperture EI, not only is a denser sampling via dithering a means to increase the spatial resolution, but it is also a crucial requirement for the retrieval of correct and unambiguous quantitative values. In this chapter, we provide further evidence supporting this concept while demonstrating that, conversely, quantitative results are independent from dithering when retrieved using coded aperture EI-CT. This is an important result showing that, in CT, the effect of dithering can simply be considered as a means to increase the spatial resolution of the reconstructed images, which enables a more flexible control of the delivered dose as no lower limit is set by sampling constraints.

Materials and Methods

The aim of the study was to assess the effect of the sampling rate on the quantitative information that can be retrieved. In particular, the number of dithering steps required for the correct and unambiguous retrieval of quantitative information was analysed. Both planar and CT data originating from the coded aperture EI scanner were considered, including simulated and experimental datasets. Numerical and custom-built phantoms were used to determine the optimal number

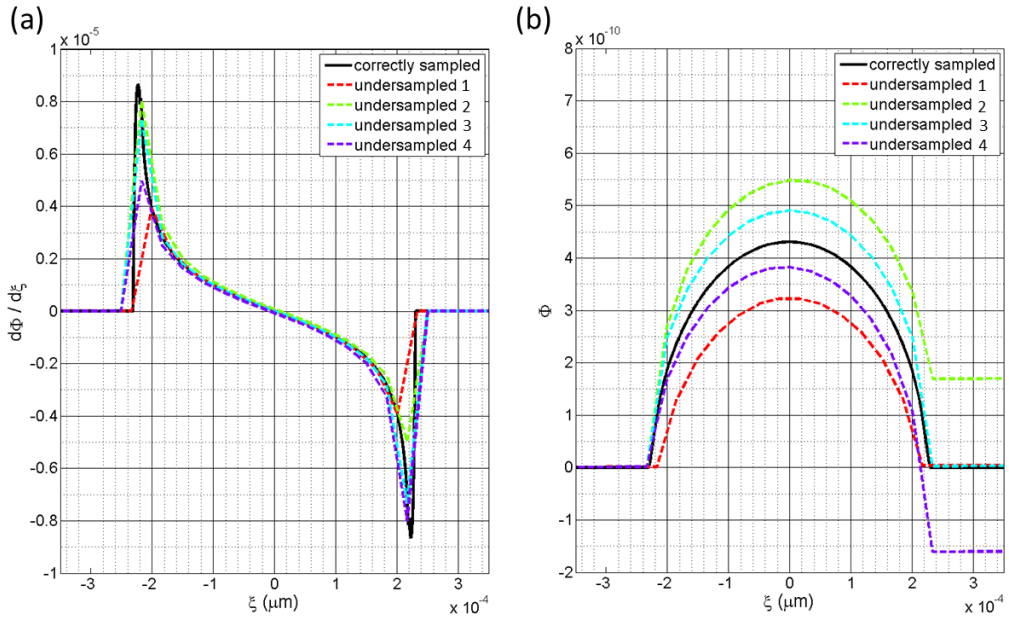

Figure 6.1: The effect of under-sampling in planar coded aperture EI, demonstrated with simulated data of a wire. (a) shows the simulated derivative of the phase function for a single cross-section of the wire, and (b) shows its integral. The black line corresponds to correctly sampled data, while the coloured lines correspond to under-sampled data.

of dithering steps; eventually, the conclusions were validated on images of a biological object (a domestic wasp).

The custom-built phantom was a cylinder containing three tilted wires, which were a subset of those used in chapter 4: PEEK (450 μm), sapphire (250 μm) and aluminium (250 μm). For further material specifications, the reader is referred to table 5.1. The material of the external cylinder was a light plastic similar to PMMA. Its diameter was 21 mm, and the wall thickness was 1.5 mm. A schematic, a transverse cross-section and a photograph of the phantom are shown in figure 6.3. The numerical phantom used in the simulation study was designed to match the real one. The external cylinder was modeled using the optical constants of PMMA.

The general strategy of the study was the following. Coded aperture EI

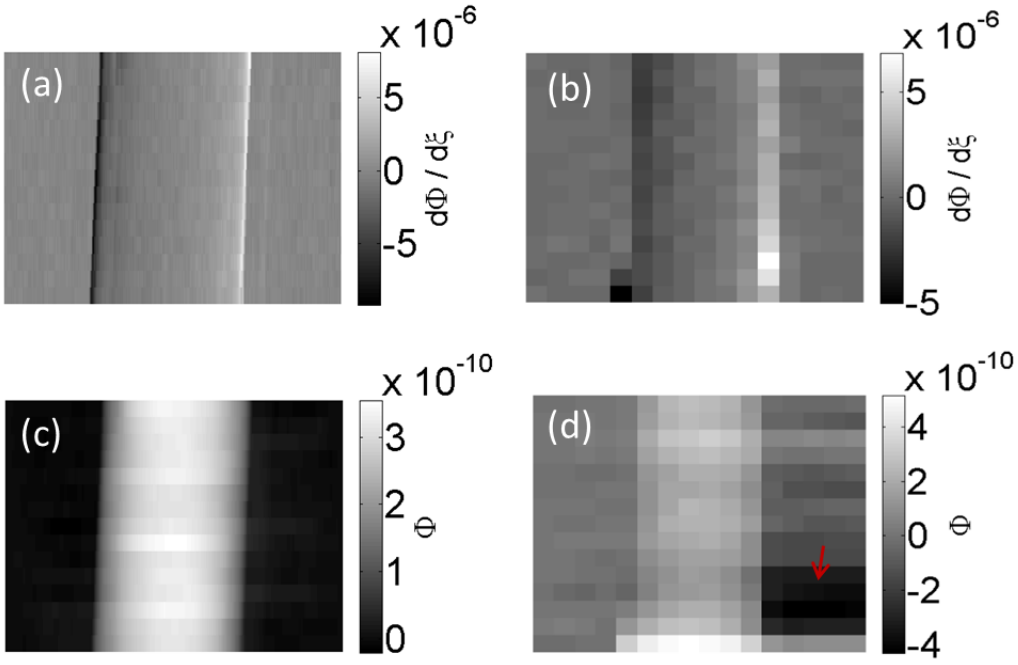

Figure 6.2: The effect of under-sampling in planar coded aperture EI, demonstrated with experimental data of a wire. (a,b) show images of the retrieved differential phase function, and (b,c) show their integral. Images (a,c) originate from correctly sampled datasets, while images (b,d) originate from under-sampled datasets. The stripe artefacts, which are a result of the under-sampling, are indicated by the red arrow.

data (planar *and* CT) were generated (simulated *and* experimentally acquired) with a very high number of dithering steps, from which quantitative values were extracted. These were used as reference values. The highly dithered datasets were then sub-sampled by factors of 2^n, with n ranging from 1 to $\log_2(N_{dither})$ (note that a sub-sampling factor of $n = \log_2(N_{dither})$ corresponds to not applying dithering at all). The number 2^n also determines how many possible sub-sampled datasets exist (for example, there are four different possibilities to sub-sample by a factor of four). The possibilities for sub-sampling mimic different locations of the sampling points. All possibilities were taken into account and *sets* of quantitative results were extracted for every sub-sampling factor (in the exemplary case of a sub-sampling factor of four, sets of four values were extracted). In order

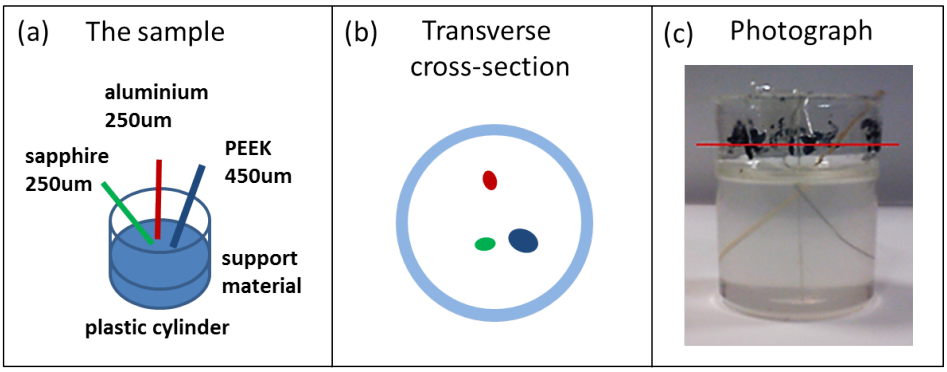

Figure 6.3: The phantom used for the planar and tomographic sampling experiments: a schematic (a), a transverse cross-section (b) and a photograph (view from side) (c).

to assess the ambiguity of the extracted quantitative values caused by the multiple possibilities to sub-sample, the minima, maxima and mean values of these sets were determined and plotted against the number of dithering steps. The number of dithering steps is inversely proportional to the sub-sampling factor (e.g. sub-sampling by a factor of four corresponds to $N_{dither}/4$ dithering steps). Finally, the number of dithering steps for which minimum, maximum and mean values overlapped was assumed to be the "optimal" one, since no ambiguity is present. This also implies that the same quantitative results would be obtained for a higher number of dithering steps.

Planar EI data generation: Projections were simulated/experimentally acquired on both slopes of the IC. On each slope, 128 dithering steps ($N_{dither} = 128$) were simulated/acquired and recombined to form a single, high resolution projection. This high number of dithering steps was chosen because the corresponding sampling step (0.52 μm) is much smaller than the projected source focal spot size ($\approx$ 17 μm), which justifies the assumption that the chosen number of steps would lead to correctly sampled data. From the two dithered projections, the derivative of the phase function was extracted via phase retrieval, this was then integrated to obtain the phase function itself. For each wire in the phantom, the maximum of the phase function was extracted. From this value, the RID can be calculated

via a division by the wire diameter. However, this division was omitted, as it was not crucial for the analysis and, moreover, the wires' nominal diameters as specified by the manufacturer are not granted to be strictly accurate. Consequently, we retrieved values of $\delta \cdot T$ rather than δ, where T stands for the wire thickness. Next, the dithered projections were successively sub-sampled as explained above. For each factor of sub-sampling 2^n a set of values $(\delta \cdot T)_1$, ..., $(\delta \cdot T)_{2^n}$ was retrieved for each wire. Finally, the maximum, minimum and mean values of these sets were determined and plotted against the respective number of dithering steps.

The simulated data were generated with the program developed by Vittoria et al. [2013], and the experimental data were acquired with the coded aperture EI scanner described in chapter 4.6. The source was operated at 25 mA and 35 kV, corresponding to a spectrum with a mean energy of 18 keV (see figure 5.9). The energy for the simulation was therefore set to 18 keV. The working points corresponding to the two slopes of the IC were chosen as $|\xi_1| = |\xi_2| = 8$ μm for both simulation and experiment. The exposure time for each acquired projection was 5 s. Gain and offset corrections were applied prior to the further processing.

EI-CT data generation: Projections over a total angular range of 180 degrees were simulated/experimentally acquired with an angular step of 1 degree. Please note that angular step size was not optimised for resolution as prescribed by equation 6.1. At every rotation angle, data was simulated/acquired on both slopes of the IC, involving 32 dithering steps ($N_{dither} = 32$) on each slope. A reference number of dithering steps smaller than in the planar case was chosen due to constraints on computation and scan time. However, the corresponding sampling step (2.09 μm) is still much smaller than the projected source size. The dithering steps were combined, and sinograms for the transverse object slices were created. The sinograms corresponding to the two slopes of the IC were processed with the phase retrieval method, yielding sinograms containing the first derivative of the phase function. These were given as input to the FBP with the Hilbert filter, yielding RID maps of the phantom. A single transverse slice was then selected, in which wire specific ROIs were defined. For each wire, a final δ-value was extracted by averaging over the respective ROI. As in the planar case, the dithered projections were then successively sub-sampled, and the

reconstruction of the RID map and the extraction of δ-values was repeated for each factor of sub-sampling. Again, for each factor of sub-sampling 2^n a set of values δ_1, ..., δ_{2^n} was retrieved for each wire. The maximum, minimum and mean values of these sets were determined and plotted against the respective number of dithering steps.

The simulation was performed using the method described in chapter 4.5, and the experimental data were acquired with the scanner described in chapter 4.6. Again, the source was operated at 35 kV and 25 mA, and the energy for the simulation was chosen to be 18 keV. The working points corresponding to the two slopes of the IC were again chosen as $|\xi_1| = |\xi_2| = 8$ μm for simulation and experiment. The exposure time for each experimentally acquired projection was only 3 s in this case. Again, the projections were corrected for detector gain and offset prior to the processing.

Finally, we performed an EI-CT scan of a domestic wasp under the same experimental conditions as stated above. The finely sampled data (with 32 dithering steps) was used to reconstruct a map showing the RID within the insect. Next, the projections were sub-sampled by a factor of 16 (corresponding to only 2 dithering steps), and the RID map was reconstructed again. The RIDs present in the map resulting from the densely sampled data were compared to those originating from the coarsely sampled data.

Results and Discussion

Results for planar EI: The generated (simulated and experimentally acquired) planar EI data and the results of the analysis are shown in figure 6.4. Figures (a-c) and (e-g) correspond to data sampled with 128 dithering steps. The plots in (a) and (e) show the EI projections of a cross-section of the wire phantom generated on both slopes of the IC. The high signal at the edges is due to the cylinder, and the three pairs of sharp peaks in the centre are due to the three wires. The material of the wires is explicitly indicated in panel 6.4 (c). Note that the phase contrast (the fringes at the edges of the wires and the cylinder) is inverted in the two profiles in (a) and (e), whereas the absorption contrast remains the same, as expected. A comparison of the profiles in (a) and (e) reveals a good match

between simulation and experiment, with the only difference being that phase contrast fringes are slightly larger in the simulated profiles. This is explained by the fact that the simulation was performed at 18 keV, while the effective energy for phase effects is slightly higher, implying smaller values of the RID. The plots in (b) and (f) show the derivatives of the phase functions that were extracted from the profiles in (a) and (e) via phase retrieval. Again, there is a good agreement between the shapes of the simulated and experimental profiles. The plots in (c) and (g) show the phase functions, which were obtained via the integration of the profiles in (b) and (f). The aluminium wire appears to be thicker in the simulated profile than in the experimental one, while a better match is obtained for the other wires. This is because the thickness of the wires is not only affected by their diameter, but also by their inclination with respect to the x-ray propagation direction. We believe that, during the design of the numerical phantom, the inclination of the aluminium wire was slightly over-estimated.

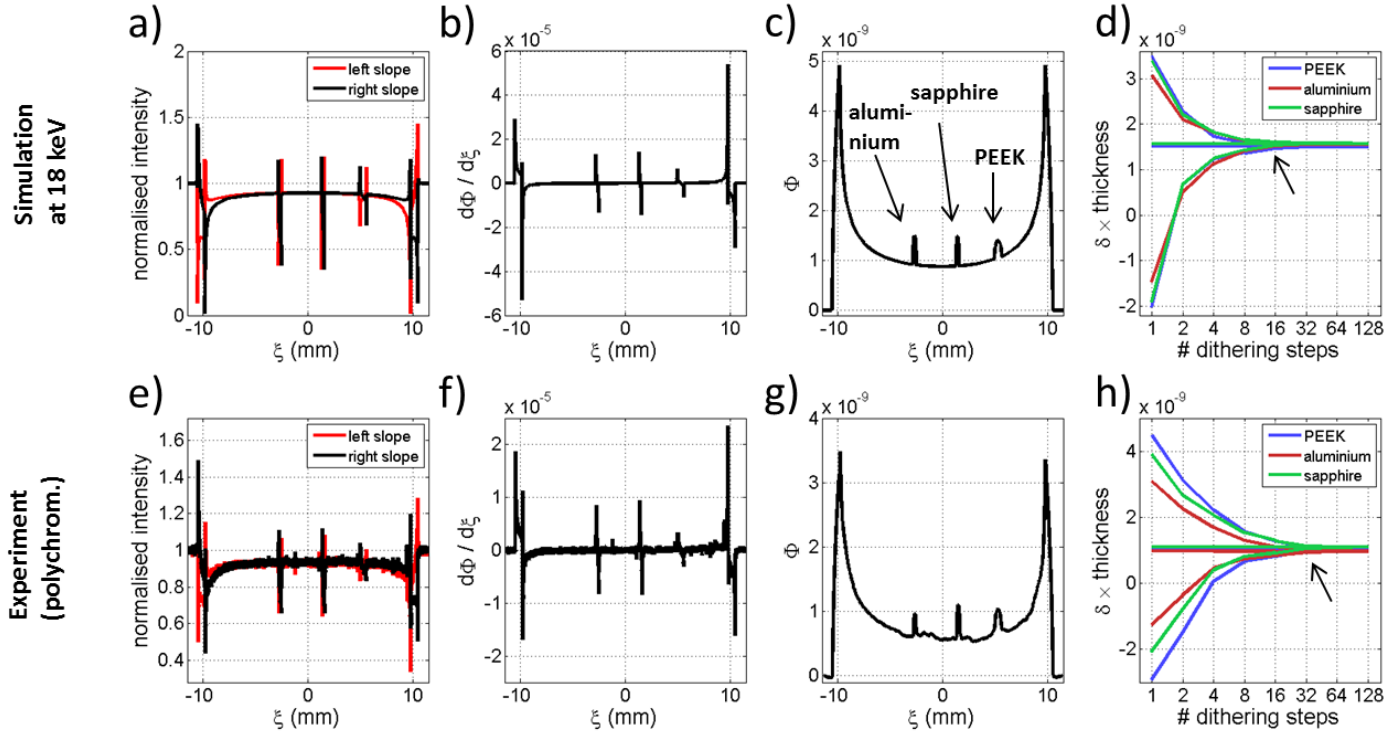

Figure 6.4: Results obtained from the planar EI simulation (top row) and experiment (bottom row): (a,e) show simulated/experimental profiles of the phantom acquired with 128 dithering steps on the two slopes of the illumination curve, (b,f) shows the corresponding differential phase function obtained through the phase retrieval method, and (c,g) show the phase function after integration. Plots (d,h) show the results of the analysis (see text): the maximum, minimum and mean values of the retrievable sets of $\delta \cdot T$ are plotted against the respective number of dithering steps.

The plots in (d) and (h) show the results of the analysis described above. Both plots contain three lines for each wire: the central lines, which are straight in both plots, describe the mean values of the sets $(\delta \cdot T)_1$, ..., $(\delta \cdot T)_{2^n}$ retrieved for each sub-sampling factor 2^n, and the top and bottom lines describe their maximum and minimum values. Although figure (h) shows experimental results, no error bars are attached to the lines since the plotted values were determined without averaging. Both the simulated and the experimental analysis plots show the same behaviour: for a low number of dithering steps the minimum and maximum values diverge significantly from the mean values, but progressively converge towards them with an increasing number of dithering steps. The large discrepancy between maximum and minimum values implies a large potential error in the retrieved $\delta \cdot T$-value. In particular, if no dithering (i.e. $\mathrm{N}_{dither} = 1$) is employed, the potential error can be larger than 200%, thus making material identification impossible. The large discrepancy also demonstrates the dependence of the retrieved $\delta \cdot T$-value on the location of the sampling points. While the number of dithering steps can be chosen in advance, the actual sampling locations depend on where the object is placed with respect to the separate beamlets in the coded aperture EI setup. This is impossible to control, especially for an unknown sample.

The correct $\delta \cdot T$-values are provided by the mean values in the plots, which are the same for all numbers of dithering steps, including the reference ($N_{dither} = 128$). The mean values for the three wires in the simulated data overlap, as the thickness of cylinder and wires in the numerical phantom may not exactly have matched those in the real one. The number of dithering steps for which maximum, minimum and mean values are the same was defined as "optimal". The convergence of the three lines for all wires in the simulated and experimental analysis plots clearly indicate that an optimal number of dithering steps exists. The simulated data suggests that this number is 16, while the experimental data suggests that it is 32 (see arrows in figures 6.4 (d,h)). We believe that the higher number suggested by the experimental data is due to noise and other errors, and that the optimal number of dithering steps is indeed 16. This theory is supported by two facts: first, the maximum and minimum values in the experimental plot are very close to the mean value also at 16 steps. Second, the sampling step

that corresponds to 16 steps is approximately 4.2 micrometres. This value is still relatively small compared to the projected source size. However, we also need to consider that the width of the beamlets poses an intrinsic limit on the highest frequency that will be present in the signal. The beamlets are shaped by the apertures in the sample mask to a width of 12 μm. Optimal sampling in the Nyquist-Shannon sense requires a sampling rate that is inversely proportional to twice the highest frequency in the signal, which implies an "optimal" sampling step of approximately 6 μm, which is very similar to that one corresponding to 16 dithering steps.

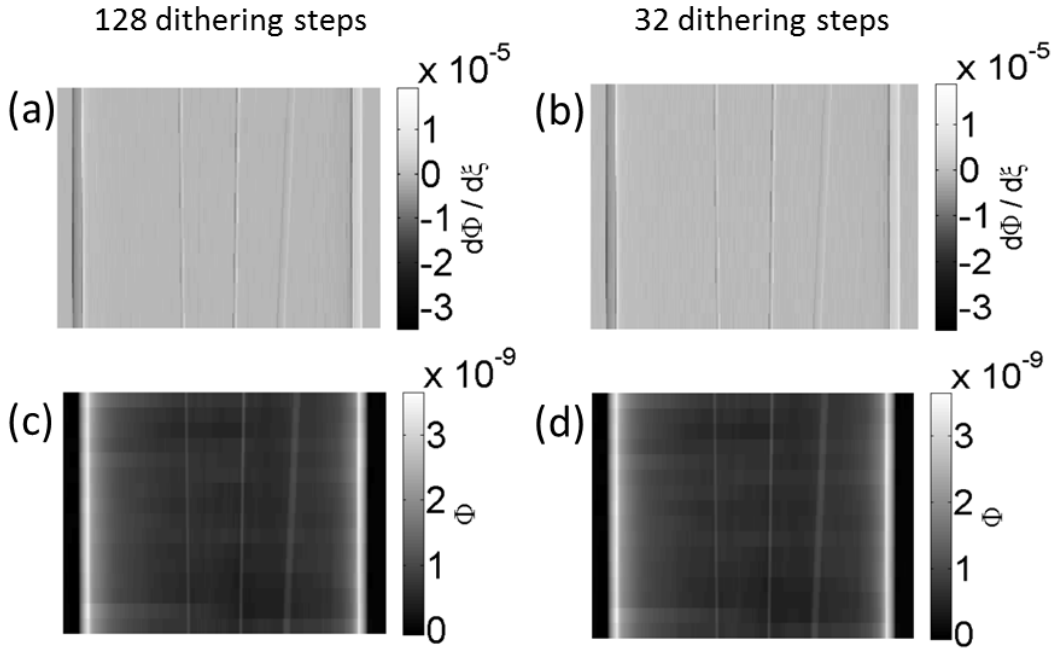

Figure 6.5: Planar experimental EI images of the phantom showing the differential phase function (top row), and the phase function after integration (bottom row). The differential phase function images were extracted from datasets acquired with 128 (a,c) and 32 (b,d) dithering steps.

The images in figure 6.5 show experimentally acquired projections of the phantom. The cylinder walls at both sides and the three wires in the centre are clearly identifiable. The images in (a,b) show the first derivative of the phase function,

and the images in (c,d) show their integral (i.e. the phase function). The images on the left (a,c) result from a dataset acquired with 128 dithering steps, while the images on the right (b,d) result from a dataset acquired with 32 dithering steps. It is easy to note that both sets of images look identical, and that no stripe artefacts along the integration trajectories are present. Moreover, the colour bars are the same, too, which implies that the same quantitative meaning can be extracted. These observations are in agreement with the results from the experimental analysis plot shown in figure 6.4 (h).

Results for EI-CT: The generated (simulated and experimentally acquired) EI-CT data and results of the analysis are shown in figure 6.6. The images in (a,c) show transverse slices of the RID, reconstructed from datasets generated with 32 dithering steps. Please note that the grey scale in the slice originating from the simulated data refers to the δ-values of the materials at 18 keV, whereas that in the slice originating from the experiment refers to values corresponding to effective energies (approximately 21 keV). These images reveal that the size of the cylinder wall was slightly under-estimated in the numerical phantom compared to the real one. The overall similarity between the simulated and experimental slices demonstrates that the CT extension of the EI simulation described in chapter 4.5 works well. The background in the experimental slice was subtracted, which had the positive effect that minor ring artefacts were removed.

The plots in (b) and (d) provide the results of the analysis described above. Again, the minimum, maximum and mean values of the sets of retrievable δ-values are plotted against the respective number of dithering steps. The reference number of dithering steps was 32. In this case, error bars were added to the lines, as the plotted values are the result of averaging over wire-specific ROIs. The sizes of the error bars correspond to one standard deviation. The lines describing the mean values are straight for all three wires in both simulated and experimental analysis plots, indicating that the corresponding δ-values are the "correct" ones, i.e. those that would be obtained with a sufficiently high number of dithering steps. It should be observed that the mean values in the simulation analysis plot correspond to δ-values which are very close to the nominal ones for the wires at 18 keV (see table 5.3). The nominal values of aluminium and sapphire are slightly

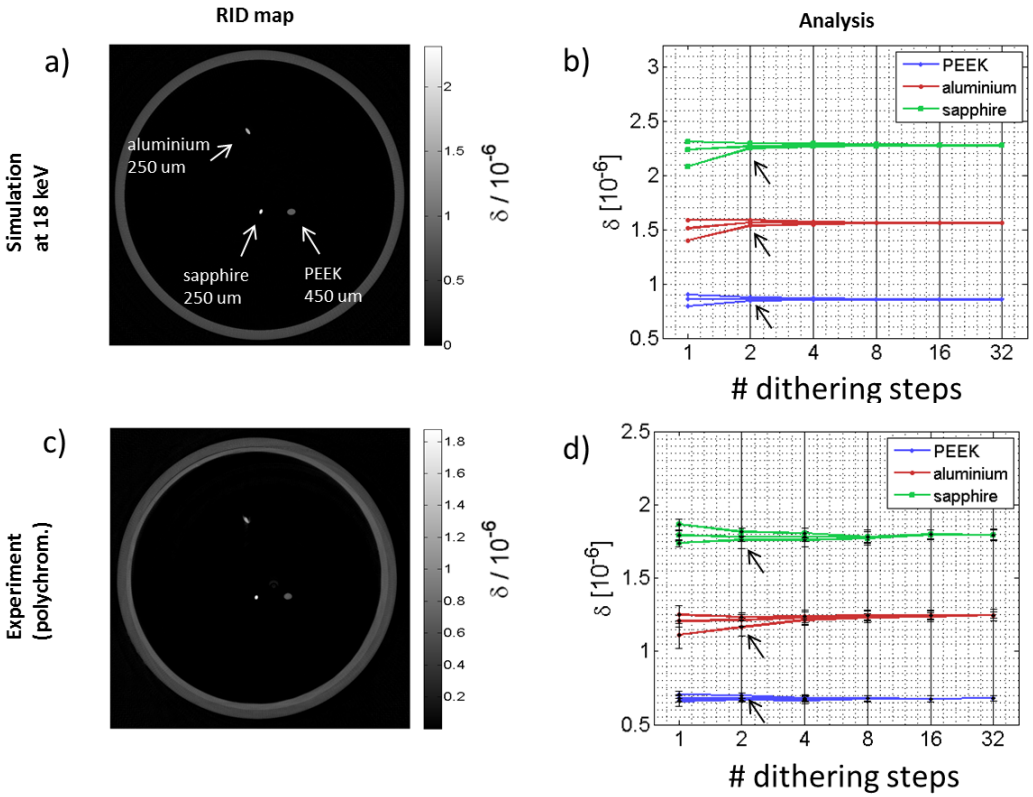

Figure 6.6: Results obtained from the EI-CT simulation (top row) and experiment (bottom row): (a,c) show reconstructed RID maps from simulated and experimental data acquired with 32 dithering steps. Plots (b,d) show the results of the analysis (see text): the maximum, minimum and mean values of the retrievable sets of δ are plotted against the respective number of dithering steps.

under-estimated, which, as explained in chapter 5.2.2, is due to photon loss at the edges of the wires. The mean lines in the experimental analysis plot correspond to δ-values which are very close to those retrieved for PEEK, aluminium and sapphire in chapter 5.2.2. This shows that the process of RID retrieval from EI-CT measurements is repeatable which supports its reliability.

The first feature that should be noticed in the CT analysis plots is that, although the lines describing maximum, minimum and mean values diverge for a low number of dithering steps, the discrepancy is significantly smaller than in the planar case. In fact, the worst possible error in the retrieval of δ occurs if only

one dithering step is used, and is smaller than 10% for all three wires. Moreover, the three lines converge very quickly, such that the optimal number of dithering steps can be determined to be two. Also in this case, the experimental analysis suggests a slightly higher number (four dithering steps), which, again, we believe is due to errors in the data. This notwithstanding, also in the experimental case, the difference between maximum, minimum and mean values is very small already for two dithering steps, which leads us to conclude that the optimal number of dithering steps is indeed two.

In summary, the analysis plots in figures 6.4 and 6.6 demonstrate that accurate quantitative determination of the RID (within the limits of the imaging system, see chapter 5.2.2) can be achieved from EI-CT measurements with only two dithering steps at each angle, while, in a planar scan, at least 16 dithering steps are required. If small errors in the retrieved δ-values can be tolerated, dithering in EI-CT is not required at all. This leads to the conclusion that dithering does not affect the quantitative meaning of the reconstructed slices in CT, while it crucially affects it in planar imaging. At the same time, also in CT, dithering can be used as a means to increase the spatial resolution. However, the obtained results demonstrate that dithering is *not* mandatory, which means that the number of dithering steps (including "1", i.e. no dithering) can be chosen according to the application. For example, if an enhanced resolution is not required, the CT scan can be performed without dithering. As stated above, the less dithering steps used in the projections, the less angular views are required to optimise the resolution in the reconstructed images. Being able to avoid dithering can therefore drastically reduce the overall scan time, and, most importantly, the delivered dose. This therefore enables the user to trade-off resolution and dose, while still achieving an artefact-free reconstruction containing accurate quantitative information.

This conclusion is supported by the images of the wire phantom in figure 6.7. The image in (a) shows a transverse slice of the RID map reconstructed from experimental EI-CT data acquired with 32 dithering steps. The image in (b) shows the same transverse slice reconstructed from data acquired with only two dithering steps. Visually, the two slices are identical, which is confirmed by

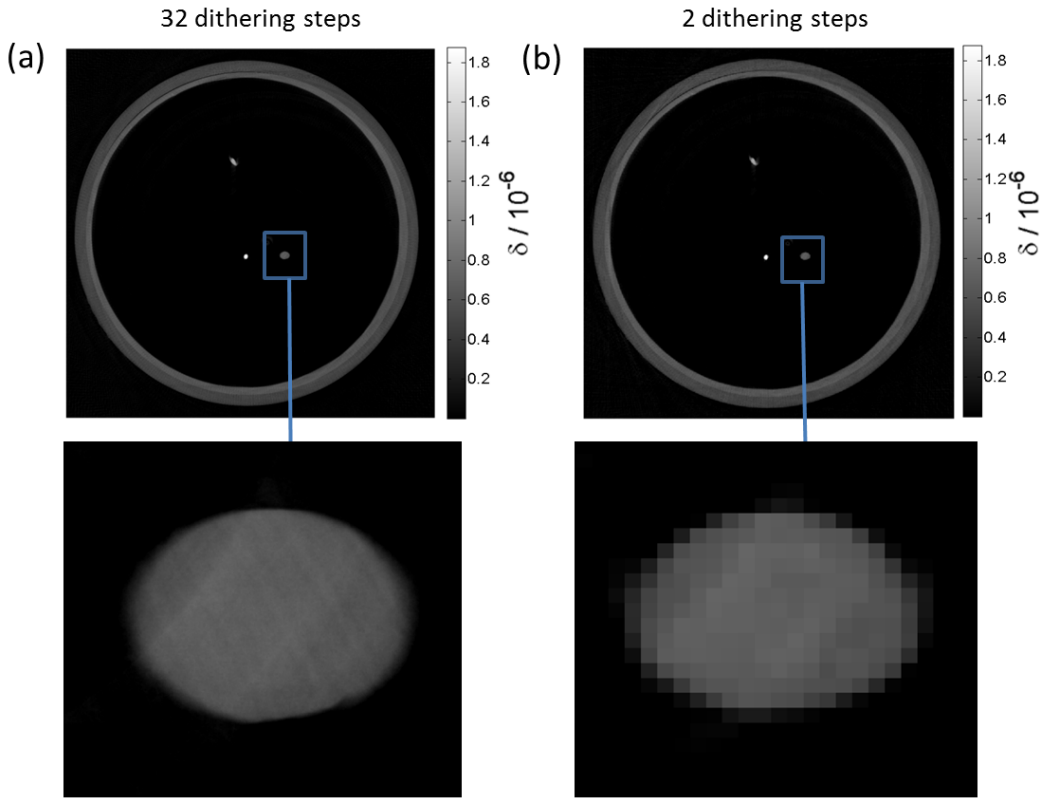

Figure 6.7: RID maps of the phantom, reconstructed from EI-CT datasets acquired with 32 (a) and 2 (b) dithering steps. The zoomed ROIs show the PEEK wire.

the matching grey scales, implying identical quantitative values. A zoom of the PEEK wire reveals that the only difference between the two images is resolution, which in (a) is higher due to the larger number of dithering steps.

The fact that in EI-CT one or two dithering steps are sufficient to extract unambiguous quantitative information, while in planar EI a minimum number of 16 steps is needed, can be explained by means of probability theory. As mentioned above, the location of the sampling points for the projections is effectively random, as it depends on the relative position between object and beamlets. Every value in the sets $(\delta \cdot T)_1$, ..., $(\delta \cdot T)_{2^n}$ (or respectively δ_1, ..., δ_{2^n} when divided

by T) is associated with a specific location of the sampling points. It can be sensibly assumed that this location follows a uniform probability distribution.

In the framework of probability theory (see e.g. Klebaner [2005]), a planar EI acquisition with a given number of dithering steps can be considered to be a "sampling experiment", in which the outcome is determined by the location of the sampling points. Consequently, an EI-CT acquisition can be considered to be a "sequence of sampling experiments", the length of which is determined by the number of angles (N). A probability space $(\Omega, \mathcal{E}, P)$ can be defined for an individual "sampling experiment", consisting of: 1. the sample space $\Omega = [\delta_{min} \cdot T, \delta_{max} \cdot T]$, which is the set of all possible outcomes, 2. the set of events $\mathcal{E}$, where each event includes one or several outcomes (chosen to be the Borel sets on Ω, which is a standard procedure in probability theory (Klebaner [2005])), 3. the probability measure P, given by $P = 1/|\Omega|$, which assigns a probability to each event. $|\Omega|$ is the number of possible outcomes. We also define a random variable X, to describe a particular outcome. In the above, the shortening notation $P(X = \omega) = P$ was used. The symbol ω denotes an element of Ω.

With regards to predicting the outcome of the CT scan, it is worthwhile to note that, during the reconstruction procedure, the back-projected values are summed and divided by the number of angles (represented in equation 2.4 for the case of non-discrete data by the integral and the division by π). Consequently, it is sensible to model the outcome of the CT scan as the average outcome of the individual experiments. For a CT scan with N rotation angles, the outcome can be described by the random variable:

$$S_N = \frac{1}{N} \sum_{k=1}^{N} X. \tag{6.2}$$

The corresponding probability space $(\Omega, \mathcal{E}, P_N)$ contains the same sample space and set of events as above. The probability distribution for S_1 is given by $P_1 = 1/|\Omega|$, as in this case, the CT scan is the same as an individual sampling experiment. Since the individual experiments are independent from each other, the probability distribution for S_N with $N > 1$ is given by:

$$P_N = P_{N-1} \star P_1. \tag{6.3}$$

(Klebaner [2005]).

For a better illustration, this theory was applied to the experimentally acquired planar and EI-CT datasets of the wire phantom, in particular, to the PEEK wire. The planar analysis plot (figure 6.4 (h)) states that, if no dithering is applied, the extractable quantitative values lie between $\delta_{min} \cdot T = -2.9 \cdot 10^{-9}$ and $\delta_{max} \cdot T = 4.5 \cdot 10^{-9}$. Therefore, the sample space of the probability model is $\Omega = [-2.9 \cdot 10^{-9}, 4.5 \cdot 10^{-9}]$. Equation 6.3 was used to compute the probability distribution for a CT scan with 1, 25, 100, 180 and 360 rotation angles. The results are plotted in figure 6.8. The distribution for the first angle (red curve) is flat, which is easily explained considering that the first projection of the CT sequence is effectively equivalent to a planar experiment. The higher the number of angles in the CT, the more the corresponding probability distribution is peaked towards the mean value of Ω, which means that it becomes more likely to extract a quantitative value that is closer to this value (rather than to the minimum and maximum of the set of possible outcomes).

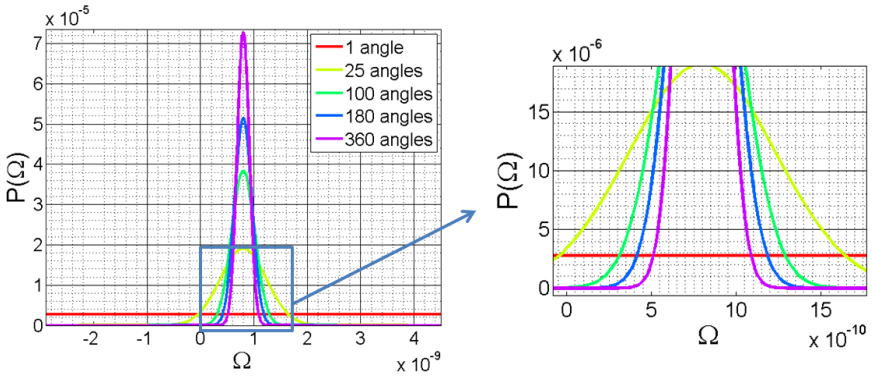

Figure 6.8: Plots of the probability distribution for PEEK, according to the theory described in the text. Different distributions are plotted for different numbers of angles.

We would like to remark that the used angular step of 1 degree is very coarse compared to the angular steps used by other groups that perform PC-CT. For example, the number of angles over a 180 degree range used for the scans described in Herzen et al. [2009], Zanette et al. [2012] and Tapfer et al. [2012] varies between 360 and 750. The presented probability model predicts that, if a higher number of angles was used in an EI-CT scan, the error interval for non-dithered acquisitions would be even narrower. Although this indicates the scope for higher quantitative accuracy in non-dithered EI-CT acquisitions, the small error interval achieved already with 180 angles provides a strong indication of our method for low-dose scans.

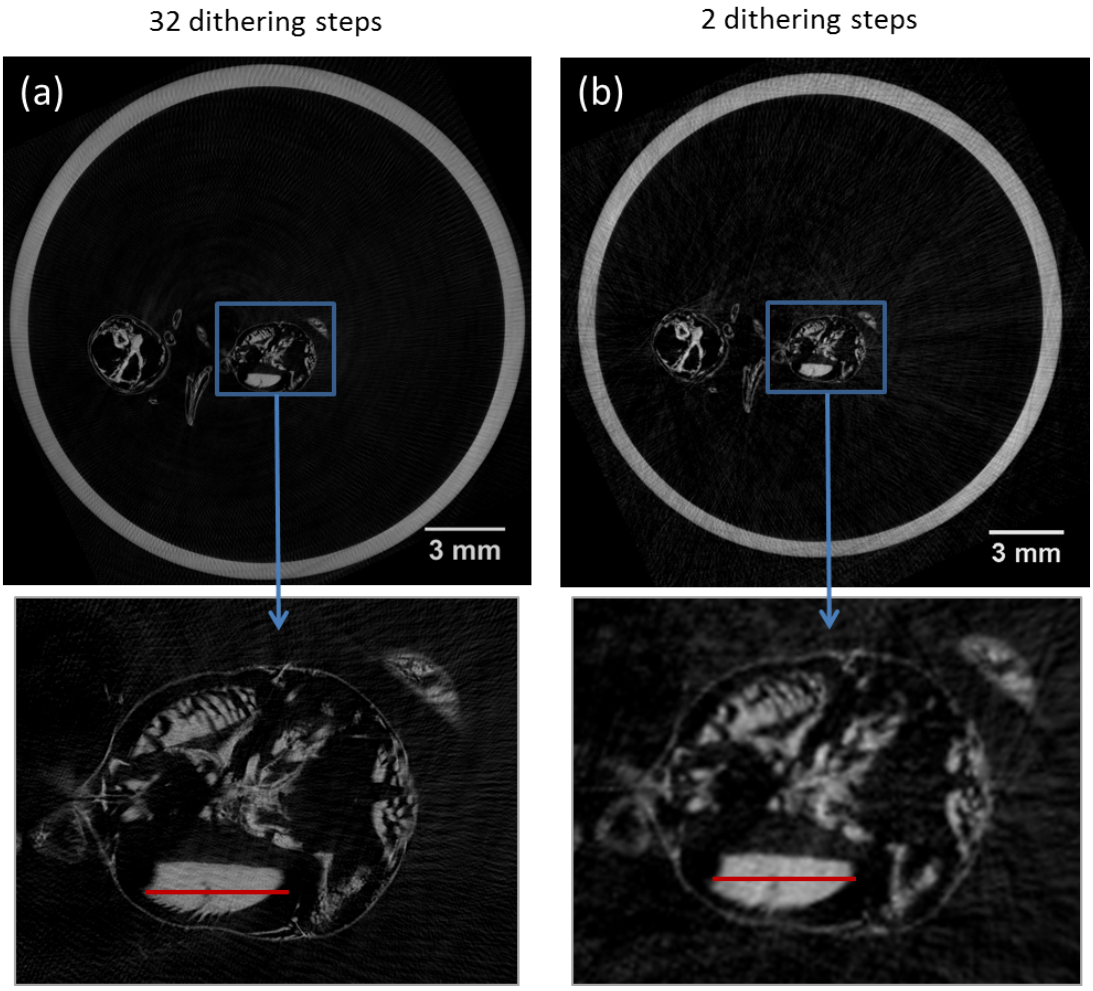

Figure 6.9: Transverse slices showing the RID of a domestic wasp, reconstructed from EI-CT datasets acquired with 32 (a) and 2 (b) dithering steps. Larger views of the indicated areas (the insect's head) are provided.

As a final test to validate the results of this chapter, an EI-CT scan of a domestic wasp was performed. Transverse slices extracted from the reconstructed 3D distribution of the RID are shown in figure 6.9. The transverse slice in (a) was obtained from data acquired with 32 dithering steps, while the slice in (b) originates from data acquired with only two dithering steps. A zoom of the wasp's head reveals that the only difference between the images in (a) and (b) is the lower resolution in (b). Profiles extracted along the indicated lines, plotted in figure

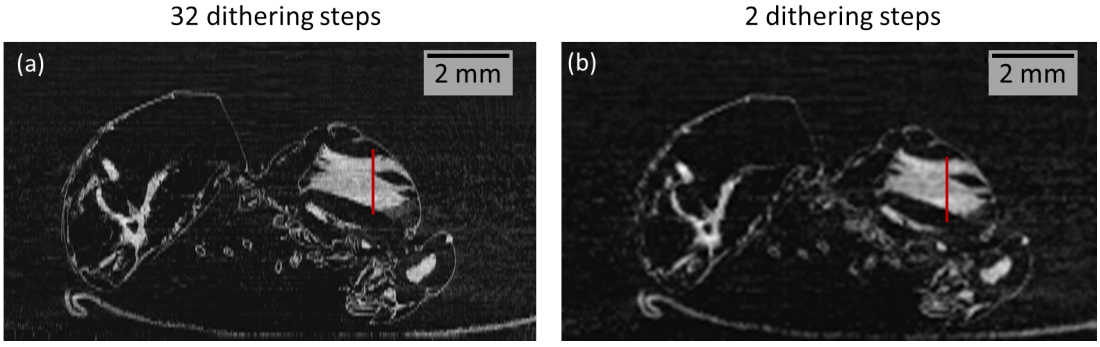

Figure 6.10: Coronal slices showing the RID of a domestic wasp, reconstructed from EI-CT datasets acquired with 32 (a) and 2 (b) dithering steps.

6.11 (a), confirm this observation: the profiles basically agree in their δ-values, but the one extracted from the 32 dithering steps slice (blue curve) shows smaller features than the one obtained with two dithering steps (red curve).

Coronal slices extracted from the same 3D volumes are shown in figure 6.10. They provide a better representation of the entire body of the wasp. Again, the slices in (a) and (b) originate from data acquired with 32 and two dithering steps, respectively. The profiles extracted across the insect's thorax along the lines indicated in figure 6.10 are shown in figure 6.11 (b). The first observation is that again the δ-values in the two curves agree well. Unlike the profiles extracted from the transverse slices, the profiles in (b) have the same resolution. The reason is that dithering enhances the resolution in the direction of phase sensitivity only, which, in the case of the used coded aperture EI-CT scanner, is the horizontal one: the transverse plane coincides with this direction, but the coronal one does not. In the coronal slices, the difference in resolution between (a) and (b) is therefore only present in the horizontal direction, but not in the vertical one, along which the profiles were extracted.

To summarise, we demonstrated that, in planar EI imaging, a high number of dithering steps is required to obtain artefact-free and quantitatively correct images. On the contrary, when CT is performed, two dithering steps are sufficient to reconstruct slices of the RID which are free of errors due to under-sampling, and that no dithering at all is required if small errors can be tolerated. This im-

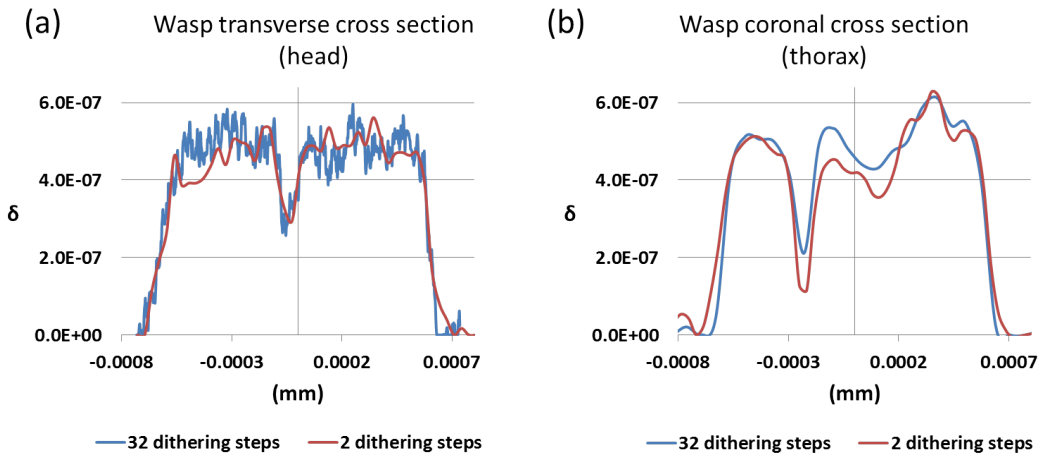

Figure 6.11: Profile plots extracted along the indicated lines in figures 6.9 (a) and 6.10 (b). The profiles originate from datasets acquired with 32 (blue curves) and 2 (red curves) dithering steps.

plies that, unlike in planar imaging, in EI-CT dithering is simply needed if there are significant requirements to increase the spatial resolution. As a consequence, object-specific optimised sampling schemes can be determined. If the imaged object does not require an enhanced resolution, the optimal scheme would be a non-dithered acquisition coupled with an appropriate number of angular projections (see equation 6.1). Conversely, if very fine details need to be resolved, the number of dithering steps can be determined accordingly and the corresponding number of angular projections chosen.

6.3 Dose Estimate for Small Animal Imaging Applications

X-ray dosimetry plays an important role in *in vivo* imaging. Dose figures that are considered acceptable vary among the irradiated tissue types, and are often determined on the basis of a risk-benefit trade-off. In small animal imaging, the boundaries for acceptable doses are far less tight than for humans, and often increased doses are delivered to optimise image quality. However, excessive dose

delivery can bias long-term studies and even kill the animal. Therefore, studies (e.g. Guldberg et al. [2004]) suggest that dose in small animal imaging should not exceed 400 milligray (mGy) per scan. Typical doses delivered during mouse imaging using microCT scanners lie between 100 and 300 mGy (Zhou and Boone [2008]).

In this sub-chapter, we will discuss the estimation of the dose delivered during a scan using the coded aperture EI-CT scanner described in chapter 4.6. We will provide an estimate of the absorbed dose, which is a measure of the concentration of energy released within a specific object, defined as deposited energy per unit mass ($D_{object} \sim [J/kg] = [Gy]$). It should be noted that the absorbed dose is not equal to the total energy absorbed by the object (integral dose), nor is it an estimate of the cancer risk to the organism (effective dose). These quantities can, however, be computed from the absorbed dose by integration over the irradiated volume, and by taking into account tissue-specific weighting factors, respectively. Since absorbed dose is an object-specific quantity, it will be estimated for the special case of small animal imaging, mouse imaging in particular. This stems from the consideration that small animal imaging is one of the most promising applications of a laboratory-based EI-CT scanner (see chapter 3.2). For simplicity's sake, we modelled the mouse as a water filled cylinder with a 2 cm diameter. Water is considered tissue equivalent and thus is frequently used as a phantom material. Although the simple cylinder model does not take into account the complex anatomy of a mouse, it is sufficient to obtain a reasonable estimate for the absorbed dose (Zhou and Boone [2008]).

In CT, the standard measure for the absorbed dose during a scan is the Computed Tomography Dose Index (CTDI) (Dixon et al. [2010]). Zhou and Boone [2008] provide the following definition of the CTDI for a homogeneous cylinder of diameter d and infinite length:

$$\mathrm{CTDI} := \frac{1}{m} \cdot \int_{-\infty}^{\infty} E(\eta)\ d\eta, \tag{6.4}$$

where $m = \rho h \pi (d/2)^2$ is the mass of the irradiated part of the cylinder. For the considered coded aperture EI-CT scanner, $h = 5$ cm, as this is the vertical

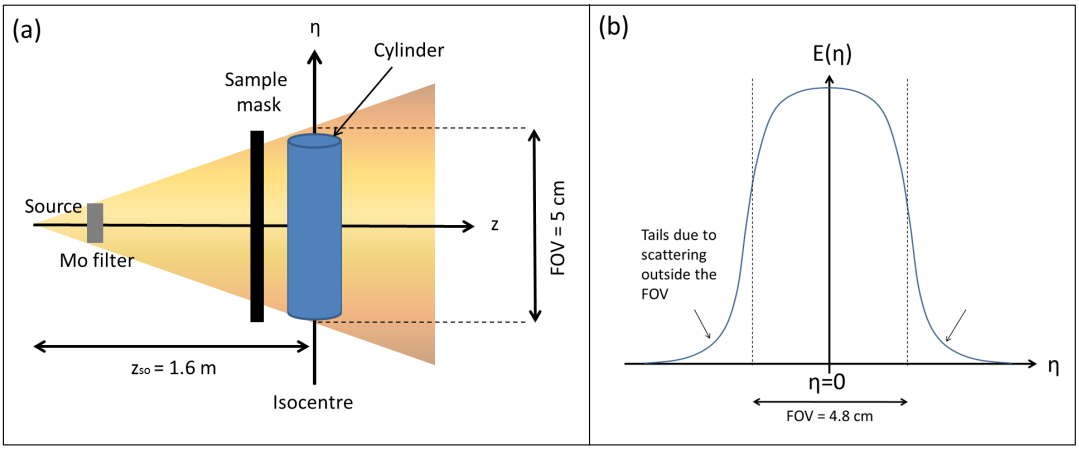

Figure 6.12: (a) Frame of reference for the described dose calculations. (b) Typical profile of the energy E_η deposited along the isocentre for a homogeneous cylinder.

dimension of the FOV. The function $E(\eta)$ refers to the energy deposited along the isocentre of the scanner, which coincides with the AOR. The isocentre is indicated in the schematic in figure 6.12 (a), and a typical distribution of the deposited energy $E(\eta)$ for a cylinder is shown in figure 6.12 (b). Please note that some energy is deposited in areas outside the FOV due to scattering, and that the integration from minus to plus infinity in equation 6.4 takes these tails into account. The CTDI as a measure for absorbed dose was originally established for third generation CT scanners, in which laminar beams are used to irradiate only one object slice at a time, and object translation is required to acquire data corresponding to different slices. The irradiation of a single slice delivers dose also to the adjacent slices due to scattering. When the object is scanned through the laminar beam, this "extra" dose is accumulated, which is accounted for by integrating the tails in figure 6.12 (b). More recently, cone beam CT scanners with a FOV large enough to image an entire region of interest without the need to scan have entered clinical practice. In this case, the energy deposited by scattering outside the FOV does not contribute to the absorbed dose. Strictly speaking, the CTDI as defined above is therefore not suited as a measure of the absorbed dose delivered by a cone beam CT system. Nevertheless, it can be used

to derive an upper bound for the absorbed dose, since including also the energy deposited outside the FOV leads to a slight over-estimation (McCollough et al. [2011]).

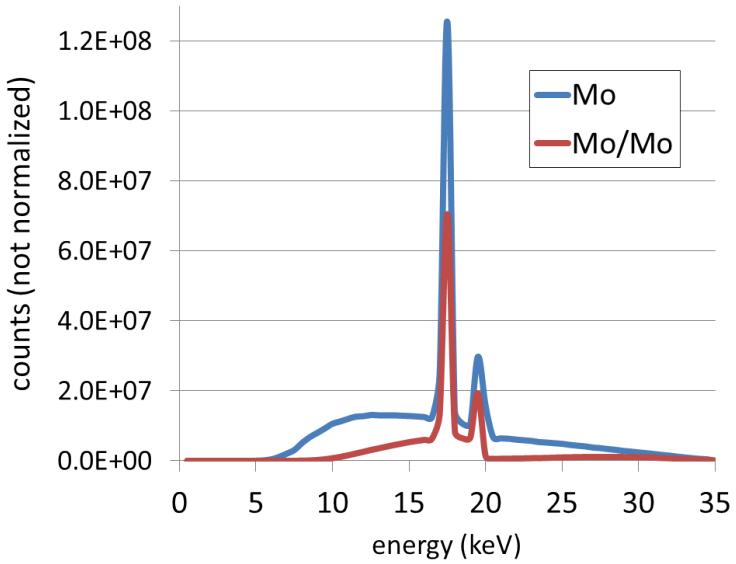

Figure 6.13: The spectrum of the molybdenum source at 35 kV: unfiltred (blue curve) and with 30 μm molybdenum filtration (red curve).

The FOV in the coded aperture EI-CT scanner is sufficiently large to fit a young mouse. Therefore, we assume the homogeneous cylinder representing the animal to be 5 cm in height. As this height is the same as the FOV, no energy due to scattering will be deposited outside it, and consequently, the CTDI will yield a slight over-estimation of the absorbed dose.

The CDTI can be measured directly; however, this requires a suitable device, typically a long pencil ion chamber placed at the scanner's isocentre. The pencil chamber has to be located *inside* the object of interest, which often makes the measurement difficult to realise in practice. Another option is to measure the air kerma ($K_{air} \sim$ [Gy]) at the isocentre, and to calculate the CTDI according to the formula:

$$\text{CTDI} = f_c \cdot K_{air}, \tag{6.5}$$

where f_c is a conversion factor that depends on the object (material and geometry) and on the x-ray energy. The factor f_c can be determined by simulating the interaction of x-rays with matter, which requires Monte Carlo modelling methods and goes beyond the scope of this thesis. However, the conversion factors for a water-filled cylinder with a diameter of 2 cm were determined for a range of monochromatic beam energies (6-140 keV, with an interval of 1 keV) by Zhou and Boone [2008]. These conversion factors are expressed in mGy / 10^6 photons per mm^2. For their Monte Carlo simulation, the authors assumed a source-to-isocentre distance (SIC) of 0.53 m, which is significantly shorter than for the coded aperture EI scanner ($z_{od} \approx 1.6$ m). However, the authors emphasize that the effect of the SIC on the conversion factors is negligible. The authors determined the conversion factors for FOV heights of 1 cm, 10 cm and 100 cm, hence we obtained the conversion factors for a FOV height of 5 cm by means of an exponential fit. These data are provided in table 6.1, alongside the original ones by Zhou and Boone.

The polychromatic conversion factor required for the molydenum target x-ray tube used in the coded aperture EI-CT scanner can be computed as a spectrally weighted average of the monochromatic ones. To match the assumptions of Zhou and Boone [2008], the source spectrum needed to be normalized to 10^6 photons per mm^2. For biological applications, in particular small animal imaging, a filter is added to the source in order to remove the low energy photons from the beam. We used a 30 μm thick molybdenum filter, which resulted in the spectrum shown in figure 6.13 (red curve). The use of all these parameters (Mo/Mo spectrum, cylinder model, monochromatic conversion factors listed for FOV height = 5 cm in table 6.1) yielded a polychromatic conversion factor $f_c = 1.553$.

Three thermoluminescent dosimeters (TLDs) were used to measure the absorbed dose to air ($D_{air} \sim$ [Gy]) at the isocentre of the coded aperture EI scanner. For the energy range of the molybdenum source, the quantities air kerma and absorbed dose to air are equivalent. The location of the TLDs for the dose mea-

Energy (keV)	FOV height: 1 cm	FOV height: 5 cm	FOV height: 10 cm	FOV height: 50 cm
5	0	0.0015	0.001553	0.001553
6	0	0.002163	0.002164	0.002164
7	0	0.0029	0.003018	0.003018
8	0	0.00406	0.004073	0.004073
9	0	0.0054	0.005284	0.005284
10	0	0.0064	0.006567	0.006567
11	0	0.0077	0.007873	0.007873
12	0	0.0091	0.009138	0.009138
13	0	0.0104	0.010423	0.010423
14	0	0.01170	0.011653	0.011653
15	0	0.0125	0.012797	0.012797
16	0	0.0137	0.013939	0.013939
17	0	0.0146	0.015	0.015001
18	0.0000114	0.016	0.016044	0.016045
19	0.000041	0.017	0.017006	0.01701
20	0.0000899	0.0173	0.017946	0.017956
21	0.000112	0.0178	0.018803	0.018825
22	0.000472	0.0188	0.019618	0.019657
23	0.000633	0.0193	0.020368	0.020435
24	0.000733	0.02	0.021072	0.021176
25	0.001187	0.0206	0.021732	0.021888
26	0.001445	0.0213	0.022319	0.022547
27	0.002085	0.0228	0.022841	0.023153
28	0.002391	0.0231	0.023292	0.023702
29	0.002482	0.0236	0.023705	0.024225
30	0.003159	0.0239	0.024036	0.02469
31	0.003545	0.0242	0.024341	0.025138
32	0.003933	0.0245	0.024584	0.02553
33	0.004085	0.02481	0.024825	0.025927
34	0.004776	0.02491	0.024948	0.026225
35	0.004937	0.025	0.02508	0.026524

Table 6.1: Monochromatic factors f_c for the conversion from air kerma to CTDI for a homogeneous water cylinder of 2 cm diameter, given in mGy / 10^6 photons per mm^2. The values for FOV height = 1, 10, 50 cm were obtained from Zhou and Boone [2008], and the value for FOV height = 5 cm was obtained from an exponential fit.

surements is shown in figure 6.14 (a). The TLDs were located behind an x-ray absorbing mask, which means that they were not irradiated uniformly (see figure

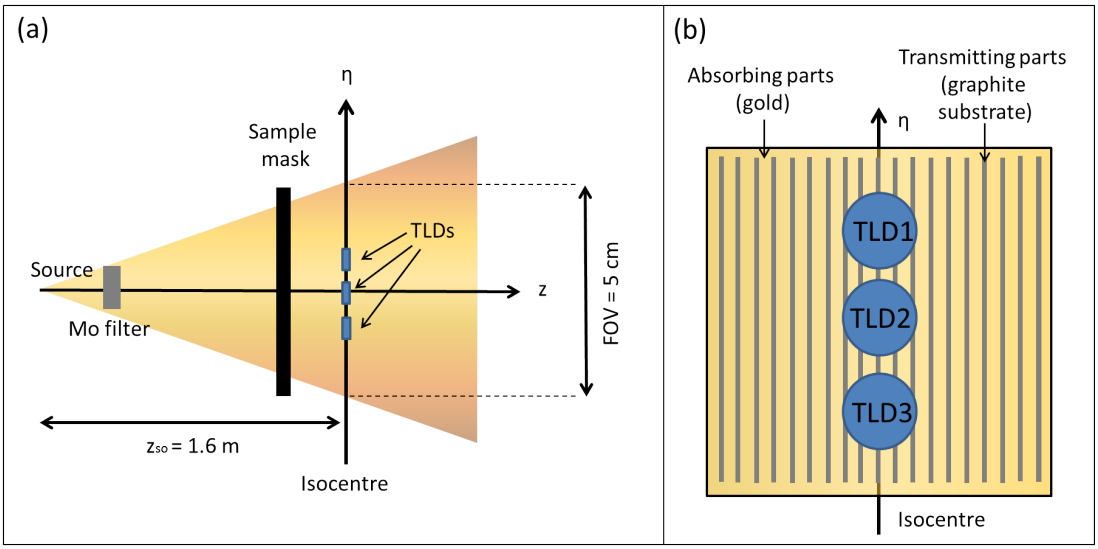

Figure 6.14: (a) Schematic showing the position of the TLDs in the imaging system. (b) Schematic showing the position of the TLDs behind the sample mask. The dimensions are not to scale.

6.14 (b)). This results in a difference between dosimetry in coded aperture EI imaging and conventional radiography. Absorbed dose is in principle a punctual quantity, but the absorbed dose in air behind the mask will vary strongly with position: areas shielded by the gold will receive a weak dose (some photons will pass through the mask as the one currently in use is slightly under-plated), while areas behind the apertures will receive a significantly higher dose. In that sense, the quantity measured by the TLDs is an "average of the absorbed dose to air over the surface of the TLD", and does not represent a punctual energy concentration. Nevertheless, these values can be considered representative, as eventually the rotation during the CT scan will average out contributions from weak and high doses. A more detailed assessment of the effect of the partial irradiation by the mask on the absorbed dose goes beyond the scope of this thesis, but will be considered in the future development of the EI method.

The three TLD readings acquired with 7 s exposure time (0.243 mGy, 0.282 mGy and 0.368 mGy) were normalised to 1 s exposure time and averaged, resulting in the single value $D_{air,1s} = 0.043$ mGy/s. This value represents the absorbed dose in air per second for a single projection. The total absorbed dose in air for

the entire CT scan can be determined via multiplication times the exposure time in seconds, the number of employed dithering steps, and the number of rotation angles (Dixon et al. [2010]). Eventually, the formula for the CTDI for the cylinder phantom can therefore be estimated by the formula:

$$\text{CTDI} = D_{air,1s} \times (\text{exposure time}) \times N_{dither} \times N_{angles} \times 2 \times f_c, \tag{6.6}$$

which provides an upper bound for the absorbed dose in the phantom. The factor of two is necessary for the current coded aperture EI scanner, since the fact that it is operated in horizontal sensitivity mode makes phase retrieval mandatory. Therefore, two complete CT datasets on both slopes of the IC are required. As an example, an EI-CT scan with two dithering steps, 180 angles and 3 s exposure per projection would result in CTDI $\approx$ 144 mGy. If no dithering was applied ($N_{dither} = 1$), the result would be CTDI $\approx$ 72 mGy. For these acquisition parameters, dose values are considerably below the acceptable bounds for small animal imaging, which leaves room for resolution enhancement (by increasing the number of dithering steps and angles) and noise reduction (by increasing the exposure time). In comparison to the "several Grays" delivered during a scan with the GI-CT small animal scanner (Tapfer et al. [2012]), the values derived for EI-CT are a significant improvement. This is an important result as it supports the suitability of a laboratory-based EI-CT scanner as a research tool for biomedical applications.

6.4 Low-Dose CT Images of Selected Biological Objects

In this section, we will present EI-CT images of two biological objects (a domestic wasp and an atherosclerotic plaque specimen) that were acquired without dithering and with 180 rotation angles over a 180 degree range. The exposure time for each projection was kept short (3 s); moreover, a 30 μm thick molybdenum sheet was used to filter out the low energies. Based on the results presented in

the previous sub-chapter, these settings should result in a low radiation dose; however, direct conclusions about the dose delivered to the wasp and the plaque specimen cannot be drawn as the previous calculations were restricted to the "mouse" geometry.

The aim of this section is to provide examples of laboratory based EI-CT imaging acquired with parameters resulting in the minimal delivered dose. The aim is not to show the best images the coded aperture EI-CT scanner can produce, but rather to demonstrate its potential under low-dose conditions. However, the images of the plaque specimen also demonstrate the superiority of PC-CT compared to absorption-based CT.

Atherosclerotic plaques are anatomic lesions forming on the inside of arterial walls. Plaques can be classified as non-vulnerable and vulnerable. Vulnerable plaques are those most likely to rupture, and to cause ischemic stroke or heart attack due to emboli preventing blood flow to parts of the brain or heart. Vulnerable plaques can also cause stenosis, which is a narrowing of the arterial lumen, due to frequent rupture and healing processes. Stenosis affects the blood circulation and can cause ischemic symptoms; moreover, the plaque forming the stenosis can itself rupture and lead to stroke and heart attack due to emboli. A plaque's likelihood to rupture has been linked to its morphology (Moreno [2010]). Plaques have various components (e.g. collagen, lipids, calcifications and intraplaque haemorrhage). A vulnerable plaque is typically characterised by a lipid-rich necrotic core contoured by a thin fibrous cap. The detection and characterisation of atherosclerotic plaques using conventional CT imaging is made difficult by poor soft-tissue contrast (Kasraie and Clarke [2012]). PC-CT was shown to be a potential alternative detection method (Hetterich et al. [2013]), in a study performed with a synchrotron implementation of GI-CT. The CT acquisitions involved a large number of angles (799-1199), which implies a high radiation dose as explicitly acknowledged by the authors.

We have recently started to look into this problem and we have imaged a plaque specimen with the laboratory-based EI-CT scanner under conditions leading to the minimal doses (molybdenum filter, no dithering, 180 angles). The aim was to obtain very preliminary results on whether or not it is possible to distin-

guish different components within the plaque. This preliminary study did not include cross-validation with histological results, and, therefore, it cannot yet be considered a definitive outcome. The imaged specimen originates from a stenosis in a human carotid artery and was removed from the patient via carotid endarterectomy. The specimen was fixed in a formalin solution. For imaging, the specimen was placed inside a tight plastic cylinder, which was mounted on the object stage of the scanner. The EI-CT imaging of the specimen was approved by the local ethics committee.

Both the wasp and the plaque specimen were imaged under the same conditions: the source was operated at 35 kV and 25 mA, all other scanning parameters were given above. At each rotation angle, projections were acquired on the two slopes of the IC. The image processing and CT reconstruction involved detector gain and offset corrections, phase retrieval, the generation of differential phase sinograms and the reconstruction of RID maps using the FBP with the Hilbert filter. For the plaque specimen, the extracted absorption sinograms were used to reconstruct a map of the absorption term using the FBP with the ramp filter. A low cut-off frequency was chosen for the latter to decrease the noise level in the reconstructed slices.

Image 6.15 (a) shows a coronal slice extracted from the reconstructed RID map of the wasp. In chapter 6.2 it was demonstrated that the optimal number of dithering steps, in terms of quantitative imaging, is two. In order to assess the effect of the omitted dithering and of the additional molybdenum filtration, we compared the image in 6.15 (a) to the one discussed in the previous chapter, which was obtained from data acquired with two dithering steps and without filtration. For ease of comparison, that image is shown again in figure 6.15 (b). As the coronal slices were extracted from two datasets acquired separately, they do not show identical cross-sections of the wasp; however, the slices were carefully selected to match as closely as possible. The zoom of the torso region in (a) reveals a slight blurring along the horizontal direction compared to the zoom of the same region in (b), which can be explained by the lower number of dithering steps. Besides the difference in resolution, the visual appearance of the two images is indeed very similar.

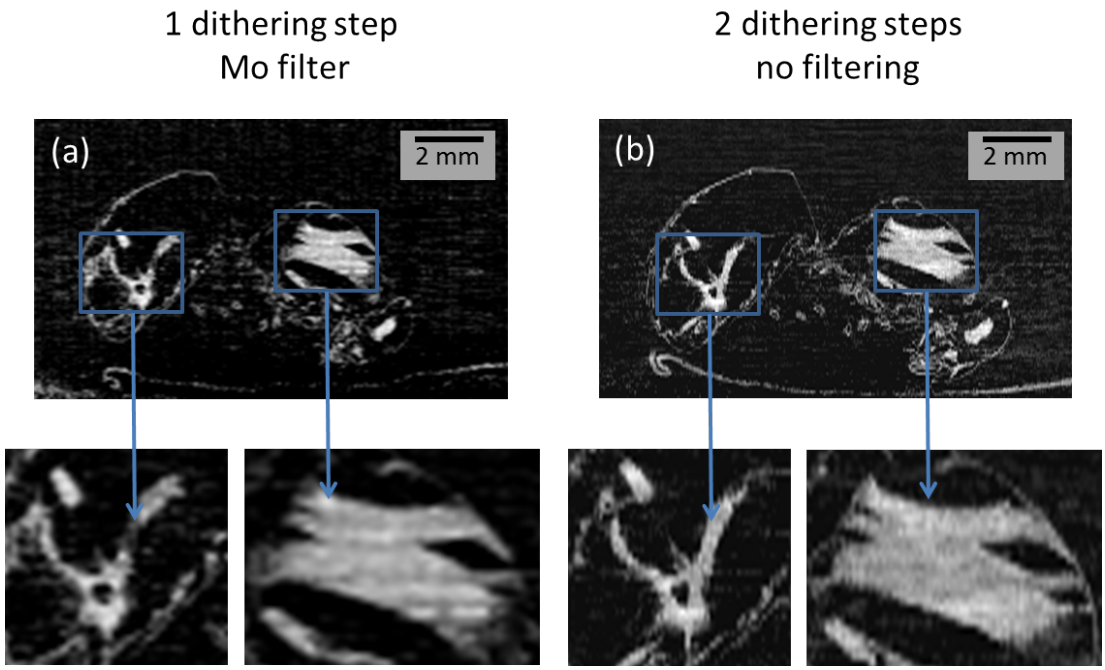

Figure 6.15: Coronal slices extracted from the RID map of a domestic wasp. The data in (a) was acquired without dithering and with a molybdenum filter, while that in (b) was acquired with 2 dithering steps without any additional filtration. Enlarged views of the indicated regions (abdomen and thorax) are provided.

Figure 6.16 shows two volume renderings of the wasp reconstructed from non-dithered projections acquired with the molybdenum filter. The volume renderings were created using ImageJ. The image in (a) shows the insect from the side, while the one in (b) provides a top view of the inside of the animal (the upper part of thorax and abdomen were cropped). The structure of the thorax, the head and the abdomen are clearly visible. Please note that, if dithering had been applied, very fine structures such as the wings and the legs of the animal would be more defined.

Figure 6.17 shows the results for the atherosclerotic plaque specimen. Transverse, coronal and sagittal cross-sections can be seen in (a-c). The narrowing and, partially, the complete obstruction of the lumen (stenosis) can be clearly appreciated. The images in (b,c) reveal a slight difference in the grey values within the plaque, which indicates different tissue components. Figures (d,e) show a

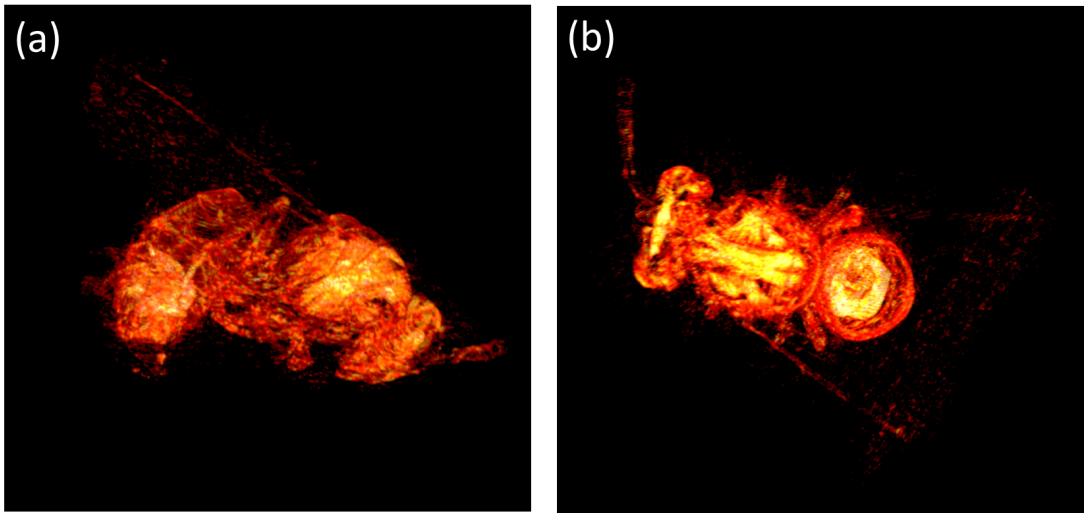

Figure 6.16: Volumetric renderings of the RID map of the domestic wasp, resulting from datasets acquired without dithering and with the molybdenum filter. (a) provides a side view, (b) shows the wasp from the top, after the upper part of its body was cropped off.

top view and a cropped side view of the volumetric renderings. While in (d), the narrowing and ultimately complete closure of the lumen are again apparent, the non-homogeneous plaque composition can be better appreciated in (e). In order to emphasize this inhomogeneity, a different colour map was used to render the volumetric data (see image in (f)). For comparison, the image in (g) shows the volumetric rendering of the reconstructed absorption term map. Here, the plaque appears entirely uniform, and no hint of different tissue components can be spotted, which confirms the lower soft tissue contrast provided by absorption-based reconstructions. These images show that EI-CT can detect differences in the composition of a plaque specimen, which indicates potential for the differentiation of vulnerable from non-vulnerable plaques. It should be noted that, in situations where dose is not a concern, even better soft tissue contrast could be achieved by removing the molybdenum filter. Moreover, a higher resolution could be achieved if needed through a higher number of dithering steps.

As clarified above, the obtained results are very preliminary, and require further investigation. Most importantly, histological examination of the imaged

specimen will be necessary in order to confirm the presence of different tissue components in the plaque. Moreover, more specimens with different pathologies will need to be imaged. Finally, in order to prove clinical usefulness, the x-ray energy used for imaging will need to be adjusted to increased specimen thickness. However, these preliminary results provide an indication of the method's usefulness in the imaging of atherosclerotic plaques.

6.5 Chapter Summary and Conclusion

This chapter was focused only on the laboratory implementation of the method. In particular, the coded aperture EI-CT scanner described in chapter 4.6 was considered.

In coded aperture EI imaging, dithering can be used to enhance the spatial resolution. This also affects the integration of the derivative of the phase function, for the reason that a higher number of dithering steps results in a denser sampling rate. However, dithering also leads to a higher radiation dose delivered to the imaged object.

In the first half of the chapter, the effect of the number of dithering steps on the quantitative information extracted from:

1. planar images of the phase function, if the object geometry is known,
2. CT reconstructions of RID maps

was studied. It was shown that at least 16 to 32 dithering steps are required to extract the quantitative information correctly and unambiguously from planar datasets. In contrast, only 1 to 2 dithering steps are required when the same information is extracted from the reconstructed RID maps. This leads to the conclusion that the quantitative accuracy of RID maps and resolution enhancement are decoupled in EI-CT. Therefore, the dose delivered during a scan can be tailored to match the structure and fine details of the object.

In the second half of the chapter, dose estimates for EI-CT imaging of small animals were provided and shown to be within the limits of what is considered

acceptable. Finally, EI-CT images of selected biological objects were shown, which were acquired under low-dose conditions.

The obtained results demonstrate the strength of the laboratory implementation of EI-CT and its suitability for small animal imaging and other biomedical areas.

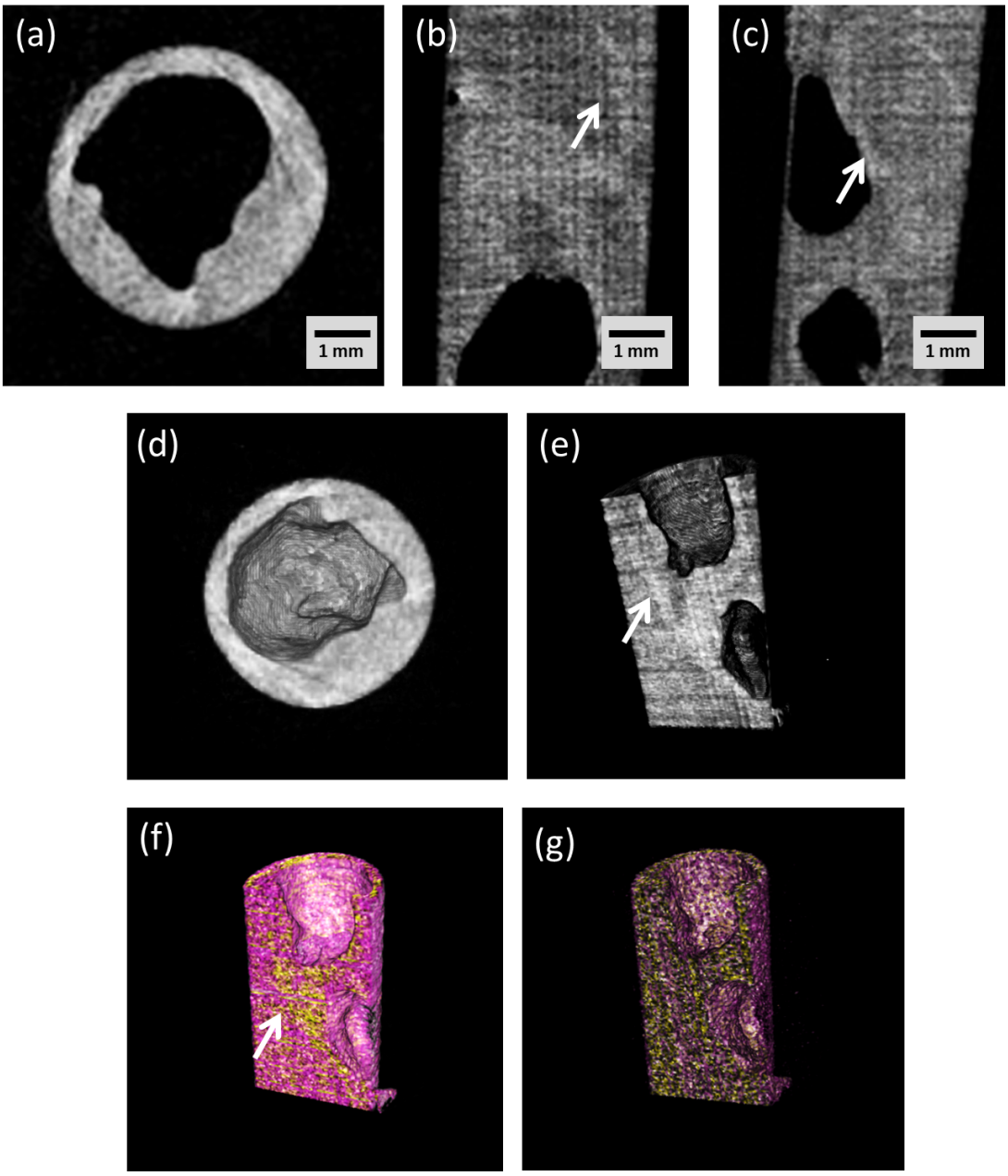

Figure 6.17: Reconstructed EI-CT images of an atherosclerotic plaque specimen: (a-c) transverse, coronal and sagittal cross-sections of the reconstructed RID map, (d,e) 3D renderings of the reconstructed RID map, (f) same rendering as in (e) but visualised in a different color map, (g) 3D rendering of the reconstructed absorption term map.

Chapter 7

Conclusion and Outlook

In the following, a summary of this thesis will be given and conclusions will be drawn from the presented work. The novelty of the work and the contributions to knowledge will be emphasized. Finally, we will point out open problems and suggest ways to improve EI-CT in future developments.

7.1 Summary and Key Contributions to the Field

The work presented in this thesis was motivated by the demand for high resolution 3D imaging modalities providing enhanced soft tissue contrast that can be implemented outside synchrotrons. PC methods provide a potential solution: contrast is driven by the RID rather than the absorption term, the former being much larger than the latter for low absorbing materials and x-ray energies typically used in biomedical applications. However, most existing PC methods suffer from drawbacks affecting their implementation outside synchrotron facilities, and therefore their wider applicability in biomedical research. These are: high demands on system alignment and stability, needs for monochromatic and quasi-parallel beams, high spatial coherence requirements, small FOVs, long acquisition times and excessive dose delivery. The EI method has the potential to overcome or at least mitigate some if not all of these drawbacks. It is readily extended to cone beams and large FOVs through the use of coded aperture masks. The low aspect ratios of the masks mean that system stability is not as critical

as for example in GI. The EI method is totally non-interferometric, hence it does not require a coherent beam. Moreover, the pre-sample mask shields the imaged object from from radiation that does not contribute to the image formation process, enabling the implementation of low-dose scans.

Until now, however, the EI method had *not* been extended to CT. The aim of the presented work was the development of EI-CT, in order to combine the strengths of EI with those of CT imaging. Not only does CT imaging solve the problem of overlapping structures in planar projections, it also enables quantitative imaging, i.e. the reconstruction of maps that can be related to the object's materials. The specific objectives of the development of EI-CT were to provide the necessary practical and theoretical bases for a CT extension, to investigate the quantitative accuracy of the reconstructed maps, to estimate the delivered dose and to explore the possibility of low-dose sampling schemes. Moreover, new scientific areas were identified that can benefit from EI-CT, among which were the imaging of murine cartilage and of acellular scaffolds for transplantable organs.

For the development of the technique, both scanning (typically implemented at synchrotrons) and coded aperture EI methods (typically used with conventional equipment) were considered. It was explained that two sensitivity modes of EI-CT need to be distinguished, differing in the relative orientation of phase sensitivity and AOR. The two modes allow for the reconstruction of maps of a number of physical quantities, amongst which are the RID, the absorption term and a linear combination of both. Depending on the sensitivity mode and on the map that has to be reconstructed, the application of a phase retrieval procedure to separate phase and absorption information is required prior to CT reconstruction. The phase retrieval formulas yield, besides the projected absorption term, the derivative of the phase function; EI can therefore be included in the class of DPC methods. One of the consequences of this is that RID maps can be reconstructed via the FBP with the Hilbert filter, or with the ramp filter after or prior to a one-dimensional integration.

The quantitative accuracy of the RID maps depends on how closely the used EI-CT scanner satisfies the assumptions underpinning the phase retrieval formulas, and whether reconstruction artefacts are present. For a synchrotron implementation of the scanning EI-CT method, the reconstructed RID maps yielded

the correct trend for a number of high and low absorbing materials; however, nominal values were slightly under-estimated due to a combination of coherence effects, which are not accounted for in the used phase retrieval formula, and reconstruction artefacts. Conversely, the recovered absorption terms were in good agreement with nominal values. For an implementation of the coded aperture EI-CT method that uses a polychromatic source, the reconstructed RID and absorption term maps were used to estimate the effective phase and absorption energies of the scanner. The possibility to reconstruct mixed phase and absorption maps which still retain a quantitative meaning (in the shape of a weighted sum of differential phase and absorption when the weights depend on the imaging system and are known in advance) was also demonstrated.

The integration step (either built into the FBP via the Hilbert filter, or applied before or after the back-projection) required for the reconstruction of RID maps can introduce artefacts, as local errors get smeared along integration trajectories. In coded aperture EI-CT, an additional potential source of error is under-sampling, as the object is illuminated spatially by separated beamlets. The sampling rate can be increased by dithering, which, however, comes at the cost of increased scan time and dose. In the CT case, however, it was shown that the quantitative accuracy of the RID maps is almost independent of the number of dithering steps (i.e. the sampling rate). The dose delivered during dithered and non-dithered EI-CT scans were estimated for the special case of small animal imaging, and shown to lie well below the acceptable limits.

Effectively, the main result of the presented research is the development of the EI-CT method, a tool for the investigation of new scientific applications at synchrotrons and for performing imaging tasks that require repeated PC-CT scans in the research laboratories (e.g. for small animal imaging). It was also shown that the method can mitigate or even remove the limitations associated with the other existing PC-CT methods. The options to implement EI-CT in two opposing sensitivity modes and to reconstruct maps of different physical quantities demonstrates the versatility and "multi-modality" of the method. The type of map to reconstruct can be chosen according to the specific application. Quantitative imaging with EI-CT is feasible, and appears to be limited only by physical effects

not accounted for in the phase retrieval model (e.g. coherence). Polychromaticity could also be considered a limit in the sense that it imposes the definition of an "effective" energy, but this is an inescapebable, intrinsic problem common to any method using polychromatic radiation. The possibility to perform low-dose scans is an additional strength of the method. It implies its suitability for biomedical applications such as, for example, tissue engineering and osteoarthritis research. This may pave the way for the eventual translation of PC-CT into clinics, e.g. for the early detection of atherosclerosis.

The presented research is substantially novel since the extension of the EI method to CT has never been attempted before. Moreover, our work added the following original contributions to the field of PC-CT and its potential applications:

- We have shown the first ever (to the best of our knowledge) PC-CT images of acellular organ scaffolds. In particular the achieved image quality, sufficiently high to extract clinically relevant information, implies the potential impact of PC-CT in this and other fields where soft tissue imaging is required.

- We have provided options for application-specific imaging, implying optimised image quality, provided by the identification of the two sensitivity modes and the consequential option to reconstruct maps of different physical quantities.

- Options to test and optimise new EI-CT reconstruction schemes (i.e. based on iterative algorithms, see next sub-chapter) on simulated data before carrying out long experimental scans, provided by the extension of an existing EI simulation software to a CT geometry.

- The extension of two planar EI systems to CT modalities. One of them is installed permanently at UCL and can be used for on site development of the method investigation of new applications; the other one can be rapidly set up both at Elettra and the ESRF as the necessary hardware is now available and the local scientists have the required expertise.

- The possibility to extract a quantitatively accurate equivalent of the Hounsfield units in conventional CT from EI-CT measurements, given by the RID. This is important for the identification of tissue types, as, for example, required for the assessment of the vulnerability of atherosclerotic plaques.

- Having overcome or at least mitigated the problems of all other existing PC-CT methods. Most importantly, the fundamental problem of excessive dose delivery (by which GI-CT seems particularly affected) was solved by demonstrating the possibility of low-dose EI-CT. This result strongly indicates the suitability the method to laboratory-based small animal studies.

7.2 Suggestions for Future Improvements of the Method

In the following, open problems and suggestions for the future improvement of EI-CT will be discussed.

7.2.1 Reconstruction Artefacts

CT imaging is always associated with reconstruction artefacts, the most common being ring and "star-pattern" artefacts. Ring artefacts originate from a non-uniform detector response that cannot be corrected by flat field normalisations, or from defective pixels. EI-CT images are prone to ring artefacts just as conventional CT methods are. A number of methods can be used for their correction (e.g. Muench et al. [2009], Anas et al. [2010]). "Star-pattern" artefacts are due to angular under-sampling, and can be mitigated by increasing the number of projections.

In addition to these common artefacts, RID maps reconstructed from EI-CT data are also prone to artefacts which are method-specific. As was explained, local errors in the differential phase sinograms are propagated across the RID maps during the integration step contained in the reconstruction procedures. This results in either stripe artefacts if a unidirectional integration is carried out,

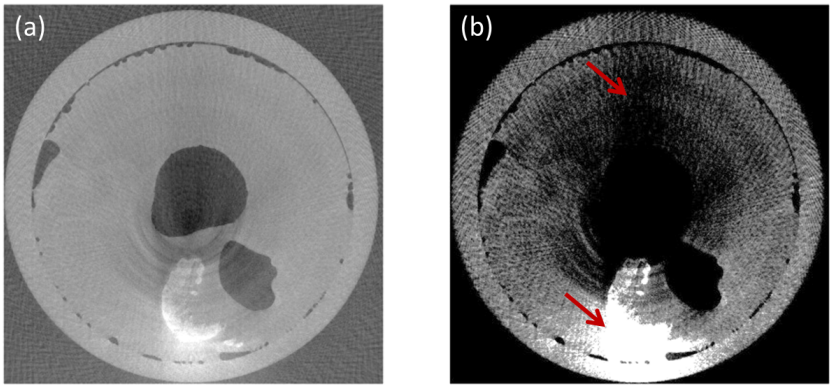

Figure 7.1: Example of a strong "gradient" artefact in a RID map reconstructed from coded aperture EI-CT measurements, displayed with normal windowing (a) and stretched contrast (b). The images show a transverse slice of an atherosclerotic plaque specimen contained within a gel-filled cylinder.

or "gradient" artefacts if the integration is carried out "implicitly" through the Hilbert filter.

Errors in the differential phase sinograms can be due to different sources. For coded aperture EI-CT, it was demonstrated that errors which are due to under-sampling do not affect the reconstructed RID maps. Under-sampling errors were shown to be random, and to average out during the CT reconstruction process. Instead, integration artefacts are caused by errors which are not random but systematic, e.g. errors that can be introduced during phase retrieval. Typically, the IC used for phase retrieval is measured as an average over the entire FOV, and the "working points", i.e. the shifts of the sample mask corresponding to the selected slope positions, are assumed to be the same for all pixels in the projections. However, due to mask imperfections or misalignment, the IC and the corresponding working points may, in reality, vary within the FOV. As a consequence, the phase retrieval formula yields incorrect differential phase values for those pixels with ICs and working points significantly different from the "average". When reconstructing RID maps from these erroneous differential phase projections via the FBP with the Hilbert filter, "gradient" artefacts appear.

An example of a "gradient" artefact originating from locally inaccurate phase

retrieval is shown in figure 7.1. Figure 7.1 (a) shows a reconstructed RID map for an atherosclerotic plaque specimen (from a different dataset as presented in chapter 6.4), reconstructed from coded aperture EI-CT data. Besides the gel-filled cylinder containing the specimen (medium grey), air bubbles (dark grey), and calcified tissue (light grey), the image shows a low frequency gradient, which becomes more apparent after stretching the contrast, as shown in (b). This gradient is indicated by arrows. Besides degrading the image quality, the strong gradient could possibly mask or be mistaken for faint structures present in the RID map. Therefore, especially when features with low RID differences are expected, it is important to avoid or reduce this type of artefact.

For this purpose, we suggest the performance of a local instead of an averaged phase retrieval. The IC should be measured on a pixel-by-pixel basis, and the working points corresponding to its slopes should be determined locally by comparing acquired flat field data to the IC values for each individual pixel. When applying the phase retrieval formula, the IC and working points should thus be pixel-specific. As a result, we anticipate a more accurate determination of the differential phase, which would lead to a reduction of "gradient" artefacts. Local phase retrieval would account for mask imperfections and misalignment, leading to an improved robustness of EI-CT.

7.2.2 The Role of Iterative CT Reconstruction Algorithms with Respect to Dose and Fast Acquisitions

The reconstruction of the EI-CT images presented in this thesis was entirely based on the FBP. A strength of the FBP is its computational speed as a result of its FFT-based implementation, however, "complete" (i.e. acquired for a relatively large number of angles) projection data are required to achieve satisfactory CT reconstructions. In contrast, iterative reconstruction algorithms based on algebraic or statistical approaches are associated with long computation times; however, they can provide satisfactory results also for "incomplete" projection data. Moreover, iterative approaches are highly flexible, as they allow incorporating elements of the image acquisition system, as well as any prior information available on the sample. These can be used to impose regularisation constraints

on the reconstruction algorithm.

The need to acquire projections at a large number of angles implies long scan times and high doses delivered to the object; therefore, the use of iterative methods can be considered advantageous. Dedicated iterative methods have already been derived and applied to PC-CT (e.g. Sidky et al. [2010], Koehler et al. [2011] Li and Luo [2011], Sunaguchi et al. [2013]). In particular, the use of the Equally Sloped Tomography (EST) algorithm by Miao et al. [2005] in ABI-CT resulted in a very low MGD for images of the breast.

In this thesis, the possibility of low-dose EI-CT was demonstrated; however, this was primarily due to the relaxed dithering requirements. The use of iterative methods could result in an additional reduction in the number of required angles, hence, if applied to EI-CT, it would enable the delivery of even lower doses and the use of reduced scan times. In order to exploit the advantages of iterative methods for EI-CT, we suggest that the following steps should be taken. First, iterative methods and their regularisation requirements should be identified. Potential candidates are those algorithms which have already been used for the other PC-CT methods, but other options could also be considered. Next, specific samples that can benefit from EI-CT imaging should be selected, for example murine cartilage, or acellular organ scaffolds. The sample geometry should be used as prior information, and incorporated in the selected iterative reconstruction method as a regularising constraint. Finally, the lowest number of angles required for a satisfactory CT reconstruction should be determined for each sample.

The use of iterative methods will enhance the flexibility of EI-CT. It will enable the individual optimisation of the acquisition parameters, e.g. with respect to dose and scan times, by "tailoring" the reconstruction method to the specific application. We expect the use of iterative methods to be a key aspect of the future development of EI-CT.

References

Als-Nielson, J. and McMorrow, D. (2001). *Elements of Modern X-ray Physics*. John Wiley and Sons, Chichester. 3

Anas, E. et al. (2010). Removal of ring artifacts in CT imaging through detection and correction of stripes in the sinogram. *Physics in Medicine and Biology*, 55:6911. 177

Arfelli, F. et al. (2000). Mammography with synchrotron radiation: phase-detection techniques. *Radiology*, 215:286. 7, 34

Arharti, B. et al. (2008). Phase imaging using a polychromatic x-ray laboratory source. *Optics Express*, 16(24):19950. 33, 34

Badylak, S. et al. (2012). Engineered whole organs and complex tissues. *Lancet*, 379:943. 55

Bansal, P. et al. (2010). Cationic contrast agents improve quantifications of glycosaminoglycan (GAG) content by contrast enhanced CT imaging of cartilage. *Journal of Orthopaedic Research*, 29:704. 46

Bech, M. et al. (2009). Soft-tissue phase contrast tomography with an x-ray tube source. *Physics in Medicine and Biology*, 54:2747–2753. 9, 38

Bonse, U. and Hart, M. (1965). An x-ray interferometer. *Applied Physics Letters*, 6(8):155. 6, 14

Boone, J. et al. (1997). Molybdenum, rhodium, and tungsten anode spectral models using interpolating polynomials with application to mammography. *Medical Physics*, 24(12):1863. 107

Born, M. and Wolf, E. (1959). *Principles of Optics*. Pergamon Press Ltd, London. 4

Braun, H. and Gold, G. (2011). Diagnosis of osteoarthritis: imaging. *Bone*, 51(2):278. 44, 45, 46

Bravin, A. et al. (2007). High-resolution CT by diffraction-enhanced x-ray imaging: mapping of breast tissue samples and comparison with their histopathology. *Physics in Medicine and Biology*, 52:2197. 8, 37

Bravin, A. et al. (2013). X-ray phase contrast imaging: from pre-clinical applications towards clinics. *Physics in Medicine and Biology*, 58:R1. 7

Bronnikov, A. (2002). Theory of quantitative phase-contrast computed tomography. *Journal of the Optical Society of America A*, 19(3):472. 33

Burvall, A. et al. (2011). Phase retrieval in x-ray phase contrast imaging suitable for tomography. *Optics Express*, 19(11):10359. 15, 57

Chapman, D. et al. (1997). Diffraction enhanced x-ray imaging. *Physics in Medicine and Biology*, 42:2015. 17, 36

Chen, A. et al. (2012). PITRE: software for phase-sensitive x-ray image processing and tomography reconstruction. *Journal of Synchrotron Radiation*, 19:836. 50

Cheng, H. et al. (2010). The acellular matrix (ACM) for bladder tissue engineering: a quantitative magnetic resonance imaging study. *Magnetic Resonance in Medicine*, 64:341. 56

Cloetens, P. et al. (1996). Phase objects in synchrotron radiation hard x-ray imaging. *Journal of Physics D: Applied Physics*, 29:133. 8, 15

Cloetens, P. et al. (1999). Holotomography: quantitative phase tomography with micrometer resolution using hard synchrotron radiation x-rays. *Applied Physics Letters*, 75(19):2912. 15

Coan, P. et al. (2006). Evaluation of imaging performance of a taper optics CCD "FReLoN" camera designed for medical imaging. *Journal of Synchrotron Radiation*, 13:260. 58

Coan, P. et al. (2008). Analyzer-based imaging technique in tomography and metal implants: a study at the ESRF. *European Journal of Radiology*, 68:S41. 8, 36

Coan, P. et al. (2010a). Characterization of osteoarthritic and normal human patella cartilage by computed tomography x-ray phase contrast imaging. *Investigative Radiology*, 45(7):347. 46

Coan, P. et al. (2010b). In vivo x-ray phase contrast analyzer-based imaging for longitudinal osteoarthritis studies in guinea pigs. *Physics in Medicine and Biology*, 55:7649. 8, 46

David, C. et al. (2002). Differential x-ray phase contrast imaging using a shearing interferometer. *Applied Plysics Letters*, 81:3287. 17

David, C. et al. (2007a). Fabrication of diffraction gratings for hard x-ray phase contrast imaging. *Microelectronic Engineering*, 84:1172. 19

David, C. et al. (2007b). Hard x-ray phase imaging and tomography using a grating interferometer. *Spectrochimica Acta Part B*, 62:626. 38

Davis, T. et al. (1995). Phase-contrast imaging of weakly absorbing materials using hard x-rays. *Nature*, 378:595. 7

Dhandayuthapani, B. et al. (2011). Polymeric scaffolds in tissue engineering application: a review. *International Journal of Polymer Science*, 2011:290682. 55

Diemoz, P. et al. (2010a). Absorption, refraction and scattering in analyzer-based imaging: comparison of different algorithms. *Optics Express*, 18(4):3494. 17

Diemoz, P. et al. (2010b). Comparison of analyzer-based imaging computed tomography extraction algorithms and application to bone-cartilage imaging. *Physics in Medicine and Biology*, 55:7663. 35, 37, 46

Diemoz, P. et al. (2011). A simplified approach for computed tomography with an x-ray grating interferometer. *Optics Express*, 19(3):1691. 11, 40, 124

Diemoz, P. et al. (2013). X-ray phase contrast imaging with nanoradian angular resolution. *Physical Review Letters*, 110:138105. 10, 21, 47, 65

Dilmanian, F. et al. (2000). Computed tomography of x-ray index of refraction using the diffraction enhanced method. *Physics in Medicine and Biology*, 45:933. 8, 35, 36

Dixon, R. et al. (2010). Comprehensive methodology for the evaluation of radiation dose in x-ray computed tomography. Technical report, American Association of Physicists in Medicine. 159, 165

Donath, T. et al. (2008). Phase-contrast imaging and tomography at 60 keV using a conventional x-ray tube. *Proceedings of SPIE*, 7078:707817. 38

Donath, T. et al. (2010). Toward clinical x-ray phase-contrast CT. *Investigative Radiology*, 45(7):445. 91

Drukteinis, J. et al. (2013). Beyond mammography: New frontiers in breast cancer screening. *The American Journal of Medicine*, 126:472. 1

Elliot, M. et al. (2012). Stem-cell-based, tissue engineered tracheal replacement in a child: a 2-year follow-up study. *Lancet*, 380:994. 55

Feeman, T. (2010). *The Mathematics of Medical Imaging*. Springer. 25, 26, 30

Feldkamp, L. et al. (1984). Practical cone-beam algorithm. *Journal of the Optical Society of America A*, 1(6):612. 27

Gasilov, S. et al. (2013). On the possibility of quantitative refractive-index tomography of large biomedical samples with hard x-rays. *Biomedical Optics Express*, 4(9):1512. 35, 37

Goldring, M. and Goldring, S. (2007). Osteoarthritis. *Journal of Cellular Physiology*, 213:626. 44, 45

Groso, A. et al. (2006). Phase oontrast tomography: an alternative approach. *Applied Physics Letters*, 88:214104. 33, 34

Guigay, J. et al. (2007). Mixed transfer function and transport of intensity approach for phase retrieval in the fresnel region. *Optics Letters*, 32(12):1617. 33

Guldberg, R. et al. (2004). Microcomputed tomography imaging of skeletal development and growth. *Birth Defects Research (Part C)*, 72:250. 159

Gureyev, T. et al. (1995). Partially coherent fields, the transport-of-intensity equation, and phase uniqueness. *Journal of the Optical Society of America A*, 12(9):1942. 4

Gureyev, T. et al. (2006). Phase-and-amplitude computed tomograhy. *Applied Physics Letters*, 89:034102. 33

Gureyev, T. et al. (2009). Refracting roentgen's rays: propagation-based x-ray phase contrast for biomedical imaging. *Journal of Applied Physics*, 105:102005. 33

Gureyev, T. and Wilkins, S. (1998). On x-ray phase imaging with a point source. *Journal of the Optical Society of America A*, 15(3):579. 4

Hart, D. et al. (2010). Frequency and collective dose for medical and dental x-ray examinations in the UK, 2008. Technical report, HPA-CRCE-012. 1

Henke, B. et al. (1993). X-ray interactions: photoabsorption, scattering, transmission, and reflection at E = 50-30000, Z = 1-92. *Atomic Data and Nuclear Data Tables*, 54(2):181. 93, 109

Herzen, J. et al. (2009). Quantitative phase-contrast tomography of a liquid phantom using a conventional x-ray tube. *Optics Express*, 17(12):10010. 9, 38, 39, 155

Hetterich, H. et al. (2013). Grating-based x-ray phase-contrast tomography of atherosclerotic plaque at high photon energies. *Zeitschrift fuer Medizinische Physik*, 23(3):194. 9, 166

Holdsworth, D. and Thornton, W. (2002). Micro-CT in small animal and specimen imaging. *Trends in Biotechnology*, 20(8):S34. 2, 40

Huang, Z. et al. (2006). Direct computed tomographic reconstruction for directional derivative projections of computed tomography of diffraction enhanced imaging. *Applied Physics Letters*, 89:041124. 30, 35

Ignatyev, K. et al. (2011). Coded apertures allow high-energy x-ray phase contrast imaging with laboratory sources. *Journal of Applied Physics*, 110:014906. 23

Ingal, V. and Beliaevskaya, E. (1995). X-ray plane-wave topography observation of the phase contrast from a non-crystalline object. *Journal of Physics D: Applied Physics*, 28:2314. 7

Jensen, T. et al. (2013). Imaging of metastatic lymph nodes by x-ray phase contrast micro-tomography. *PLOS ONE*, 8(1):e54047. 8

Kak, A. and Slaney, M. (1987). *The principles of computerized tomography*. Society for Industrial and Applied Mathematics USA. 25, 30, 84, 138

Kao, T. et al. (2009). Characterization of diffraction-enhanced imaging contrast in breast cancer. *Physics in Medicine and Biology*, 54:3247. 37

Kasraie, N. and Clarke, G. (2012). Characterizing atherosclerotic plaque with computed tomography: a contrast-detail study. *Proceedings of SPIE*, 8318:83181M–1. 166

Keyrilaeinen, J. et al. (2008). Toward high-contrast breast CT at low radiation dose. *Radiology*, 249(1):321. 1, 8, 37

Kido, K. et al. (2010). Bone cartilage imaging with x-ray interferometry using a practical x-ray tube. *Proceedings of SPIE*, 7622:762240. 47

Klebaner, F. (2005). *Introduction to Stochastic Calculus with Applications, Second Edition*. Imperial College Press, London. 153, 154

Koehler, T. et al. (2011). Iterative reconstruction for differential phase contrast imaging using spherically symmetric basis functions. *Medical Physics*, 38(8):4542. 180

Kottler, C. et al. (2007). A two-directional approach for grating based differential phase contrast imaging using hard x-rays. *Optics Express*, 15(3):1175. 35, 137

Krasnokutsky, S. et al. (2007). Osteoarthritis in 2007. *Bulletin of the NYU Hospital for Joint Diseases*, 65(2):222. 44, 45

Langer, M. et al. (2008). Quantitative comparison of direct phase retrieval algorithms in in-line phase tomography. *Medical Physics*, 35(10):4556. 4, 15, 33

Lee, Y. et al. (2010). Articular cartilage imaging by the use of phase-contrast tomography in a collagen-induced arthritis mouse model. *Academic Radiology*, 17(2):244. 47

Lewis, R. (2004). Medical phase contrast x-ray imaging: current status and future prospects. *Physics in Medicine and Biology*, 49:3573. 4, 9

Li, X. and Luo, S. (2011). A compressed sensing-based iterative algorithm for CT reconstruction and its possible application to phase contrast imaging. *BioMedical Engineering OnLine*, 10(73). 180

Luu, M. et al. (2011). Quantitative phase imaging with polychromatic x-ray sources. *Optics Express*, 19(9):8127. 33, 34

Marenzana, M. et al. (2012). Visualization of small lesions in rat cartilage by means of laboratory-based x-ray phase contrast imaging. *Physics in Medicine and Biology*, 57:8173–8184. 8, 46, 47

Marenzana, M. et al. (2013). Synchrotron and lab-based x-ray phase contrast imaging for imaging mouse articular cartilage in absense of radiopaque contrast agents. *Accepted for publication in Philosophical Transactions of the Royal Society A*. 45, 46, 49

McCollough, C. et al. (2011). CT dose index and patient dose: they are not the same thing. *Radiology*, 259(2):311. 161

Miao, J. et al. (2005). Equally sloped tomography with oversampling reconstruction. *Physical Review B*, 72:052103. 37, 180

Millard, T. et al. (2013). Method for automatization of the alignment of a laboratory based x-ray phase contrast edge illumination system. *Review of Scientific Instruments*, 84:083702. 9, 24, 87

Mollenhauer, J. et al. (2002). Diffraction-enhanced x-ray imaging of articular cartilage. *Osteoarthritis and Cartilage*, 10:163. 8, 37, 46

Momose, A. (2005). Recent advances in x-ray phase imaging. *Japanese Journal of Applied Physics*, 44(9A):6355. 15

Momose, A. et al. (1996). Phase-contrast x-ray computed tomography for observing biological soft tissues. *Nature Medicine*, 2(4):473. 8, 15, 33

Momose, A. et al. (2003). Demonstration of x-ray talbot interferometry. *Japanese Journal of Applied Physics*, 42:L866. 7, 17

Momose, A. et al. (2006). Phase tomography by x-ray talbot interferometry for biological imaging. *Japanese Journal of Applied Physics*, 45(6A):5254. 8, 38

Momose, A. et al. (2011). Four-dimensional x-ray phase tomography with talbot interferometry and white synchrotron radiation: dynamic observation of a living worm. *Optics Express*, 19(9):8423. 41

Momose, A. and Fukuda, J. (1995). Phase-contrast radiographs of non-stained rat cerebellar specimen. *Medical Physics*, 22(4):375. 14

Moreno, P. (2010). Vulnerable plaque: Definitions, diagnosis and treatment. *Cardiology Clinics*, 28(1):1. 166

Muehlemann, C. et al. (2004). X-ray detection of structural orientation in human articular cartilage. *Osteoarthritis and Cartilage*, 12:97. 46

Muehlemann, C. et al. (2009). Diffraction-enhanced imaging of musculoskeleteral tissues using a conventional x-ray tube. *Academic Radiology*, 16(8):918. 47

Muench, B. et al. (2009). Stripe and ring artifact removal with combined wavelet - fourier filtering. *Optics Express*, 17(10):8567. 177

Munro, P. et al. (2010a). The relationship between wave and geometrical optics models of coded aperture type x-ray phase contrast imaging systems. *Optics Express*, 18(5):4103. 79

Munro, P. et al. (2010b). Source size and temporal coherence requirements of coded aperture type x-ray phase contrast imaging systems. *Optics Express*, 18(19):19681. 9, 79, 80, 99

Munro, P. et al. (2012). Phase and absorption retrieval using incoherent x-ray sources. *Proceedings of the National Academy of Sciences USA*, 109:13922. 23

Munro, P. et al. (2013a). A quantitative, non-interferometric x-ray phase contrast imaging method. *Optics Express*, 21(1):648. 23

Munro, P. et al. (2013b). A simplified approach to quantitative coded aperture x-ray phase imaging. *Optics Express*, 21(9):11187. 9, 23, 48, 65, 109

Munro, P. and Olivo, A. (2013). X-ray phase contrast imaging with polychromatic sources and the concept of effective energy. *Physical Review A*, 87:053838. 34, 40, 107, 112, 119

Natterer, F. (1986). *The Mathematics of Computerized Tomography*. Teubner. 25

Nesterets, Y. et al. (2006). On qualitative and quantitative analysis in analyser-based imaging. *Acta Crystallographica A*, 62:296. 37

Noel, P. et al. (2013). Evaluation of the potential of phase-contrast computed tomography for improved visualization of cancerous human liver tissue. *Zeitschrift fuer Medizinische Physik*, 23:204. 8

Olivo, A. et al. (2001). An innovative digital imaging setup allowing a low-dose approach to phase contrast applications in the medical fields. *Medical Physics*, 28(8):1610. 7, 9, 19

Olivo, A. et al. (2009). A non-free-space propagation x-ray phase contrast imaging method sensitive to phase effects in two directions simultaneously. *Applied Physics Letters*, 94:044108. 64

Olivo, A. et al. (2011). A coded-aperture based method allowing non-interferomentric phase contrast imaging with incoherent x-ray sources. *Nuclear Instruments and Methods in Physics Research*, A(648):S28. 22

Olivo, A. et al. (2013). Low-dose phase contrast mammography with conventional x-ray sources. *Medical Physics*, 40(9):090701. 8, 23

Olivo, A. and Speller, R. (2006). Experimental validation of a simple model capable of predicting the phase contrast imaging capabilities of any x-ray imaging system. *Physics in Medicine and Biology*, 51:3015. 15, 108

Olivo, A. and Speller, R. (2007a). Coded-aperture technique allowing x-ray phase contrast imaging with conventional sources. *Applied Physics Letters*, 91(1):074106. 7, 9, 21

Olivo, A. and Speller, R. (2007b). Modelling of a novel x-ray phase contrast imaging technique based on coded apertures. *Physics in Medicine and Biology*, 52:6555. 9, 21, 23, 79

Paganin, D. et al. (2002). Simultaneous phase and amplitude extraction from a single defocused image of a homogeneous object. *Journal of Microscopy - Oxford*, 206:33. 15, 57

Peterzol, A. et al. (2005). The effects of the imaging system on the validity limits of the ray-optical approach to phase contrast imaging. *Medical Physics*, 32(12):3617. 4, 5

Pfeiffer, F. et al. (2006). Phase retrieval and differential phase-contrast imaging with low-brilliance x-ray sources. *Nature Physics*, 2:258. 7, 9, 18, 38

Pfeiffer, F. et al. (2007a). Hard x-ray phase tomography with low brilliance x-ray sources. *Physical Review Letters*, 98:108105. 9

Pfeiffer, F. et al. (2007b). High-resolution brain tumor visualization using three-dimensional x-ray phase contrast tomography. *Physics in Medicine and Biology*, 52:6923. 8

Pisano, E. et al. (2000). Human breast cancer specimens: Diffraction-enhanced imaging with histologic correlation - improved conspicuity of lesion detail compared with digital radiography. *Radiology*, 214:895. 7

Pogany, A. et al. (1997). Contrast and resolution in imaging with a microfocus x-ray source. *Review of Scientific Instruments*, 68(7):2774. 15, 16

Qi, Z. and Chen, G. (2008). Direct fan-beam reconstruction algorithm via filtered backprojection for differential phase-contrast computed tomography. *X-Ray Optics and Instrumentation*, 2008:835172. 30, 38

Rigon, L. et al. (2008a). Generalized diffraction enhanced imaging: application to tomography. *European Journal of Radiology*, 68S:S3. 35

Rigon, L. et al. (2008b). PICASSO: A silicon microstrip detector for mammography with synchrotron radiation. *IEEE Nuclear Science Symposium Conference Records*, page 1536. 85

Ruan, M. et al. (2013). Quantitative imaging of murine osteoarthritic cartilage by phase-contrast micro computed tomography. *Arthritis and Rheumatism*, 65(2):388. 47

Rutishauser, S. et al. (2011). A tilted grating interferometer for full vector field differential x-ray phase contrast tomography. *Optics Express*, 19(25):24890. 38

Saxena, A. et al. (2010). Comparison of collagen scaffold tubes for possible esophagus organ tissue engineering applications: In-situ omental implantation study in an ovine model. *European Surgery*, 42(6):309. 55

Sidky, E. et al. (2010). Image reconstruction exploiting object sparsity in boundary-enhanced x-ray phase-contrast tomography. *Optics Express*, 18(10):10404. 180

Snigirev, A. et al. (1995). On the possibilities of x-ray phase contrast microimaging by coherent high energy synchrotron radiation. *Review of Scientific Instruments*, 66:5486. 7, 15

Stampanoni, M. et al. (2011). The first analysis and clinical evaluation of native breast tissue using differential phase-contrast mammography. *Investigative Radiology*, 46(12):801. 7, 41

Stutman, D. et al. (2011). Talbot phase-contrast x-ray imaging for the small joints of the hand. *Physics in Medicine and Biology*, 56:5697. 47

Sun, Y. et al. (2007). Computerized tomography based on DEI refraction information. *Computerized Medical Imaging and Graphics*, 31:383. 35

Sunaguchi, N. et al. (2013). Iterative reconstruction algorithm for analyzer-based phase-contrast computed tomography of hard and soft tissue. *Applied Physics Letters*, 103:143702. 180

Szafraniec, M. et al. (2014). Proof-of-concept demonstration of edge-illumination x-ray phase contrast imaging combined with tomosynthesis. *Physics in Medicine and Biology*, 59:N1–N10. 80

Sztrokay, A. et al. (2012). High-resolution breast tomography at high energy: a feasibility study of phase contrast imaging on a whole breast. *Physics in Medicine and Biology*, 57:2931. 36

Takeda, M. et al. (1982). Fourier-transform method of fringe-pattern analysis for computer-based topography and interferometry. *J. Opt. Soc. Am.*, 72(1):156. 14, 41

Tapfer, A. et al. (2011). Development of a prototype gantry system for preclinical x-ray phase-contrast computed tomography. *Medical Physics*, 38(11):5910. 40

Tapfer, A. et al. (2012). Experimental results from a pre-clinical x-ray phase contrast CT scanner. *Proceedings of the National Academy of Sciences USA*, 109:15691. 9, 19, 40, 155, 165

Tapfer, A. et al. (2013). X-ray phase-contrast CT of a pancreatic ductal adenocarcinoma mouse model. *PLOS ONE*, 8(3):e58439. 8

Thuering, T. et al. (2011). Non-linear regularized phase retrieval for inudirectional x-ray differential phase contrast radiography. *Optics Express*, 19(25):25545. 35, 137

Totonelli, G. et al. (2012). A rat decellularized small bowel scaffold that preserves villus-crypt architecture for intestinal regeration. *Biomaterials*, 33:3401. 55, 56

Totonelli, G. et al. (2013). Detergent enzymatic treatment for the development of a natural acellular matrix for oesophageal regeration. *Pediatric Surgery International*, 18(47):6900. 55, 56, 58, 62

Vittoria, F. et al. (2013). Strategies for efficient and fast wave optics simulation of coded-aperture and other x-ray phase-contrast imaging methods. *Applied Optics*, 52(28):6940. 67, 79, 80, 81, 93, 109, 138, 143

Wagner, A. et al. (2013). Chance and limit of imaging articular cartilage in vitro in healthy and arthritic joints: DEI (diffraction enhanced imaging) in comparison with MRI, CT and ultrasound. *Proceedings of SPIE*, 5746:542. 46

Wang, J. et al. (2006). Reconstruction of the refractive index gradient by x-ray diffraction enhanced computed tomography. *Physics in Medicine and Biology*, 51:3391. 35, 36, 38

Weitkamp, T. et al. (2005). X-ray phase imaging with a grating interferometer. *Optics Express*, 12(16):6296. 8, 18, 38

Wilkins, S. et al. (1996). Phase-contrast imaging using polychromatic hard x-rays. *Nature*, 384:335. 7, 15, 16, 47

Willner, M. et al. (2013). Quantitative x-ray phase contrast computed tomography at 82 keV. *Optics Express*, 21(4):1455. 39

Wu, X. and Liu, H. (2007). Clarification of aspects in in-linephase-sensitive x-ray imaging. *Medical Physics*, 34(2):737. 15

Xie, L. et al. (2009). Quantitative assessment of articular cartilage morphology via EPIC-μCT. *Osteoarthritis and Cartilage*, 17:313. 46

Zanette, I. et al. (2011). Quantitative phase and absorption tomography with an x-ray grating interferometer and synchrotron radiation. *Physica Status Solidi A*, 208(11):2526. 39, 104

Zanette, I. et al. (2012). Trimodal low-dose x-ray tomograhy. *Proceedings of the National Academy of Sciences USA*, 109(26):10199. 41, 155

Zhao, Y. et al. (2012). High-resolution, low-dose phase contrast x-ray tomography for 3D diagnosis of human breast cancers. *Proceedings of the National Academy of Sciences USA*, 109:18290. 8, 37

Zhou, H. and Boone, J. (2008). Monte Carlo evaluation of CTDI in infinitely long cylinders of water, polyethylene and PMMA with diameters from 10 mm to 500 mm. *Medical Physics*, 36(6):2424. xvii, 159, 162, 163

Zhu, P. et al. (2005). Computed tomography algorithm based on diffraction-enhanced imaging setup. *Applied Physics Letters*, 87:264101. 31, 35

Zhu, P. et al. (2010). Low-dose, simple, and fast grating-based x-ray phase-contrast imaging. *Proceedings of the National Academy of Sciences USA*, 107:13576. 41

Zysk, A. et al. (2010). Transport of intensity and spectrum for partially coherent fields. *Optics Letters*, 35(13):2239–2241. 5